

EXPERIMENTAL INVESTIGATIONS ON FRICTION STIR WELDED JOINT OF DISSIMILAR ALUMINIUM ALLOYS

Thesis

Submitted in partial fulfillment of the requirements for the degree of

DOCTOR OF PHILOSOPHY

by

ANIL KUMAR K. S.



DEPARTMENT OF MECHANICAL ENGINEERING
NATIONAL INSTITUTE OF TECHNOLOGY KARNATAKA,
SURATHKAL, MANGALORE – 575025
SEPTEMBER, 2019

D E C L A R A T I O N

I hereby *declare* that the Research Thesis entitled “**EXPERIMENTAL INVESTIGATIONS ON FRICTION STIR WELDED JOINT OF DISSIMILAR ALUMINIUM ALLOYS**” which is being submitted to the **National Institute of Technology Karnataka, Surathkal** in partial fulfillment of the requirements for the award of the Degree of **Doctor of Philosophy** in **Department of Mechanical Engineering** is a *bonafide report of the research work carried out by me*. The material contained in this Research Thesis has not been submitted to any University or Institution for the award of any degree.

Register Number : **145020ME14P01**

Name of the Research Scholar : **ANIL KUMAR K.S.**

Signature of the Research Scholar :

Department of Mechanical Engineering

Place : NITK, Surathkal

Date :

CERTIFICATE

This is to *certify* that the Research Thesis entitled “**EXPERIMENTAL INVESTIGATIONS ON FRICTION STIR WELDED JOINT OF DISSIMILAR ALUMINIUM ALLOYS**” submitted by **Mr. ANIL KUMAR K.S. (Register Number: 145020ME14P01)** as the record of the research work carried out by him, is *accepted as the Research Thesis submission* in partial fulfillment of the requirements for the award of degree of **Doctor of Philosophy**.

Research Guide(s)

Prof. S.M. Murigendrappa

Professor

Department of Mechanical Engineering

NITK, Surathkal.

Dr. Hemantha Kumar

Associate Professor

Department of Mechanical Engineering

NITK, Surathkal.

Chairman-DRPC

Date:

Place: NITK, Surathkal.

Date:

ACKNOWLEDGEMENTS

With a deep sense of gratitude, I wish to express my sincere thanks to my supervisors **Prof. S.M. Murigendrappa** and **Dr. Hemantha Kumar**, Department of Mechanical Engineering, National Institute of Technology Karnataka (NITK), Surathkal, for their excellent guidance and support throughout the work. I received very useful, encouraging and excellent academic feedback from them, which has stood in good stead while writing this thesis. Their constant encouragement, help and review of the entire work during the course of the investigation were invaluable. I profoundly thank them.

I take this opportunity to acknowledge my thanks to **Prof. Shrikantha S. Rao, Head of the Department of Mechanical Engineering and Chairman, DRPC** for his continuous and timely suggestions. I express my heartfelt thanks to the **Director**, NITK, Surathkal.

I wish to thank all the members of the Research Program Assessment Committee including **Dr. Srikanth Bontha**, Associate Professor, Department of Mechanical Engineering and **Dr. Basavaraju Manu**, Associate Professor, Department of Civil Engineering for their appreciation and criticism all through this research work.

I gratefully acknowledge the help for providing the lab facilities and support received from **Prof. Sathish V Kailas**, Professor, Department of Mechanical Engineering, Indian Institute of Science (IISc.), Bangalore, Karnataka. I also acknowledge help rendered by **Prof. Narayanaprabhu**, Professor, Department of Metallurgical and Materials Engineering, NITK, Surathkal, Karnataka.

I acknowledge the support from scanning electron microscopy (SEM) lab and experimental facility provided by A Centre of excellence at NITK, Surathkal.

I wish to express my sincere gratitude to all the faculty members of the Department of Mechanical Engineering, NITK, Surathkal, for their help, encouragement and support all through this research work.

My sincere thanks to my friends Dr. Madhusudana C. K., Dr. Gurubasavaraju T. M., Dr. Gangadhar, Dr. Hemanth K, Dr. Gopi K.R, Mr. Bala Narasimha G., Mr. Suman M.L.J., Mr.

Vipin Allien J., Mr. Ravikumar K.N., and Mr. Subhash Acharya of Department of Mechanical Engineering, NITK Surathkal, for their help and support to carry out this dissertation work.

I am grateful to my dearest friends Dr. Madhu H.C., Dr. Amlan kar, Dr. Anbukkarasi R., Mr. Rajaneesh H., and Mr. Himanshu Shekar of Department of Mechanical Engineering, IISc., Bangalore, for extending their support whenever I required.

Finally, my sincere gratitude to my parents, wife and son who have trusted me throughout my life. I would like to share this moment of happiness with my mother Mrs. Jayasheela, my son Mr. Pranav. A., my wife Mrs. Rohini C., and her family, my sister Mrs. Araunashree K.S., my nephew Mr. Srujan Shaiva for their constant encouragement. I would like to dedicate my dissertation work to my father late Sri. K.P. Shivamurthy, without his dedication to provide me the best education and facilities throughout my carrier, I would not have reached this position in my life.

The list goes on and there are many others I should mention. There are people who have helped me all the way and provided me support when I didn't even realize I needed it, or needed it now, or needed it constantly. Listing all of them would fill a book itself, so I merely will have to limit myself to a few words: I THANK YOU ALL.....!

(Anil Kumar K.S.)

ABSTRACT

Friction stir welding (FSW) is solid-state joining process for producing similar or dissimilar joints of plates. Joining process carried out by means of a non-consumable rotating tool passed along the joining edges of plates, after developing sufficient amount of heat. The joints may prone to have defects such as pin-hole, cracks, tunnel defects, worm-hole defects, sharp boundary defects, etc. lead to influence the mechanical properties and microstructures. Main motivation of the present study is to produce defect-free joints and, improve the mechanical properties and microstructures of the friction stir welded dissimilar aluminium alloys joint. To achieve these, it is necessary to choose the optimum FSW parameters such as tool plunge depth, tool rotational speed, tool traverse speed, tool tilt angle, etc.

The present study focuses on selection of an optimum FSW parameters using a bottom-up optimization experimental approach for joining dissimilar aluminium alloys. Further focuses on the combined effect of tool probe offset and the tool traverse speed on the properties of welded joint. Study also focuses on the fabrication of metal matrix nano composite (MMNC) at the weld nugget zone (WNZ) of the FSW dissimilar aluminium alloys joint.

The bottom-up experimental approach has been successfully adopted for joining two dissimilar aluminium alloys of AA2024-T351 and AA7075-T651 in butt-joint configuration for optimizing the FSW parameters such as tool plunge depth (TPD), tool rotation speed (TRS) and tool travel speed (TTS). Optimized FSW parameters for taper threaded cylindrical tool are TPD, 6.20 mm, TRS, 650 rpm and TTS, 150 mm/min yields higher tensile properties such as ultimate tensile strength (UTS) of 435 MPa, yield strength (YS) of 290 MPa, percentage elongation (% EL) of 13, and maximum weld joint efficiency (η_{WJ}) of 92% with defect-free microstructures of weld region. Similarly, for taper triangle tool the TPD, 6.20 mm, TRS, 950 rpm and TTS, 90 mm/min yields a higher UTS, 440 MPa, YS, 350 MPa, % EL, 17.5 and η_{WJ} of 93% with enhanced microstructure characteristics at the weld region. The tool probe offset of 1 mm towards AA7075-T651 favours the flow characteristics of AA7075-T651 towards WNZ. In addition, increase in the TTS ranging from 20-120 mm/min has revealed higher tensile properties. Higher UTS of 435 MPa, YS of 375 MPa, % EL of 13.6 and η_{WJ} of 92% obtained for tool probe offset of 1 mm towards AA7075-T651 and TTS of 110 mm/min with constant TPD of 6.20, and TRS of 650 rpm. For the fabrication of

MMNC at the WNZ produced with varying % vol. fractions (5, 8 and 13) of SiC_{NP} revealed a higher tensile properties of UTS of 418 MPa, YS of 247 MPa and % EL of 14.5 for 5% vol. fraction SiC_{NP} with FSW second pass. The decrease in the grain size range 2-4 μm observed at the WNZ of the MMNC compared to the WNZ without SiC_{NP} having grain size range 6-8 μm .

The novelty of this work lies in the demonstration of friction stir welded joint of dissimilar aluminium alloys.

Keywords: Friction stir welding; Bottom-up approach; Optimization technique; Dissimilar aluminium alloys; Composites; Nano silicon carbide particles; Microstructure; Mechanical properties;

CONTENTS

Declaration	
Certificate	
Acknowledgements	
Abstract	
Contents	i
List of figures	viii
List of tables	xviii
Abbreviations	xx
Nomenclature	xxii
1. INTRODUCTION	
1.1 Overview.....	01
1.2 Aluminium alloys of 2000 and 7000 series.....	03
1.3 Friction stir welding (FSW).....	04
<i>1.3.1 Terminologies used in the FSW</i>	06
<i>1.3.1.1 FSW parameters and its significance</i>	06
<i>1.3.1.2 Tool geometry</i>	08
<i>1.3.1.3 Microstructure</i>	08
<i>1.3.2 Temperature distribution in the weld region</i>	10
<i>1.3.3 Mechanical properties, microstructure evaluation of the FSW joints and its significance</i>	11
<i>1.3.3.1 Tensile strength</i>	11
<i>1.3.3.2 Microstructure characterization</i>	12
<i>1.3.3.3 Hardness properties</i>	12
1.4 FSW and its application to other materials	12
1.5 Friction stir processing (FSP).....	14
1.6 Organisation of the thesis.....	15

2. LITERATURE REVIEW

2.1 Introduction.....	17
2.2 Influence of FSW parameters on microstructure and mechanical properties of similar and dissimilar materials FSW joint	17
2.2.1 Friction stir welding of similar materials	17
2.2.2 Friction stir welding of dissimilar materials.....	19
2.3 Different optimization techniques to obtain optimum FSW parameters.....	21
2.3.1 Design of experiments (DOE) techniques and analytical methods.....	21
2.3.2 Computational techniques and simulation.....	22
2.3.3 Bottom-up experimental approach.....	24
2.4 Effect of material location and tool probe offset on FSW dissimilar materials joint properties.....	24
2.4.1 Effect of material location in joining dissimilar material	24
2.4.2 Tool probe offset method in joining dissimilar materials.....	26
2.5 Production of composites at the weld nugget zone.....	27
2.5.1 Production of composites using FSP.....	27
2.5.2 Production of composites using FSW.....	27
2.6 Research gap	29
2.7 Objectives of the research work	30
2.8 Scope of the research work	31
2.9 Summary	32

3. MATERIALS, MACHINES AND METHODS

3.1 Introduction.....	33
3.2 Materials.....	33
3.2.1 Aluminium alloys.....	33
3.2.2 Reinforcement.....	34
3.3 Friction stir welding machine.....	35
3.3.1 Friction stir welding tools.....	38
3.3.2 Tool holder.....	40

3.4 Mechanical properties evaluation.....	40
3.4.1 Tensile test.....	41
3.4.2 Hardness tests.....	42
3.5 Microstructural characterisation.....	43
3.5.1 Preparation of the specimen.....	44
3.5.2 Optical microscopy (OM).....	44
3.5.3 Scanning electron microscopy (SEM).....	45
3.5.4 Transmission electron microscopy (TEM).....	45
3.5.5 Image analysis	46
3.6 Compositional characterisation	46
3.6.1 Energy dispersive spectroscopy (EDS)	46
3.6.2 X-ray diffractometer (XRD).....	46
3.7 Density measurement	47
3.8 Summary.....	47
4. A BOTTOM-UP EXPERIMENTAL APPROACH FOR OPTIMIZING THE FSW PARAMETERS	48
4.1 Introduction.....	48
4.2 Experimental techniques for bottom-up approach	48
4.3 Optimization procedures for a bottom-up experimental approach	50
4.3.1 Optimization of tool plunge depth (TPD) by varying plunge depth (VPD) experiment.....	51
4.3.2 Optimization of tool rotation speed (TRS) by varying rotation speed (VRS) experiment	54
4.3.3 Optimization of tool traverse speed (TTS) by varying traverse speed (VTS) experiment	55
4.3.4 Final optimized FSW parameters.....	56
4.4 Mechanical testing	57
4.4.1 Tensile testing.....	57
4.4.2 Micro-hardness testing.....	57
4.5 Macro and microstructure examination.....	57
4.6 Results and discussion	58

4.6.1	<i>Tensile properties</i>	58
4.6.1.1	<i>Varying plunge depth, rotation speed and traverse speed experiments using taper threaded tool</i>	58
4.6.1.2	<i>Varying plunge depth, rotation speed and traverse speed experiments using taper triangle tool</i>	65
4.6.2	<i>Macro and microstructure</i>	74
4.6.2.1	<i>Varying plunge depth, rotation speed and traverse speed experiments using taper threaded tool</i>	74
4.6.2.2	<i>Varying plunge depth, rotation speed and traverse speed experiments using taper triangle tool</i>	86
4.6.3	<i>Microhardness</i>	96
4.6.3.1	<i>Varying rotation speed experiments using taper threaded tool</i>	97
4.6.3.2	<i>Varying traverse speed experiments using taper threaded tool</i>	99
4.6.4	<i>Fractography</i>	100
4.6.4.1	<i>FSW dissimilar joint produced from taper threaded tool</i> ..	101
4.6.4.2	<i>FSW dissimilar joint produced from taper triangle tool</i>	104
4.6.5	<i>Overall conclusions for optimizing the FSW parameters using the bottom-up experimental approach</i>	105
4.7	<i>Summary</i>	106
5.	INFLUENCE OF TOOL PROBE OFFSET AND TOOL TRAVERSE SPEED ON FSW DISSIMILAR ALUMINIUM ALLOYS JOINT	
5.1	<i>Introduction</i>	107
5.2	<i>Experimental procedure for tool probe offset and varying tool traverse Speed</i>	107
5.2.1	<i>Tensile and microstructure specimen extraction</i>	109
5.3	<i>Mechanical testing</i>	110
5.4	<i>Macro and microstructure examination</i>	110
5.5	<i>Results and discussion</i>	110
5.5.1	<i>Macro and microstructure of the joints</i>	110

5.5.1.1	<i>Effect of tool probe offset towards AA2024-T351 and traverse speed.....</i>	110
5.5.1.2	<i>Effect of zero tool probe offset and traverse speed.....</i>	115
5.5.1.3	<i>Effect of tool probe offset towards AA7075-T651 and traverse speed.....</i>	119
5.5.1.4	<i>Effect of tool probe offset and traverse speed on grain size</i>	123
5.5.2	Tensile properties	126
5.5.2.1	<i>Effect of tool probe offset towards AA2024-T351 on tensile properties</i>	126
5.5.2.2	<i>Effect of zero tool probe offset on tensile properties.....</i>	128
5.5.2.3	<i>Effect of tool probe offset towards AA7075-T651 on tensile properties.....</i>	129
5.5.3	Fractography.....	131
5.5.4	Overall influence from the tool probe offset methods and traverse speed in joining dissimilar aluminium alloys joint by FSW.....	134
5.6	Summary.....	135
6.	EFFECT OF SILICON CARBIDE NANO PARTICLES REINFORCEMENT AND FSW PARAMETERS ON THE PROPERTIES OF FSW DISSIMILAR ALUMINIUM ALLOYS JOINT	
6.1	Introduction	136
6.2	Production of FSW dissimilar aluminium alloys joint reinforced with fixed volume fraction of SiC _{NP} and tool rotation speeds using FSW first pass.....	136
6.3	Production of FSW dissimilar aluminium alloys joint with varying percentage volume fractions of SiC _{NP} , without SiC _{NP} using FSW first and second pass.....	138
6.4	Tensile and microstructure specimens extraction	140
6.5	Mechanical testing	142
6.5.1	Tensile testing.....	142

6.5.2	Hardness testing.....	143
6.6	Macro and microstructure examination.....	143
6.7	Results and discussion.....	144
6.7.1	Macro and microstructure of the FSW dissimilar aluminium alloys joint produced with SiC _{NP} reinforcement and using varying tool rotation speeds.....	144
6.7.2	Tensile strength of the FSW dissimilar aluminium alloys joint produced with SiC _{NP} reinforcement and using varying tool rotation speeds.....	148
6.7.3	Macro and microstructure of the FSW dissimilar aluminium alloys joint produced with varying % vol. fractions of SiC _{NP} reinforcement using FSW first and second pass.....	150
6.7.3.1	Effect of varying percentage volume fractions of SiC _{NP} and number of FSW pass on the WNZ of the MMNC.....	151
6.7.4	X-Ray diffraction (XRD) analysis	164
6.7.5	Density measurement at the WNZ.....	165
6.7.6	Mechanical properties.....	168
6.7.6.1	Effect of varying percentage volume fractions of SiC _{NP} on tensile properties.....	168
6.7.6.2	Effect of varying percentage volume fractions of SiC _{NP} and number of FSW pass on hardness properties.....	171
6.7.7	Strengthening mechanism	173
6.7.7.1	Coefficient of thermal expansion (CTE).....	174
6.7.7.2	Rule of mixture (ROM)	175
6.7.7.3	Load bearing mechanism	176
6.7.7.4	Hall-Petch strengthening	176
6.7.7.5	Orowan-strengthening	177
6.7.8	Fractography	179
6.7.9	Overall conclusion from the effects of SiC _{NP} reinforcement on FSW dissimilar aluminium alloys joint.....	181
6.8	Summary	183

7. CONCLUSIONS	
7.1 Summary	184
7.2 Key contributions	185
7.3 Conclusions.....	186
7.4 Scope for further research.....	188
REFERENCES	189
LIST OF PUBLICATIONS.....	208
BIO-DATA	

LIST OF FIGURES

Figure No.	Description	Page No.
Figure 1.1	Representation of aluminium alloys series number according to IADS	2
Figure 1.2	Schematic representation of friction stir welding process	5
Figure 1.3	Schematic of a taper triangle tool presenting the geometrical parts	8
Figure 1.4	A typical macrograph showing the various zones in the transverse cross-section of the FSW joint	9
Figure 1.5	Schematic representation of friction stir process on the workpiece	14
Figure 3.1	Photographs of a typical aluminium alloy plate used in the FSW experiments	34
Figure 3.2	TEM images showing the (a) average size of the SiC _{NP} between 40 – 50 nm and (b) SAED pattern of SiC _{NP}	35
Figure 3.3	Photographs showing the (a) Five-Axes friction stir welding machine (b) Plate mounting table with fixtures (c) Table movement in X, Y and Z- direction	37
Figure 3.4	(a) Schematic of taper threaded cylindrical showing the tool dimension and (b) photograph of tool.	39
Figure 3.5	(a) Schematic of taper triangle tool showing the dimension and (b) photograph of tool	39
Figure 3.6	Photograph showing the (a) front view and (b) top view of the tool holder	40
Figure 3.7	Schematic representations of tensile specimen and its dimensions according to the ASTM standard of E8M-04	41
Figure 3.8	An example of the microstructure specimen used for measuring the micro-hardness	42

Figure 3.9	Schematic showing the measurement of indentation in micro Vickers hardness test method	43
Figure 4.1	Flow chart illustrating the experimental techniques for bottom-up approach	49
Figure 4.2	Schematic of the tool pass in linearly varying plunge depth (VPD) from 5.8 mm to 6.2 mm in the z -direction for weld length of 150 mm	51
Figure 4.3	Schematic illustrating the (a) VPD experiment procedure and the specimens removal layout (b) top view of the butt weld joint showing the orientation of tensile specimens 'T' extraction and micro-structural specimens 'M'	53
Figure 4.4	Schematic illustrating the VRS experiment for TRS range 400 to 1100 rpm and extraction locations of tensile specimens (T1 to T8) and microstructure specimens (M1 to M8)	55
Figure 4.5	Schematic illustrating the VTS experiment for TTS range 20 to 120 mm/min and extraction locations of tensile specimens (T1 to T8) and microstructure specimens (M1 to M8)	56
Figure 4.6	Variation of UTS, YS and % EL for the case of VPD experiment with TPD range from 5.8 to 6.2mm. Note, % EL is scaled to 10	59
Figure 4.7	Macrograph of defect free weld region of the FSW joint for the TPD of 6.20 mm. Arrow heads pointing towards existence of sharp boundaries between the interface of WNZ and TMAZ	60
Figure 4.8	Photograph showing the surface morphology of the FSW joint plate for VPD of ranging from 5.80 to 6.20 mm	60
Figure 4.9	Variation of UTS, YS and % EL for the case of VRS experiment with TRS range 400 rpm to 1800 rpm. Note, % EL is scaled to 10	61

Figure 4.11	Macrograph of the cross section of weld region of the FSW joint for TRS of 650 rpm, optimum TPD 6.20 mm and constant TRS of 120 mm/min	62
Figure 4.12	Photographs of surface morphology of FSW joint plate for VRS range of (a) 400-1100 rpm and (b) 1100-1800 rpm	62
Figure 4.13	Variation of UTS, YS and % EL for the case of VTS experiment with TTS range from 20 mm/min to 200 mm/min. Note, % EL is scaled to 10	63
Figure 4.14	Macrograph of the cross section of weld region FSW joint for TTS of 150 mm/min, optimum TPD of 6.20 mm and optimum TRS of 650 rpm	64
Figure 4.15	Photographs of surface morphology of FSW joint plate for VTS range of (a) 20-120 mm/min and (b) 120-200 mm/min.	64
Figure 4.16	Variation of tensile properties in relation with varying the TPD. Note, % EL is scaled up to $\times 10$	65
Figure 4.17	Macrostructure image of the transverse section of WNZ at an optimum TPD of 6.20 mm	66
Figure 4.18	Variation of tensile properties in relation with varying the TRS. Note % EL is scaled up to $\times 10$	68
Figure 4.19	(a) and (b) photograph showing the surface morphology and tool failure location in the weld crown region for the two separate set of repeated varying the TRS experiments for the 1100 to 1800 rpm	69
Figure 4.21	(a) and (b) tool force recorded for the TRS experiments range 1100 to 1800 rpm	70
Figure 4.22	Macrostructure image of the transverse section of WNZ at the TRS, 950 rpm	71

Figure 4.23	(a) Variation of tensile properties in relation with the TTS range 20 to 120 mm/min. (b) photograph showing tool stuck location for the second set of VTS experiment for the TTS range 120 to 200 mm/min	72
Figure 4.24	Macrostructure images of the WNZ obtained for the final optimized FSW parameters viz. TPD, 6.20 mm, TRS, 950 rpm and TTS, 90 mm/min with the taper triangle too	74
Figure 4.25	Low magnification SEM images for VPD experiment. Plunge depth in 'mm' is highlighted at the top right corner of each figure	77
Figure 4.26	Grain size at the WNZ for the TPD of 6.20 mm	77
Figure 4.27	Low magnification SEM images of VRS experiment. Unit of rotation speed in 'rpm' mentioned at the top right corner of each figure	81
Figure 4.28	Low magnification SEM images of of FSW joint for VTS at (a) 40mm/min and (b) 110mm/min. Unit of traverse speed in 'mm/min' highlighted at the top right corner of each figure	85
Figure 4.29	(a) SEM and (b) SEM-BSE of WNZ region for the optimized parameters, (c) SEM image for magnification 1000x showing grain size at WNZ region	86
Figure 4.31	Macrostructure images of the WNZ obtained from the varying the TPD for the range 5.80 to 6.20 mm	87
Figure 4.32	(a) Mixed flow region at centre of WNZ, (b)-(c) stacking of layers 1-3 at the top of WNZ (d) arrow marks indicating material flow deflected towards WNZ (e) cracks along the weak interface stacking boundary layers	89
Figure 4.33	Macrostructure images of the WNZ obtained from the varying the TRS experiment for the TRS from 400 rpm to 1100 rpm	90

Figure 4.34	SEM images showing (a) sharp boundary at the interface and (b) pin driven mixed flow at WNZ and unmixed region at RS for TRS of 850 rpm (c) and (d) the presence of both shoulder and pin driven material flow pattern at TRS of 950 rpm	92
Figure 4.35	Macrostructure images of the WNZ obtained from the VTS experiment for the TTS range 20 to 110 mm/min	93
Figure 4.36	SEM images showing the grain size of the WNZ for the FSW joint for the varying the TTS experiment for the range 20 to 90 mm/min.	96
Figure 4.37	Hardness profile at mid thickness transverse to the welding direction of the joints for VRS experiment from TRS range 400-1100rpm	98
Figure 4.38	Hardness profile at mid thickness transverse to the welding direction of the joints for VRS range 1100-1800 rpm	98
Figure 4.39	Hardness profile at mid thickness transverse to the welding direction of the joints for VTS ranging between 20-120 mm/min	99
Figure 4.41	Hardness profile at the mid thickness transverse to the welding direction of the joint for VTS ranging between 120-200 mm/min	100
Figure 4.42	SEM images of typical fracture surface of base material of AA2024-T351 are showing (a) micro-voids (b) large number of dimples, and base material AA7075-T651 showing (c) tearing edges (d) cleavages	101
Figure 4.43	(a) Photograph showing fractured specimen failure location under optimum FSW parameters fractured at HAZ of AS. (b) and (c) are SEM images of fracture surface of FSW joint of (a)	102
Figure 4.44	(a) Photograph showing fractured FSW joint failure location for un-optimized FSW parameters. (b)- (e) SEM images of FSW joint of (a)	103

Figure 4.45	Macrographs showing failure location FSW joint at (a) interface boundaries of WNZ/TMAZ towards RS (b) WNZ and (c) TMAZ/HAZ towards AS. (d) and (e) are SEM images of fracture surface of the specimen of (c)	104
Figure 5.1	Schematic illustrations of tool probe offset and varying the TTS experiment. Tool probe offset of (a) 1 mm towards AA2024-T351 (b) 0 mm, zero tool probe offset and (c) 1 mm towards AA7075-T651 (d) top view illustrating the experimental procedure	108
Figure 5.2	Schematic of extraction of tensile specimens (T1-T8) and microstructure specimens (M1-M8) from FSW dissimilar aluminium alloys joint of AA2024-T351 and AA7075-T651 for different tool probe offset conditions	109
Figure 5.3	Macrographs of FSW dissimilar aluminium alloys joint for tool offset of 1 mm towards AA2024-T351 and VTS range 20-120 mm/min	111
Figure 5.4	SEM images for tool offset of 1 mm towards AA2024-T351 and TTS range 20-120 mm/min	113
Figure 5.5	(a)-(d) Mapping elemental analysis and (e) EDS elemental analysis in the WNZ of the sample welded for tool probe offset of 1 mm towards AA2024-T351 and for TTS of 110 mm/min	115
Figure 5.6	Macrographs of FSW dissimilar aluminium alloys joint for zero tool probe offset and TTS range 20-120 mm/min	116
Figure 5.7	SEM images for zero tool probe offset distance and TTS range 20-120 mm/min	117
Figure 5.8	(a)-(e) Mapping elemental analysis and (f) EDS elemental analysis in the WNZ of the sample welded for zero tool probe offset and for TTS of 110 mm/min	118

Figure 5.9	(a)-(g) Macrographs of FSW dissimilar aluminium alloys joint for tool probe offset of 1 mm towards AA7075-T651 and VTS range 20-120 mm/min	120
Figure 5.11	SEM images for tool offset of 1 mm towards AA7075-T651 and TTS range 20-120 mm/min	121
Figure 5.12	(a)-(e) Mapping elemental analysis and (f) EDS elemental analysis in the WNZ of the sample welded for tool probe offset of 1 mm towards AA7075-T651 and for TTS of 110 mm/min	122
Figure 5.13	(a)-(c) Grain size at the WNZ for tool probe offset of 1 mm towards 2024-T351	123
Figure 5.14	(a)-(c) Grain size at the WNZ for zero tool probe offset	124
Figure 5.15	(a)-(c) Grain size at the WNZ for tool probe offset of 1 mm towards 7075-T651	125
Figure 5.16	Average grain size for the different tool probe offset conditions and for TTS range 20-120 mm/min	125
Figure 5.17	Variation of tensile strength for tool probe offset of 1 mm towards AA2024-T351 for the TTS range 20 - 120 mm/min	127
Figure 5.18	Variation of tensile strength for zero tool probe offset and for the TTS range 20 - 120 mm/min	129
Figure 5.19	Variation of tensile strength for tool probe offset 1 mm towards AA7075-T651 and for the TTS range 20 - 120 mm/min	130
Figure 5.21	SEM images of typical fracture surface of FSW dissimilar aluminium alloys joint for tool probe offset (a)-(c) 1 mm towards AA2024-T351, (d)-(f) Zero offset and (g)-(i) 1 mm towards AA7075-T651 for VTS range 20 - 120 mm/min	132
Figure 6.1	Schematic of FSW dissimilar aluminium alloys joint in (a) front and top view (b) isometric view illustrating the FSW experiment process	137

Figure 6.2	Schematic of an example of aluminium alloy plate with rectangular section edge-groove	138
Figure 6.3	Aluminium alloy plates kept in butt configurations having a rectangular section edge-groove of total width (a) 0.4 mm, (b) 0.6 mm (c) 1 mm, and (d) top view showing the tool traverse and rotation direction for FSW first and second pass (f) increment in the plunge depth with difference of 0.1 mm from first to second pass	139
Figure 6.4	Schematic of approximate location of extraction of tensile (T) and microstructure (M) specimens from FSW joint	141
Figure 6.5	Schematic of two plates with butt joint showing the orientations of tensile specimens and micro-structural samples for FSW first pass and second pass	142
Figure 6.6	FSW dissimilar aluminium alloys joints produced with SiC _{NP} reinforcement for varying TRS experiment for (a) 400 to 1100 rpm (b) 1100 to 1800 rpm	144
Figure 6.7	(a)-(h) SEM images showing the distribution of SiC _{NP} in the WNZ of FSW dissimilar joints specimens produced with SiC _{NP} reinforcement for varying TRS range 400 to 1100 rpm	147
Figure 6.8	(a)-(g) SEM showing the distribution of SiC _{NP} in the WNZ of FSW dissimilar joints specimens produced with SiC _{NP} reinforcement for varying TRS range 1100 to 1800 rpm	148
Figure 6.9	Tensile behaviour of the FSW dissimilar aluminium alloys joint produced with SiC _{NP} reinforcement for varying TRS experiment range 400 rpm to 1100 rpm	149
Figure 6.11	Tensile behaviour of the FSW dissimilar aluminium alloys joint produced with SiC _{NP} reinforcement for varying TRS 1100 rpm to 1800 rpm	150

Figure 6.12	(a)-(d) Photographs showing the surface morphology of FSW dissimilar aluminium alloys joint with varying % volume fraction of SiC _{NP} reinforcement	151
Figure 6.13	Projected area of the tool pin of taper threaded cylindrical used in the experiment	153
Figure 6.14	SEM images of the FSW first pass WNZ area considered for the Image-J analysis showing (a) ~5% (b) ~8% and (c) ~13% vol. fraction of SiC _{NP}	155
Figure 6.15	Comparison of the volume fractions V_{th} with V_{fp} and V_{sp} , after FSW first pass and second pass processing	155
Figure 6.16	The distribution of 5% vol. fraction SiC _{NP} (a) and (b) defects due to agglomeration of SiC _{NP} , (c) and (d) alternate layer of SiC rich and free region, (e) pores around SiC _{NP} (f) EDS peaks of SiC (g) homogeneous distribution of SiC _{NP} after the FSW second pass and (h) Grain size range 2-3.5 μ m	157
Figure 6.17	SEM images showing the distribution of 8% vol. fraction SiC _{NP} in the WNZ for FSW (a) and (b) first pass. (c) alternate layer of SiC rich and free region (d) magnified image of (c), (e) BSE images of (d), (f) EDS peaks of SiC (g) FSW second pass, (h) Grain size range 3-5 μ m in the WNZ	159
Figure 6.18	SEM images showing the distribution of 13% vol. fraction SiC _{NP} in the WNZ for (a) FSW first pass and (b) partially closed groove (c) FSW second pass (d) Grain size range 3-4 μ m in the WNZ (e) Spot EDS analysis for the region 1 of (b). (f) surface EDS for the region 2 of (c)	160
Figure 6.19	(a) SEM images of the WNZ of FSW joint without SiC _{NP} for FSW second pass (b) showing grain size range 6-8 μ m, (c) average grain size after performing FSW second pass with different % vol. fractions of SiC _{NP} (5, 8, 13%) and without SiC _{NP}	162

Figure 6.21	XRD analyses showing the intensity peaks in the MMNC at the WNZ for the FSW first pass specimen	164
Figure 6.22	An example of the specimen extraction locations marked '1', '2', and '3' from the MMNC at the WNZ after the FSW second process	166
Figure 6.23	Comparison of the density of the FSW joint as a function of varying % vol. fraction of SiC _{NP} at the WNZ for the FSW second pass	167
Figure 6.24	Comparison of UTS, YS and %EL for varying % vol. fractions of SiC _{NP} (5, 8, 13%) and without SiC _{NP} (0%) at the WNZ and after the FSW first pass	169
Figure 6.25	Comparison of UTS, YS and %EL for varying % vol. fractions of SiC _{NP} (5, 8, 13%) and without SiC _{NP} (0%) at the WNZ and after the FSW second pass	169
Figure 6.26	Microhardness profile for varying % vol. fractions of SiC _{NP} (0, 5, 8 and 13%) after FSW first pass	172
Figure 6.27	Microhardness profile for varying % vol. fractions of SiC _{NP} (0, 5, 8 and 13%) after FSW second pass	173
Figure 6.28	Tested tensile specimens and fracture locations corresponding to each %vol. fractions of SiC _{NP} (a) 5% , (b) 8%, (c) 13%, and FSW pass	179
Figure 6.29	SEM images showing fracture features of FSW joint for varying % vol. fractions of SiC _{NP} 5% with FSW (a) first pass and (b) second pass; 8% with FSW (c) first pass and (d) second pass ; and 13 % with FSW (e) first pass and (f) second pass	180

LIST OF TABLES

Table No.	Description	Page No.
Table 3.1	Chemical composition of AA2024-T351 and AA7075-T651	34
Table 3.2	Mechanical properties of AA2024-T351 and AA7075-T651	34
Table 3.3	The specifications of the FSW machine	38
Table 4.1	Macrographs of FSW dissimilar aluminium alloys joint for VPD experiment. The TPD depth in 'mm' indicated on the top right corner of each figure	75
Table 4.2	Macrographs of FSW dissimilar aluminium alloys joint for VRS experiment. Tool rotation speed in 'rpm' indicated on the top right corner of each figure	79
Table 4.3	Macrographs of FSW dissimilar aluminium alloys joint for VRS experiment. Tool rotation speed in 'rpm' indicated on the top right corner of each figure	80
Table 4.4	Macrographs of FSW dissimilar aluminium alloys joint for VTS experiment. Tool traverse speed in 'mm/min' indicated on the top right corner of each figure	83
Table 4.5	Macrographs of FSW dissimilar aluminium alloys joint for VTS experiment. Tool traverse speed in 'mm/min' indicated on the top right corner of each figure	84
Table 5.1	Failure location of the fracture tensile specimen of FSW dissimilar aluminium alloys joint produced for different tool probe offset and TTS range 20-120 mm/min	133
Table 6.1	Macrostructure for varying FSW tool rotation speeds range 400 rpm to 1800 rpm, constant tool plunge depth, 6.2mm and traverse speed, 40 mm/min	145

Table 6.2	Macrograph images of the FSW dissimilar aluminium alloys joint showing the WNZ of MMNC for the varying %vol. fractions of SiC _{NP} reinforcement and without SiC _{NP} for FSW first and second pass	152
Table 6.3	Theoretical volume fraction (V_{th}) of SiC _{NP} before the FSW process	154
Table 6.4	Theoretical Zener limiting grain size (dz) and actual grain size in the WNZ after performing FSW second pass	163
Table 6.5	Theoretical density from ROM and the actual density of the composite with varying %vol. fractions of SiC _{NP} as a reinforcement at the WNZ	167
Table 6.6	Tensile properties of FSW dissimilar aluminium alloys joint fabricated with varying % vol. fractions of SiC _{NP} (5, 8,13%) and without SiC _{NP} (0%) at the WNZ for FSW first pass and second pass	170
Table 6.7	Predicted inter particle spacing, λ , and Orowan strengthening, σ_{orowan} , for the composite with varying %vol. fractions of SiC _{NP} (5, 8, 13) as a reinforcement at the WNZ	178
Table 6.8	Experimental yield strength obtained for the composites with varying %vol. fractions of SiC _{NP} (0, 5, 8, 13) as a reinforcement at the WNZ	178

ABBREVIATIONS

FSW	: Friction stir welding
FSP	: Friction stir processing
AA	: Aluminium alloy
UTS	: Ultimate tensile strength
YS	: Yield strength
%EL	: Percentage elongation
IADS	: International alloy designation system
AS	: Advancing side
RS	: Retreating side
CW	: Clockwise
CCW	: Counter clockwise
WNZ	: Weld nugget zone
SZ	: Stir zone
TMAZ	: Thermo-mechanically affected zone
HAZ	: Heat affected zone
CDRX	: Continuous dynamic recrystallization
SPD	: severely plastic deformation
DXZ	: Dynamically recrystallized zone
BM	: Base material
MMC	: Metal matrix composites
MMNC	: Metal matrix nano composites
UMR	: Unmixed region
MMR	: Mechanically mixed region
DOE	: Design of experiment
RSM	: Response surface method
OA	: Orthogonal array
GRA	: Grey relation analysis
CA	: Cellular automaton
ANOVA	: Analysis of variance

NN	: Neural network
FEM	: Finite element method
ANN	: Artificial neural network
ANFIS	: Adaptive neuro-fuzzy inference systems
SiC _{NP}	: Silicon carbide nano particles
% vol.	: Percentage volume
VPD	: Varying plunge depth
VRS	: Varying rotation speed
VTS	: Varying traverse speed
EDM	: Electric discharge machine
SEM	: Scanning electron microscopy
TEM	: Transmission electron microscopy
OM	: Optical microscope
EDS	: Energy dispersive spectroscopy
BSE	: Back scattered emission
AW	: As-welded
ASTM	: American society for testing material
SAED	: Selected area electron diffraction
XRD	: X-ray diffractometer
TPD	: Tool plunge depth
TRS	: Tool rotation speed
TTS	: Tool traverse speed
BS	: Banded structure
ROM	: Rule of mixture
CTE	: Coefficient of thermal expansion

NOMENCLATURE

F_Y	: Welding force
F_z	: Vertical force
% vol	: Percentage volume fractions
η_{WJ}	: Weld joint efficiency
V_{th}	: Theoretical volume fraction
V_{fp}	: Actual volume fraction of SiC _{NP} after FSW first pass
V_{sp}	: Actual volume fraction of SiC _{NP} after FSW second pass
A_{fp}	: Area of the WNZ after FSW first pass
A_{sp}	: Area of the WNZ after FSW second pass
A_g	: Total area of the groove
A_p	: Projected area of the tool pin
G_w	: Total groove width
G_d	: Total groove depth
dz	: zener limiting grain size
UTS_{AJ}	: UTS of the dissimilar aluminium alloys joint
UTS_{BM}	: UTS of the base material plate
ρ_{CTE}	: Strengthening from coefficient of thermal expansion
σ_{orowan}	: Orowan strengthening
$\Delta\sigma_{load}$: Load bearing strengthening mechanism
λ	: mean inter-particle spacing

CHAPTER-1

INTRODUCTION

1.1 OVERVIEW

The development in the manufacturing technology over the last few years and continuous research has led to the extensive use of light alloys and composites in the automotive, marine and aerospace industries. Materials such as aluminum (Al), titanium (Ti), magnesium (Mg) and their alloys, and the metal matrix based composites of these materials are used extensively in the design of lightweight and corrosion resistant structures resulting in significant fuel consumption reduction, extended life of the component and advantageous impact on the environment. Thus, in order to reduce the weight, improve resistance to the corrosion and fatigue, the production of the new materials and their alloys are the concern of the material producers and aircraft designers. Much of the research work is carried out to develop the materials that can be used in different components of aircraft like fuselage, upper and lower wing surface, body stiffeners, body stringers, upper lobe and lower lobe, etc.

Aluminium finds a wide and primary used material for the different structural parts of aircraft because of its moderate cost and lightweight, ease of fabrication, high specific stiffness and strength, higher plasticity, thermal conductivity, malleability and resistant both to mechanical strains and oxidation. The heat treatment on aluminium and its alloys yields to withstand the high levels of stresses and load. Even though, use of composite materials has increased and reduced the application of aluminium up to some extent, aluminium alloys having higher strength remain important in airframe construction. Aluminium alloys are classified mainly as given below,

- (i) Cast alloys and
- (ii) Wrought heat-treatable alloys.

The mechanical properties of wrought heat-treatable alloys are superior compared to the cast alloys and widely used in aircraft structures. Further, the wrought alloys are classified as (i) Non age-hardenable alloys and (ii) Age-hardenable alloys.

The non age-hardenable alloys are usually cannot be strengthened by age or precipitation hardening. The aluminium alloy series 1000, 3000, 4000 and 5000 are categorised as non age-hardenable alloys. The yield strength (YS) of the non age-hardenable alloys is less than 300 MPa and are not suitable for aerospace structures. On the other side, age-hardenable alloys after heat treatment result in high strength because of combined strengthening from solid solution hardening and precipitation hardening. The aluminium alloy series 2000, 6000, 7000 and 8000 are categorised as age-hardenable alloys. The YS of age-hardenable alloys are in the range 400 MPa to 600 MPa and finds suitable for making different components in the aerospace structure.

International Alloy Designation System (IADS) classify the aluminium alloys used in aircraft industries into different categories according to the chemical composition (Mouritz 2012). These alloys are in the series of 1000, 2000, 3000, 4000, 5000, 6000, 7000 and 8000. Generally, these aluminium alloy series are represented by four-digit number: XXXX.

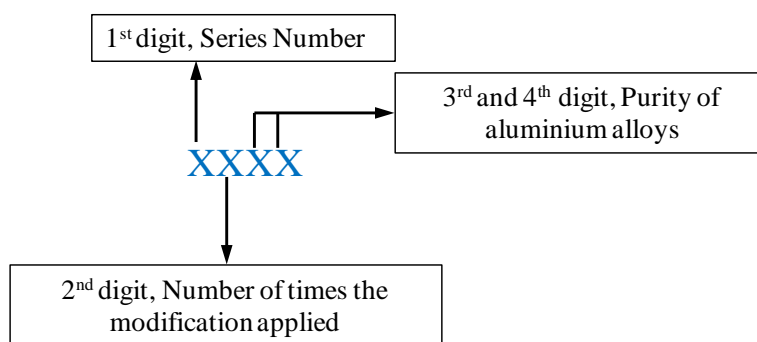


Figure 1.1 Representation of aluminium alloys series according to IADS.

In Figure 1.1, the first digit indicates the series. For e.g. 1XXX indicates, it is 1000 series alloys. The second digit indicates the number of times the modification applied to the alloy. For e.g. in 1200, the '2' indicates the alloy has been modified two times.

The 'third' and 'fourth' digit indicates the purity of the aluminium alloy. For e.g. in 1145 Al, the purity is at least 99.45%. Similarly, in 1200 Al, purity is 99.00%. However, in 2000 and 8000 series, the 'third' and 'fourth' digits are used only to identify the alloy type in the series.

1.2 ALUMINIUM ALLOYS OF 2000 AND 7000 SERIES

The aluminium alloys of 2000 and 7000 series used in many structural components of aircraft. The copper (Cu) and Zinc (Zn) are the main alloying element in the 2000 and 7000 series aluminium alloys, respectively. The presence of Cu and Zn helps in increasing the strength of the aluminium alloys. There are many 2000 series aluminium alloys available. However, the most commonly used 2000 series are 2024 aluminium alloys and finds its application in making the components such as stringers, lower wing skins, stressed skins and trusses (Mouritz, 2012). The 7000 series aluminium alloys are having higher strength than the 2000 series. The 7000 series find common application together with 2000 series alloys. The 7000 series are commonly used in upper wing surface, stringers, frameworks and pressure bulkheads etc. Among the different 7000 series aluminium alloys, the most commonly used aluminium alloys are 7075.

The aluminium alloys often designated with temper performed on these alloys. This method of numbering is called a 'Temper designation system'. The temper is referred depending upon the forging (e.g. cold working, hot working) and thermal treatment (e.g. annealing, age hardening). The temper designation system consists of an individual capital letter of 'F' and 'T'. The letter 'F' stands for aluminium alloys being fabricated and the 'T' stands for the aluminium alloy subjected to age-hardened. As mentioned earlier, the heat treatment process on age-hardenable alloys helps in increasing the mechanical properties of the material in order to suitable to be made for its application in aerospace structure. In the aluminium alloy of 2024-T351, T-refers to 'age hardened' and the temper designation T351 denotes alloys are tempered to a T3 condition by solution treatment, quenched, tensile deformed and naturally aged. Similarly, for 7075-T651 the T651 refers to alloys tempered to a T6 condition by solution treatment followed by artificially ageing.

In order to fabricate the different components, structure applications and body parts of aircraft the high strength the aluminium alloys of 2000 and 7000 series as to be joined by the welding process. A conventional joining technique like tungsten inert gas (TIG) welding and metal inert gas (MIG) welding process introduces serious problems like porosity, slag inclusion, solidification cracks etc., while joining these non-weldable aluminium alloys. The difficulty of fabricating the high-strength, defect-free and fracture resistant weld joints in aerospace grade aluminium alloys have limited the use of TIG and MIG welding techniques in joining aerospace structure. In order to overcome the difficulty in joining aluminium alloys, a solid-state joining process called friction stir welding (FSW), was invented. At present, application of FSW technique in joining the different materials has been increased in the aerospace, automotive, marine and military industries.

1.3 FRICTION STIR WELDING (FSW)

Friction stir welding invented at the Welding Institute (TWI), UK in 1991 by Thomas et al. (1991). The FSW is a solid-state welding process. During the FSW process, temperature approach is near the solidus temperature of the material to be welded but remain below it. In the process, the material is plastically deformed by local frictional heat generated by combination of rotating tool shoulder and pin with faying surface of the material. A non-consumable rotating tool having specific designed tool shoulder geometry with pin is inserted between the joining edges of sheets or plates to be welded. After developing a sufficient amount of heat, the FSW tool traversed along the weld line of the joint. The localized heat generated softens the material and thus helps in material flow around the pin from front to the backside of the pin, and a weld-joint is produced in the solid-state. Figure 1.2 depicts the schematic representation of two plates placed in simple square butt-joint configuration and welded by FSW technique. In Figure 1.2, the FSW tool rotates in the clockwise (CW) direction and the left side to the tool rotation is the advancing side (AS). The right side to the tool rotation is considered as the retreating side (RS).

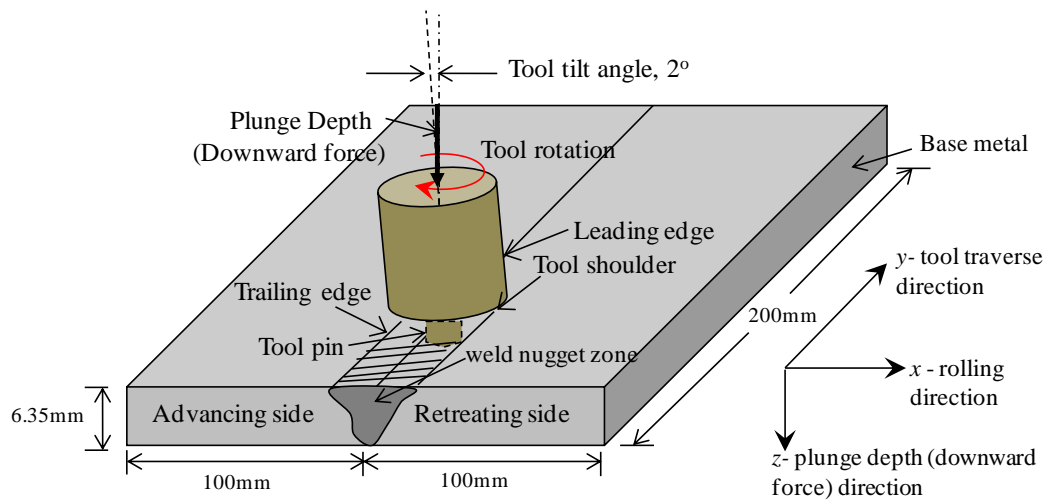


Figure 1.2 Schematic representation of friction stir welding process.

Initially, a non-consumable rotating tool in the CW direction with geometrically designed tool shoulder and the pin is plunged to the sufficient depth in the tool plunge depth direction, z , at exactly in the weld-joint line interface between the two plates. The tool plunge depth is maintained by controlling the normal force acting downwards axially along the z -direction. The tool is dwell at this position for the required time and after developing a sufficient amount of heat, it is traversed along the weld-joint line in the tool traverse direction, y . The quality of the butt-joint depends upon major FSW parameters: (i) tool rotation speed (ii) tool traverse speed (iii) tool plunge depth or axial force (iv) tool tilt angle (Mishra and Ma, 2005). In addition, the various designed tool shoulder geometry (convex, concave, knurling on shoulder), and pin profile (threaded, hexagonal, square, triflute, triangle, simple cylinder, etc.), pin length and its diameter, also plays a significant role in developing sufficient amount of heat due to the friction between the rotating tool shoulder, tool pin and the faying surface of the workpiece. Thus, the tool rotation and translation contributes for the workpiece to undergo severely plastic deformation (SPD) and helps in the movement of the softened material around the tool pin. As the tool traverse forward in the y - direction, the softened and the stirred material fill the tool weld path. The FSW process is the most important development technique in metal joining and it is gaining popularity because of its environment friendly, energy efficiency and its versatility in its operation. As compared to conventional TIG, MIG welding technique, the FSW is less energy consuming process and it does not use

consumables such as filler material, and flux in joining process. Thus, the process has no harmful emission. The FSW technique used to join the two materials in butt, lap, T-butt and fillet type joint configurations. Among these joint configurations, the butt and lap joint configurations are considered the most convenient.

1.3.1 Terminologies used in the FSW

The mechanical properties and metallurgical characteristics of the FSW joint specimens depend on the selection of the FSW parameters and the tool geometry. In this section, few major FSW parameters, tool geometry and the terminologies related to the macro and microstructure of the FSW joint specimens are explained.

1.3.1.1 FSW parameters and its significance

The terminologies and their definitions are explained concerning the FSW joining process (Mishra and Ma, 2005).

- (i) Tool rotation speed:** The tool rotation speed also referred to as rotation speed, is the rotation rate of the tool in either CW direction or counter-clockwise (CCW) direction. The tool rotation speed has a major contribution in the heat generation and plasticised material movement or flow around the FSW tool pin. The material stirring or mixing around the tool pin is achieved by the tool rotation speed in CW or CCW direction. The friction between the rotating tool and workpiece at higher the tool rotation speed generates higher temperature, whereas the lower rotation speed results in low heat input to the workpiece. The tool rotation speed expressed in revolution per minute, rpm.

- (ii) Tool traverse speed:** The tool traverse speed also referred to as tool welding speed, is the rate at which the tool translation occurs in the y-direction (Figure 1.2) along the weld joint line. The tool translation helps in moving the stirred material from the leading edge to trailing edge of the tool and finishes the FSW process. Tool traverse speed is expressed in the

unit of mm/min or mm/sec. The tool traverse speed is considered as an important FSW parameter in heat input during the FSW process. The lower the tool traverse speed and higher tool traverse speed results in increased heat input and reduced heat input to the weld region of the FSW joint, respectively.

(iii) Tool plunge depth: The tool plunge depth also referred as plunge depth, is the total depth of the tool inserted into the workpiece considering the tool pin height and shoulder from the faying (top) surface of the workpiece. The insertion depth is associated with both the tool pin height and shoulder, and it is important in producing the sound quality weld joint. The proper insertion depth helps in proper interaction of the tool pin and shoulder with the workpiece. At lower insertion depth, the shoulder does not make sufficient contact with the workpiece and results in the insufficient stirring of the material around the tool pin leading to the formation of weld defects. On the other side, higher insertion depth results in the generation of the excessive flash of the material on the weld crown region and deteriorates the quality of the weld joint. Tool plunge depth is generally expressed in mm.

(iv) Tool plunge rate: Tool plunge rate is the rate at which the tools shoulder and pin are plunged into the workpiece during the FSW process. It controls the axial force (in kN) and builds-up the heat generation during the initial stage of the FSW process.

(v) Tool tilt angle: Tool tilt angle also called as an angle of the spindle. The angle between the plane normal of the workpiece (x -axis, Figure 1.2) to the shaft of the spindle is expressed in terms of ' θ ', tool tilt angle. Generally, the ' θ ' in the range 0° to 3° is chosen for the FSW process. A suitable ' θ ' towards the trailing edge of the workpiece helps for the tool shoulder to hold sufficient plasticised stirred material to move it efficiently around the tool pin.

1.3.1.2 Tool geometry

The material of the workpiece to be weld, the type of joint (butt or lap joint), tool material, FSW tool parameters and users own experience are the important factors to be considered for selecting the tool geometry. In general, the tool geometry includes tool shoulder, pin and cylinder. Tool shoulders geometry consists of shoulder diameter (d) whose surface consists of a specific profile feature (flat, concave, or convex). These profiles may consist of machining cut of knurling, groves and concentric circles. Similarly, the tool pin consists of pin probe length (L). There are different types of tool pin probe profile such as simple cylindrical, cylindrical threaded, cylindrical taper threaded, taper triangle, taper square, triflute, and hexagonal, etc. In addition, the tool geometry consists of height of the cylinder (H) and diameter of the cylinder (D). An example of a schematic illustration of the FSW tool consisting of tool shoulder and pin is as shown in Figure 1.3. The two important functions of the tool are (a) heating of the workpiece, (b) movement or flow of material to produce the joint.

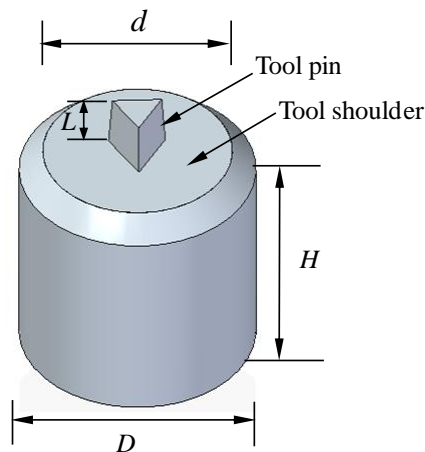


Figure 1.3 Schematic of a taper triangle tool presenting the geometrical parts.

1.3.1.3 Microstructure

The friction between the FSW tool and the workpiece results in plastic deformation of workpiece material and transverse cross section of the FSW joint specimen identifies the different zones (Mishra and Ma, 2005). Figure 1.4 shows an example of the cross-

section of the weld region of a typical macrograph of the FSW dissimilar materials joint produced by the FSW technique.

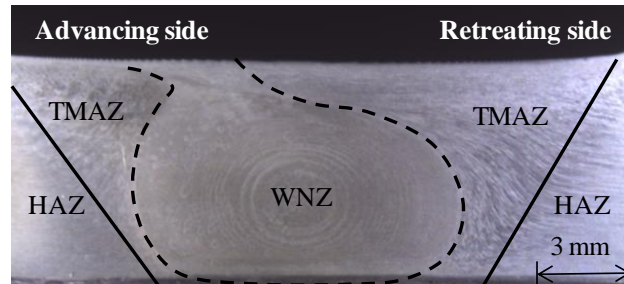


Figure 1.4 A typical macrograph showing the various zones in the transverse cross-section of the weld region of the FSW joint.

Macrograph shown in the Figure 1.4 presents the cross-section of the weld region distinguished into distinct zone as follows:

- (i) **Weld nugget zone:** The intense plastic deformation and high-temperature generation during the FSW process result in the zone consisting of fully recrystallized and fine equiaxed grain microstructure in the weld nugget zone (WNZ) also referred as stir zone (SZ) or nugget zone (NZ) or dynamically recrystallized zone (DXZ). Depending upon the type of tool geometry, FSW process parameters and the temperature exposure of the workpiece, the different shapes of the WNZ are observed. The WNZ can be classified into two types: (i) basin type and (ii) elliptical.
- (ii) **Thermo-mechanically affected zone:** The thermo-mechanically affected zone (TMAZ) does not contain fully recrystallized grains due to insufficient deformation strain of the grains. However, the TMAZ consists of base material elongated grains moving upwards and around the WNZ. There exists a distinct boundary between the TMAZ and WNZ. The TMAZ is present in both the AS and the RS of the weld region of the FSW joint.
- (iii) **Heat affected zone:** Heat affected zone (HAZ) present next to the TMAZ observes an absence of plastic deformation of the material. As a result, even though HAZ experiences the thermal cycle, the region retains the same grain

size as that of the base material. The HAZ is present in both the AS and RS of the weld region of the FSW joint.

- (iv) **Base material / Parent material:** The base material (BM) region is present next to the HAZ on either side of the AS and RS of the transverse cross-section of the weld region. These regions although experiences a thermal cycle of the FSW process, its microstructure or mechanical properties are unaffected by heat.

1.3.2 Temperature distribution in the weld region

The rotating FSW tool pin and shoulder being a source of heat generation, its good amount of interaction with the BM is required in order to produce defect-free weld joints. These two factors play a significant role in contributing to the temperature increase in the weld region and at its distinct zones i.e. WNZ, TMAZ, HAZ and the BM. As the temperature in the FSW joint specimens weld region has a direct influence on the microstructure characteristics (grain size, the interface of the grain boundaries, coarsening and dissolution of strengthening precipitates) and the mechanical properties of the FSW joint specimens, it is important to know the temperature distribution in the weld region.

Several investigations (Rhodes et al., 1997; Liu et al., 1997; Murr et al., 1998; Sato et al., 1999) report the temperature distribution in the weld region. However, the measurement of the temperature at the WNZ is difficult as it experiences an intense plastic deformation due to the rotating and transverse movement of the FSW tool. In addition, as the FSW tool is in rotating action, the embedding of the thermocouple for the temperature measurement at the WNZ is difficult. Therefore, the temperature at the WNZ is recorded by embedding the thermocouple next to the WNZ (Sato et al., 1999; Tang et al., 1999; Kwon et al., 2002) or estimating the temperature at the WNZ by studying its microstructure (Rhodes et al., 1997; Liu et al., 1997; Murr et al., 1998; Sato et al., 1999). Rhodes et al. (1997) in their study on the FSW process on 7075-T651 reports that the temperature distribution range is 400 to 480°C in the weld region and maximum temperature being observed close to the WNZ. Similarly, the

studies carried out by Sato et al. (1999) and Mahoney et al. (1998) report that the maximum temperature records close to the WNZ and decreased temperature with the increase in the distance away from the WNZ.

1.3.3. Mechanical properties, microstructure evaluation of the FSW joints and its significance

The FSW process parameters chosen in joining similar or dissimilar materials leads to the significant microstructure evolution in the different zones of the weld region such as WNZ, TMAZ and HAZ, which in turn results in substantial changes in the mechanical properties of the post weld FSW joints. The mechanical properties, microstructure evaluation and their significance are briefly discussed.

1.3.3.1 Tensile strength

After the FSW process, the tensile specimens are machined from the weld joint in the two directions namely: (i) normal (transverse) to the weld joint, (ii) parallel to the weld joint along the WNZ. The specimens machined in normal to the weld joint possess all the four zone of the weld region, i.e., WNZ, TMAZ, HAZ and BM. On the other hand, the tensile specimens extracted parallel to the weld joint along the WNZ consists of only WNZ having fully recrystallized grain structure. The tensile specimen extraction normal to the weld joint is the most common practice. The tensile specimens extracted in the AW condition from the FSW joint are evaluated for tensile properties such as UTS, YS and % EL. The tensile properties of the FSW joint depend upon the selection of the FSW parameters (tool rotation speed, traverse speed, plunge depth, tilt angle, etc.) and the FSW tool geometry. Because, the during the FSW process the FSW parameters and the FSW tool geometry is chosen governs the heat input, material flow around the tool pin in the weld region that leads to significant microstructure modification and grain size. These microstructure changes result in substantial changes in the mechanical properties of the post weld FSW joints.

1.3.3.2 Microstructure characterization

The changes in the microstructure of the specimens extracted from the FSW joints are carefully prepared according to the standard metallographic procedure. The macro and microstructures studies are carried out for the presence of any defects i.e. pin hole, worm hole, sharp boundary defects at the interface boundary, tunnel defect, piping defect, hooking defect etc., at the WNZ, TMAZ and HAZ of the weld region.

1.3.3.3 Hardness properties

The hardness properties of the FSW joint are measured across the weld regions of the specimens extracted and prepared for the microstructure analyses. The distinct zones of the FSW joint such as WNZ, TMAZ, HAZ and BM are considered for measuring the hardness. The hardness in the weld region depends on the FSW parameters chosen which in turn decides the amount of heat input to the weld region. The FSW process softens the weld region of the precipitation hardenable alloys (Liu et al. 1997; Li et al., 1999, Sato et al., 1999). During the FSW process, the hardness at the weld region strongly affected primarily by the coarsening, distribution, and dissolution of the strengthening precipitates and grain size being secondary that result in the softening of the weld region (Sato et al., 1999). In addition, the hardness of the FSW joint specimens depends on the distribution of reinforcement nano or microparticles (silicon carbide, aluminium oxide, titanium carbide) in the production of metal matrix composites (MMC) by FSW techniques.

1.4 FSW AND ITS APPLICATION TO OTHER MATERIALS

The successful implementation of the FSW technique for the aluminium alloys and the rapid progress in the FSW process has motivated the implementation of the FSW technique to the other non-ferrous materials, similar or dissimilar materials and for fabricating the composites. The materials such as Mg, Ti, Cu, steel, etc., successfully welded using FSW technique.

The successful joining of aluminium alloys to Cu is of great interest because of their application in aerospace, automobile, transportation and electronic industries (Al-

Roubaiy et al., 2014). The joining of aluminium to Cu is a challenging task because of the difference in chemical properties and formation of inter metallic compounds (IMCs). Many investigations have successfully joined Cu to aluminium (Sahu et al., 2016; Firouzdor and Kou, 2012; Liu et al., 2008; Galvao et al., 2012; Xue et al., 2010) by using FSW technique.

The FSW being solid-state joining technique is the optimum choice for welding Mg and its alloys with the aluminium, Ti alloys. Recently, successful attempts has been made to join Mg to aluminium and its alloys (Mohammadi et al., 2015; Fu et al., 2015) and AM20-Mg alloy (Sahu et al., 2015). Even though the welding the Ti and its alloys are generally carried out by Gas Tungsten Arc Welding (GTAW), the weld joint requires post weld heat treatment (PWHT) process in order to restore lost mechanical properties. As a result, the PWHT is added to the production cost. The FSW technique eliminates the requirement of PWHT on welded Ti and its alloys to aluminium and other materials. Many researchers in their investigation have successfully welded Ti to aluminium alloys (Song et al., 2014; Wu et al., 2015) and Ti to Mg alloys (Aonuma and Nakata, 2012).

Similarly, the difficulty in joining steels by fusion welding that leads to hydrogen cracking, distortion, residual stress, and metallurgical changes in HAZ while welding thick sections of the steels are eliminated by using solid-state FSW technique. The studies carried out by Chen and Kovacevic (2004), Yazdipour and Heidarzadeh (2016), Derazkola et al. (2015) and Lan et al. (2016) have successfully joined steels and its alloys to aluminium alloys using FSW technique.

Most of the literature (Abbasi et al., 2015; Bahrami et al., 2014; Tabasi et al., 2016; Liu et al., 2015; Byung-Wook et al., 2012; Pantelis et al., 2016; Sun and Fujii, 2011; Hamdollahzadeh et al., 2015) report fabrication of the MMC via FSW by incorporating micro and nano particles into the rectangular section edge-groove of definite size between the two adjoining plates. Further, they found with proper FSW parameters condition result homogeneous distribution of nano or micro particles in the WNZ. Further, they report the addition of reinforcing particles has shown

decreased grain size, increased in both ductility and strength, compared to the FSW processed joint without reinforcement nano or micro particles.

1.5 FRICTION STIR PROCESSING

Friction stir processing (FSP) is an adaptation of FSW. In the FSP, the tool is made to traverse along the desired path to modify the microstructure rather than joining two pieces. Mishra et al. (1999) developed the FSP and it finds application in enhancing the specific property of the material by inserting the rotating FSW tool in the workpiece, and the modification of the microstructure is achieved by high heat generation due to the friction between the rotating tool and the workpiece. Further, the FSP technique has been used for the fabrication of the surface composite by reinforcing the micro or nano particles in to the groove made on the faying surface of the workpiece (Don-Hyun et al., 2012; Akramifard et al., 2014; Wang et al., 2009; Dolatkhah et al., 2012; Azizieh et al., 2011; Sathiskumar et al., 2013), reports on the fabrication of MMC by FSP technique. In all of these work, the composites were successfully fabricated by FSP on the metal surface but not focusing on joining. Figure 1.5 presents a schematic of the FSP technique. Similar to the distinct zones present in the weld region of the FSW techniques, the FSP weld region is also characterised with the presence of SZ, TMAZ and HAZ. The SZ is the region where the material is plastically deformed to achieve microstructural modification to enhance the property of the material.

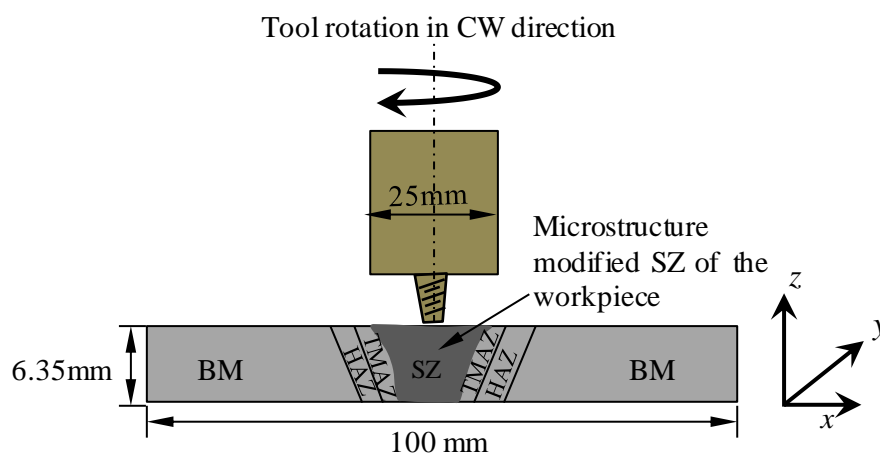


Figure 1.5 Schematic representation of friction stir process on the workpiece.

1.6 ORGANISATION OF THE THESIS

The thesis comprises of seven chapters, following paragraphs present brief note on each chapter.

Chapter 1 introduces the types of aluminium alloys, FSW technique and FSP, the terminology used in FSW, FSW parameters, tool geometry, the temperature distribution in the weld region, the significance of mechanical property and microstructure of the FSW joints, and application of FSW to other materials.

Chapter 2 presents a comprehensive literature review on the influence of FSW parameters in joining similar and dissimilar materials, types of optimization method used to obtain optimum FSW parameters, the effect of material location and tool probe offset, production of composites using FSW and FSP techniques at the WNZ, research gap, objectives and scope of the research work .

Chapter 3 covers the details of the types of materials and its properties used in the investigation, FSW machine experimental setup, the procedure and methods deployed to evaluate the mechanical properties and microstructural characterisation of the FSW dissimilar aluminium alloys joint.

Chapter 4 covers the experimental procedure of bottom-up optimization approach employed to obtain optimum FSW parameters in joining dissimilar aluminium alloys. The Chapter also discusses the details of various experimental trials conducted by using the taper threaded and taper triangle tool.

Chapter 5 is dedicated for the investigation of the influence of the tool probe offset in conjunction with the traverse speed on the mechanical properties, macro and microstructural characteristics of the FSW dissimilar aluminium alloys joint. The results of materials mixing, composition and grain size at the WNZ and, the fractography of the tested FSW joint specimens also discussed.

Chapter 6 reports the effect of tool rotation speed and the role of FSW first and second pass, the effect of varying percentage volume fractions of SiC nano particles

reinforcement on mechanical properties and microstructure of FSW dissimilar aluminium alloys joint.

Chapter 7 concludes the finding from the present research work, the scope for the future work and provides key contributions. Finally, this chapter is followed by references and list of publications.

CHAPTER-2

LITERATURE REVIEW

2.1 INTRODUCTION

In this chapter, comprehensive literature review pertaining to the (i) influence of FSW parameters on mechanical properties and microstructure of similar and dissimilar materials FSW joint , (ii) different optimization techniques and experimental methods to obtain optimum FSW parameters, (iii) effect of the location of the materials, FSW tool probe offset on the microstructure and mechanical properties of FSW dissimilar joints and, (iv) production of composites by reinforcing micro or nano particles at the WNZ of the similar or dissimilar joints using FSW technique and fabrication of surface composites using FSP technique, have been discussed.

2.2 INFLUENCE OF FSW PARAMETERS ON MICROSTRUCTURE AND MECHANICAL PROPERTIES OF SIMILAR AND DISSIMILAR MATERIALS FSW JOINT

In order to produce the defect-free FSW joint of similar or dissimilar materials, the FSW process parameters must be optimized for the particular type of materials being selected for joining purpose. The proceeding section discusses the influence of FSW parameters on mechanical properties and microstructure characteristics of similar and dissimilar materials FSW joint.

2.2.1 Friction stir welding of similar materials

In joining of similar aluminium alloys series such as 2000, 5000, 6000 and 7000, and to obtain high tensile strength, increased hardness, refined grain structure, reduced residual stress and material flow depends on the selection of optimized FSW parameters. Mishra et al. (2005) summarised the review on FSW parameters and concluded that among all the FSW parameters rotation speed, traverse speed, plunge depth and tool pin profile plays a very important role in overall increasing the

mechanical properties of the FSW joint. The higher tool rotation speed and lower traverse speed results in excessive heat input to the weld region (Radisavljevic et al., 2013; Ma et al., 2013; Rodriguez et al., 2015; Trimble et al., 2015; Peel et al., 2003).

Radisavljevic et al. (2013) studied the effect of tool rotation speeds of 750, 950, 1180 rpm to traverse speeds between the range 73 to 190 mm/min ratio in joining FSW similar joint of AA2024-T351. Further, authors report that the mechanical properties and microstructure of the WNZ can be effectively controlled by selection optimum rotation speed to traverse speed ratio. Further, the speed ratio of 8.06, 10.17 and 10.27 the FSW joint yields higher mechanical properties and better material flow in the WNZ. Ma et al. (2013) in their investigation in joining 2198-T8 aluminium alloys considered the rotation speeds of 800, 600, 400 rpm and traverse speeds of 400, 200, 100 mm/min. Further, they concluded that an increase in rotation speed to welding speed ratio decrease the hardness. However, for the same ratio observes an increase in the tensile strength of the FSW joint. Zhang et al. (2015) in their study on FSW joint of high strength Al-Zn-Mg-Cu cast aluminium alloy report reduction in the grain size with the increase in the welding speed or decreasing the rotation speed. Further, they report that the among the rotation speeds range 350-950 rpm and traverse speed range 50-150 mm/min, the combination of 350 rpm to 100 mm/min and 350 rpm to 50 mm/min yield higher UTS and %EL of the FSW joint.

Li et al. (2014) in their investigation to find the effect of FSW parameters of rotation speeds of range 750 to 1500 rpm and traverse speeds of range 100 to 300 mm/min for joining AA6061-T6 report that increase in the rotation speed results in higher heat generation, increase width of WNZ, TMAZ and HAZ, and insensitive to the tensile strength of the FSW joint. Further, they report that the increase in the tensile strength of the FSW joint achieved by increasing the traverse speed at higher rotation speed. Moshwan et al. (2015) in their investigation for joining similar AA5052-O by FSW technique studied the effect of tool rotational speeds in the range 800 to 1300 rpm keeping traverse speed of 120 mm/min as constant. Further, they report that higher tensile strength of 132 MPa obtained for the FSW joint produced with 1000 rpm. Rajakumar et al. (2011) in their study on joining AA7075-T6 by FSW technique investigated the effect of tool rotation speeds range 900 to 1800 rpm and traverse

speeds range 20 to 100 mm/min in conjunction with different tool pin and shoulder diameter. Further, they report a higher rotation speed of 1800 rpm results in the excessive stirring of the material and slow cooling rate of the FSW joint that leads to the formation of micro-voids. Similarly, lower traverse speeds of 20 and 40 mm/min, higher traverse speeds of 80 and 100 mm/min results in higher heat input and lack of bonding, respectively, leading to the reduction in the tensile strength of the FSW joint. Balasubramanian (2008) in their study in joining similar FSW butt joints of AA1050, AA6061, AA2024, AA7039 and AA7075 investigated the influence of individual parameter of tool rotation speeds and traverse speeds on the microstructure of the FSW joints. Further, they report defect-free welds are obtained for rotation speed and traverse speed of 900 rpm and 135 mm/min in AA1050, 1100 rpm and 100 mm/min in AA6061, 1200 rpm and 75 mm/min for AA2024, 1300 rpm and 45 mm/min for AA7039, 1500 rpm and 22 mm/min for AA7075 alloys joint.

Several literatures report the influence of tool geometry (pin profile, tool shoulder) and axial force on the microstructure and mechanical properties of the FSW joints. Kumar and Kailas (2008) in their investigation to study the influence of the tool shoulder on material flow pattern in joining similar FSW joint of AA7020 found that the proper interaction of the tool pin and shoulder results in better material flow and produce defect-free joint. Trimble et al. (2015) in their investigation to find the effect of different tool pin profile, rotation speed and welding speed in joining AA2024-T35 similar joints report that triflute tool with concave shoulder gave a good result of tensile strength and minimized the internal defects. Rajakumar et al. (2011) developed an empirical relation between axial force, tool pin, shoulder diameter, rotation speed and welding speed on tensile strength, hardness and corrosion rate in joining AA6061-T6 and concluded their work in obtaining optimum FSW parameters to maximize the tensile properties and minimize the corrosion rate of the joint.

2.2.2 Friction stir welding of dissimilar materials

In the aerospace industry, in order to withstand complex loading conditions and adverse chemical environment, and to increase the overall strength of the joints, there is a need for joining dissimilar materials for structural applications. Hence, the

selection of major FSW parameters to fabricate joints of dissimilar materials is a challenging task for many researchers.

Several literature (Khodir et al., 2008; Guo et al., 2014; Park et al., 2010; Rodriguez et al., 2015; Dinaharan et al., 2012; Ouyang and Kovacevic, 2002) reported that the quality and properties of the dissimilar materials FSW joint are affected by material location, FSW process parameters, material flow between AS and RS. Also, the WNZ of the dissimilar joint exhibits three different kinds of the regions, namely unmixed region (UMR), mixed flow region and mechanically mixed region (MMR) (Ouyang and Kovacevic, 2002). The UMR consists of the microstructure of any one type of material. Alternate layer-by-layer forming a lamellae pattern consisting of both the material characterizes the mixed flow region, and the MMR contains the microstructure of both the materials.

Khodir et al. (2008) examined the effect of different welding speed of 0.7, 1.2, 1.7, 3.3 mm/s and the constant rotation speed of 1200 rpm on mechanical properties and microstructure characteristics of AA2024-T3 and AA7075-T6 joints. Further, they report the presence of 'onion ring' patterns in the WNZ and concluded that when AA2024-T3 located on the AS results in highest joint efficiency with UTS of 423 MPa for welding speed of 1.67 mm/s. Guo et al. (2014) in their investigation in joining AA6061 to AA7075 report that locating AA6061 in the AS yields higher UTS of 245 MPa for the FSW joint. Rodriguez et al. (2015) in their investigation to study the effect of tool rotation speed in joining AA6061 to AA7050, and by placing AA7050 in the AS reports that increase in the tool rotation speed increased the mechanical properties and enhance the material mixing. Further, they report for low tool rotation speed yields a decreasing trend in the mechanical properties and failure of the joints at the WNZ due to inadequate material intermixing. Dinaharan et al. (2012) studied the contribution of material placed in AS and RS at four rotation speeds (800, 1000, 1200 and 1400 rpm) on the cast and wrought aluminium typical AA6061 alloy. The authors observed that for the tool rotation speeds 800 and 1000 rpm, the material kept at RS occupying a major portion of the WNZ. However, for increased tool rotation speeds from 1200 rpm to 1400 rpm has shown more contribution of the material kept at the AS occupying the WNZ. Ouyang and

Kovacevic (2002) studied the material flow and microstructure of dissimilar alloys joint of AA6061 and AA2024, and reports that the WNZ of FSW joint consisting of MMR, UMR and stirring-induced plastic flow region (SPFR). Further, they report that increase in the rotation speed result in improvement in mechanical mixing of the dissimilar alloys at the WNZ. In identifying appropriate FSW parameters for fabricating FSW joints of AA2024-T3 and AA7075-T6 alloy, Silva et al. (2011) studied the effect of tool rotation speeds (400, 1000 and 2000 rpm) and axial forces (13.4, 12 and 9.8 kN), and reports that the rotation speed, 1000 rpm, welding speed, 254 mm/min, yields higher weld efficiency and tensile strength. Palanivel et al. (2012) and Amancio et al. (2008) investigated the importance of mixed flow and unmixed flow region at the WNZ of dissimilar materials FSW joint of AA5083-H111 to AA6351-T6, and AA2024-T351 to AA6056-T4, respectively. Further, these authors report presence of alternate lamellae pattern of both materials at the WNZ.

2.3 DIFFERENT OPTIMIZATION TECHNIQUES TO OBTAIN OPTIMUM FSW PARAMETERS

Different types of optimization techniques that are extensively carried out pertaining to the optimization of FSW parameters consists of numerical methods, statistical method, computational techniques and experimental methods or with the combination of both. Brief details about the familiar and most common methods of the optimization techniques that have been practiced in FSW and FSP techniques are discussed.

2.3.1 Design of experiments (DOE) techniques and analytical methods

Design of experiments (DOE) is a critically important tool in the engineering field for improving the performance in the manufacturing process (Montgomery, 2017). Most of the literature (Koilaraj et al., 2012; Vijayan et al., 2010; Javadi et al., 2014; Sundaram and Murugan, 2010) report the selection of optimum FSW parameters using DOE statistical tools via Taguchi method and Response Surface Method (RSM) in joining similar and dissimilar materials by FSW technique, fabrication of MMC using FSW technique, fabrication of surface composites using FSP techniques.

Koliraj et al. (2011) in their investigation adopted Taguchi L_{16} (level 16) orthogonal array (OA) to optimize the FSW parameters to join dissimilar alloys of AA2219-T87 to AA5083-H321. Vijayan et al. (2010) investigated for attaining the optimal FSW parameter in joining similar alloy plates of AA5083 using the combination of optimization techniques of Taguchi L_9 OA and grey relation analysis (GRA). Further, they report the combination of rotational speed, 650 rpm, welding speed, 115 mm/min and tool axial force, 9 kN yields FSW joints with UTS of 275 MPa. Salehi et al. (2012) and Javadi et al. (2014) optimized the FSW process parameters using Taguchi technique. Sundaram and Murugan (2010) have applied mathematical regression model developed by using RSM for predicting the UTS and tensile elongation (TE) of dissimilar alloys joint of AA2024-T6 and AA5083-H321. Similarly, Rajakumar and Balasubramanian (2012) have applied the RSM technique to develop the empirical relation between input FSW parameters of traverse speed, axial force, rotation speed, shoulder and pin diameter with the output response as maximum tensile strength and minimum corrosion rate. Their developed relation is validated by studying the mechanical properties of FSW joint of AA1100. Similar work was carried out by Rajakumar et al. (2010) in developing the empirical relationship between input FSW parameters (rotational speed, traverse speed, axial force, shoulder diameter, pin diameter, tool hardness) to the output response (tensile strength, corrosion, hardness) in joining AA6061-T6 alloys using RSM technique. Further, the authors report that the rotation speed, 1100 rpm, traverse speed, 80 mm/min, axial force, 8 kN, shoulder diameter, 15 mm, and pin diameter, 5 mm yields higher tensile strength compared to the other FSW process parameters.

2.3.2 Computational techniques and simulation

Extensive research work has been performed in optimising the FSW parameters and simulating the grain structure using different types of computational techniques. These computational techniques involving numerical methods are very convenient in the analysis and simulating the correlation between FSW input parameters and output responses in terms of strength of the weld joint, material flow and grain size in the WNZ. The microstructure in the WNZ has a great influence on the mechanical properties of the weld joints. Thus, enhancing the strength of the weld joints depends

on the fine grain size in the WNZ and grain refining can be used as an effective method to improve the properties of the weld joint.

Shojaeefard et al. (2014) in their experimental investigation to join the similar alloys of AA1100 by FSW technique reports using cellular automaton (CA) method to simulate the grain structure of the weld zone. Further, they report a better agreement between the simulated and the experimental results. Rajakumar et al. (2010) established an empirical relationship for predicting the grain size and tensile strength of the FSW joint of AA6061 using RSM and analysis of variance (ANOVA). Rajakumar and Balasubramanian (2011) predicted the grain size of the AA7075-T6 FSW joint using ANOVA, and developed empirical relationship between the FSW input parameters and output mechanical properties using RSM. Fratini et al. (2009) in their investigation to obtain FSW joints of alloy plates of AA2139-T8 with combination of three joint configurations via butt, lap and T-joints, used trained neural network (NN) linked to the 3D finite element method (FEM), and predicts the average grain size in the weld region. Buffa et al. (2007) in their study simulated the continuous dynamic recrystallization (CDRX) phenomenon in the FSW process using 3D FEM model to predict the microstructure average grain size during joining AA7075-T6 in butt joint configuration.

Several literatures report the predicted correlation between the FSW parameters and the mechanical properties of the FSW joint. Okuyucu et al. (2005) in their investigation joining the aluminium alloy by FSW technique used an artificial neural network (ANN) considering the input FSW parameter of tool rotation speed to predict the output parameters such as UTS, YS and hardness of the HAZ. Shojaeefard et al. (2012) in their investigation to join AA7075-O and AA5083-O developed ANN model to correlate the relationship between input FSW parameters and output mechanical properties. Zhang and Zhang (2009) carried out the numerical analyses using finite element package ABAQUS to find the effect of traverse speed on the material flow during the FSW process. Qian et al. (2013) developed an analytical model based on the principle of material flow and temperature to optimize the tool rotation, welding speed to produce the defect-free joint. Roshan et al. (2013) in their investigation used Adaptive Neuro-Fuzzy Inference Systems (ANFIS) to build the

relationship between FSW parameters such as tool pin profile, rotation speed, traverse speed, axial force to the output response of tensile properties of the FSW joint of AA7075.

2.3.3 Bottom-up experimental approach

A bottom-up experimental approach is typically an optimization technique that focuses on the effect of the individual FSW parameter on the mechanical properties and microstructure characteristics of the specimens produced by FSW and FSP technique. In the approach, the optimum individual parameter is obtained by varying one parameter for every trial, while the remaining parameters are kept constant. Nadammal et al. (2015) in their investigation for obtaining the optimum FSP parameters for AA2024-T3 adopted the bottom-up approach for the first time. Further, they report the optimized FSP parameters produce higher tensile properties and defect-free FSP sample of AA2024-T3. However, the application of bottom-up experimental approach for joining similar or dissimilar materials using FSW technique to obtain the optimum FSW parameters is not reported in the literature.

2.4 EFFECT OF MATERIAL LOCATION AND TOOL PROBE OFFSET ON FSW DISSIMILAR MATERIALS JOINT PROPERTIES

In joining dissimilar materials, the asymmetry in temperature, stress and materials flow between the AS and RS of the weld joint affects the FSW joint quality and properties. In addition to the chosen FSW parameters, the quality and properties of dissimilar materials joint depend on the location of the materials and tool probe offset from the weld joint lone.

2.4.1 Effect of material location in joining dissimilar material

Many researchers (Khodir et al., 2008; Guo et al., 2014; Park et al., 2010; Lee et al., 2003) in their study suggested for placing higher strength material in the RS. In addition, they conclude that the joint strength and properties are more dependent on the alloy on the RS, and the WNZ mainly consists of material from the RS. However, placing the higher strength material in the AS results in the development of high flow stress and prevents the flow of low strength material towards WNZ. Khodir et al.

(2008) in their investigation to find the effect of material location and traverse speed in joining AA2024-T3 to AA7075-T6 report higher tensile strength of the FSW joint with AA2024-T3 located on the AS. Further, they report presence of kissing bond defects and pores for rise in traverse speed with AA2024-T3 plate located on the RS. Guo et al. (2014) in their investigation in joining dissimilar aluminium alloys of AA6061 to AA7075 report effective material mixing and higher joint strength for higher welding speed with AA6061 located on the AS. Park et al. (2010) in their study report proper materials mixing with AA5052-H32 located in the AS and AA6061-T6 in the RS. Aval et al. (2011) in their investigation in joining AA5086 to AA6061 report that the efficient material flow and mixing is obtained when the AA5086 kept in the AS and AA6061 in the RS. Lee et al. (2003) in their study on FSW dissimilar materials joint of AA6061 and A356 reports that the dominant material in the WNZ microstructure mainly came from the harder material AA6061 kept in the RS. Further, they report that irrespective of welding speed, higher longitudinal tensile properties of the weld joint are obtained by fixing relatively soft material A356 in the AS. Luijendijk et al. (2000) recommends placing the softer AA2024-T351 in the AS when it is weld with harder AA6056-T4 alloy.

On the other hand, in most of the studies carried out in joining dissimilar material concludes that material flow found to be primary and important compared to the material location being secondary. Silva et al. (2011) studied the effect of rotation speed and axial force with constant welding speed on material flow and mechanical properties of FSW dissimilar materials joint of AA2024-T3 and AA7075-T6 by placing AA7075-T6 on the AS. Further, they found that at increased rotation speed results in good material mixing and mechanical properties of the joint. Rodriguez et al. (2015) in their studies on strength of FSW dissimilar materials joint of AA6061 to AA7050 by placing AA7050-T745 in the AS reports that the increase in the tool rotation speed increased the strength. Further, they report low rotation speed reduced the tensile strength and materials mixing, and FSW joints failed at WNZ. The contribution of material placed in RS at various rotation speeds was studied by Dinaharan et al. (2012) in joining cast and wrought AA6061. Further, they report that

increase in the tool rotation speed enhanced the contribution of the material placed in the AS and occupied the major portion of the WNZ.

2.4.2 Tool probe offset method in joining dissimilar materials

Several literatures (Cavaliere et al., 2008; Cole et al., 2014; Liang et al., 2013; Sahu et al., 2016; Galvao et al., 2012; Song et al., 2014; Kumar and Sathish, 2008) reports the implementation of tool offset as a method to diminish the effect of strength reduction in production of FSW joint of dissimilar materials. Tool offset found to be beneficial in enhancing the material flow characteristics and exhibits higher mechanical properties of the dissimilar materials FSW joint.

Cavaliere et al. (2008) used the tool-offset distance of 0, 0.5, 1 and 1.5 mm towards AA2024 in fabricating FSW dissimilar aluminium alloys joint of AA2024 to AA7075. Further, they report tool offset of 1 mm towards AS of the AA2024 results in higher UTS of 460 MPa, YS of 395 MPa and % EL of 4.5. However, further moving the tool offset distance towards AA2024 yields decrease in the mechanical properties. Cole et al. (2014) in their investigation in joining FSW dissimilar materials of AA6061-T6 to AA7075-T6 suggested tool offset towards higher-hot strength AA7075-T6 kept in the RS results in increased amount of AA7075 material flow into WNZ and enhancing the tensile strength of the joint. Sahu et al. (2016) in their investigation in joining the dissimilar materials of AA1050 to Cu by FSW report that tool offset distance of 1.5 mm towards AA 1050 yield higher UTS of 126 MPa and YS of 119 MPa. Song et al. (2014) in their investigation to study the influence of tool-offset distance 0-1.2 mm towards titanium alloy (Ti_6Al_4V) in joining dissimilar materials Ti_6Al_4V to AA6061-T6 report that tool offset of 0.9 mm, rotation speed of 750 rpm and 1000 rpm yields higher UTS and YS. Kumar and Sathish (2008) in their study in joining similar AA7020-T6 report a safe range of tool deviation from the weld interface as 1 mm towards RS and 1.6 mm towards AS from the selected tool interface position range of 3.1. Further, they report a decrease in the tensile strength when the tool deviates slightly away from the safe range.

2.5 PRODUCTION OF COMPOSITES AT THE WELD NUGGET ZONE

Extensive research works have been carried out to produce the composites using FSP and FSW techniques. Compared to unreinforced alloys, the composites prepared by reinforcing nano or micro particles during FSW/FSP techniques have shown improvement in tribological, mechanical properties and better microstructure characteristics.

2.5.1 Production of composites using FSP

FSP technique used to fabricate the surface composites on the metal surface rather than in joining the two materials. Several literature (Don-Hyun et al., 2012; Akramifard et al., 2014; Wang et al., 2009; Dolatkhah et al., 2012; Azizieh et al., 2011; Sathiskumar et al., 2013) reports on the fabrication of MMC by FSP technique. In all of these work, the composites were successfully fabricated by FSP on the metal surface but not focusing on joining.

2.5.2 Production of composites using FSW

Most of the literature (Abbasi et al., 2015; Bahrami et al., 2014; Tabasi et al., 2016; Liu et al., 2015; Byung-Wook et al., 2012; Pantelis et al., 2016; Sun and Fujii, 2011; Hamdollahzadeh et al., 2015) reports on the fabrication of MMC via FSW by incorporating micro or nano particles into the rectangular section edge-groove of definite size between the two adjoining plates.

FSW parameters such as tool rotation speed, traverse speed, tool geometry and number of FSW pass plays an important role in uniform distribution of nano particles in the SZ or WNZ, TMAZ and HAZ region of FSW joint. Abbasi et al. (2015) investigated the effect of tool rotation speeds and traverse speeds on the FSW joint of AZ31 magnesium alloy fabricated by incorporating SiC particle of size 55 μm into the plates. Authors report selection of proper FSW parameter condition results in a homogeneous distribution of SiC particles in the SZ. Further, they report that the addition of SiC has decreased grain size in the SZ, increased in both ductility and strength of the joint compared to the FSW processed joint without SiC. Bahrami et al.

(2014) did similar work in their study on the effect rotation speed, traverse speeds and FSW single pass on FSW joint of 7075-O aluminium alloy plates reinforced with SiC_{NP} of size 45-65 nm. They found that the high rotation speed of 1250 rpm and traverse speed of 40 mm/min results in good powder dispersion, 31% superior UTS of FSW joint reinforced with SiC_{NP} compared to without SiC_{NP}. Further, they report, an increase in UTS was the result of the pinning effect and increased nucleation sites caused by the inclusion of SiC_{NP}.

Byung-wook et al. (2012) in their study on producing SiC/AA5083 composites by reinforcing the SiC powder reports that the SiC particles distribution was uniform in FSW second pass compared to the first pass. Further, they report the pinning effect by SiC particles results in smaller grain size at SZ of FSW joint compared joint without SiC. Pantelis et al. (2016) fabricated FSW dissimilar materials joint of AA5083-111 and AA6082-T6 reinforced with SiC_{NP} of size 20-30 nm with a constant rotation speed of 750 rpm, traverse speed of 85 mm/min and increasing the number of FSW pass. They found that the FSW dissimilar materials joint with first pass shows agglomeration. However, the FSW second pass result in a better distribution of SiC_{NP}, higher UTS, % EL and the increased hardness in the SZ. Sun and Fujii (2011) in their study on pure Cu FSW joint report that FSW second pass helped in the uniform distribution of SiC of size 5 μm and the pores formed around the agglomerated SiC particles during the FSW first pass were refilled after the FSW second pass. Further, the SZ exhibited the particle rich region having a grain size of 2 μm , while particle free region consists of a grain size of 8 μm . Contrary to the study on FSW second pass, Hamadollahzadeh et al. (2015) investigated the effectiveness of FSW second pass using a square pin tool on the mechanical properties and microstructure of nano SiC fortified AA7075. They found that FSW second pass processed FSW joint exhibited much uniform distribution of SiC particles than the first pass. However, the FSW joint after second pass results in inferior UTS and an increase in the grain size compared to joint prepared with first pass. Further, they report such a contradiction was due to the dominating “heat input” over the “pinning effect” by the SiC particles.

2.6 RESEARCH GAP

Based on the literature review most of the published works have focused on following aspects mentioned below:

- Most of the works are focused on to find the optimal FSW parameters by using the statistical tool of DOE techniques (Taguchi, RSM etc.). Also, the computational and simulation techniques such as ANN, CA, GRA, FEM, ABAQUS, ANFIS, have been used to predict the mechanical properties, the microstructure of the FSW joints. The empirical relationship between FSW input parameters and output properties has been developed to predict the FSW joint strength and other properties of the weld.

These optimization techniques (DOE, Taguchi, RSM) involve the procedure complexity and more numbers of experimental runs. In addition, the predicted mechanical properties and microstructure of the FSW joints using computational and simulation techniques (ANN, CA, GRA, FEM, ABAQUS, and ANFIS) may vary after the actual experiments. In addition, the building the empirical relationship between input and output parameters involves the procedure complexity and more numbers of experimental runs are needed to validate these empirical relationships.

- For joining the dissimilar material by FSW process, studies have been carried out by considering the position of the high strength material in both sides of tool rotation i.e. AS and RS.

However, the studies on the relationship between the welding condition of varying traverse speed (VTS) along the weld length and tool-probe offset distance from the joint interface on the microstructure evaluation and mechanical properties of FSW dissimilar AA2024-T351 to AA7075-T651 is found to be scant.

- In most of the studies, FSW joints are fabricated by introducing a fixed concentration of reinforcement nano/micro particles to develop MMC/MMNC at the WNZ. The role of relevant FSW parameters, FSW first

and second pass are also studied on the distribution of reinforcement particles.

However, there is a gap in understanding the effect of varying percentage volume fraction of SiC_{NP} reinforcement after the FSW first pass and second pass in the MMNC at the WNZ and its effect on the microstructure and mechanical properties FSW dissimilar joints.

Based on the above facts, it is required to carry out the investigations with main goals of this research study to utilize the bottom-up experimental approach to obtain optimum FSW parameters to join dissimilar aluminium alloys joint, implementing tool probe offset and traverse speed to join dissimilar aluminium alloys joint, and to fabricate composites at the WNZ of FSW dissimilar aluminium alloys joint. The objectives set out to achieve these main goals were derived and listed in the proceeding section.

2.7 OBJECTIVES OF THE RESEARCH WORK

1. To arrive at the optimal FSW parameters for joining the dissimilar aluminium alloys using a bottom-up experimental approach.
2. To investigate the effect of different tool probe offset condition in conjunction with the traverse speed on mechanical properties and microstructure characteristics of FSW dissimilar aluminium alloys joint with butt-joint configuration.
3. To investigate the influence of tool rotation speed and FSW first pass on the distribution of fixed %vol. fraction of SiC_{NP} at the WNZ, mechanical properties and microstructure characteristics of the FSW dissimilar aluminium alloys joint.
4. To investigate the effect of varying % vol. fractions of SiC_{NP} reinforcement at the WNZ, FSW first pass and second pass on the mechanical properties and microstructure characteristics of the FSW dissimilar aluminium alloys joint.

2.8 SCOPE OF THE RESEARCH WORK

The scope of the present research work is drawn as follows:

- Present research work focuses on conducting an experimental investigation to obtain the optimum FSW parameters in joining two dissimilar aluminium alloys with butt-joint configuration. Most of the existing techniques or methodology discussed in the literature review adopt with complex procedure and more number of experimental runs to obtain optimum FSW parameters. Whereas, the present study adopt bottom-up experimental approach for obtaining the optimum FSW parameters. The bottom-up experimental approach is a simple and potential candidature that eliminates the complexity in the procedure further, with a few number experimental runs.
- The research work also focuses on obtaining the FSW dissimilar aluminium alloys joint that exhibit enhanced mechanical properties and better metallurgical characteristics by making use of tool probe offset method in conjunction with the varying traverse speed along the joint line of the weld. The tool-probe offset distance from the joint line interface towards either of any one material changes the material flow towards the WNZ. Thus, the presence of dominating material at the WNZ at each tool probe offset condition and its effect on the mechanical, microstructure properties can be investigated. In addition, the heat input into the WNZ varies with the change in the traverse speed and affects the grain size at the WNZ in turn decides the strength of the weld joint.
- In the present study, the effect of varying percentage of SiC_{NP} reinforced in the WNZ to produce composite at the WNZ. The effect of reinforcing the varying percentage of SiC_{NP} in the WNZ on the mechanical properties and microstructure of the dissimilar aluminium alloys joint investigated and compared with joint produced without SiC_{NP}. In addition, the research work focuses on the effect of FSW first and second pass on the distribution of SiC_{NP} at the WNZ. Further, the actual percentage volume fraction of SiC_{NP} after the FSW first pass (V_{fp}) and

second pass (V_{sp}) in the MMNC at the WNZ and its effect on the mechanical properties and microstructure are investigated.

2.9 SUMMARY

This chapter reported the comprehensive review on the existing optimization techniques for optimizing the FSW parameters for joining similar or dissimilar joints made up of different materials. In addition, the implementation of the tool probe offset method to diminish the strength reduction in the FSW joint discussed. Further, the investigation carried out by researchers for the production of the composites at the weld nugget zone using FSP and FSW techniques by reinforcing the nano particles into the rectangular groove also discussed. The objectives and scope of the present research work also discussed in this chapter. The materials, machines and experimental method are described in Chapters 3 to 6.

CHAPTER-3

MATERIALS, MACHINES AND METHODS

3.1 INTRODUCTION

This chapter discusses selection of materials, machines and tools, and methodology required for experimental investigations.

3.2 MATERIALS

3.2.1 Aluminium alloys

Two aluminium alloys considered for all the FSW experiments for fabricating the dissimilar aluminium alloys joint are typical rolled commercially available alloy metal plates of AA2024-T351 and AA7075-T651. Each plate is having a standard thickness of 6.35 mm and the plates are cut for the length dimensions of 200 mm long and 75 mm wide (along rolling direction) using wire cut electric discharge machine (EDM) process suitable to fix the plates on the mounting table during the FSW experiments. The AA2024 consists of Cu as the main alloying element, and AA7075 consists of Cu and Zn as its main alloying element, with Zn in a higher percentage of more than three times compared to the Cu. In the AA2024-T351, T-refers to ‘age hardened’ and the temper designation T351 denotes alloys tempered to a T3 condition by solution treatment, quenched, tensile deformed and naturally aged. Similarly, for AA7075-T651 the T651 refers to alloys tempered to a T6 condition by solution treatment followed by artificially ageing. Tables 3.1 and 3.2 provides the nominal chemical compositions in weight percent and mechanical properties obtained after conducting the standard test procedure on these two grade alloy plates, respectively. Figure 3.1 shows an example of the photographs of the aluminium alloy plate.

Table 3.1 Chemical compositions of AA2024-T351 and AA7075-T651.

Material type	Cu	Mg	Cr	Zn	Mn	Si	Fe	Ti	Al
2024-T351	4.38	1.5	0.01	0.02	0.49	0.05	0.12	0.05	Balance
7075-T651	1.3	2.3	0.19	5.6	0.02	0.03	0.14	0.05	Balance

Table 3.2 Mechanical properties of AA2024-T351 and AA7075-T651.

Material type	Yield strength (MPa)	Ultimate tensile strength (MPa)	Percentage elongation (% EL)	Vickers microhardness at 1 kgf load at 15s (Hv)
2024-T351	410±4	477±6	15±2	138±2
7075-T651	520±8	568±6	12±2	173±2

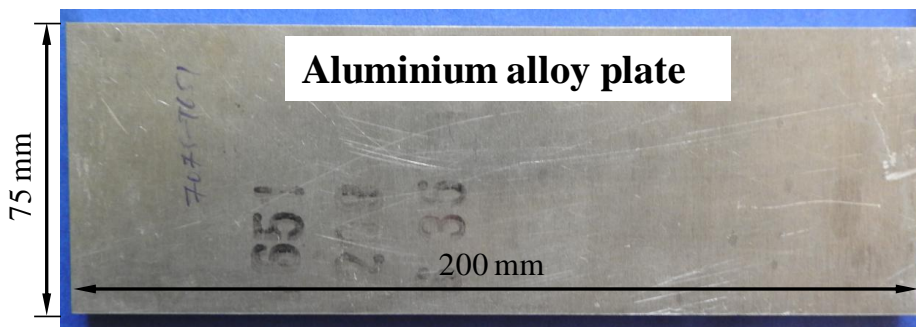


Figure 3.1 Photographs of a typical aluminium alloy plate used in the FSW experiments.

3.2.2 Reinforcement

Experimental investigation involving the production of MMNC at the WNZ of the dissimilar aluminium alloys joint of AA2024-T351 to AA7075-T651 having a rectangular groove of definite size cut at the adjoining surface of the two plates are reinforced with SiC_{NP} particles. Commercially available Beta (β)-Phase SiC_{NP} powder (purity ~ 98.5%) and having density (ρ) of 3.2 gm/cc with a mean particle size in the range of 40-50 nm (supplier: Alfa Aesar Pvt. Ltd, Lancashire, United Kingdom) is used as a reinforcement to produce MMNC at WNZ. Figure 3.2 shows transmission electron microscopy (TEM) image with selected area electron diffraction (SAED) of the SiC_{NP} powder.

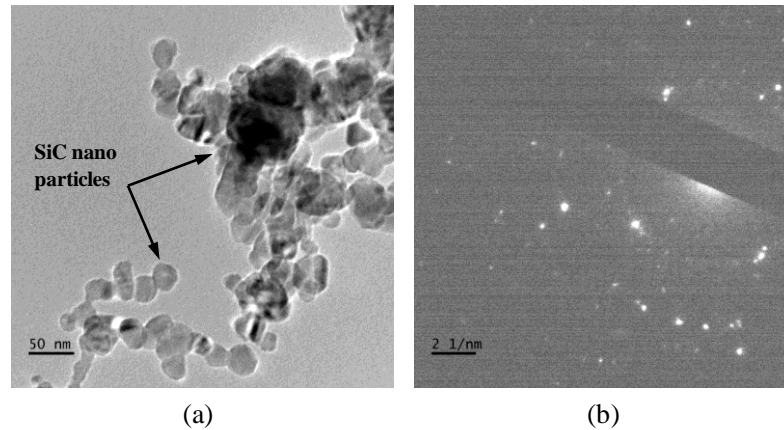


Figure 3.2 TEM images showing the (a) average size of the SiC_{NP} between 40 – 50 nm and (b) SAED pattern of SiC_{NP}.

3.3 FRICTION STIR WELDING MACHINE

The FSW experiments involving the fabrication of the dissimilar aluminium alloys joint are carried out using a custom designed five-axis FSW machine (Make: Bangalore Integrated System Solution (BISS) Pvt. Ltd., Bangalore, India). The FSW machines have a feature of high-stiffness, precision-aligned load frame with up to five-axis movements and independently controlled servo-actuators with the advanced features of 2370 MS controller to provide translation and deformation control of each axis (*X*, *Y* and *Z*-axis). The FSW machine is capable of varying the tool plunge depths, rotation speeds and traverse speeds during the FSW process along the weld joint line. Figure 3.3 (a-c) shows the photographs of the five-axis FSW machine available at the department of mechanical engineering, Indian Institute of Science (IISc.), Bangalore, India.

Figure 3.3 (a) shows the front view of the five-axis FSW machine built on stiff and the self-reacting base frame, and side reaction brackets. It has two double-ended double acting hydraulic actuators for *X* and *Y*-axis driven and movement controlled by servo motors. It uses double acting, single ended servo-hydraulic actuators for *Z*-axis. The *X*, *Y* and *Z*-axis are mounted on high-quality Linear Motion (LM) bearings. The servo motor of 2000 rpm, 18 kW is used to drive vertical actuators for *Z* movement of spindle assembly and horizontal actuators for movement of *X* – *Y* bed assembly. The

servo motor of 3000 rpm, 10 kW is used for superior bearing mounted spindle rotation at a maximum torque of 133 N-m.

Two-axes (X , Y -axis) of the FSW machine are controlled for the translation of the welding table in mutually perpendicular directions. Third-axis (Z -axis) used for the translation of the spindle in the direction perpendicular to the plane of the table. In addition, the spindle can also be tilted in X and Y planes. The linear hydraulic actuators control the movement along X , Y and Z -axis, while a rotary hydraulic actuator powers the spindle rotation. The two electric motors, one for each plane are used to provide spindle tilt.

Figure 3.3 (b) shows the photographs containing the plate-mounting table in which the metal plates are fixed and welded either in butt or lap joint configuration. In order to hold the plates of different dimensions, the fixtures made up of high-grade steel are used. The spindle responsible for the tool rotation is provided with the provision to fix the tool holder. The tool holder along with the tool can be rigidly fixed and held in the spindle using fasteners. Figure 3.3 (c) shows the photograph of the table capable of moving in X , Y and Z -axis direction with the maximum 500 mm stroke length in each axis direction. Table 3.3 provides the detail specifications of the FSW machine along with the operating range of the FSW parameters.

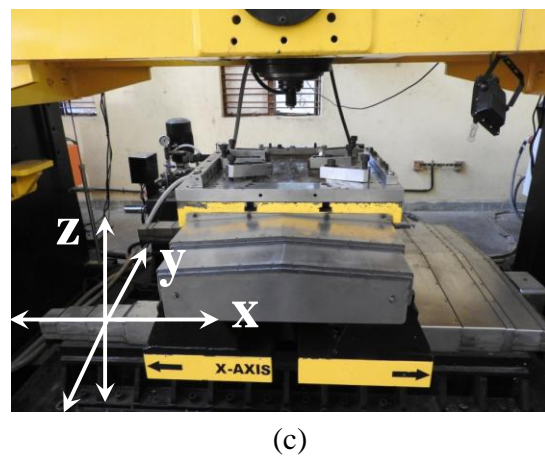
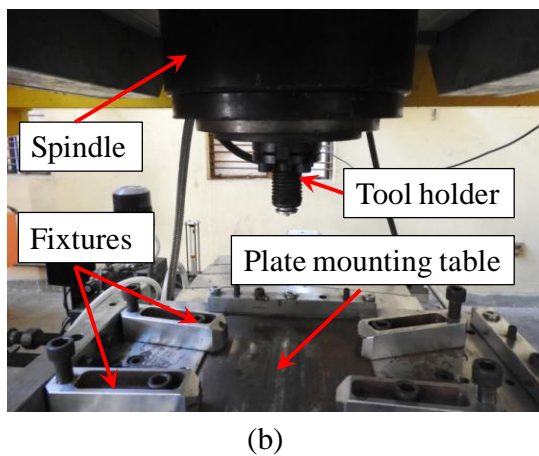
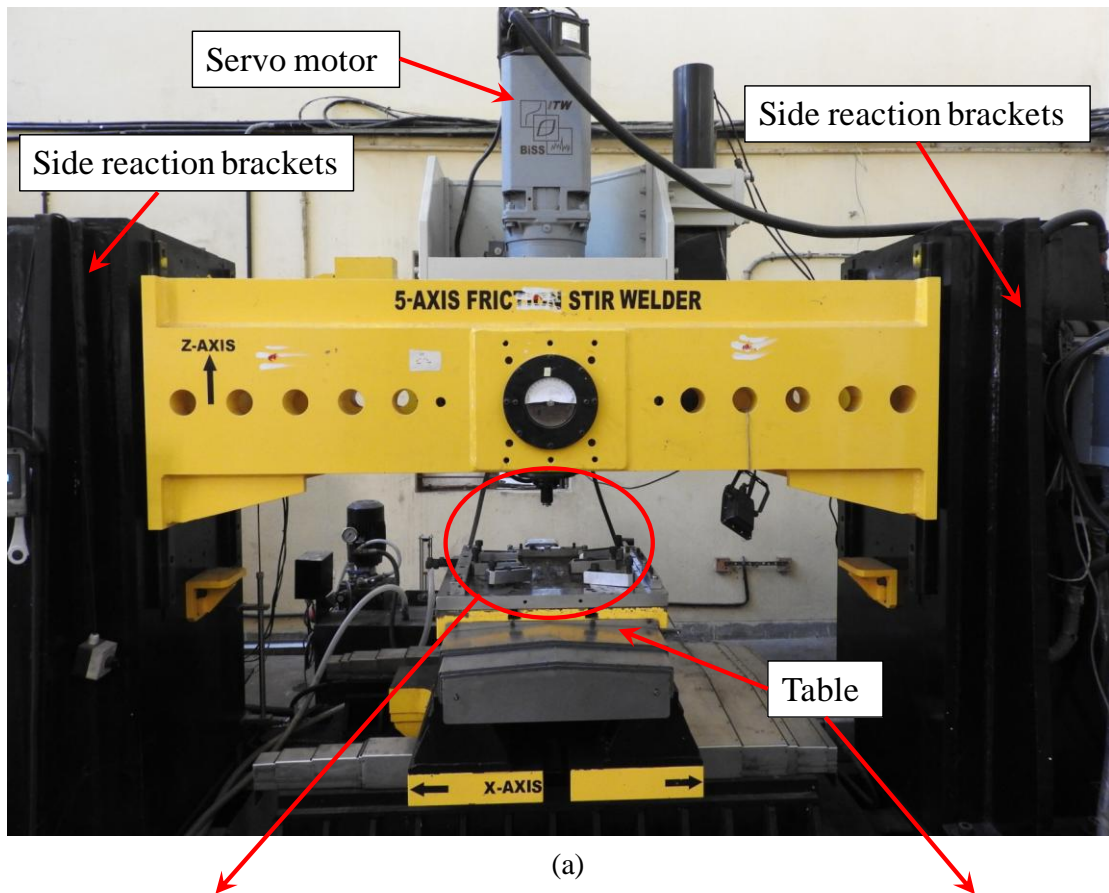


Figure 3.3 Photographs showing (a) Five-Axes friction stir welding machine, (b) Plate mounting table with fixtures and (c) Table movement in X, Y and Z- direction.

Table 3.3 The specifications of the FSW machine.

Sl. No.	Item	Specification
1	Table size	500 mm × 500 mm
2	Maximum vertical load (Z)	50 kN
3	Maximum X and Y-axis thrust load	25 kN
4	Spindle rotational speed	100 to 3000 rpm
5	Table speed	1 to 250 mm/min
6	Tool Tilt	-6 to +6 degrees in both X and Y plane
7	Cooling system	Water cooled
8	Axes speed	X and Y up to 3000 mm/min , Z up to 250 mm/min
9	Servo motor speed, rpm	2000 to 3000
10	Spindle motor power, kW	10

3.3.1 Friction stir welding tools

In the present study, the FSW experiments are carried out using two types of tool geometry.

- i. Taper threaded cylindrical tool
- ii. Taper triangle tool

The FSW experiments for obtaining the optimum FSW parameters using a bottom-up experimental approach are carried out employing taper threaded cylindrical and taper triangle tool. However, the FSW experimental investigation for the fabrication of FSW dissimilar aluminium alloys joint by tool probe offset method and production of MMNC at the WNZ are carried out using taper threaded cylindrical tool.

Figures 3.4 and 3.5 shows the schematic and photographs of taper threaded cylindrical and taper triangle tool, respectively. Both the tools are made from hot die steel (HDS) material and in H13 hardened condition. Figure 3.4 (a) presents the taper threaded cylindrical tool geometry consists of shoulder diameter, $d = 20$ mm which was chamfered from a cylinder diameter, $D = 25$ mm, height of cylinder, $H = 22.5$ mm, chamfered height of the cylinder, $h = 2.5$ mm, pin bottom diameter, $d_1 = 6$ mm, pin top diameter, $d_2 = 7.5$ mm, thread pitch equal to 1.5 mm and pin probe length, $L = 5.8$ mm. The tool shoulder has a flat feature.

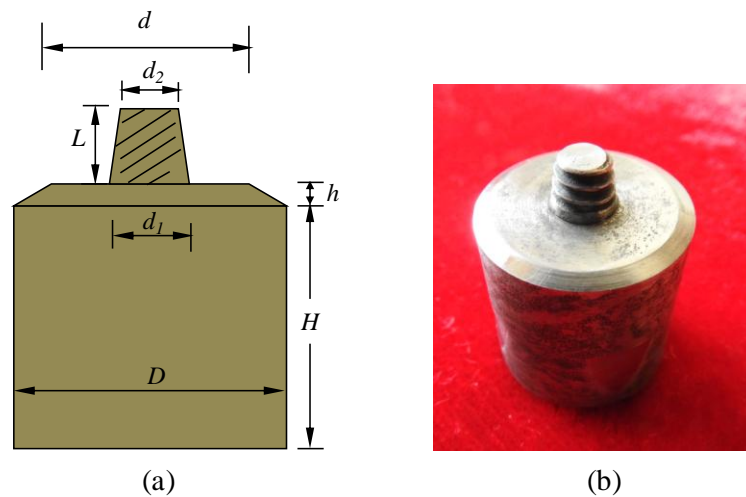


Figure 3.4 (a) Schematic of taper threaded cylindrical showing the tool dimension and (b) photograph of tool.

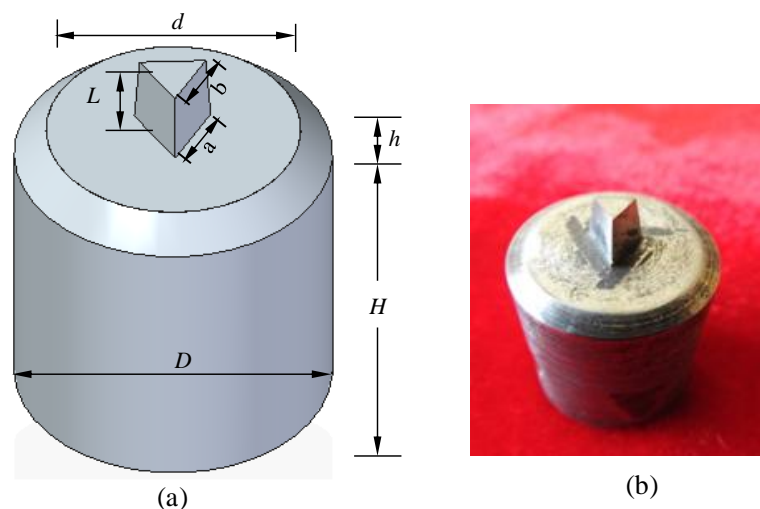


Figure 3.5 (a) Schematic of taper triangle tool showing the tool dimension and (b) photograph of tool.

Similarly, Figure 3.5 (a) presents the schematic of the taper triangle tool geometry consists of same dimensions as that of taper threaded cylindrical tool, except the pin profile shape of taper triangle with pin top edge length, $b = 5$ mm and pin bottom edge length, $a = 6$ mm. The tool shoulder has a flat feature. Both the tools presented are used for a set of particular type of FSW experiment.

3.3.2 Tool holder

Figure 3.6 (a) and (b) presents the front and top view photographs of the tool holder, respectively. The tool holder inner diameter is $D = 25$ mm and the tool shoulder of either taper threaded cylindrical or taper triangle tool is inserted into the tool holder and tighten with the screws. The entire assembly of tool holder along and the tool is fitted to the FSW machine spindle using four set of nut and bolt fasteners.

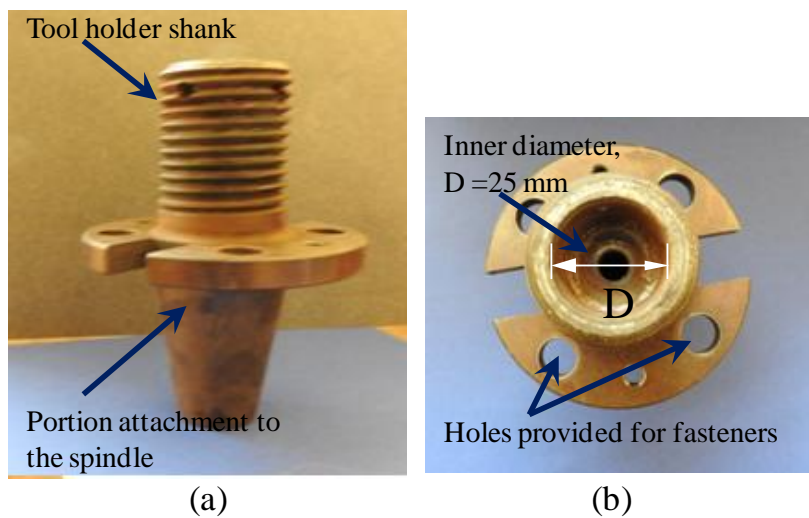


Figure 3.6 Photograph showing (a) front view and (b) top view of the tool holder.

3.4 MECHANICAL PROPERTIES EVALUATION

The dissimilar aluminium alloys joint fabricated using FSW technique is evaluated for its mechanical properties such as tensile strength and micro hardness. The detailed procedure involving the tensile testing and micro hardness measurement are explained in the proceeding sections.

3.4.1 Tensile test

After the completion of the welding by FSW process, the tensile specimens are machined from the FSW dissimilar aluminium alloys joint in the ‘as-welded’(AW) condition and in the direction normal (transverse) to the welding direction, y , (Figure 1.2). The tensile specimens extracted using wire cut EDM process is prepared according to the American Society for Testing Material (ASTM) of code E8M-04 having dimension of total length, $L = 100$ mm, gauge length, $G = 25$ mm, width, $W = 6 \pm 0.1$ mm, length of the reduced cross section, $A = 32$ mm, length of grip section, $B = 30$ mm, width of grip section, $C = 10$ mm, and thickness, $T = 6$ mm. The tensile specimens extracted from the dissimilar aluminium alloys joint possess all the four zones of the weld region, i.e., WNZ, TMAZ, HAZ and BM, and are evaluated for tensile properties such as UTS, YS and % EL. Figure 3.7 shows a schematic of the tensile specimen and its dimensions according to the ASTM of code E8M-04.

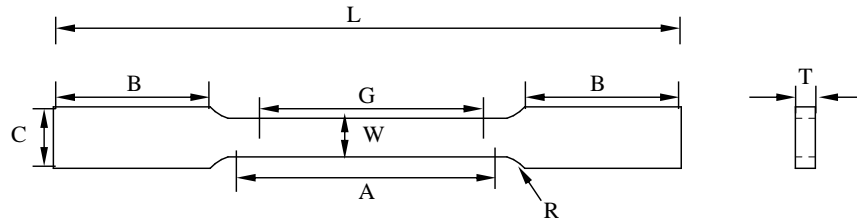


Figure 3.7 Schematic representations of tensile specimen and its dimensions according to the ASTM standard of E8M-04.

Further, the weld joint efficiency, η_{WJ} is the ratio of UTS of the tested tensile specimen from the dissimilar aluminium alloys joint (UTS_{AJ}) to the UTS of the tensile specimen tested from the base material plate (UTS_{BM}). i.e.,

$$\eta_{WJ} = \frac{UTS_{AJ}}{UTS_{BM}} \quad (3.1)$$

The tensile tests are performed using a SHIMADZU type AGS-X series servo hydraulic tensile testing machine (Make: SHIMADZU Corporation, Tokyo, Japan). The machine has a capacity of 100 kN. The machine is capable of testing the tensile specimen having a width up to 600 mm. The tensile load applied axially and the test is performed at a strain rate of $0.001s^{-1}$ with gauge length of 25 mm. The load and

displacement data recorded. From the recorded load-displacement data, the plots of stress-strain are obtained for the evaluation of UTS, YS and % EL of the tested tensile samples of FSW dissimilar aluminium alloys joint.

3.4.2 Hardness tests

The hardness properties of the FSW dissimilar aluminium alloys joint are measured across the weld regions of the specimens that are extracted and prepared for the microstructure analyses. The distinct zones of the specimen such as WNZ, TMAZ, and HAZ of adjoining the AS, RS, and the BM are considered for measuring the hardness. Figure 3.8 shows a typical example of the specimen with indent locations on the transverse cross-section of the weld region for hardness measurement. The location of the indent was selected with a depth of 3 mm from the top crown surface and across the transverse cross-section of the specimen as depicted in Figure 3.8.

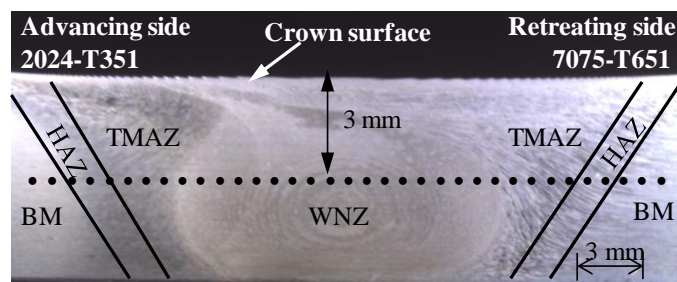


Figure 3.8 An example of the microstructure specimen used for measuring the micro-hardness.

The hardness of the specimens was measured using SHIMADZU type HMV-G20ST micro-Vickers hardness testing machine (Make: SHIMADZU Corporation, Tokyo, Japan). For the indentation reading method, the manual reading is employed for the length measurement of the indentation mark made on the image captured by optical microscope (OM). The hardness test is carried out by applying a load of 1 kgf for 15s holding time and the measured parameters are shown in the Figure 3.9. The calculation of the hardness by the Vickers pyramid number (HV) is given in the equation (3.2).

$$HV = \frac{2P \sin \left(\frac{\alpha}{2} \right)}{d^2} \quad (3.2)$$

where α is the angle at the vortex of the pyramid indenter, 136° , P is the test force in kg-force (kgf), d is the arithmetic mean of the two diagonals d_1 and d_2 . By substituting the value of $\alpha=136^\circ$ in to equation (3.2),

$$HV = \frac{1.8544P}{d^2} \quad (3.3)$$

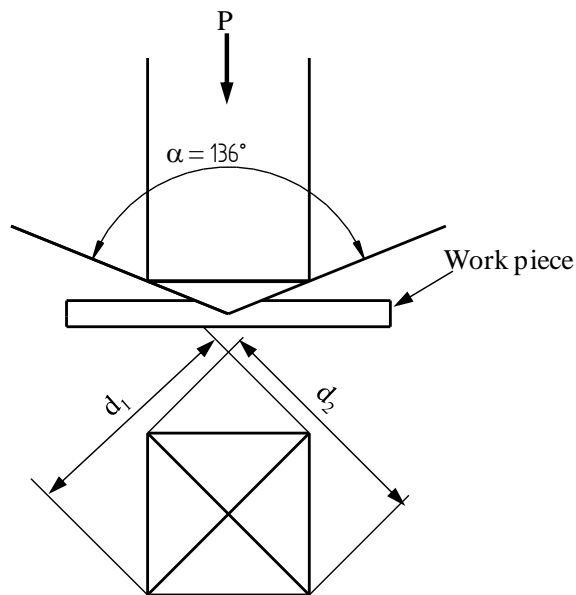


Figure 3.9 Schematic showing the measurement of indentation in micro-Vickers hardness test method.

3.5 MICROSTRUCTURAL CHARACTERISATION

After the FSW process, the specimens for microstructure investigation are extracted from the fabricated FSW dissimilar aluminium alloys joint in the direction normal (transverse) to the welding direction or tool traverse direction, y (Figure 1.2.). The location of the microstructure specimen is next to the tensile specimen. A wire cut EDM process used for the extraction of the specimen from the dissimilar aluminium alloys joint. The microstructure specimen are prepared with a height, 10 mm, and width, 40 to 45 mm, ensuring that the width of the specimen covers the distinct zones

of a typical FSW specimen such as such as WNZ, TMAZ, HAZ of adjoining the AS, RS, and the BM. The standard metallographic procedure in preparing the specimen to study the macro and microstructures features using optical microscopy, SEM, TEM etc., are explained in the proceeding sections.

3.5.1 Preparation of the specimen

Microstructure specimens for metallographic examination are prepared by performing the three stages of surface polishing. In the first stage, each specimen is polished using SiC water proof emery papers with grades from P400 to P3000. In the second stage, the velvet cloth is fitted to the disc of the variable speed tabletop BAINPOL-VTD polishing machine (Make: Chennai Metco Pvt. Ltd., Chennai, India). The specimens are polished by applying the alumina powder with particles of size 1 micron on the velvet cloth fitted to the polishing machine. In the last case, the fine polishing of surface achieved using diamond particles of 0.5 microns. After completing the polishing procedure, the samples are etched with standard Keller's reagent prepared by using 1 ml of Hydrofluoric (HF) acid, 2.5 ml of Nitric (HNO₃) acid, 1.5 ml of Hydrochloric (HCl) acid and 95 ml of distilled water.

3.5.2 Optical microscopy

The microstructure specimens prepared are observed to obtain the macrostructure (or macrograph) of the weld region by two stages and using two types of OM devices as given below,

- 1) Stereo-Zoom microscope
- 2) ZEISS-AXIO-CAM 105

In the first stage, the specimens prepared are examined to obtain the macrostructure of the weld region covering the distinct zones such as WNZ, TMAZ, HAZ of both AS and RS of the FSW dissimilar aluminium alloys joint. The shape and size of the WNZ, the interface boundary between WNZ and TMAZ, the presence of any macroscopic level defects such as sharp boundary, pin hole, worm hole etc., are examined. These details are captured using a stereo zoom microscope having the low

magnification of 10x attached with PixeLINK PL-E423CU camera kit (Make: Navitar company, New York, USA).

In the second stage, the specimens are examined to obtain the material flow pattern in the weld region covering the WNZ, TMAZ, HAZ, and intermixing of the dissimilar material consisting of the ‘onion ring’ structure with alternate lamellar pattern, and presence of defects such as cracks, pin-hole, and worm hole, etc. These details are captured using a ZEISS AXIO-CAM 105 optical microscope with a magnification range 50X to 1000X (Make: Carl-ZEISS company, Germany). The macrostructures of the specimens are captured, processed and analysed using Axio-Vision imaging software supplied along with ZEISS AXIO-CAM-105 optical microscope.

3.5.3 Scanning electron microscopy

The detailed microstructure analysis of the specimen was carried out on the three zones of the weld region covering WNZ, TMAZ and HAZ of both AS and RS of the FSW dissimilar aluminium alloys joints. Grains distribution and size at the weld region, interface boundary between WNZ and TMAZ, the presence of microscopic level defects, etc., are investigated. For the composite specimens prepared by adding SiC_{NP} reinforcement at the WNZ, the microstructure examination was carried out to investigate the bonding between the reinforced SiC_{NP} and the matrix, presence of agglomeration defects of SiC_{NP}, and for the presence of pores around SiC_{NP}. These details are investigated using the JEOL type JSM-6380-LA model analytical scanning electron microscopy (SEM) machine (Make: JEOL ltd., Tokyo, Japan). The SEM machine is equipped with energy dispersive spectroscopy (EDS) microprobe.

3.5.4 Transmission electron microscopy

The SiC_{NP} used as reinforcement in the FSW experiments to fabricate the composites are examined using JEOL type JEM-2100-HR transmission electron microscopy (TEM) machine (Make: JEOL ltd., Tokyo, Japan). The TEM machine as a high resolution of 0.19 nm. The size of the SiC_{NP} and the selected area electron diffraction (SAED) is obtained from the TEM machines.

3.5.5 Image analysis

Image analysis is carried out using Image-J software on the captured SEM image of specimen extracted from the FSW dissimilar aluminium alloys joint reinforced with SiC_{NP} at the WNZ. The possible effects of FSW process parameters on the SiC_{NP} distributions are investigated using image analysis.

3.6 COMPOSITIONAL CHARACTERISATION

During the FSW process, weld region experiences higher heat generation due to the rotating tool and shoulder contact with the material surface, and results in intense plastic deformation and material flow at the different zones of the weld region. Thus, the weld region observes intense material mixing of different materials. In addition, SiC_{NP} reinforcement results in the complex compositions at the WNZ of the weld region. These compositions at the WNZ are studied using EDS and X-ray diffractometer (XRD) technique.

3.6.1 Energy dispersive spectroscopy

The chemical compositions at the WNZ of the fabricated FSW dissimilar aluminium alloys joint and MMNC reinforced with SiC_{NP} were analysed using SEM machine equipped with EDS. The EDS analyses are carried out choosing a point and the exposed surface on the specimen. In addition, various elemental particle distributions in the WNZ are identified by conducting elemental mapping analysis. The APEX software program (Make: EDAX-AMETEK Instruments India Pvt. Ltd, India) is used to collect and analyse the EDS data.

3.6.2 X-ray diffractometer

The samples with the dimension of length, 8 mm, width, 4 mm and thickness, 2 mm are extracted from the WNZ of the microstructure specimens for the X-ray diffraction (XRD) studies. The different phase (elemental or intermetallic or crystalline or non-crystalline phase) and its concentration levels present in the WNZ were identified and corresponding results of intensity peaks are obtained in a diffractogram. The samples

are scanned through a range of 2θ angles. The PANalytical X-ray diffractometer machine (Make: Malvern Panalytical Ltd, Netherland) is used for XRD studies.

3.7 DENSITY MESAUREMENT

The mechanical properties and microstructure characteristics of the fabricated MMNC by the FSW process depends on the higher densification mechanism. These properties depend on the uniform distributions of the varying volume fractions of SiC_{NP} (5, 8, 13%) reinforcement and their bonding with the aluminium alloy matrix in the WNZ. The non-uniform distributions of SiC_{NP} reinforcement results in the formation of pores around the nano particles. The actual density (ρ) is measured by extracting the specimens from the WNZ of MMNC in a ‘cube’ shape with equal dimensions of length, width and height equal to 2.15 mm from three different regions of WNZ including the porous region present around the SiC_{NP}. The weight of the specimen is measured using Vibra HT-224 analytical balance machine (Make: VIBRA Company, Canada) having precision up to 0.0001 gm and capacity up to 220 gm. The density of the specimen is measured using following equation.

$$\rho = \frac{m}{v} \quad (3.4)$$

where m is the mass of the specimen (g) and v is the volume of specimen (cc). The size of side of the cubic specimen considered in the entire investigation is 2.15 mm.

3.8 SUMMARY

In this chapter, materials and their properties, FSW machine used for the fabrication of the FSW dissimilar aluminium alloys joint, the detail procedure and methods deployed to evaluate the mechanical properties, microstructure and compositional characterisation of the FSW dissimilar aluminium alloys joint have been reported. A bottom-up experimental approach for optimizing the FSW parameters for joining dissimilar aluminium alloys joint are reported in Chapter 4.

CHAPTER-4

A BOTTOM-UP EXPERIMENTAL APPROACH FOR OPTIMIZING THE FSW PARAMETERS

4.1 INTRODUCTION

This chapter discusses the bottom-up experimental approach employed to join dissimilar aluminium alloys joint of AA2024-T351 and AA7075-T651 plates in butt-joint configuration by FSW technique. The major FSW parameters such as tool plunge depth (TPD), tool rotation speed (TRS) and tool traverse speed (TTS) are optimized using a bottom-up approach for the FSW dissimilar aluminium alloys joint for the first time.

4.2 EXPERIMENTAL TECHNIQUES FOR BOTTOM-UP APPROACH

A bottom-up experimental approach is typically an optimization technique involves two important aspects. In the first case, each experimental trial focuses on the effect of the major individual parameter (TPD or TRS or TTS) on the mechanical properties and microstructure characteristics of the FSW dissimilar aluminium alloys joint, rather than all the three major FSW parameters. A bottom-up approach assumes that each individual parameter shows the improvement in weld joint properties of the dissimilar aluminium alloys. In the approach, the optimum individual parameter is achieved by varying any one parameter for every trial, while the remaining parameters are kept constant. In the second case, the range of parameters that can be investigated using a bottom-up approach in a single experimental trial is much larger in numbers compared to the other DOE techniques (e.g., Taguchi, RSM, ANN, etc.) requires more number of experimental runs and trials. An experimental technique associated bottom-up approach for obtaining the optimum FSW parameters is one of the potential candidatures to eliminate complexity in the procedure further with few numbers of runs.

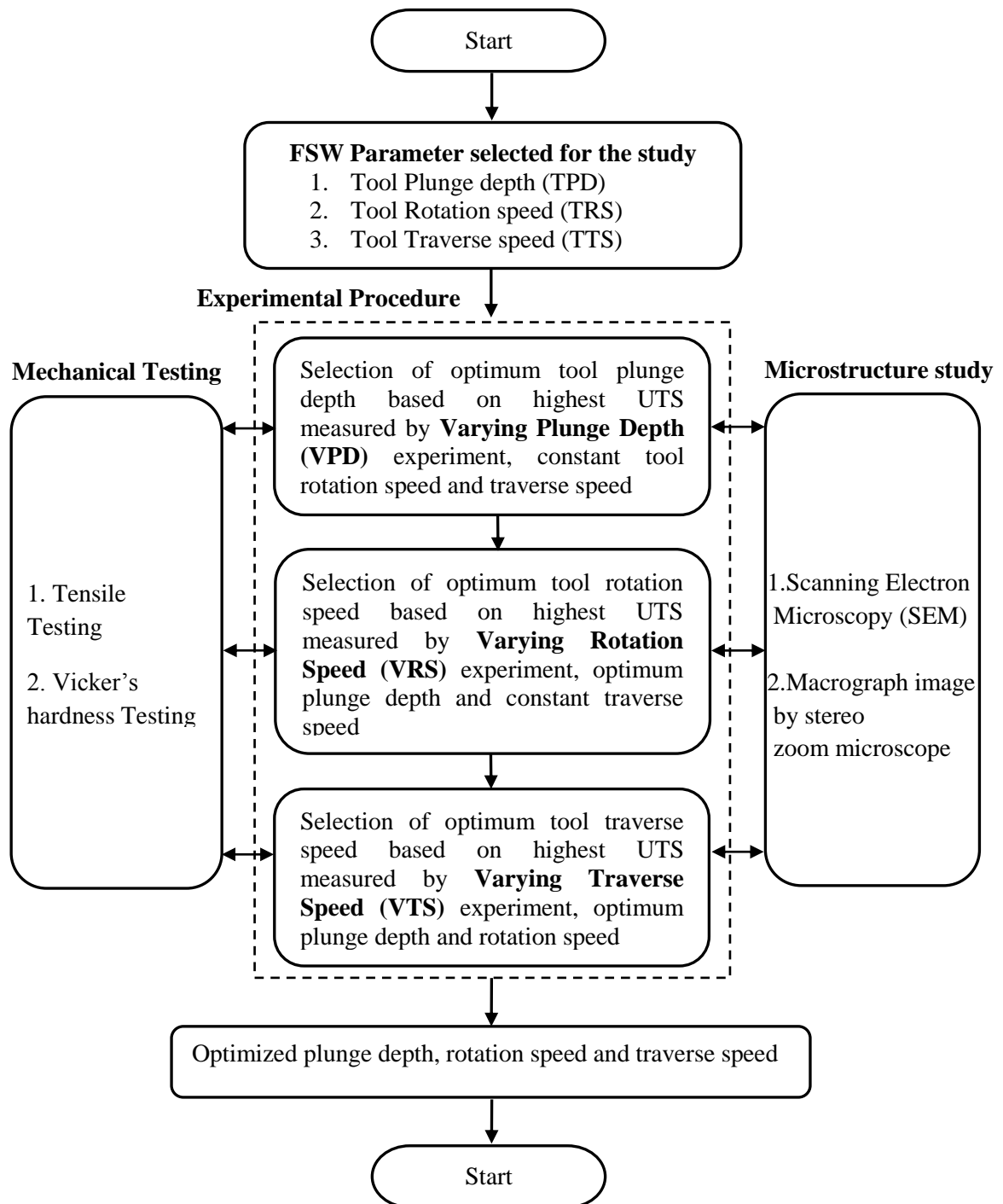


Figure 4.1 Flow chart illustrating the experimental techniques for bottom-up approach.

Figure 4.1 illustrates the flow chart of the experimental technique for the bottom-up experimental approach that has been applied for the optimization of the major FSW parameters such as TPD, TRS and TTS. The bottom-up experimental approach involves conducting the trials by varying any one parameter in each experimental trial

for a fixed weld length while the other two parameters kept as constant. The range of the individual parameter is varied over a fixed weld length along the weld joint line of the two dissimilar aluminium alloys kept in butt-joint configuration. As shown in Figure 4.1, in the first stage of the experiment the optimum TPD is obtained by conducting the varying plunge depth (VPD) experiment, while the TRS and TTS are kept constant. In the second stage of the experiment, the optimum TRS is obtained by conducting the varying rotation speed (VRS) experiment, while the optimum TPD and TTS are kept as constant. Similarly, in the final stage of the experiment, the optimum TTS is obtained by conducting the varying traverse speed (VTS) experiment while the optimized TPD and TRS from the previous stages of the experiment are kept constant. By the end of the final stage of the experiment, all the FSW parameters such as TPD, TRS and TTS were in the optimized condition.

In the experimental investigation under each trial, the optimization procedure is focused on each individual parameter that contributes in enhancing the mechanical properties and microstructure characteristics of the FSW dissimilar aluminium alloys joint and de-emphasizes the significance of the other two FSW parameters. However, the higher UTS of the tested tensile from the FSW dissimilar aluminium alloys joint is the basis for the selection of an optimum individual parameter. The type of tool geometry, the range of individual parameters selected for the study, the experimental procedure and the investigation are discussed in detail in the proceeding sections.

4.3 OPTIMIZATION PROCEDURES FOR A BOTTOM-UP EXPERIMENTAL APPROACH

The bottom-up experimental approach has been used for obtaining the optimum FSW parameters for joining the two dissimilar aluminium alloys joint of typically AA2024-T351 and AA7075-T651. The dissimilar aluminium alloys joints are fabricated by separate experiment trials and using two types of tool geometry.

The two types of tool geometries used in producing FSW dissimilar aluminium alloys joint are,

- i. Taper threaded cylindrical tool
- ii. Taper triangle tool

The tool material and the geometrical details of taper threaded cylindrical and taper triangle tool geometry that includes shoulder and pin profile are discussed in the Chapter 3, Section 3.3.1 (Figures 3.4 and 3.5). The experimental procedures of bottom-up experimental approach for achieving the optimum individual FSW parameters are discussed in the proceeding subsections.

4.3.1 Optimization of tool plunge depth (TPD) by varying plunge depth (VPD) experiment

In the first stage, the optimum TPD is achieved by conducting the VPD experiments and by keeping the other two parameters i.e. TRS and TTS as constant. In addition, for all the experimental trials the tool tilt angle (θ) is kept as 2° . The tilt angle, θ , is generally kept in the range 0 to 3° . A suitable tilt angle towards the trailing edge of the work piece helps in providing the sufficient forging force that helps the tool shoulder to hold sufficiently the plasticized stirred material and to move it efficiently around the tool pin. Increasing the tilt angle above 3° establish more contact between the tool shoulder and trailing edge of the tool that result in excessive flash in the weld crown surface and deteriorate the weld quality. The trail for VPD experiment is carried out by varying the TPD in the range from 5.80 mm to 6.20 mm along the z -direction (tool plunge direction) for the weld length of 150 mm by traversing the tool in the y -direction (tool traverse direction) along the butt-joint line of two dissimilar aluminium alloys. The VPD experiment trail is conducted as shown in Figure 4.2 by increasing the TPD from the range 5.80 mm to 6.20 mm continuously ensuring the interaction of the tool pin and shoulder with both the alloy plates is linearly increased along the interface of the butt-weld joint line for weld length, 150 mm.

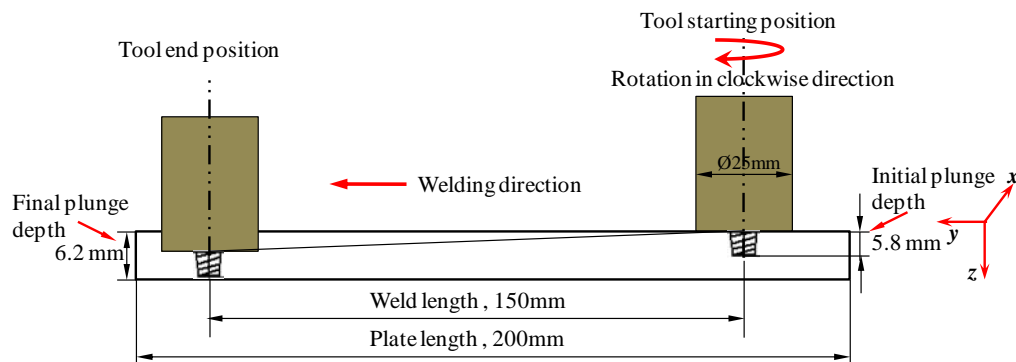
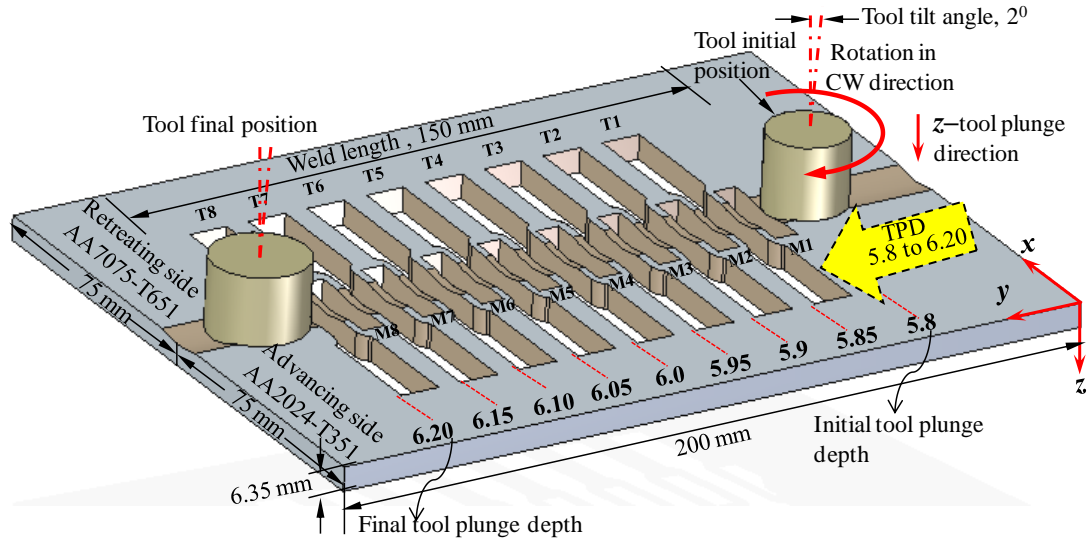


Figure 4.2 Schematic of the tool pass in linearly varying plunge depth (VPD) from 5.8 mm to 6.2 mm in the z -direction for weld length of 150 mm.

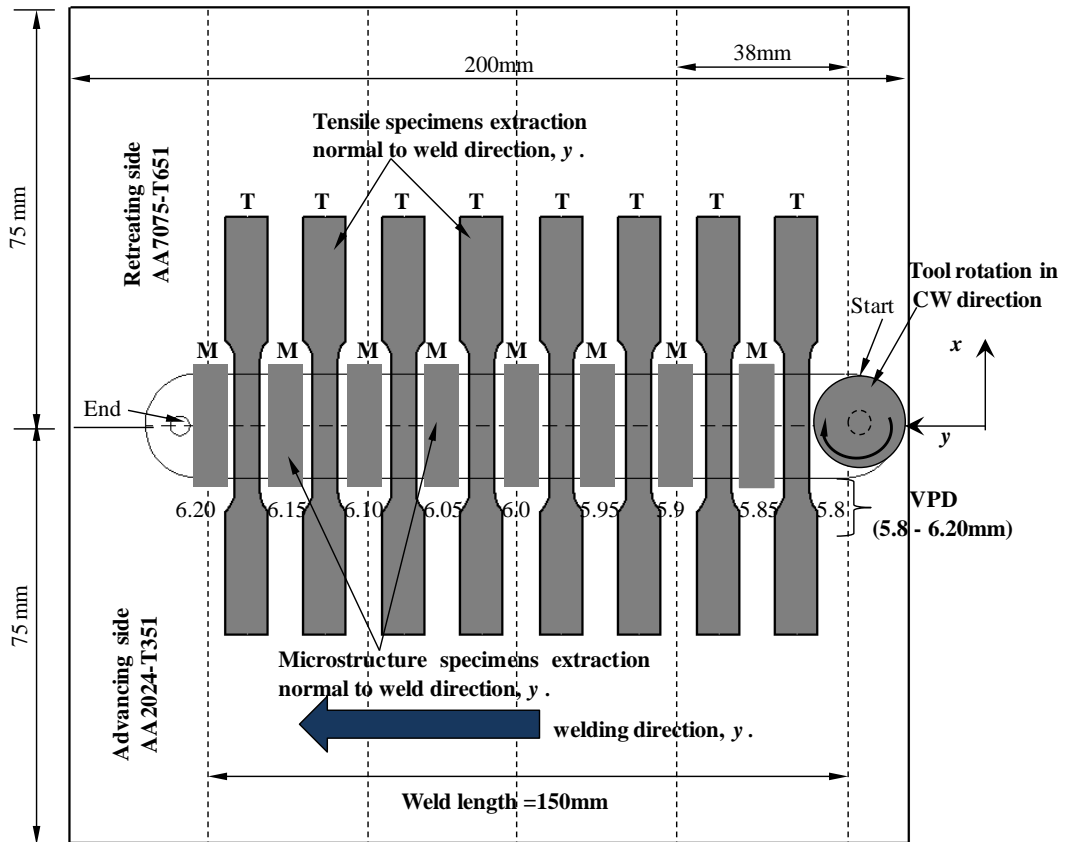
The increase in the TPD helps in increasing the interference between the tool shoulder and the aluminium alloy plates. Initially, the FSW tool pin of length, $L = 5.80$ mm, is plunged to the plates base materials to a depth of 5.80 mm in such a way that the tool shoulder makes initial contact with the faying surface of both alloy plates in the butt-joint. The tool dwells time of 15 s is chosen in order to develop a sufficient amount of heat generation. Then, the TPD is linearly increased until the tool is plunged to a maximum depth of 6.20 mm and reaches the end position of the weld length. The maximum TPD of 6.20 mm selected in order to avoid any possible damage to the tool pin when it makes contact with the surface of the plate mounting area of the FSW machine at higher plunge depth. During the VPD experiment, the other two FSW parameters i.e TRS of 1000 rpm and TTS of 120 mm/min, respectively are kept as constants. The higher TRS and lower TTS results in excessive heat input in to the weld region. In addition, lower TRS and higher TTS both results in insufficient material mixing at the WNZ that leads to the formation of defects. Thus, these two parameters are carefully selected and kept as constant based on the investigation reports available in the literatures.

After the FSW process, the tensile specimens and microstructure specimens are extracted from the FSW dissimilar aluminium alloys joint plate by means of wire cut EDM process. The locations of specimen removal layout are shown in Figure 4.3 (a-b). The Figure 4.3 (a-b) depicts the experimental procedure, location of tensile specimens namely, T1 to T8, and microstructure specimens, namely, M1 to M8, extracted perpendicular to the tool traverse direction (y). The each tensile and microstructure specimens are extracted from within the weld length distance of 19 mm such that the TPD difference of 0.05 mm is maintained from one specimen to the other specimen. The tensile specimens are tested for tensile properties such as UTS, YS and % EL. The microstructure specimens are investigated for the presence of defects, bonding between the two materials and grain refinement at the WNZ, AS and RS of the dissimilar aluminium alloys joint using OM and SEM analyses. The optimum TPD is selected based on higher UTS measured from the tensile test and correlating the results with macro or microstructure analysis. This optimized TPD

obtained is kept as a constant for further experimental trials conducted to determine the optimum TRS and TTS.



(a)



(b)

Figure 4.3 Schematic illustrating the (a) VPD experiment procedure and the specimens removal layout (b) top view of the butt weld joint showing the orientation of tensile specimens ‘T’ extraction and micro-structural specimens ‘M’.

4.3.2 Optimization of tool rotation speed (TRS) by varying rotation speed (VRS) experiment

The second stage of the experiment for obtaining the optimum FSW parameter of TRS is achieved by conducting the VRS experiment. In the VRS experiments, the dissimilar aluminium alloys joints are fabricated by continuously varying the TRS from 400 rpm to 1800 rpm, whereas the TTS of 120 mm/min and optimized TPD (obtained from the first stage of the experiment of preceding Section 4.3.1) are kept as constant. The FSW dissimilar aluminium alloys joints are produced from the two sets of VRS experiment trials on the individual set of plate. In the first set of experiment, the dissimilar aluminium alloys joint is fabricated by varying the TRS from the range 400 rpm to 1100 rpm along the tool traverse direction (y) and at the interface of the butt-weld joint line for weld length, 150 mm. In the second set of VRS experiment, the joint is fabricated by varying the TRS from 1100 rpm to 1800 rpm for the same weld length.

Figure 4.4 depicts the simple schematic diagram to understand the VRS experiment procedure for the first set of the experiment for TRS range 400 to 1100. In the first set of VRS experiment, the TRS range 400 to 1100 rpm is increased continuously along the joint line for a weld length of 150 mm. Similarly, in the second set of VRS experiment, the TRS range 1100 to 1800 rpm is increased continuously along the weld joint line for a weld length of 150 mm. In addition, Figure 4.4 depicts the tensile specimens (T1 to T8) and microstructure specimens (M1 to M8) extraction locations after the FSW process and using a wire cut EDM process. Each set of tensile and microstructure specimens are extracted within the weld length of 19 mm such that a difference of TRS of 75 rpm to 100 rpm is maintained between the extraction locations from one specimen to the other as shown in Figure 4.4. Similarly, for the second set of VRS experimental trials, the tensile specimens (T9 to T16) and microstructure specimens (M9 to M16) are removed from the FSW dissimilar aluminium alloys joint. The tensile specimens extracted are tested for tensile properties such as UTS, YS and % EL. The selection of an optimum TRS depends upon the higher UTS of the tested tensile specimens of the FSW dissimilar aluminium alloys joint, and results are correlated with the macro and microstructure analysis.

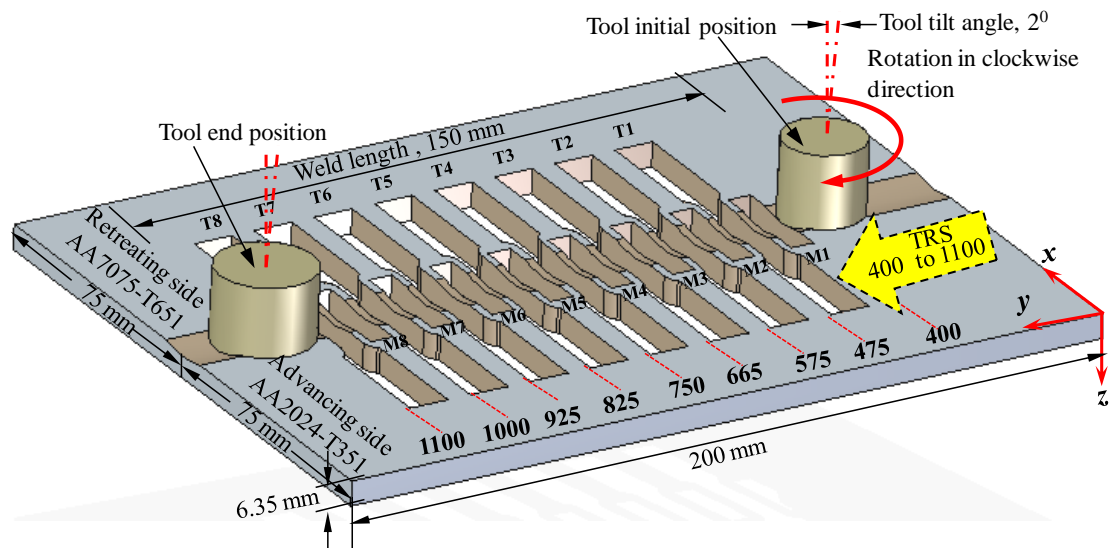


Figure 4.4 Schematic illustrating the VRS experiment for TRS range 400 to 1100 rpm and extraction locations of tensile specimens (T1 to T8) and microstructure specimens (M1 to M8).

4.3.3 Optimization of tool traverse speed (TTS) by varying traverse speed (VTS) experiment

The third order of the experiment for obtaining the optimum traverse speed is achieved by conducting the VTS experiment. In this VTS experiment, the FSW dissimilar aluminium alloys joints are fabricated by varying the TTS from 20 to 200 mm/min, whereas the already optimized TPD and TRS from the previous experiments of preceding sections, 4.3.1 and 4.3.2, respectively, are kept as constant. The FSW dissimilar aluminium alloys joints are produced from the two sets of VTS experiment trials on the individual set of plates. In the first set of VTS experiment, the joint is produced by varying the TTS from the range 20 to 120 mm/min along tool traverse direction and at the interface of the butt-weld joint line for weld length, 150 mm. In the second set of VTS experiment, the joint is produced by varying the TTS from 120 to 200 mm/min for the same weld length.

Figure 4.5 depicts simplified schematic diagram to understand the procedure explained to conduct the first set of VTS experiment by varying the TTS from 20 to 120 mm/min. The tensile specimens, T1 to T8, and microstructure specimens, M1 to

M8, are extracted from the locations as shown in Figure 4.5 using wire cut EDM process. Each set of tensile and microstructure specimens are extracted within the weld length distance of 19 mm such that a difference of TTS of 12 mm/min to 15 mm/min is maintained between the extraction location from one specimen to the other. Similarly, the second set of VTS experiment is conducted by varying the TTS from 120 to 200 mm/min. The similar procedure is adopted for extracting tensile specimens, T9 to T16, and microstructure specimens, M9 to M16 for the second set of VTS experiment. The tensile specimens extracted are tested for tensile properties such as UTS, YS and % EL. The selection of an optimum TTS depends upon higher UTS of the tested tensile specimens of FSW joints, and correlating the results with macro and microstructure analysis.

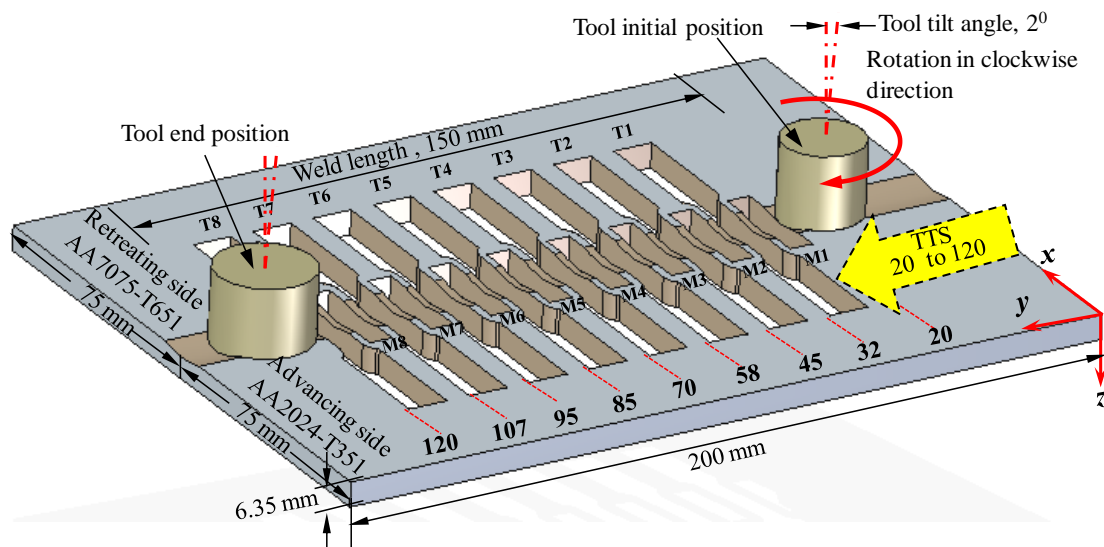


Figure 4.5 Schematic illustrating the VTS experiment for TTS range 20 to 120 mm/min and extraction locations of tensile specimens (T1 to T8) and microstructure specimens (M1 to M8).

4.3.4 Final optimized FSW parameters

The selection of the optimum TPD, TRS and TTS are based on higher UTS of the specimens of FSW dissimilar aluminium alloys joint produced at each stage of the bottom-up experimental procedures of VPD, VRS and VTS experiment explained in the Section 4.3.1, 4.3.2 and 4.3.3, respectively.

4.4 MECHANICAL TESTING

In the present study, the tensile properties such as UTS, YS, % EL and hardness across the weld region covering WNZ, TMAZ, HAZ and BM are measured for the FSW dissimilar joint specimens produced using both the taper threaded cylindrical and taper triangle tool through the individual experiments of VPD, VRS and VTS.

4.4.1 Tensile testing

The tensile specimens extracted from the FSW dissimilar aluminium alloys joint as depicted in Figure 4.3, Figure 4.4 and Figure 4.5 of the preceding Sections of 4.3.1, 4.3.2 and 4.3.3 are tested for tensile properties such as UTS, YS, % EL. The details of specimen preparation, testing procedure and the machine used for the tensile testing are given in Chapter 3, Section 3.4.1.

4.4.2 Micro-hardness testing

Micro-hardness testing was carried out on the same specimens extracted for microstructure analyses. The tests are performed only for the FSW dissimilar aluminium alloys joint fabricated for VRS and VTS conditions. The specimens are extracted perpendicular to the tool traverse direction, y , in the AW condition from the FSW joint as depicted in Figure 4.4 and Figure 4.5 of the preceding Sections of 4.3.2 and 4.3.3 of experiments conducted for optimization trials of VRS and VTS using taper threaded cylindrical tool. The details of specimen preparation, testing procedure and the machine used for the hardness measurement are given in Chapter 3, Section 3.4.2.

4.5 MACRO AND MICROSTRUCTURE EXAMINATION

The microstructure specimens extracted from the FSW dissimilar aluminium alloys joint produced from the experiment trials performed at VPD, VRS and VTS experiments have been carefully prepared according to the standard metallographic procedure to study the macro and microstructures features as explained in Chapter 3, Section 3.5.1. The macrostructure examination performed using a stereo zoom microscope with a low magnification of 10X and light optical microscope. The detail

microstructure examination was carried out using the SEM. The equipment details for carrying out the macro and microstructure analysis are given in Chapter 3, Sections 3.5.2 and 3.5.3.

4.6 RESULTS AND DISCUSSION

4.6.1 Tensile properties

The FSW dissimilar aluminium alloys joint produced from the experimental techniques of the bottom-up approach involving three stages of experiments viz. VPD, VRS and VTS considering both the tool geometry i.e. taper threaded cylindrical tool, taper triangle tool are tested for the UTS, YS and % EL. The results are discussed in the following sections.

4.6.1.1 Varying plunge depth, rotation speed and traverse speed experiments using taper threaded tool

Figure 4.6 shows the graph plot for UTS, YS and % EL of the tested tensile specimens of VPD experiments for the TPD range from 5.80 mm to 6.20 mm. Referring to Figure 4.6, it is observed that the UTS, YS and % EL followed the same tendency of variations in their values. Further, lower UTS, YS and the % EL were observed for TPD between the range 5.8 to 6.05 mm. The UTS of 173 MPa, YS of 136 MPa was observed for the TPD of 5.8 mm. As expected, this is due to the low TPD, lack of good interaction between the shoulder and the base material (Buffa et al., 2006; Kumar and Kailas, 2008; Sundaram and Murugan, 2010). During the initial stage of the TPD, the primary source of the heat generated was due to the friction between tool shoulder and pin with the work-piece (Mishra and Ma, 2005; Heidarzadeh et al., 2012; Buffa et al., 2006). Improper softening and poor flow of the material observed in the case of lower TPD is due to low friction between shoulder and work-piece. This results in insufficient heat generation at local weld zone and leads to the formation of defects in the weld region. One can observe from the plot that at the initial stage, the UTS increased from 173 MPa to 327 MPa for the TPD ranging between 5.8 to 6.0 mm, and for the TPD of 6.05 mm the UTS decreased to 156 MPa. Further, increase in the YS from 136 MPa to 180 MPa was also observed

for a TPD ranging between 5.8 to 6.0 mm and for the TPD of 6.05 mm the YS decreased to 101 MPa. As the TPD increased above 6.10 mm, sufficient amount of contact between shoulder and pin with the BM is ensured and frictional heat generation facilitate the flow of material. Thus, increase in UTS, YS and ductility of the weld joint was observed for higher TPD (Kumar and Kailas, 2008; Sundaram and Murugan, 2010; Buffa et al., 2006). For TPD of 6.20 mm the tested tensile specimen yields maximum UTS of 398 MPa, YS of 190 MPa and % EL of 7.31. Thus, TPD of 6.20 mm is considered as an optimum TPD for the experiment trial of VPD with constant TRS of 1000 rpm and TTS of 120 mm/min.

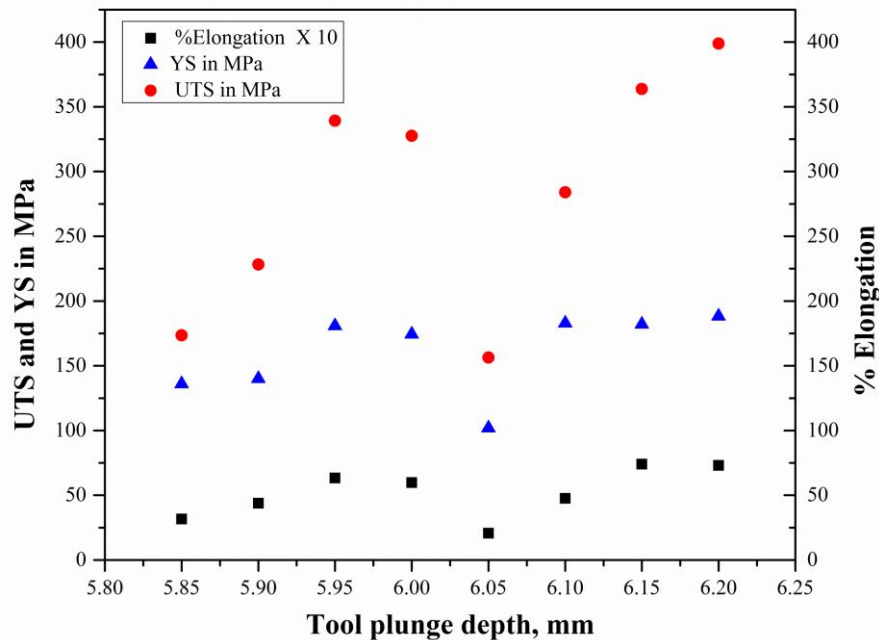


Figure 4.6 Variation of UTS, YS and % EL for the case of VPD experiment with TPD range from 5.8 to 6.2mm. Note, % EL is scaled to 10.

Figure 4.7 depicts the macrograph of the transverse section of the weld region of FSW dissimilar aluminium alloy joint obtained for optimum TPD of 6.20 mm. The weld region is free from defects. However, the presence of a sharp boundary between the interface of WNZ and TMAZ of both AS and RS can be observed. The sharp boundary between the WNZ and TMAZ diffused in the RS and it is relatively sharp on the AS. These sharp boundaries acts as a region of discontinuity and fracture can occur along any one of these sharp boundaries leading to the early failure of the joints.

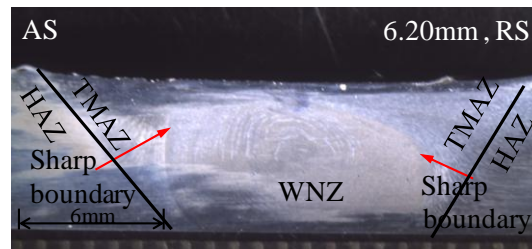


Figure 4.7 Macrograph of defect free weld region of the FSW joint for the TPD of 6.20 mm. Arrow heads pointing towards existence of sharp boundaries between the interface of WNZ and TMAZ.

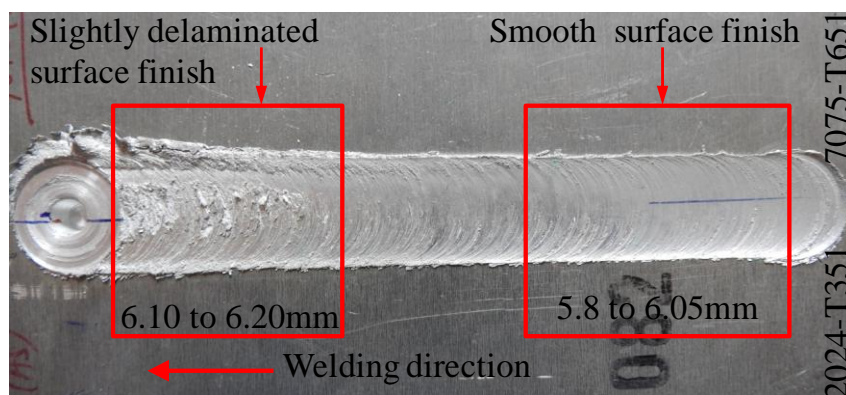


Figure 4.8 Photograph showing the surface morphology of the FSW joint plate for VPD of ranging from 5.80 to 6.20 mm.

Figure 4.8 presents the photograph of the surface morphology of the FSW dissimilar aluminium alloys joint produced from the VPD experiment. The weld crown region had a smooth surface finish without any defects such as cracks, tunnelling and excessive flash for the TPD between 5.80 to 6.05 mm. However, the appearance of the surface finish was slightly deteriorated with moderate flash as seen at the weld crown area for the TPD range between 6.10 to 6.20 mm.

Figure 4.9 shows the result of tensile properties of the tested tensile specimen from the FSW dissimilar aluminium alloys joint produced for VRS experiment for the TRS range 400 to 1800 rpm, optimized TPD of 6.20 mm (obtained from the previous VPD experiment) and constant TTS of 120 mm/min. It was observed from Figure 4.9 that higher UTS, YS and % EL obtained for the TRS range between 500 to 650 rpm. The UTS, YS, % EL range from 417-419 MPa, 185-200 MPa and 11-13%, respectively. The UTS and YS of the FSW joint increased from 309 MPa to 419 MPa, 160 MPa to 200 MPa, respectively, for varying the TRS range from 400 to 650 rpm. A

considerable decrease in the UTS, YS and % EL of the FSW joint observed as the TRS increases above 1000 rpm.

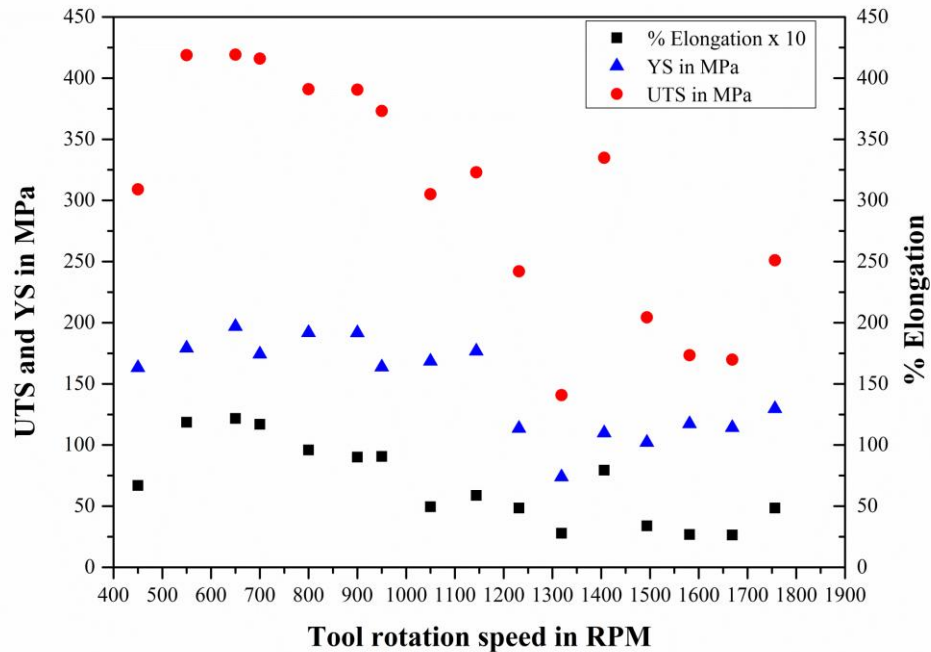


Figure 4.9 Variation of UTS, YS and % EL for the case of VRS experiment with TRS range from 400 rpm to 1800 rpm. Note, % EL is scaled to 10.

For the TRS above 1250 rpm, the UTS, YS and % EL become sensitive and decreased due to the formation of worm-hole defects at the weld region of the FSW joint. Among these varying TRS range 400-1800 rpm, the maximum UTS of 419 MPa, YS of 200 MPa and % EL of 13 is achieved for the tested tensile specimen extracted from the weld region of FSW dissimilar aluminium alloys joint produced for TRS of 650 rpm. Thus, the TRS of 650 rpm selected as an optimum.

Figure 4.11 presents the macrograph of the transverse cross-section of the weld region of the FSW dissimilar aluminium alloys joint obtained from the optimum TRS of 650 rpm. The sharp boundaries between the interface of WNZ and TMAZ of both AS and RS more diffused when compared to the macrograph of the optimized sample as presented in Figure 4.9 from the VPD experiment.

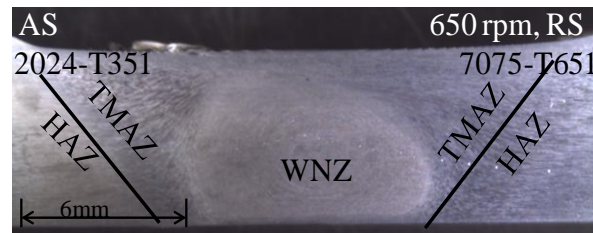
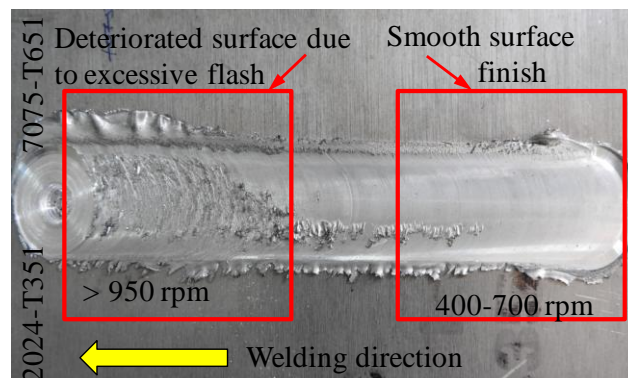
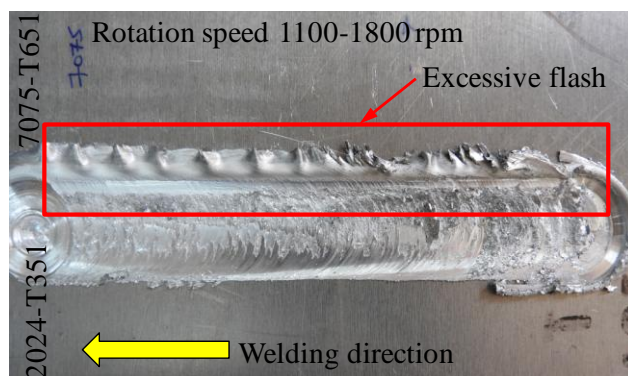


Figure 4.11 Macrograph of the cross section of weld region of the FSW joint for TRS of 650 rpm, optimum TPD 6.20 mm and constant TRS of 120 mm/min.

Figure 4.12 (a) and (b) shows the photographs of the surface morphology of the FSW dissimilar aluminium alloys joint produced for varying TRS experiment. Figure 4.12 (a) shows a weld crown with smooth surface finish for the TRS ranging between 400-700 rpm. However, the deterioration in surface smoothness with excessive flash (Figure 4.12 (b)) are observed in the weld crown area for TRS range 1100 to 1800 rpm and causing thinning in the cross section of the weld plates.



(a)



(b)

Figure 4.12 Photographs of surface morphology of FSW joint plate for VRS range of (a) 400-1100 rpm and (b) 1100-1800 rpm.

Figure 4.13 shows the graph plot for the result of tensile properties such as UTS, YS and % EL of the FSW dissimilar aluminium alloys joint produced from the VTS experiment for TTS ranging 20-200 mm/min with optimum TPD of 6.20 mm and TRS of 650 rpm. Lower UTS of 290 MPa to 390 MPa, YS of 170 MPa to 200 MPa and % EL of 5 to 9 are observed for the FSW joint produced for lower TTS range from 20 to 50 mm/min. This may be due to an increase in the frictional heat and slower cooling rate, causing deterioration of tensile properties (Vijayavel et al., 2014; Rajakumar et al., 2011). The UTS and YS found to be almost constant for the TTS range 50 to 80 mm/min. The UTS, YS and % EL shows an increasing trend with the increase of TTS range 80 mm/min to 150 mm/min.

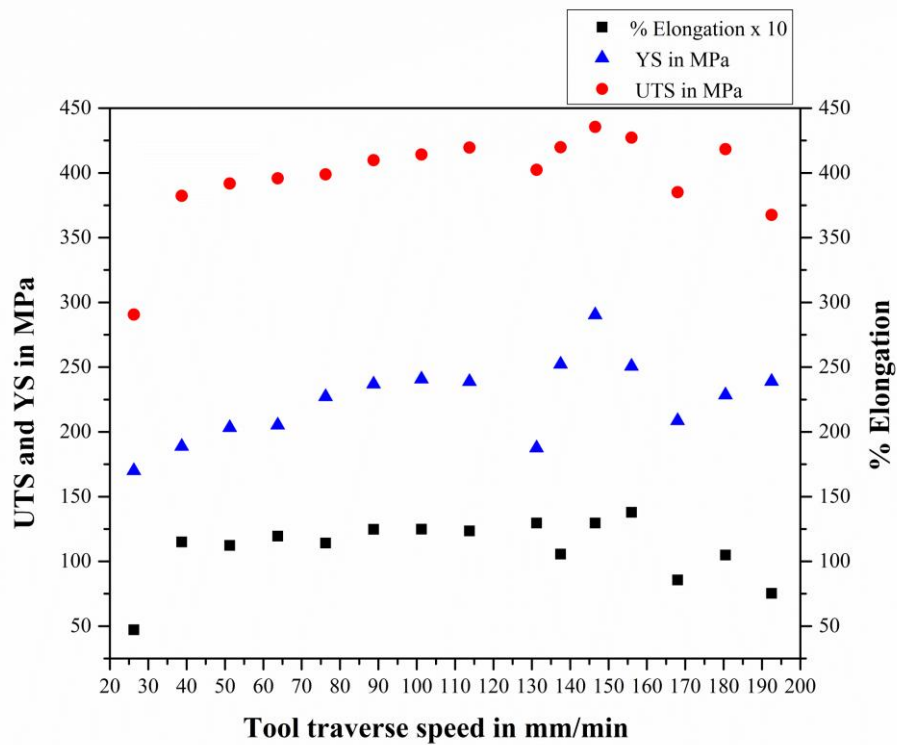


Figure 4.13 Variation of UTS, YS and % EL for the case of VTS experiment with TTS range from 20 mm/min to 200 mm/min. Note, % EL is scaled to 10.

Higher UTS, YS and % EL observed for TTS of 150 mm/min before falling again for TTS above 150 mm/min. The change in the UTS, YS and % EL becomes sensitive above the TTS of 150 mm/min and shows decreasing trend with increasing in TTS. Thus, increase in the TTS reduces the heat input to the weld region, lack of metallurgical bonding and sharp boundary between two materials, and yields lower

strength of the FSW joint (Rajakumar et al., 2011). Thus, FSW dissimilar aluminium alloys joint fabricated from for lower TTS and higher TTS yields lower UTS and YS. The highest value of UTS of 435 MPa, YS of 290 MPa, % EL of 13 and η_{WJ} of 92% obtained for a specimen tested for a TTS range 145-150 mm/min. Hence, in this range the TTS of 150 mm/min selected as an optimum TTS.

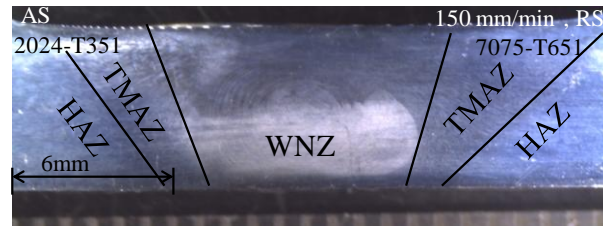
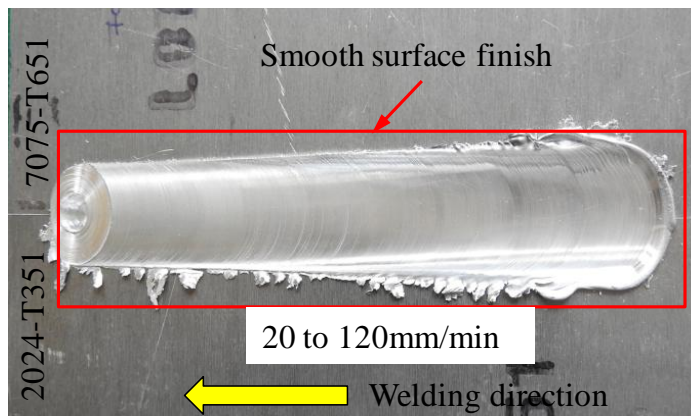
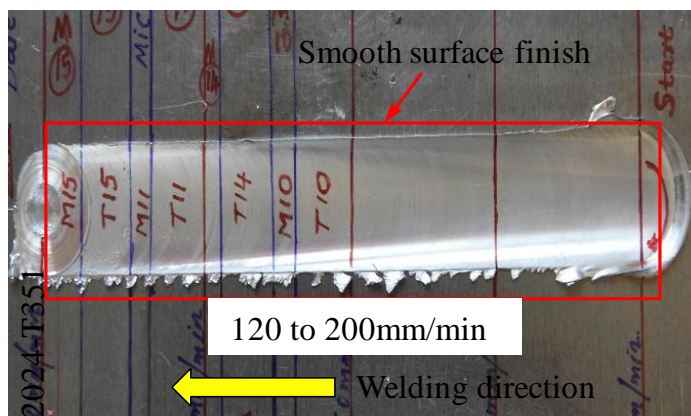


Figure 4.14 Macrograph of the cross section of weld region of FSW joint for TTS of 150 mm/min, optimum TPD of 6.20 mm and optimum TRS of 650 rpm.



(a)



(b)

Figure 4.15 Photographs of surface morphology of FSW joint plate for TTS range of (a) 20-120 mm/min and (b) 120-200 mm/min.

Figure 4.14 shows the macrograph of the transverse cross-section of the weld region of the FSW dissimilar aluminium alloys joint produced with final optimized FSW parameters of TTS, 150 mm/min, TPD, 6.20 mm and TRS, 650 rpm. It consists of diffused sharp boundaries between WNZ and TMAZ. Figure 4.15 (a) and (b) presents the photographs of surface morphology having smooth surface finish without any defects on weld crown.

4.6.1.2 Varying plunge depth, rotation speed and traverse speed experiments using taper triangle tool

Figure 4.16 illustrates the graph plot for the result of variation of tensile properties obtained from the tested tensile specimens of FSW dissimilar aluminium alloys joint produced for VPD experiment by varying the TPD ranging from 5.80 mm to 6.20 mm and using taper triangle tool.

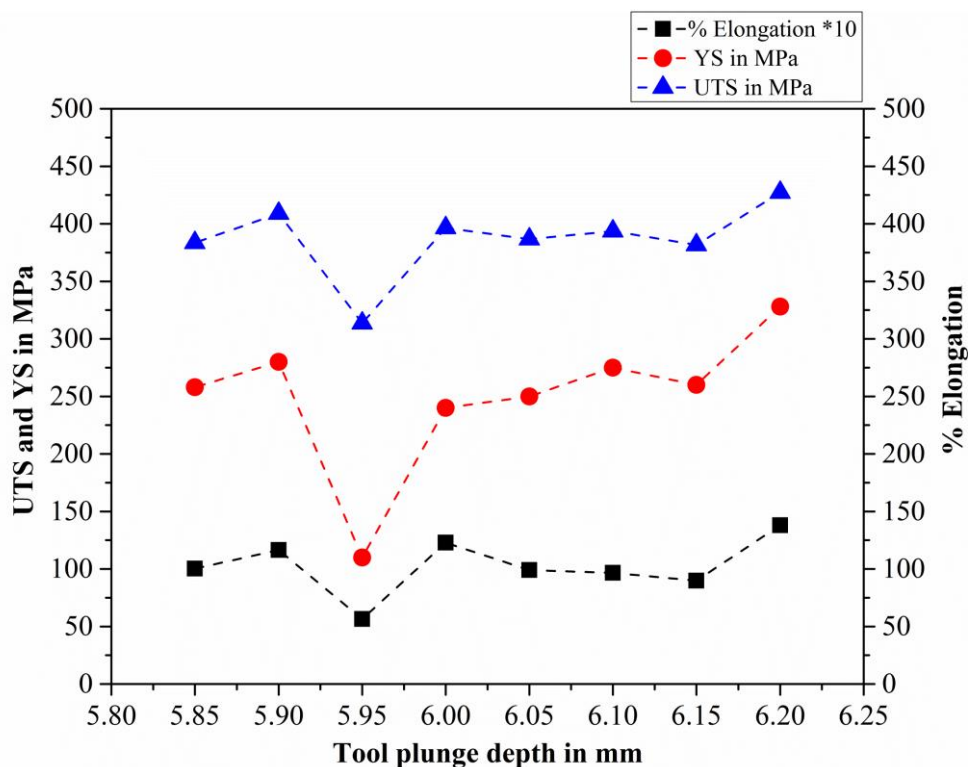


Figure 4.16 Variation of tensile properties in relation with varying the TPD.
Note, % EL is scaled up to $\times 10$.

Referring to Figure 4.16, the TPD of 5.80 mm observes a lower UTS, 383 MPa, YS, 258 MPa and % EL, 10.03. Increase in TPD from 5.85 mm to 5.90 mm results in the

UTS to 409 MPa, YS to 280 MPa and % EL of 11.6. At TPD of 5.95 mm, the FSW dissimilar aluminium alloys joint have shown a considerable drop in the tensile properties. These decreasing trends in the tensile properties are due to inadequate heat input condition because of lower TPD. The tool shoulder being a source of heat generation and its good amount of interaction with the base material is required in order to produce defect-free weld joints and sufficient amount of plasticized material flow in to the WNZ. (Kumar and Kailas, 2008; Heidarzadeh et al., 2012; Buffa et al., 2006). Increase in the TPD (or axial force) results in an increasing amount of plasticized material underneath the tool shoulder, which results in the sound weld joints without any defects and yields higher tensile properties (Rajakumar et al. 2011). In the present study, at the initial stage of the FSW process for lower TPD, the contact between the tool shoulder and the base materials is not sufficient to generate a good amount of heat. Thus, the TPD range 5.80-5.95 mm yields lower tensile properties. Increase in the TPD from 5.95 mm to 6.00 mm observes a gradual increase in the UTS from 313.5 MPa to 396.5 MPa, YS from 110 MPa to 240 MPa and % EL from 5.64 to 12.3. Further increase in the TPD from 6.00 mm to 6.15 mm observes the same tendency of variation of tensile properties and are almost equal in their values. At the TPD of 6.20 mm, the tested tensile specimen of FSW dissimilar aluminium alloys joint has shown maximum UTS, 427 MPa, YS, 328 MPa and % EL, 13.8. This increase the tensile properties again confirms that when the TPD is increased the adequate amount of heat is input to the WNZ, as a result, the transferred material from the leading edge is confined within the WNZ (Kumar and Kailas 2008). Thus, in the VPD experiment, the TPD of 6.20 mm was considered as an optimum TPD.

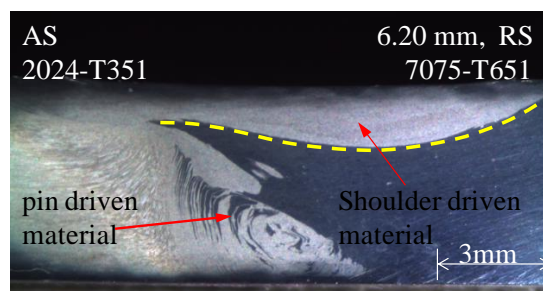


Figure 4.17 Macrostructure image of the transverse section of WNZ at an optimum TPD of 6.20 mm.

Figure 4.17 shows the macrostructure image of the transverse cross-section of the weld region of the specimen of FSW dissimilar aluminium alloys joint produced at an optimum TPD of 6.20 mm. One can observe from Figure 4.17, the WNZ of the dissimilar joint specimens are distinguished by the presence of material flow pattern influenced by the (i) shoulder driven and (ii) pin driven. The material flow pattern above the parting line (indicated by yellow dotted line) near to the top surface of the WNZ is influenced by the sliding action of the tool shoulder, while the flow below the parting line at the middle region of the WNZ is influenced by pin. The material flow pattern is characterized by the banded structure (BS) of both the materials kept on the AS and RS (Kumar and Kailas, 2008). In general, higher TPD promotes the interaction of the tool shoulder and pin with the base materials to be joined. As a result, the material is confined within the WNZ.

Figure 4.18 illustrates the graph plot for the results of tensile properties of the specimens of FSW dissimilar aluminium alloys joint produced by conducting the VRS experiment for TRS range 400 rpm to 1100 rpm, optimum TPD, 6.20 mm and constant TTS, 120 mm/min. Referring to the Figure. 4.18, the FSW dissimilar aluminium alloys joint produced at the TRS of 450 rpm have shown a lower UTS, 365 MPa, YS, 248 MPa and % EL, 12.6. This is due to the inadequate material mixing and insufficient amount of heat generation at lower TRS leading to the decrease in the tensile properties (Sundaram and Murugan, 2010; Rodriguez et al., 2015; Sharma et al., 2012; Rajakumar et al., 2011). With the increase in the TRS range from 550 to 875 rpm, the tensile specimens have shown a slightly linear increase and almost equal in the UTS, YS and % EL from the range between 396 MPa to 406 MPa, 250 MPa to 305 MPa and 9.5 to 12.8, respectively. This is an indication of an adequate amount of heat generation contributed by the increased TRS (Sharma et al., 2012). Further, the FSW joints produced above the TRS of 1000 rpm have also shown a decrease in the UTS, 409 MPa, YS, 308 MPa, % EL, 12.4 and this is may be due to the slower cooling rate, which causes the coarsening of grains, lower hardness at the WNZ of the weld joints (Rajakumar et al., 2011). These variations in the tensile properties are the result of the variation in the material flow and heat generation at different TRS (Sundaram and Murugan, 2010). However, compared to the other TRS, the FSW

dissimilar aluminium alloys joint produced with the TRS of 950 rpm yields a maximum UTS, 416 MPa, YS, 328 MPa and %EL, 16.6.

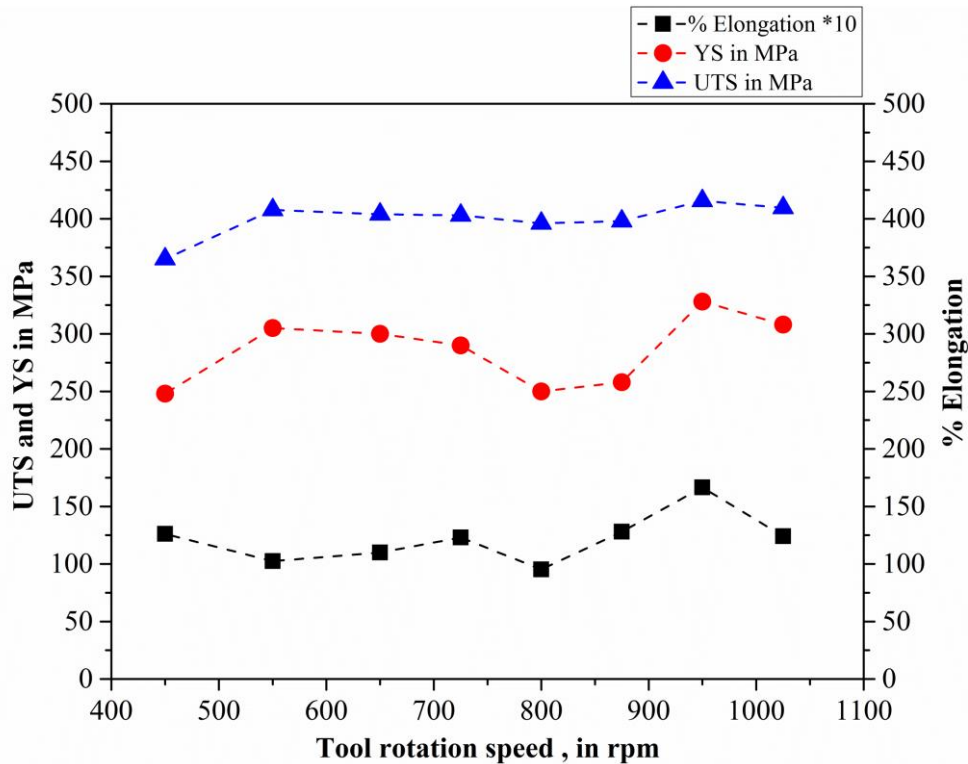
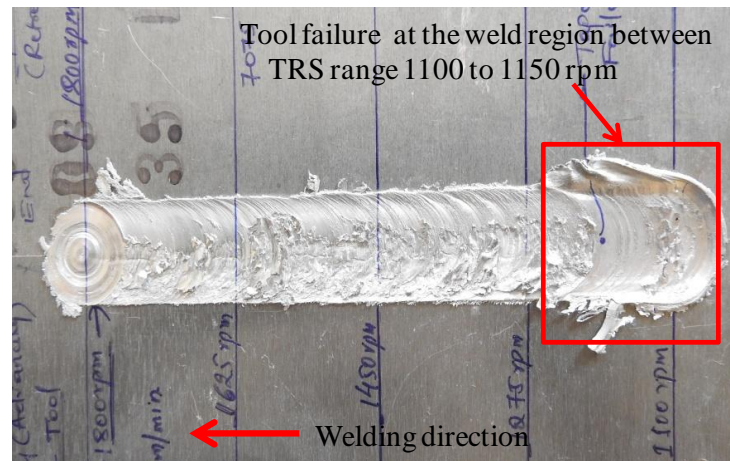
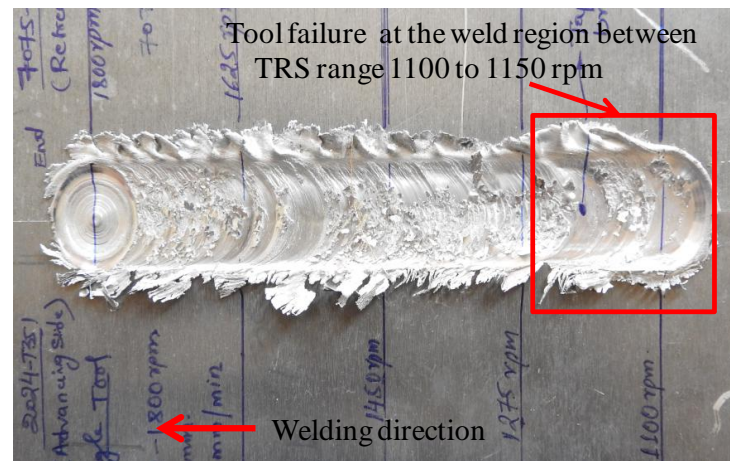


Figure 4.18 Variation of tensile properties in relation with varying the TRS.
Note, % EL is scaled up to $\times 10$.

Figure 4.19 (a) and (b) shows the photographs of surface morphology of two repeated experiments for joining the FSW dissimilar joint specimens from the second set of VRS experiments conducted by considering the TRS range 1100 rpm to 1800 rpm. Figure 4.19 (a) and (b) illustrates the taper triangle pin failure locations marked in the red colour box for the TRS range 1100 to 1150 rpm on the weld crown area. The failure is due to the considerable larger tool forces acting on the taper triangle tool during the FSW process. Thus, the experiment trail for producing FSW joints at higher TRS above 1150 rpm could not be carried out. Thus, the FSW dissimilar aluminium alloys joint produced from the TRS of 950 rpm that yields highest tensile properties is considered as an optimum TRS.



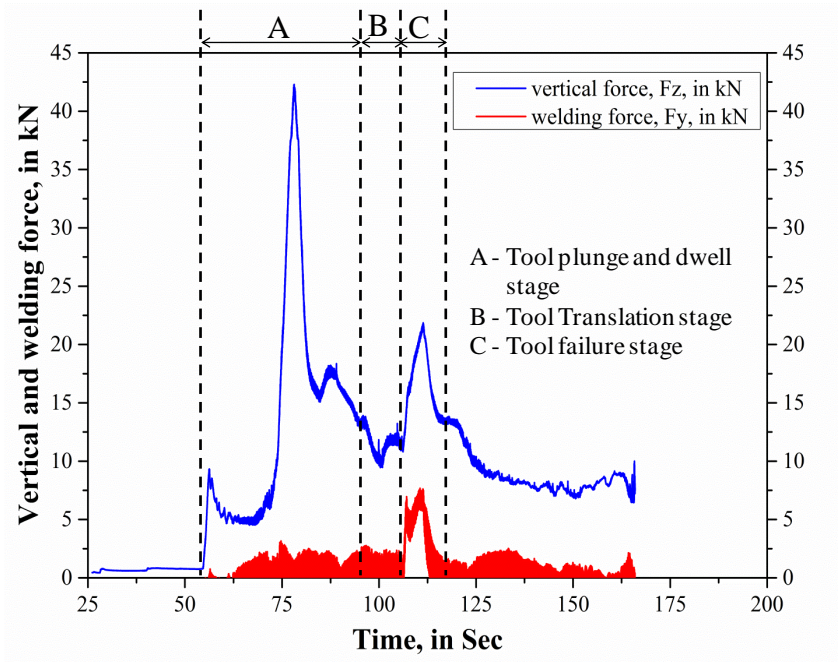
(a)



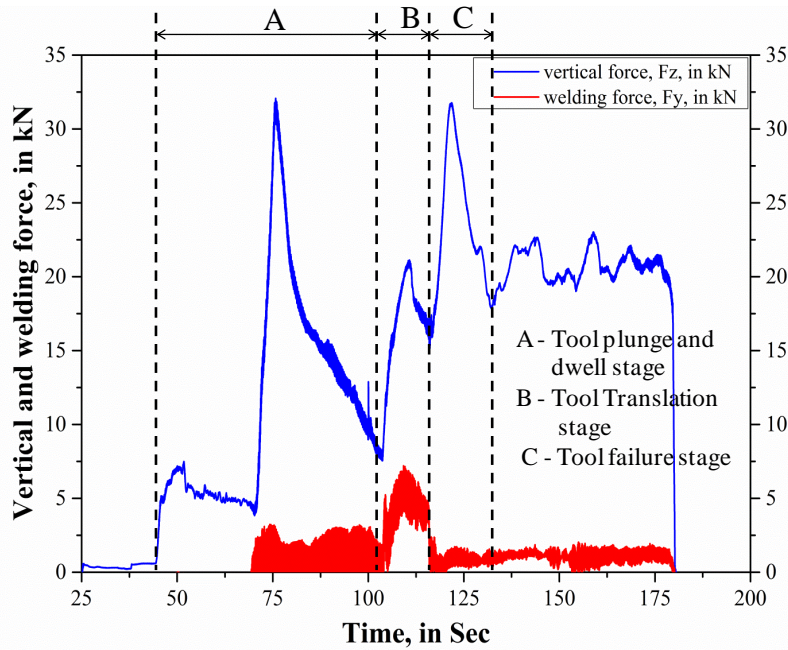
(b)

Figure 4.19 (a) and (b) photograph showing the surface morphology and tool failure location in the weld crown region for the two separate set of repeated varying the TRS experiments for the 1100 to 1800 rpm.

In order to investigate the reason for the tool pin failure, the tool forces acting in the X, Y and Z-axis direction is measured using five-axis FSW machine capable of recording the forces, time and torque during the FSW joining process. The tool forces acting in the two main axes: Y and Z-axis are considered. The tool force acting parallel to the welding direction (or tool traverse direction) along the Y-axis i.e. welding force (F_Y), and tool force acting perpendicular to the plates towards plunge direction along the Z-axis i.e. vertical force (F_Z) are considered for the investigation.



(a)



(b)

Figure 4.21 (a) and (b) tool force recorded for the TRS experiments range 1100 to 1800 rpm.

Figure 4.21 (a) and (b) depicts the graph plot from the recorded tool forces: (i) F_z and (ii) F_y for the set of experiments carried out whose photographs are presented in the Figure 4.19 (a) and (b), respectively. In both the Figure 4.21 (a) and (b), during the

phase ‘A’-tool plunge and dwell stage, the vertical force reach peak values as a result of tool plunge in to the base material still in “cold” condition and the tool shoulder reaches to the higher TPD of 6.20 mm (Trimble et al., 2012; Astarita et al., 2014). Further, it was followed by a dwell stage for 20 s during which the F_z reduced significantly due to material softening because of higher friction heat (Astarita et al., 2014). In the phase ‘B’ the beginning of the tool translational stage observes a reduction in both the F_z (60% reduction) and F_y as a result of less amount of force acting on the tool due to the softening of the base material during initial plunge dwell time of 20 s. However, with further tool translation in the welding direction (y), the phase ‘C’- tool failure stage observes a sudden peak value in both the F_z and F_y force (Figure. 4.21 (a)). This is due to insufficient heat input to the base materials because of higher TTS (or tool advancing speed) (Astarita et al., 2014). This leads to the tool pin failure at the weld region for the combination of TRS from the range 1100 to 1150 rpm and higher TTS of 120 mm/min. In the present study, as the combination of higher TTS, 120 mm/min, and higher TRS range, 1100-1150 rpm, was not good enough to generate the required amount of heat to soften the base material leading to the failure of tool pin at the phase ‘C’- tool failure stage (Astarita et al., 2014). Figure 4.21 (b) shows the recorded F_z and F_y force at the phase ‘A’, ‘B’ and ‘C’ for the second trial of the experiment (Figure 4.19 (b)) and observes a tool failure at the stage-C. As the FSW joints fabricated at the TRS, 950 rpm, yields maximum tensile properties, the same TRS is considered as an optimum TRS and corresponding macrostructure image of the transverse cross section of the WNZ of the FSW dissimilar joint specimen is shown in Figure 4.22 consisting of banded structure of the two materials at the WNZ.

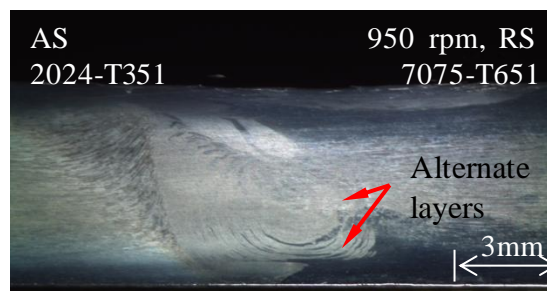
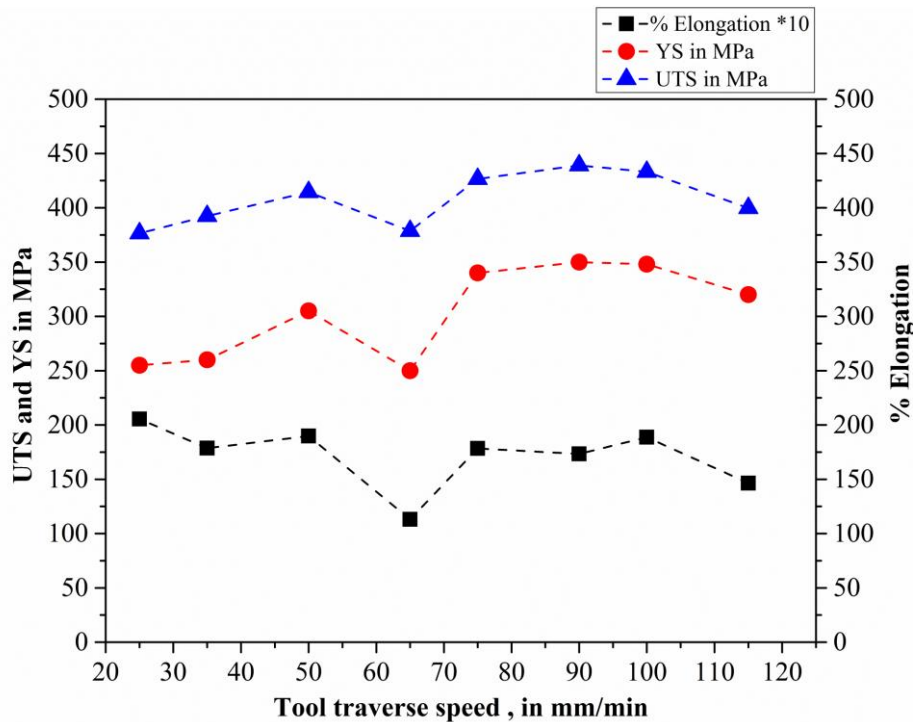
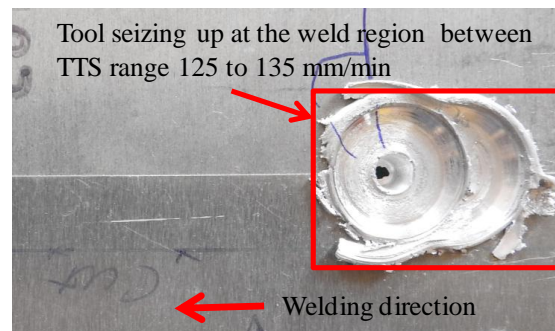


Figure 4.22 Macrostructure image of the transverse section of WNZ at the TRS, 950 rpm.



(a)



(b)

Figure 4.23 (a) Variation of tensile properties in relation with the TTS range 20 to 120 mm/min. (b) photograph showing tool stuck location for the second set of VTS experiment for the TTS range 120 to 200 mm/min.

Figure 4.23 (a) shows the result of tensile properties of the of the tested FSW dissimilar aluminium alloys joint produced from VTS experiment conducted for TTS range 20 to 120 mm/min and using a taper triangle tool. As it can be observed from the Figure 4.23 (a), the FSW joint fabricated from a lower TTS between the range 25 to 40 mm/min yields lower tensile properties and for TTS range between 75 to 90 mm/min yields higher tensile properties. In general, at lower TTS, the higher frictional heat between tool shoulder and base material, slower cooling rate promotes the grain growth and dissolution of strengthening precipitates that leads to the

deterioration of the tensile properties of the FSW joint (Rajakumar et al., 2011; Palanivel et al., 2014; Elangovan and Balasubramanian, 2008). Thus, for lower TTS of 25 mm/min the FSW joint have shown lower UTS, 376 MPa, YS, 255 MPa and % EL, 20.5. Figure 4.23 (a), the FSW joint fabricated with the TTS range 35 mm/min to 50 mm/min have shown an increasing trend in the UTS from 376 MPa to 414 MPa, YS from 255 MPa to 305 MPa, and % EL from 17 to 19. Increase in the UTS, YS and % EL is the result of the lower amount of heat input to the weld region due to the increase in the TTS. From the TTS range 20 to 120 mm/min, the tested tensile specimen from FSW dissimilar aluminium alloys joint fabricated for the TTS, 90 mm/min yields higher UTS, 440 MPa, YS, 350 MPa and % EL, 17.5 and η_{WJ} of 93%. Increase in the TTS to 115 mm/min as significantly reduced the UTS, YS and % EL of the FSW joints. Higher TTS results in the lack of heat generation, poor bonding between materials, faster cooling rate leads insufficient stirring of the material and drag of material from AS to RS, and yields poor tensile properties (Rajakumar et al., 2011; Palanivel et al., 2014).

The second set of VTS experiment for the TTS range 120 to 200 mm/min could not be carried out because the tool pin becomes stuck at higher TTS above 130 mm/min. Figure 4.23 (b) shows the photographs of the tool stuck location in the welding region between TTS of 120 to 130 mm/min. This is mainly attributed to the decreased heat input to the weld region with the increase in the TTS that reduces the amount of softening of the material (Astarita et al., 2014). As a result, the tool traversing movement becomes difficult and the tool pin is stuck into the base material. Thus, as the FSW joint produced for the TTS of 90 mm/min has shown higher tensile properties, the same is considered as an optimum TTS. The corresponding macrostructure image of cross section of the weld region of the FSW dissimilar aluminium alloys joint is shown in the Figure 4.24. The macrostructure consists of a mixed region and alternate layers pattern of both the materials at the middle of the WNZ.

Thus, final optimized FSW parameters obtained from the bottom-up experimental approach for producing the FSW dissimilar aluminium alloys joint considering the

VPD, VRS and VTS experiment, and using taper triangle tool are TPD, 6.20 mm, TRS, 950 rpm and TTS, 90 mm/min.

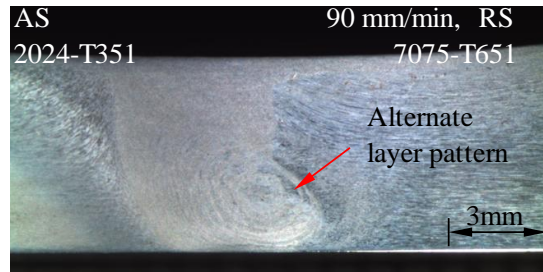


Figure 4.24 Macrostructure images of the WNZ obtained for the final optimized FSW parameters viz. TPD, 6.20 mm, TRS, 950 rpm and TTS, 90 mm/min with the taper triangle tool.

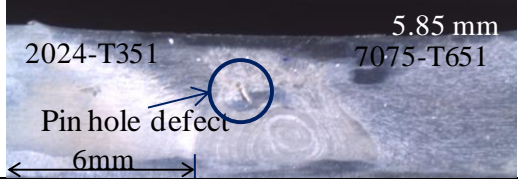
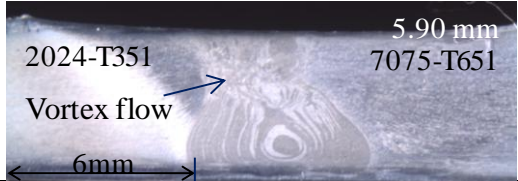
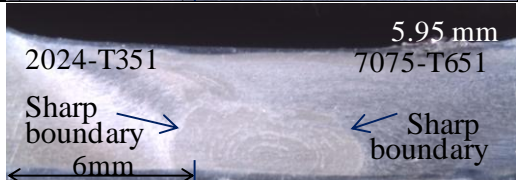
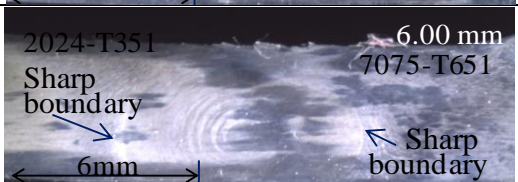
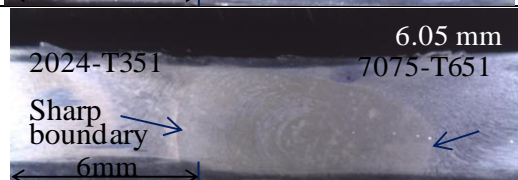
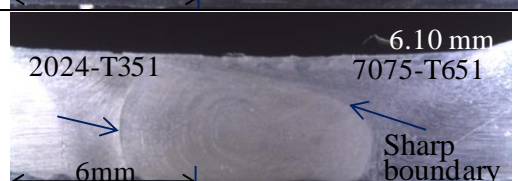
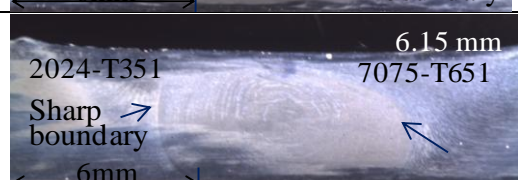
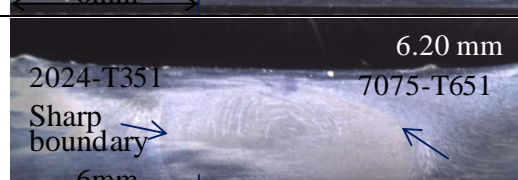
4.6.2 MACRO AND MICROSTRUCTURE

In this section, the detail analysis of macro and microstructure of the FSW dissimilar aluminium alloys joint of typically AA2024-T351 and AA7075-T651 fabricated from VPD, VRS, VTS experiment using taper threaded cylindrical and taper triangle tool have been investigated and the observations are correlated with the tensile properties of the tested specimens.

4.6.2.1 Varying plunge depth, rotation speed and traverse speed experiments using taper threaded tool

The optical macrographs of the transverse cross sections of the weld region of the FSW dissimilar aluminium alloys joint produced for the VPD experiment by varying the TPD range 5.80 to 6.20 mm are presented in the Table 4.1. In the Table 4.1, the macrograph for low TPD of 5.85 mm shows clear visible pin-hole defect above the WNZ towards the AS. This is also one of the reasons for the decrease in UTS of the FSW joint (Figure 4.6). Low TPD or lack of shoulder contact with the dissimilar materials joint results in less amount of heat input to the material, reduced smoother flow of the material and unmixed region (Da Silva et al., 2011; Kumar and Kailas, 2008; Sundaram and Murugan, 2010). Similarly, for the TPD of 5.85 mm and 5.90 mm the optical macrograph and corresponding SEM images (Figure 4.25 (a- b)) consists of unmixed region close to the top surface of the weld and results in defects above the WNZ.

Table 4.1 Macrographs of FSW dissimilar aluminium alloys joint for VPD experiment. The TPD depth in ‘mm’ indicated on the top right corner of each figure.

Tool rotation speed (rpm)	Tool traverse speed (mm/min)	Varying plunge depth (mm)	Macrograph	
			Advancing side (AS)	Retreating side (RS)
1000	120	5.85		
1000	120	5.90		
1000	120	5.95		
1000	120	6.00		
1000	120	6.05		
1000	120	6.10		
1000	120	6.15		
1000	120	6.20		

For the TPD of 5.95 mm, the macrograph and SEM image (Figure 4.25 (c)) shows ‘no defect’ at the top of the WNZ. However, there exists a sharp boundary between two materials towards the AS and as well as RS of the joint. These sharp boundaries formed as the result of an insufficient diffusion phenomenon between both the alloys. For the TPD of 6.0 mm, SEM images (Figure 4.25 (d)) reveals the presence of crack above the WNZ and thus results in the decreased UTS (Figure 4.6). The SEM images in Figure 4.25 (e) for the TPD of 6.05 mm shows the boundary between the WNZ and TMAZ of RS consisting of a clearly visible separation. These discontinuities are weaker region and fracture can originate along these leading to the early failure of the joints. The lowest UTS of 156 MPa, YS of 101 MPa (Figure 4.6) is observed for the TPD of 6.05 mm. In the other cases, the macrograph and SEM image shown in the Figure 4.25 (f-h) for the TPD above 6.10 mm reveals that with the increase in the TPD, defects have disappeared (Kim et al., 2006). However, a minimum sharp boundary was observed between WNZ and TMAZ on the AS and RS. Compared to the TPD of 6.15 mm, the UTS, YS and % EL (Figure 4.8) records high for the TPD of 6.20 mm and the same is selected as an optimum TPD for the FSW joint of dissimilar aluminium alloys. For the optimum TPD of 6.20 mm, the SEM image of the WNZ shown in the Figure 4.26 consists of equiaxed grain structure with an average grain size of 4.5 – 8 μm .

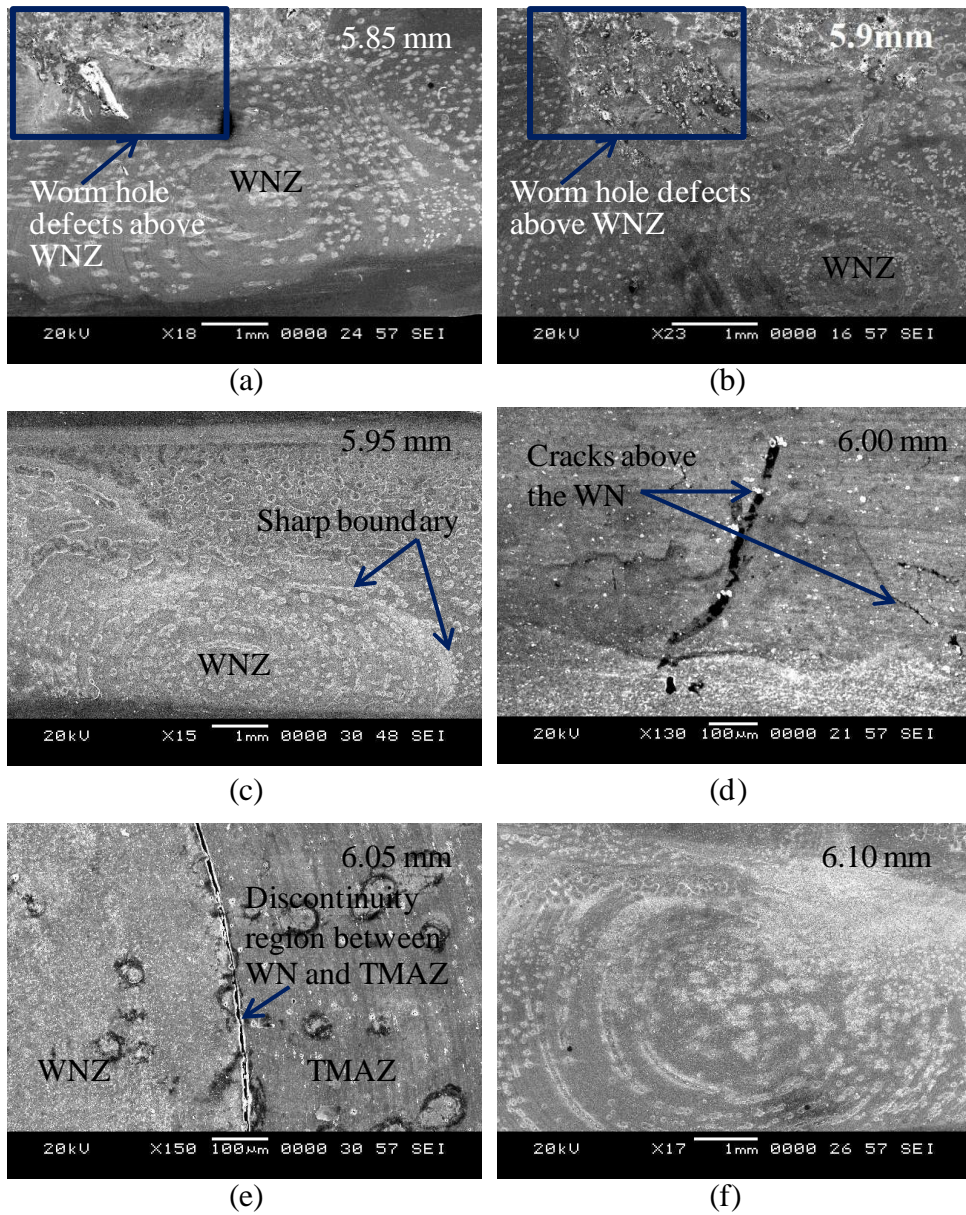


Figure 4.25 Low magnification SEM images for VPD experiment. Plunge depth in ‘mm’ is highlighted at the top right corner of each figure.

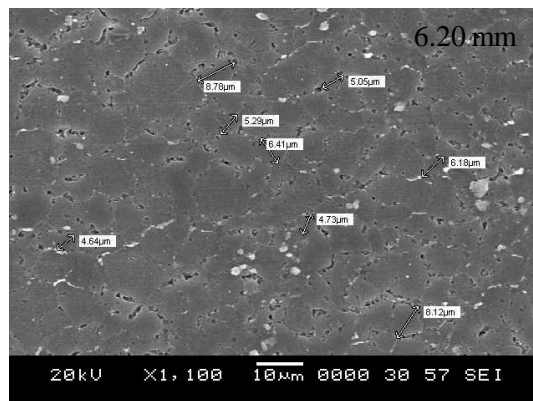


Figure 4.26 Grain size at the WNZ for the TPD of 6.20 mm.

The optical macrographs of the transverse cross sections of the dissimilar FSW joint region of the specimens produced for the two stages VRS experiments by varying the TRS range 400 to 1100 rpm and TRS range 1100 to 1800 rpm are presented in Table 4.2 and Table 4.3, respectively. The corresponding SEM images are shown in Figure 4.27.

It is evident from the macrograph presented in Table 4.2 and Table 4.3 that for the TRS between 400-1250 rpm, sound joints are produced without any defects of wormholes, kissing bond or pin-hole. The experiments performed at higher TRS above 1250 rpm produced defects in the weld, particularly above the WNZ and near to the top surface of the weld. It can be observed from Figure 4.27 (b-h), the FSW joints produced at the higher TRS of 1250 rpm onwards, consists of wormhole defects above the WNZ and towards the AS. This is due to the excessive plastic deformation and stirring at a higher rotation rate, resulting in defects in the weld region (Trimble et al., 2015). Figure 4.9 for higher TRS the tested tensile specimen shows a decrease in UTS owing to the presence of a defective weld region. This is consistent with the early investigation reported by Zhang et al. (2015). These authors found that the defects and grain size at WNZ increased with increasing in TRS and results in decreased tensile strength. In the present study also, rotation speed range 400-700 rpm was good enough to produce defect-free joints. The tested tensile specimen for the TRS of 650 rpm results in highest UTS, YS and % EL (Figure 4.9).

Table 4.2 Macrographs of FSW dissimilar aluminium alloys joint for VRS experiment. Tool rotation speed in 'rpm' indicated on the top right corner of each figure.

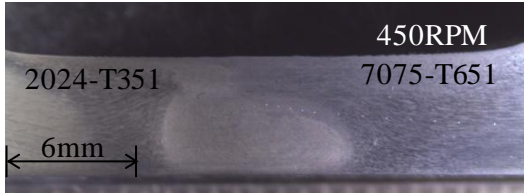
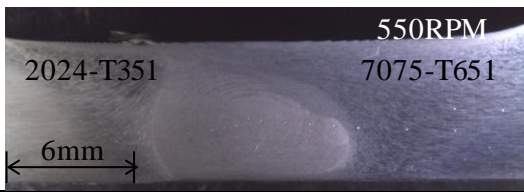
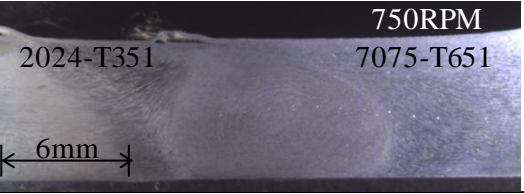

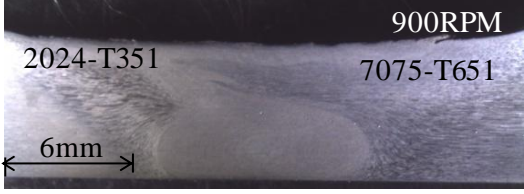

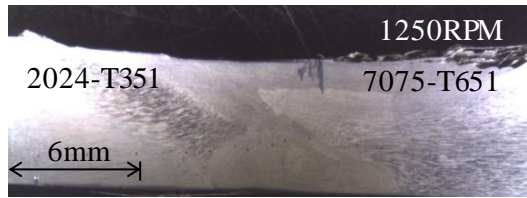

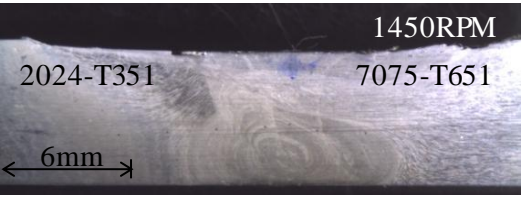
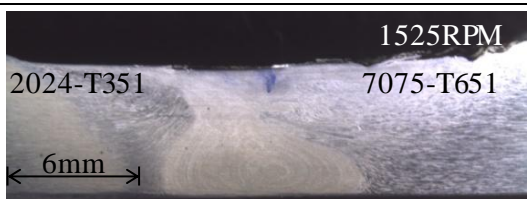


Optimum Tool plunge depth (mm)	Tool traverse speed (mm/min)	Varying rotation speed (rpm)	Macrograph	
			Advancing side (AS)	Retreating side (RS)
6.20	120	450		
6.20	120	550		
6.20	120	750		
6.20	120	800		
6.20	120	900		
6.20	120	1050		

Table 4.3 Macrographs of FSW dissimilar aluminium alloys joint for VRS experiment. Tool rotation speed in ‘rpm’ indicated on the top right corner of each figure.

Optimum Tool plunge depth (mm)	Tool traverse speed (mm/min)	Varying rotation speed (rpm)	Macrograph	
			Advancing side (AS)	Retreating side (RS)
6.20	120	1250		
6.20	120	1350		
6.20	120	1450		
6.20	120	1525		
6.20	120	1625		
6.20	120	1725		

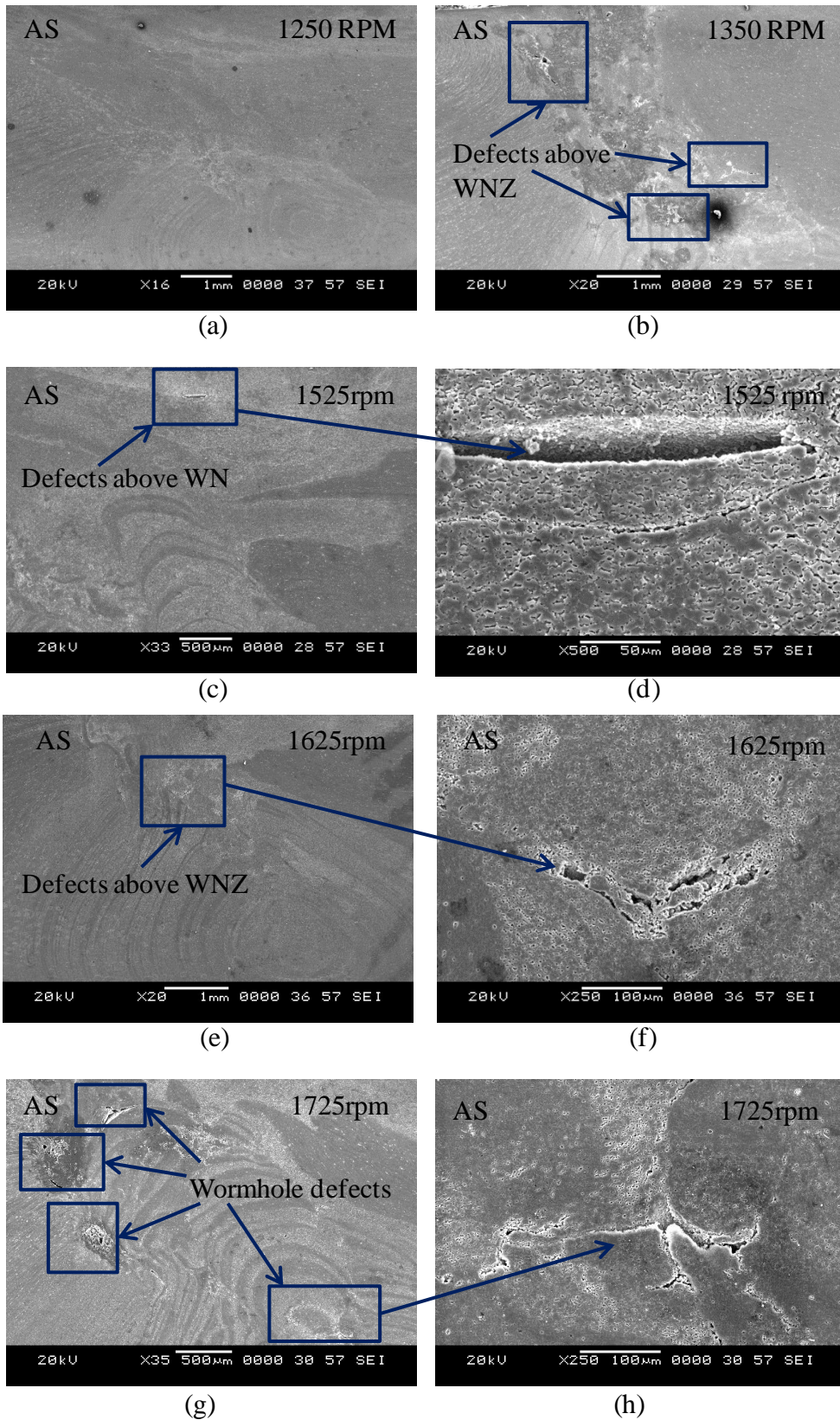



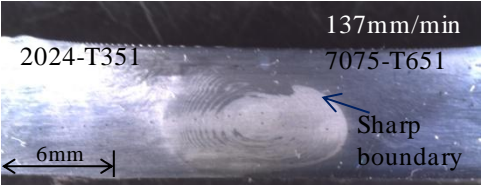

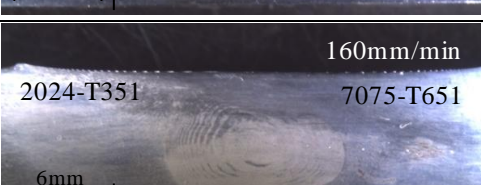
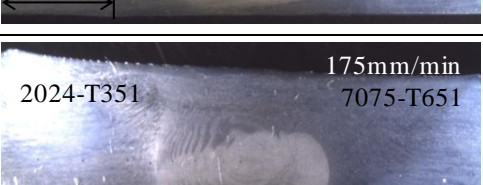

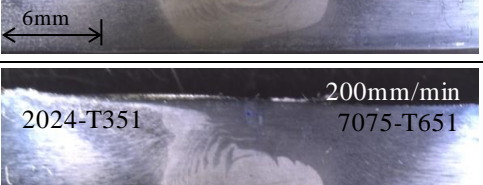
Figure 4.27 Low magnification SEM images of VRS experiment. Unit of rotation speed in 'rpm' mentioned at the top right corner of each figure.

Table 4.4 and Table 4.5 shows the macrograph of the transverse section of the weld region for the FSW dissimilar aluminium alloys joint produced from the two stage of VTS experiment with FSW parameter conditions of TTS range 20-120 mm/min and 120- 200 mm/min, respectively. Optimized TPD, 6.20 mm and optimized TRS, 650 rpm are considered for both stages of the experiment. The macrographs in the Table 4.4. and 4.5 clearly presents the influence of TTS on the width of WNZ, TMAZ and HAZ of the weld region. At the lower TTS of 25 mm/min because of high heat input observes a flat and wider WNZ measuring about 11 mm (Peel et al., 2003) and results in severe plastic flow of the material. As the TTS increases, the width of the WNZ, TMAZ and HAZ decreased due to the low heat input and less plastic flow, and confirms the results reported in the literature (Peel et al., 2003; Zhang et al., 2015; Lomolino et al., 2005; Li et al., 2014). It is also evident from the tensile test results presented in Figure 4.13 that the UTS of these weld joints are greatly influenced by these heat input and width of WNZ, and yields lower UTS for TTS range between 20-55 mm/min compared to the FSW dissimilar aluminium alloys joint produced from higher TTS (Figure 4.13). Classical formation of ‘onion rings’ was observed in the TTS range 55-150 mm/min. However, these ‘onion rings’ are not identical in shape and these depend on TTS. The macrograph images for the TTS 137, 160 and 175 mm/min consists of slightly broken WNZ associated with the less sharp boundary between WNZ and TMAZ of both AS and RS. These sharp boundaries are the result of low heat input and linear microstructure at the interface of the WNZ to TMAZ (Zhang et al., 2014). The presence of these sharp boundaries leads to weaker joint and results in lower UTS and YS (Figure 4.13). Therefore, the boundary separating the WNZ and TMAZ may be the weakest zone and to be taken into consideration for investigation of the UTS of the FSW dissimilar materials joint.

Table 4.4 Macrographs of FSW dissimilar aluminium alloys joint for VTS experiment. Tool traverse speed in ‘mm/min’ indicated on the top right corner of each figure.

Optimum Tool plunge depth (mm)	Optimum Tool rotation speed (rpm)	Varying traverse speed (mm/min)	Macrograph	
			Advancing side (AS)	Retreating side (RS)
6.20	650	25		
6.20	650	40		
6.20	650	55		
6.20	650	70		
6.20	650	80		
6.20	650	90		
6.20	650	110		

Table 4.5 Macrographs of FSW dissimilar aluminium alloys joint for VTS experiment. Tool traverse speed in ‘mm/min’ indicated on the top right corner of each figure.

Optimum Tool plunge depth (mm)	Optimum Tool rotation speed (rpm)	Varying traverse speed (mm/min)	Macrograph	
			Advancing side (AS)	Retreating side (RS)
6.20	650	125		
6.20	650	137		
6.20	650	150		
6.20	650	160		
6.20	650	175		
6.20	650	187		
6.20	650	200		

Dinaharan et al. (2012), Palanivel et al. (2012) and Amancio-Filho et al. (2008) report the importance of the mixed flow region in the FSW joints of dissimilar materials to produce a sound weld joints. In general, the WNZ consists of UMR, MMR and mixed flow region. Mixed flow is required for the dissimilar materials in order to produce sound welds without any defects. In the present study, it was also observed from selected VTS condition, the SEM images (Figure 4.28 (a-b)) at the WNZ exhibiting proper mixed flow consisting of alternate layers by layer forming a lamellae pattern of both AA2024-T351 and AA7075-T651.

Figure 4.29 (a) and (b) presents the SEM and BSE images of the transverse cross-section of weld region of the FSW dissimilar aluminium alloys joint produced from the final optimized sample at TTS of 150 mm/min with optimum TRS, 650 rpm and optimum TPD, 6.20 mm using taper threaded cylindrical tool. As a result of intense plastic deformation caused by stirring action of the tapered threaded tool pin and material flow between the two dissimilar alloys AA2024-T351/ AA7075-T651, the SEM (Figure 4.29 (a)) and BSE (Figure 4.29(b)) images at the WNZ composed of proper mixed flow evidenced by alternate dark and bright lamella pattern. The SEM-BSE image shown in Figure 4.29 (b) indicates that the dark lamellae in the image results from 2024-T351 and bright lamellae from the 7075-T651 alloy. Figure 4.29 (c) shows SEM images at WNZ region within the lamellae pattern consisting of very fine equiaxed grains with an average size of 3 to 5 μm .

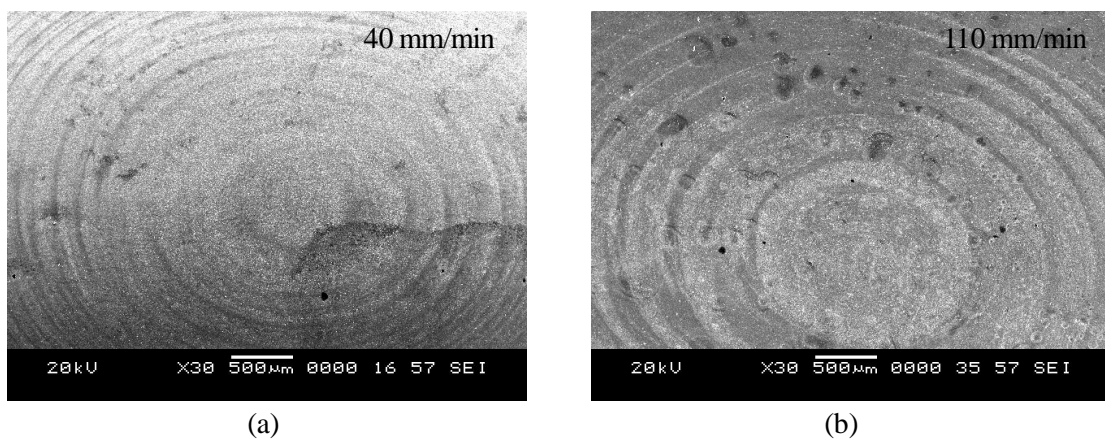


Figure 4.28 Low magnification SEM images of FSW joint for VTS at (a) 40 mm/min and (b) 110 mm/min. Unit of traverse speed in ‘mm/min’ highlighted at the top right corner of each figure.

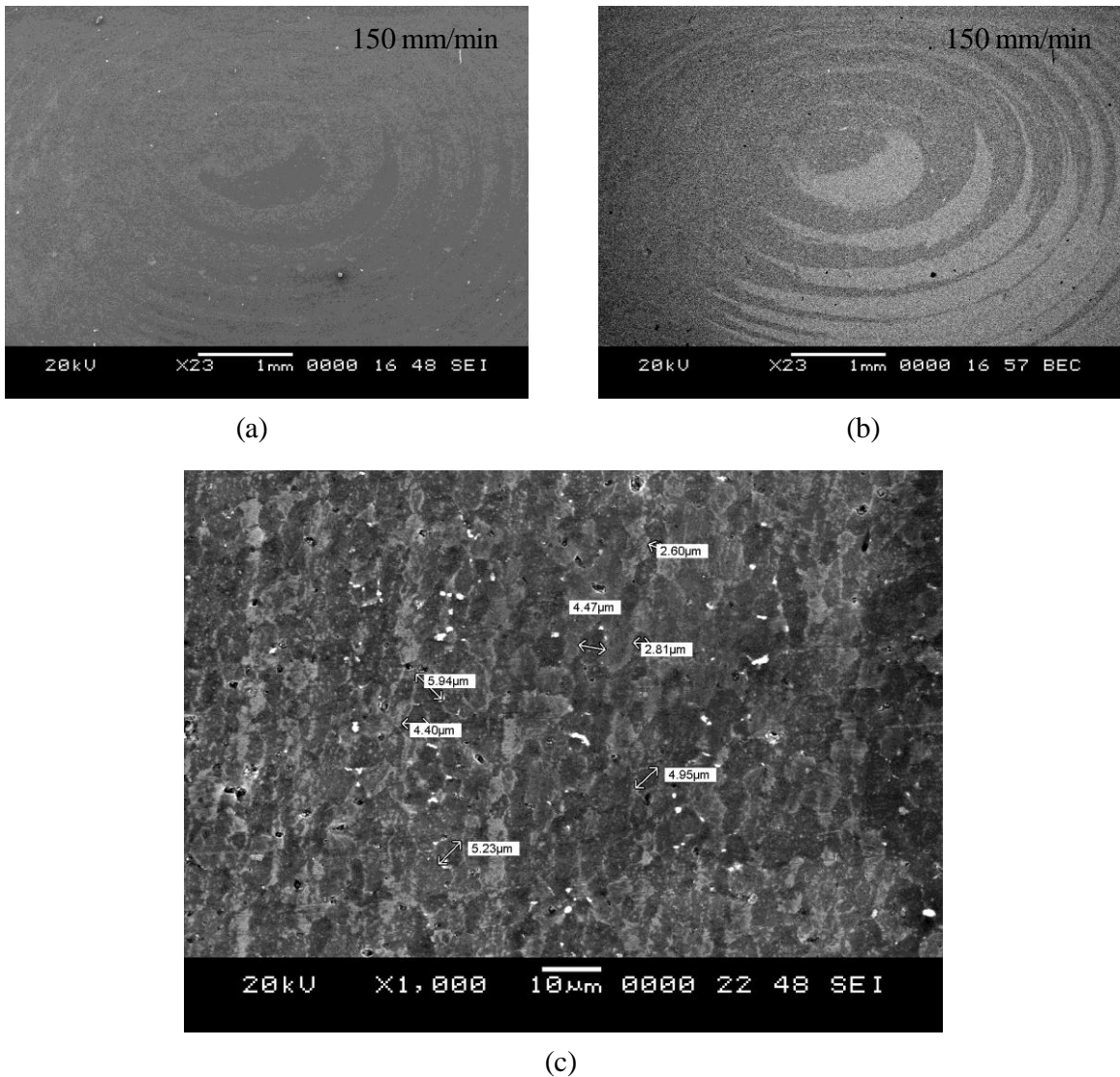


Figure 4.29 (a) SEM and (b) SEM-BSE of WNZ region for the optimized parameters, (c) SEM image for magnification 1000x showing grain size at WNZ region.

4.6.2.2 Varying plunge depth, rotation speed and traverse speed experiments using taper triangle tool

Figure 4.31 presents the macrostructure of the cross sections of WNZ of FSW dissimilar joint specimens fabricated from the VPD experiment at various tool interference levels with TPD range 5.80 to 6.20 mm, and with other two parameters i.e. TRS, 1000 rpm, and TTS, 120 mm/min, kept as constant. One can observe from Figure 4.31, the WNZ of the dissimilar joint specimen can be distinguished by two types of material flow: (i) shoulder driven and (ii) pin driven.

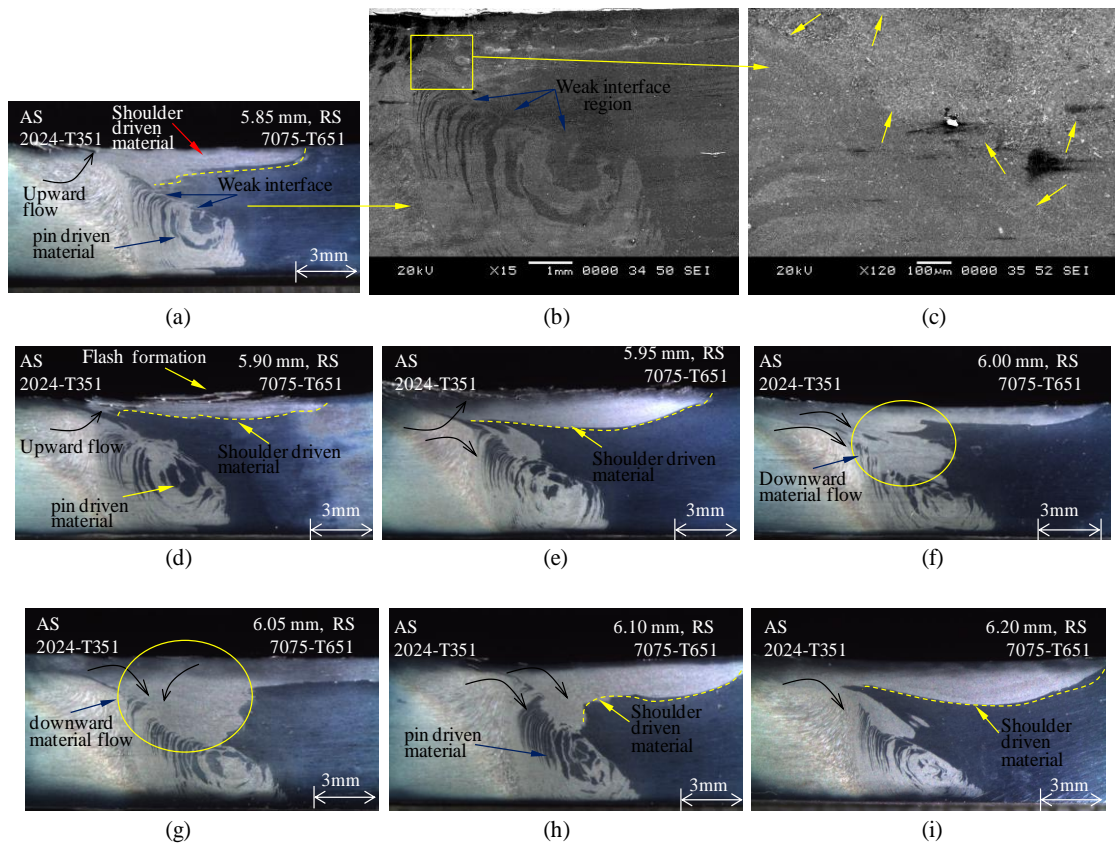


Figure 4.31 Macrostructure images of the WNZ obtained from the varying the TPD for the range 5.80 to 6.20 mm.

It can be observed from the Figure 4.31 (a-i) that the tool shoulder interaction with the base material increases at each stage of increasing in the vertical TPD. As a result, the size of the shoulder dominated region near the top of the WNZ increases with the increase in the TPD. In Figure 4.31 (a), one can observe two distinct material flow pattern influenced by the tool shoulder and pin. At the top of the WNZ, the flow pattern confirms the material transfer occurs by the sliding action of the shoulder (Kumar and Kailas 2008) and is shown by parting yellow line, while the centre of the WNZ observes the material transfer is mainly by tool pin. In the Figure 4.31 (a-d), when the TPD is low in the range 5.85-5.90 mm, there is no sufficient heat generation by the shoulder and the material driven by the pin escapes out of the weld cavity and flow towards the top (indicated by black arrow) leading to the formation of flash at the weld crown. In addition, one can observe the presence of the weak interface between the boundary regions in Figure 4.31 (a-c), which are also the results of the

lack of shoulder contact with the base material. As it can be noticed from the higher magnified SEM images (Figure 4.32 (a-c)), the bonding between stacking layers 1-3 (the region marked as '1' and Figure 4.32 (c)) was incomplete and results in weaker interface boundary regions between the stacking layers. Thus, it leads to the condition of the early failure of the tested tensile specimen of FSW dissimilar aluminium alloys joint and yields lower tensile properties (Figure 4.16).

In the Figure 4.31 (f), increase in the TPD above 6.15 mm, the tool shoulder interaction with the base material increases and more material flow towards AS from the leading edge and confined within the WNZ (Kumar and Kailas, 2008; Colegrove and Shercliff, 2005). Thus, at lower TPD range 5.85 to 6.00 mm the material that escapes towards the top of WNZ (Figure 4.31 (a-d)) are seen to be pushed and deflect back towards the centre of the WNZ at higher TPD above 6.00 mm (Figure 4.31 (f-i)). As a result, the cracks that are observed along the weaker interface region of the unbonded stacking layers (Figure 4.32 (e)) at lower TPD diminish at higher TPD. Hence, at higher TPD, 6.20 mm, leads to the defect-free weld joints with higher tensile properties (Figure 4.18) which may be attributed to the increased plasticized flow and good consolidation of material within the WNZ.

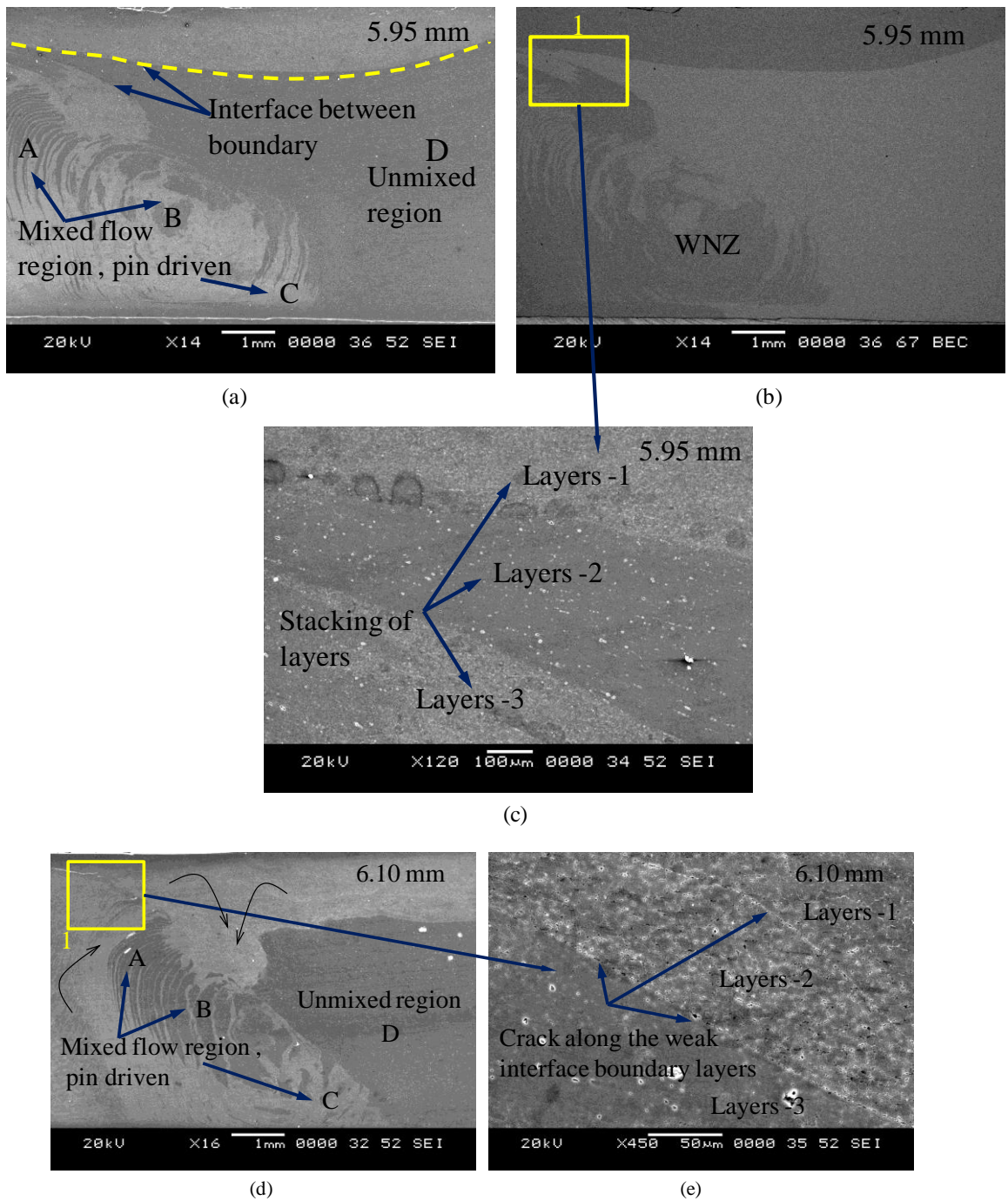


Figure 4.32 (a) Mixed flow region at centre of WNZ, (b)-(c) stacking of layers 1-3 at the top of WNZ (d) arrow marks indicating material flow deflected towards WNZ (e) cracks along the weak interface stacking boundary layers.

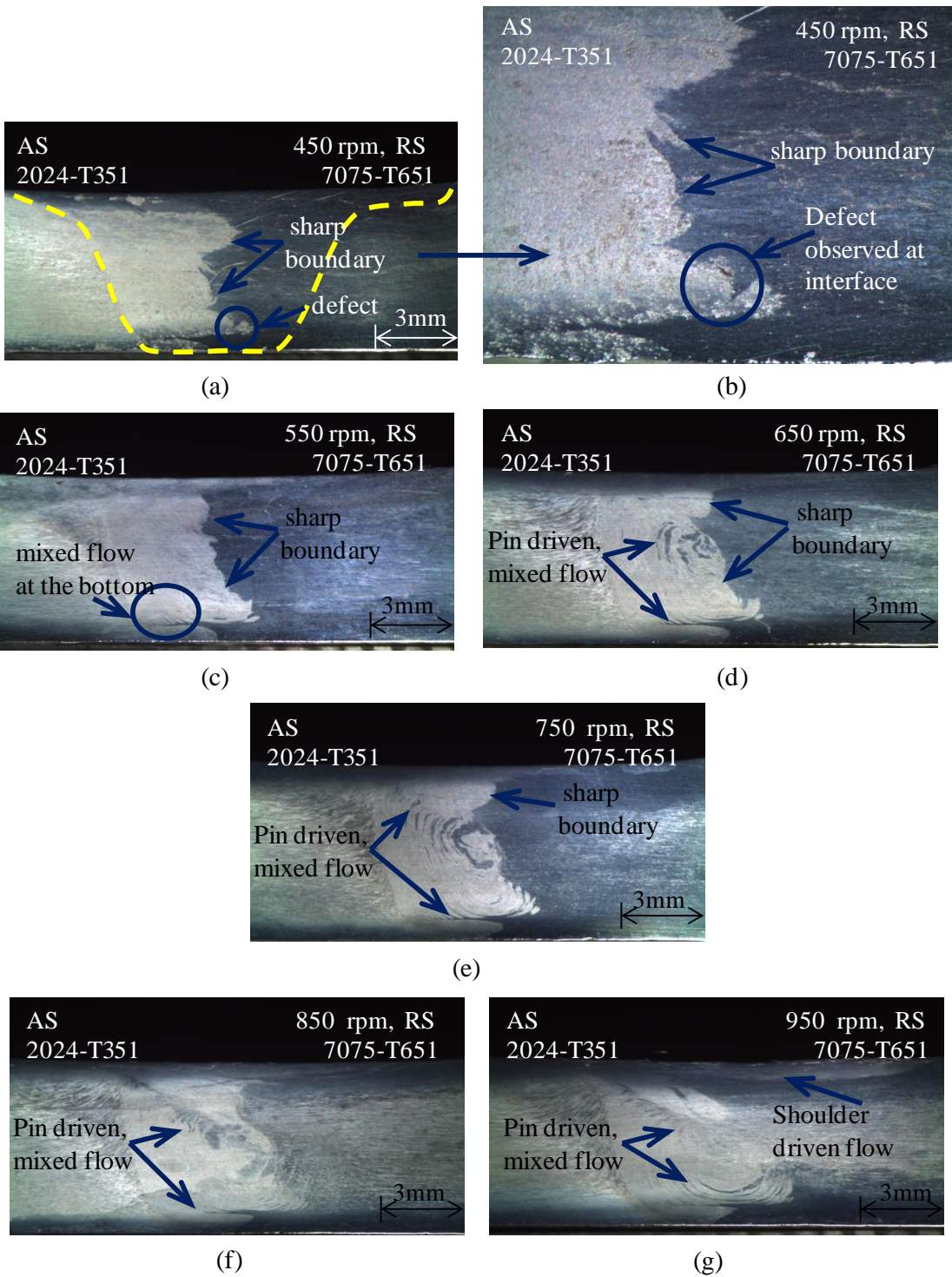


Figure 4.33 Macrostructure images of the WNZ obtained from the varying the TRS experiment for the TRS from 400 rpm to 1100 rpm.

The macrostructure images shown in the Figure 4.33 (a-g) depicts an evaluation of mixing state in the WNZ of the FSW dissimilar aluminium alloys joint starting from 'no mixing' state for TRS of 450 rpm to 'intense mixing' at TRS of 950 rpm. In the Figure 4.33 (a-c) for the TRS of 450 rpm, a clear sharp boundary between two materials can be seen evidenced with 'no mixing' and porosity defects at the interface of the two material boundaries (Figure 4.33 (b)). As a result, the FSW joint yields lower tensile properties (Figure 4.18). The macrostructure image (Figure 4.33 (d)) for the TRS above 550 rpm shows material mixing condition driven by pin at the centre of the WNZ. Thus, for higher TRS the heat input to the WNZ increases and leads to 'intense mixing' conditions from 'no mixing' condition observed for lower TRS (Silva et al., 2011; Sato et al., 2006). The increase in the TRS from 650 rpm to 950 rpm results in the WNZ evidenced with intercalated banded structure consisting of both aluminium alloys AA2024-T351 and AA7075-T651, and driven by pin (Figure 4.33 (d-g)).

The FSW tool parameters conditions of traverse speed and rotation speed influence the mechanical properties and microstructure characteristics of the FSW joint (Khodir et al., 2008; Guo et al., 2014; Dinaharan et al., 2012). Higher magnified SEM images for material mixing condition at TRS of 650, 850 and 950 rpm is shown in Figure 4.34 (a-f). Figure 4.34 (a-b) observes the initiation of mixing condition with diffusion phenomenon of the two alloys in the WNZ for TRS of 650 rpm. Even though the alternate banded structure does not resemble a complete circle, some evidence of material mixing driven by pin can be observed at the middle of the WNZ. However, the AS and RS of the WNZ observes UMR composed of just one material either AA2024-T351 in the AS and AA7075-T651 in the RS (Figure 4.34 (b)). In addition, the WNZ consists of a narrow and sharp boundary, which separates both the alloys. These sharp boundaries also observed for the TRS of 850 rpm and yield lower tensile properties (Figure 4.18). However, for TRS of 850 rpm the intensity of material mixing condition at the WNZ increased compared to TRS of 650 rpm. As shown in the Figure 4.34 (e-f), increase in the TRS to 950 rpm helps in generating sufficient heat to transfer the material from the leading edge to confine within the WNZ and as a result, a clear intercalated banded structures of both AA2024-T351 and AA7075-

T651 are observed. In addition, the sharp boundary which was observed at the interface separating both alloys at the rotation speed 650 rpm (Figure 4.34 (a-b)) and 850 rpm (Figure 4.34 (c-d)) appears to be diffused for increasing the TRS to 950 rpm (Figure 4.34 (e-f)). Thus, the higher TRS of 950 rpm helps in intense material mixing at the WNZ, straining rate of plasticized material and yields maximum tensile properties of the FSW joints (Figure 4.18).

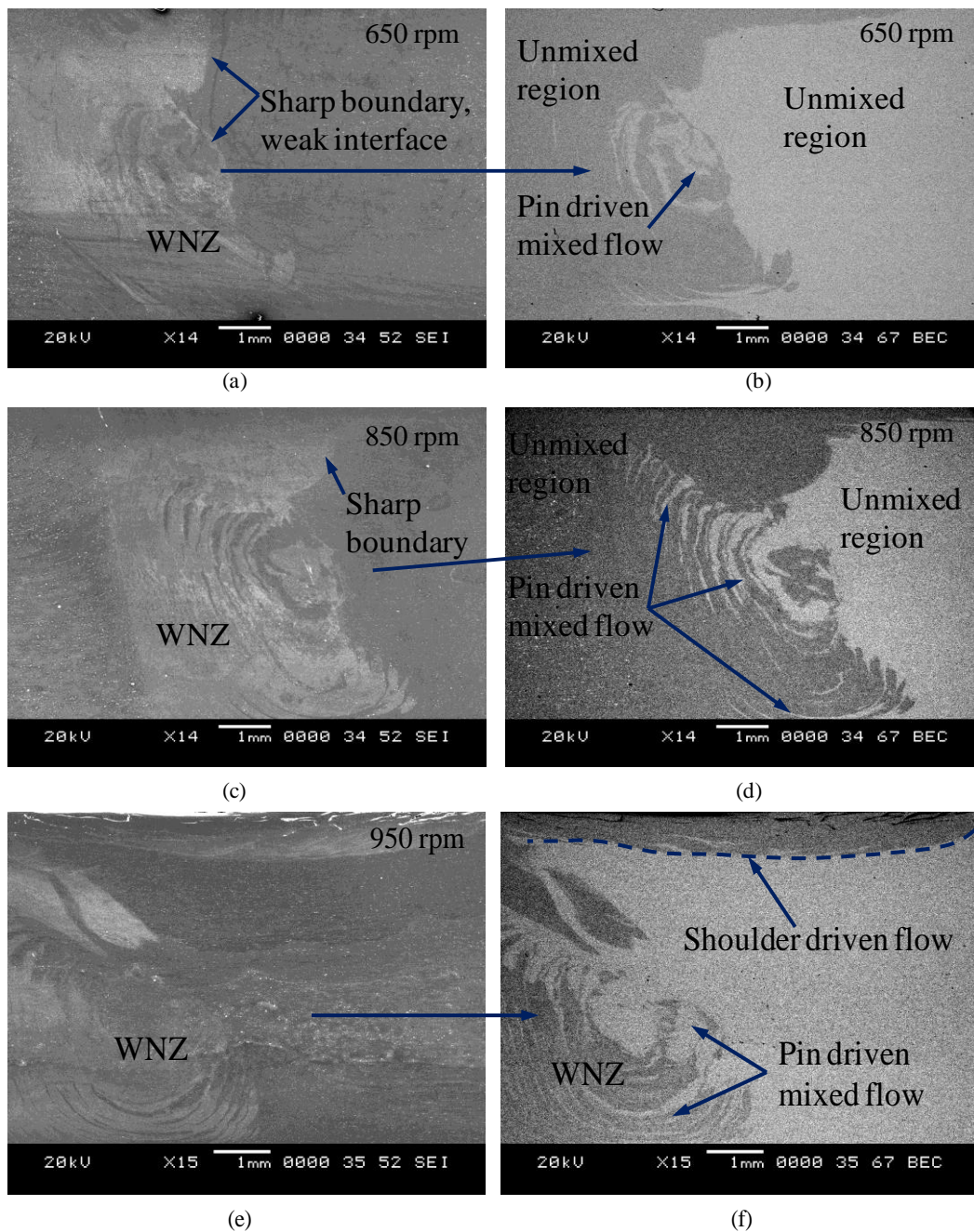


Figure 4.34 SEM images showing (a) sharp boundary at the interface and (b) pin driven mixed flow at WNZ and unmixed region at RS for TRS of 850 rpm (c) and (d) the presence of both shoulder and pin driven material flow pattern at TRS of 950 rpm.

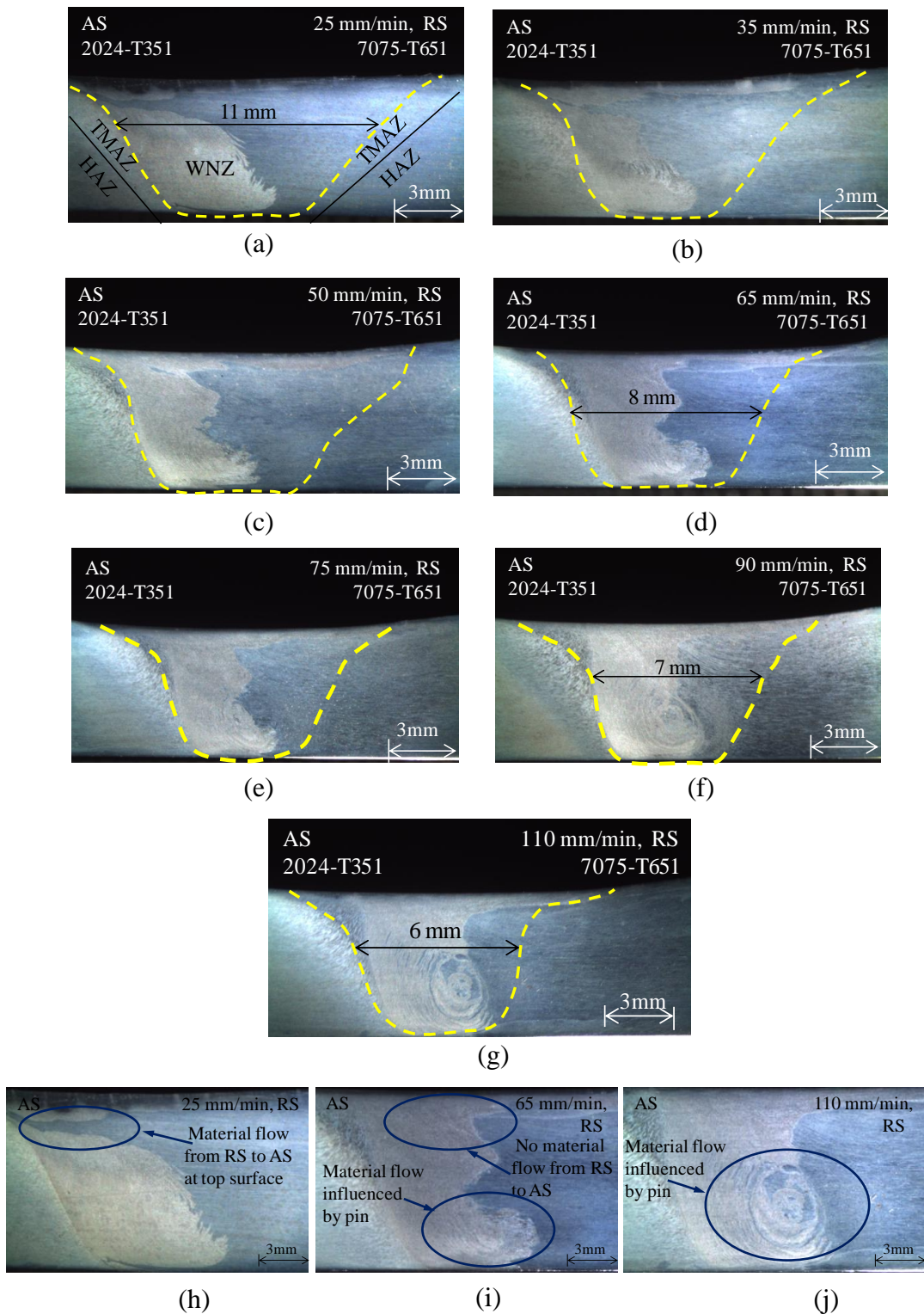


Figure 4.35 Macrostructure images of the WNZ obtained from the VTS experiment for the TTS range 20 to 110 mm/min.

Figure 4.35 (a-j) presents the macrostructure of the cross sections of weld region from the centre of WNZ of the FSW dissimilar aluminium alloys joint from the VTS

experiment for the TTS range 20 to 120 mm/min and the corresponding grain sizes are shown in the SEM images Figure 4.36 (a-f). It can be seen from Figure 4.35, with the increase in the TTS, the weld region observes a gradual reduction in the size of the WNZ. The TTS shows an inverse relationship effect on the heat input and thereby influences the size of the WNZ and grain growth (Kumar and Murugan, 2014). The size of WNZ measuring about 11 mm wide at the lower TTS of 25 mm/min gradually decreases and reaches the 6 mm wide for TTS of 110 mm/min. The changing condition in the heat input with the varying TTS is the result of variation in the size of the WNZ (Sakthivel et al., 2009). It is also evident from Figure 4.35 that the TTS have shown its influence on the material flow and mixing pattern at the WNZ of FSW dissimilar aluminium alloys joint. As the tool pin is non-threaded, the macrograph does not show any “onion ring” structure in the WNZ of the weld region of FSW joint produced from all the varying TTS condition. In addition, when flat face tool pin is used the material swept and transportation of material from the top to the bottom of the surface in the WNZ is not uniform (Palanivel et al., 2012). The taper triangle tool pin profile which has flat faces leads to pulsating stirring action and results in better material flow with excess turbulence (Kumar and Murugan, 2014; Roshan et al., 2013). Higher tool residence time for lower TTS leads to the WNZ exposure for more heat generation and distribution in a broad throughout the width of the tool shoulder.

At lower TTS of 25 mm/min, one can observe from the Figure 4.35 (h) that the top surface of the FSW joint is influenced by the rubbing action of the shoulder and sufficient heat generated transfers the plasticized material from the RS to AS. However, the middle and bottom portion of the WNZ, which depends mainly on stirring action of the pin, observes unmixed region UMR. Increase in the TTS to 65 mm/min, the Figure 4.35 (i) observes ‘no evidence’ of material flow at the top surface owing to the lesser heat generation. This is due to the sliding condition of shoulder instead of sticking (Sakthivel et al., 2009, Rai et al., 2011). However, the middle region of the WNZ presents the initiation of stirring action influenced by the pin and in-situ extrusion of AA2024-T351 and AA7075-T651 alloys. Further, increasing the TTS to 110 mm/min, the WNZ (Figure 4.35 (j)) observes a complete mixed flow pattern at the middle region of the WNZ and the extreme plasticized material

consisting of alternate layers of both aluminium alloys. At higher TTS, the WNZ exposure for the heat generated is narrowed down. Thus, heat exposure of the FSW dissimilar aluminium alloys joint at the varying TTS experiments have shown a strong influence on their tensile properties. The TTS of 90 mm/min yields higher tensile properties (Figure 4.23 (a)).

At the TTS from 25 to 50 mm/min, the increase in tool residence time results in higher heat input per unit of weld length. Further, slower cooling rate leads to the grain coarsening, grain growth and softening of the WNZ. Thus, these factors affects the mechanical and microstructure characteristics of the FSW dissimilar aluminium alloys joint. Thus, at a lower TTS of 25 mm/min, higher magnification microstructure SEM images (Figure 4.36 (a)) of the WNZ observes grain size measuring in the range 6 - 10.5 μm and FSW joint yields lower tensile properties (Figure 4.23(a)). The joints fabricated with the TTS above 50 mm/min have shown the decrease in the size of the WNZ measuring about 8 mm wide with average grain size range 3 - 6 μm (Figure 4.36 (d)). This may be attributed to the shorter time exposure of the FSW joint to the frictional heat generated by tool shoulder and pin, faster cooling rate and confirms the result reported in the early investigations (Sato et al., 2006; Khodir et al., 2008; Guo et al., 2014; Sakthivel et al., 2009). The Figure 4.36 (f) depicts the average grain size of 2-3.5 μm at the WNZ of the final optimized sample of FSW dissimilar aluminium alloys joint produced by the taper triangle tool with the optimized FSW parameters such as TPD of 6.20 mm, TRS of 950 rpm and the TTS of 90 mm/min.

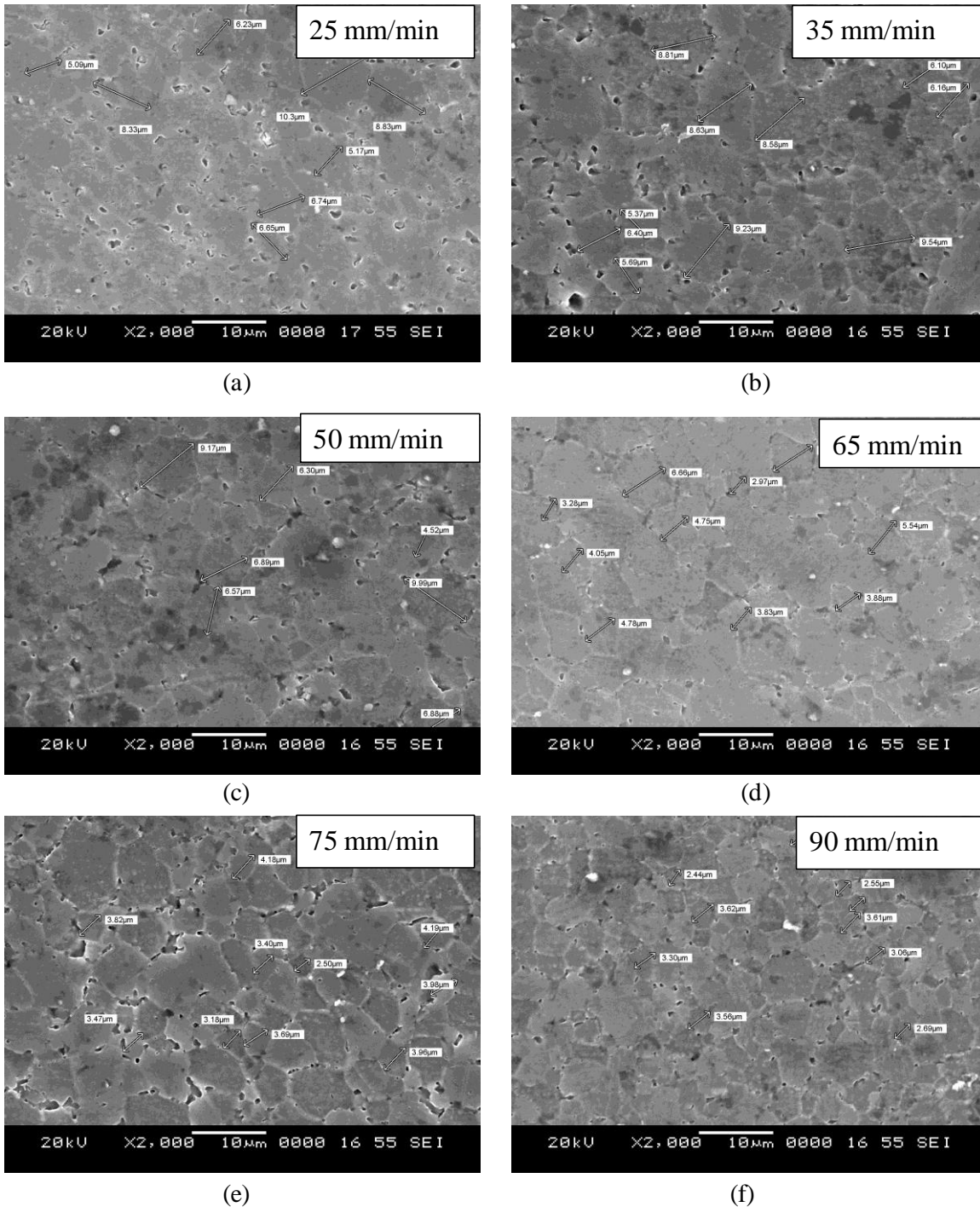


Figure 4.36 SEM images showing the grain size of the WNZ for the FSW joint for the varying the TTS experiment for the range 20 to 90 mm/min.

4.6.3 Microhardness

The micro-hardness profile at across the transverse cross section of the weld region of the FSW dissimilar aluminium alloys joint fabricated by conducting the VRS and

VTS experiment for the TTR range 400 to 1800 rpm and TTS range 20 to 200 mm/min and using taper threaded tool are presented in the proceeding section. As the effect of TPD on hardness of the FSW dissimilar aluminium alloys joint is not important the same is not considered.

4.6.3.1 Varying rotation speed experiments for taper threaded tool

Figure 4.37 and Figure 4.38 presents the microhardness profiles of the weld region of the FSW dissimilar aluminium alloys joints fabricated for the VRS range 400-1100 rpm and 1100-1800 rpm, respectively. The microhardness profile plot in Figure 4.37 shows higher hardness at the WNZ compared to the base material 2024-T351 hardness of 138Hv. This increase in the hardness at WNZ may be due to two reasons: (i) the formation of ‘onion rings’ structure at WNZ consisting of alternate lamellae band pattern having a chemical composition of both AA7075-T651 and AA2024-T351 and (ii) finer grain size at WNZ compared to the base materials. According to the Hall-Petch relation, smaller the grain size leads to the harder material property. The lower hardness observed in the TMAZ and HAZ of both AS and RS of the FSW joint are the results of severe coarsening and the dissolution of strengthening precipitates (Guo et al., 2014; D’Urso et al., 2014; Sato et al., 1999; Su et al., 2003). It can be observed that TRS range between 400-1100 rpm with a constant TTS, 120 mm/min exerted not much considerable difference in average microhardness at TMAZ and HAZ of both AS and RS of the FSW joint. However, the hardness at WNZ slightly increased with an increase in the VRS above 750 rpm owing to the proper stirring of both the alloys. The microhardness profile resembles a typical characteristics curve ‘W’ that is generally observed in the FSW joint.

Microhardness profile for the second set of VRS experiment for TRS range 1100-1800 rpm is as shown in Figure 4.38. For the TRS range between 1275 rpm to 1350 rpm, one can observe a sharp decrease in hardness to 55 Hv within the WNZ owing to the presence of a large number of wormhole defects (Figure 4.28 (b)). Higher TRS above 1400 rpm resulted in the higher heat generation and slower cooling rate. Higher heat generation leads to the formation of coarse grains. This led to the formation of micro voids and defects (Figure 4.28 (c-h)). Thus, it results in the lower hardness in

the AS above the WNZ compared to the RS. In general, the presence of wormhole defects, coarsening of the grains and lower hardness observed in the VRS range of 1100-1800 rpm deteriorated the UTS of the FSW dissimilar joints.

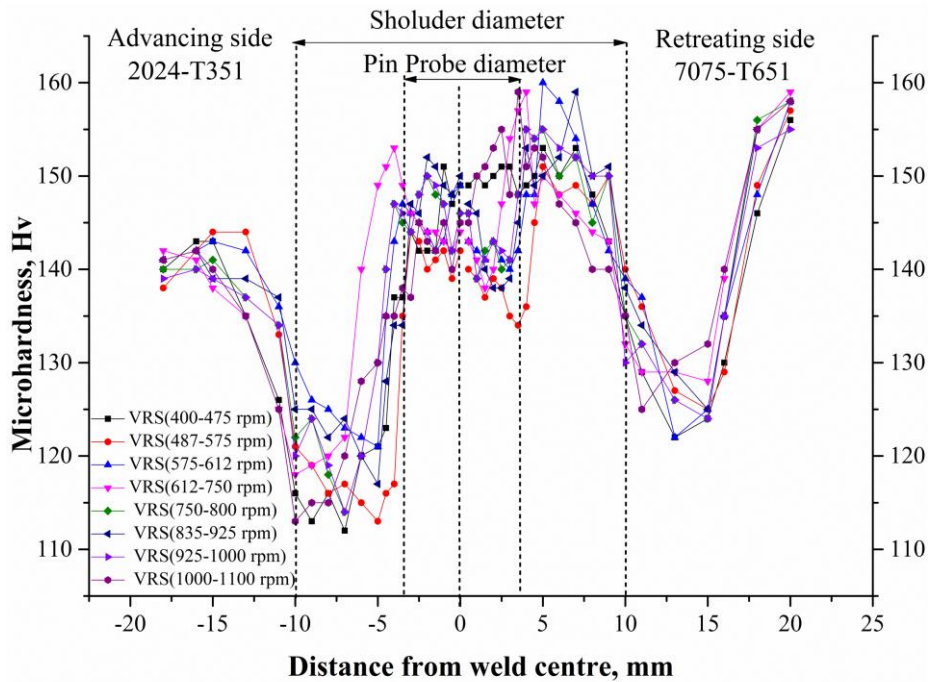


Figure 4.37 Hardness profile at mid thickness transverse to the welding direction of the joints for VRS experiment from TRS range 400-1100rpm.

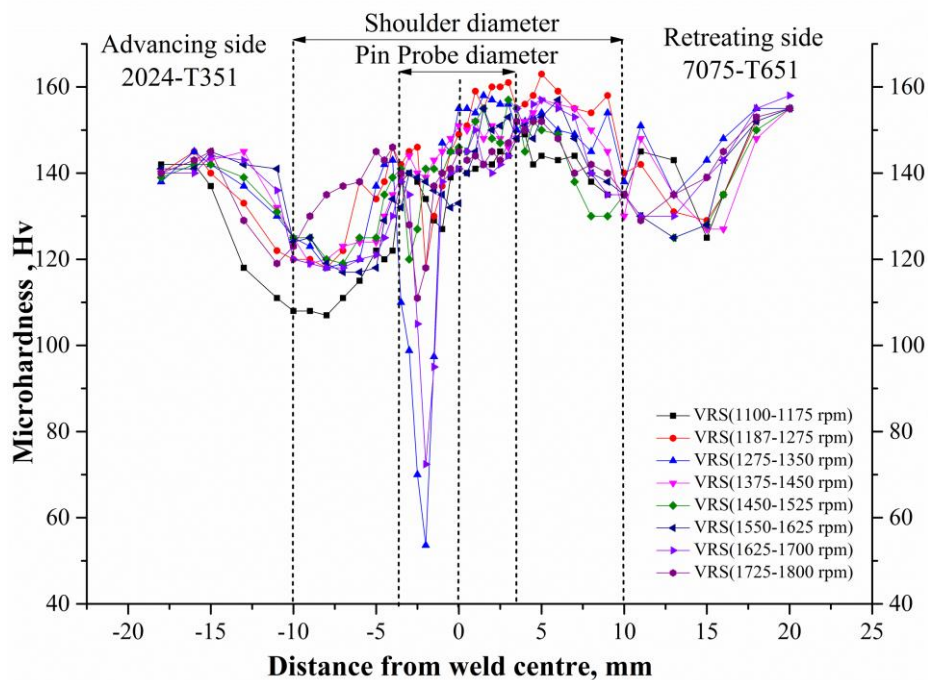


Figure 4.38 Hardness profile at mid thickness transverse to the welding direction of the joints for VRS range 1100-1800 rpm.

4.6.3.2 Varying traverse speed experiments using taper threaded tool

Figure 4.39 and Figure 4.41 presents the microhardness profile for the FSW dissimilar aluminium alloys joint fabricated from the VTS experiment carried out for the TTS range 20-200 mm/min. At the lower TTS range of 20 to 50 mm/min, higher temperature and slower cooling rate results in a wider and softened WNZ (Table 4.4) evidenced with a minimum hardness range 95-100 Hv observed in WNZ, TMAZ and HAZ regions of both AS and RS. For the TTS range from 50-120 mm/min, the hardness profile in WNZ, TMAZ and HAZ shows gradual improvement in the hardness.

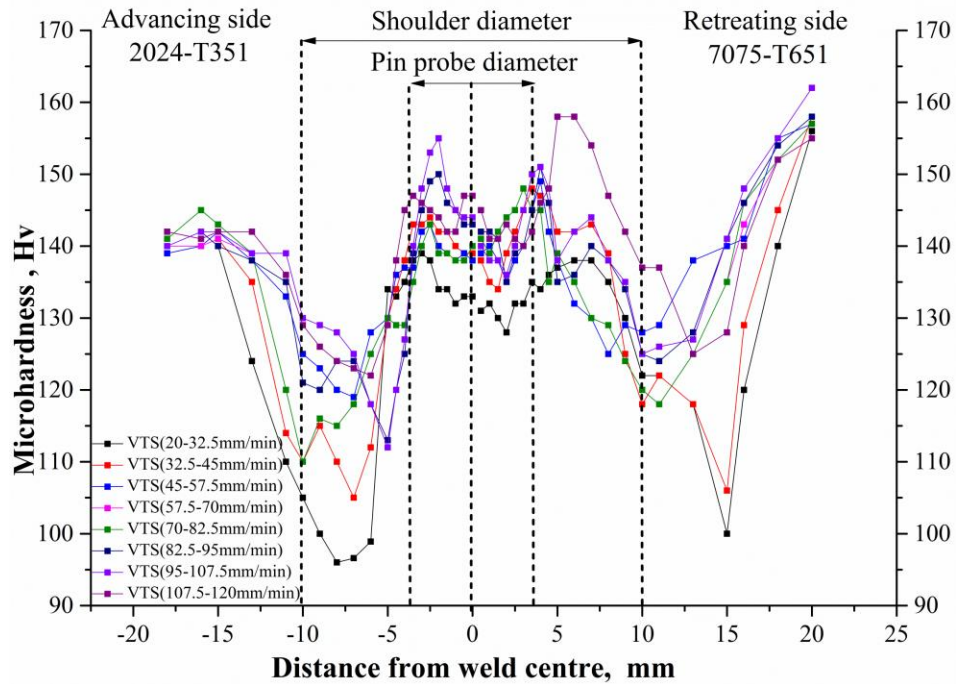


Figure 4.39 Hardness profile at mid thickness transverse to the welding direction of the joints for VTS ranging between 20-120 mm/min.

Figure 4.41 shows that at higher TTS range 120-200 mm/min, the softened area becomes narrower because of reduced heat input and faster cooling rate (Peel et al., 2003). Further, it is observed that the softened zone existing near to the shoulder diameter region on both AS and RS in Figure 4.39 is shifted near to the pin diameter region in Figure 4.41. This is due to the increase in the TRS. The average

microhardness at the WNZ region for the FSW joint tested for VRS and VTS experiments found to be higher compared to regions of TMAZ and HAZ.

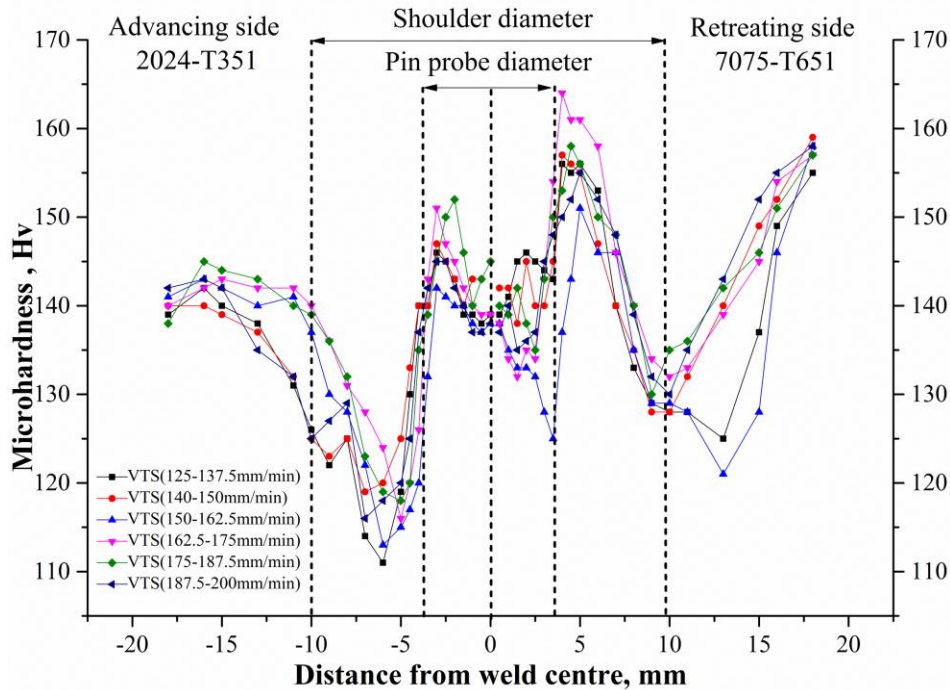


Figure 4.41 Hardness profile at the mid thickness transverse to the welding direction of the joint for VTS ranging between 120-200 mm/min.

4.6.4 Fractography

The SEM images of the tested tensile specimens of base material AA2024-T351 and AA7075-T651 are as shown in the Figure 4.42. The fracture surface of BM of AA2024-T351 is characterized by the micro-voids (Figure 4.42 (a)) and a large number of equiaxed very fine dimples of different sizes close to the microscopic voids (Figure 4.42(b)). The fractography of the tensile specimen of BM of AA7075-T651 is composed of tearing edges (Figure 4.42(c)) and cleavages (Figure 4.42(d)). The observation of fracture surface of both the BM of AA2024-T351 and AA7075-T651 indicates that the joint failure is ductile in nature and both the BM showed ductile behaviour during fracture progress.

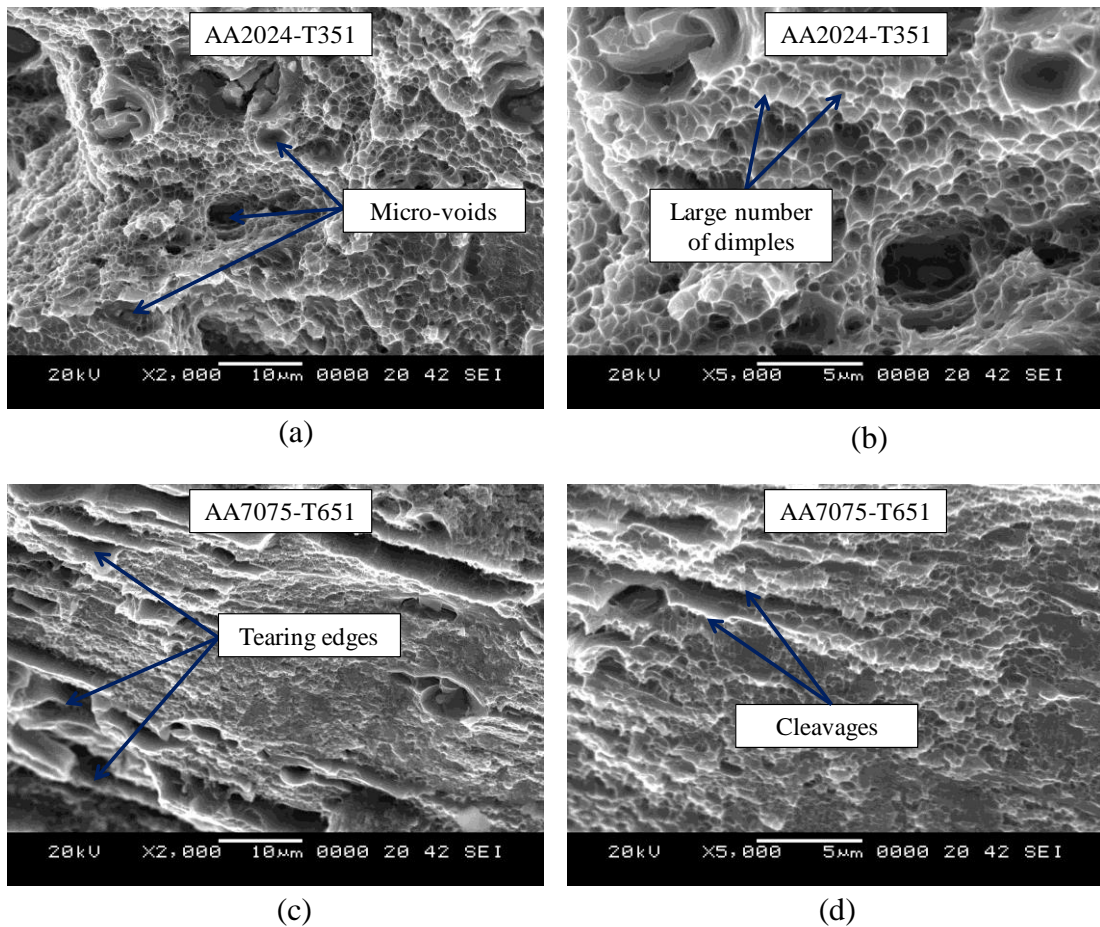


Figure 4.42 SEM images of typical fracture surface of base material of AA2024-T351 are showing (a) micro-voids (b) large number of dimples, and base material AA7075-T651 showing (c) tearing edges (d) cleavages.

4.6.4.1 FSW dissimilar joint produced from taper threaded tool

The SEM images shown in the Figure 4.43 are obtained from the fracture surface of the tensile specimen of FSW dissimilar aluminium alloys joint produced from the optimum process conditions of TPD, 6.20 mm, TRS, 650 rpm and TTS, 150 mm/min.

The analysis of the fractured surface from the FSW parameter optimized sample (Figure 4.43 (a)) consists of micro voids and a very large number of equiaxed dimples of different size, shape and are close to micro voids (Figure 4.43(c)). The observation of fracture surface indicates that the joint failure is ductile in nature and material showed ductile behaviour during fracture progress. This specimen having a fractured location in the interface of the boundaries of the WNZ/TMAZ of AS (Figure 4.43(a))

and exhibits the fracture surface morphology, which resembles that of BM of AA 2024-T351.

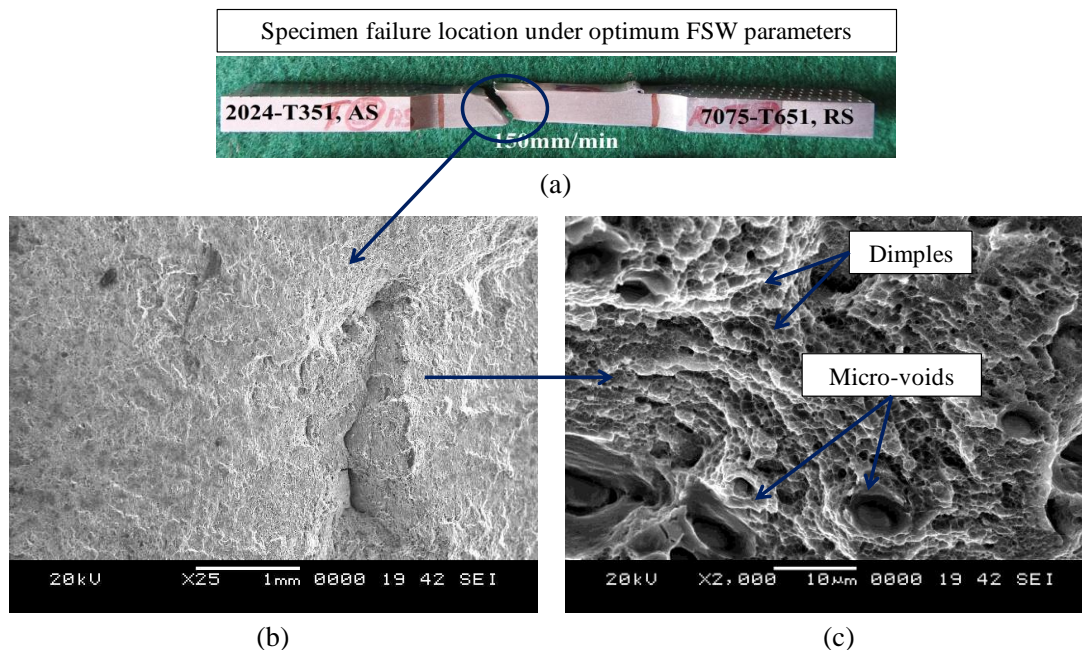


Figure 4.43 (a) Photograph showing fractured specimen failure location under optimum FSW parameters fractured at HAZ of AS. (b) and (c) are SEM images of fracture surface of FSW joint of (a).

Figure 4.44 depicts the SEM images obtained from the fracture surface of the tensile specimen of FSW dissimilar aluminium alloys joint produced from the un-optimized FSW parameter of TTS of 130 mm/min but for the other two parameters in optimum condition viz. the TPD and TRS as 6.20 mm and 650 rpm, respectively. Figure 4.44 (c) shows the magnified fracture surface SEM image of failure location of the specimen consisting of smoothly curved fracture surface morphology, the absence of any severe deformation and alternate distribution of dark and white stripes. The morphology between these two alternate dark and white stripes are shown in Figure 4.44 (d). Few specimens have failed due to the sharp boundary or lack of metallurgical bonding between materials exhibits this kind of fracture surface morphology along the discontinuity region and results in early failure of the joints. High magnification SEM images (Figure 4.44(e)) at these locations shows the presence of a large number of small size dimples and confirms that the specimen

having characteristics of ductile fracture. The fractography analysis carried out at the top portion (shown as '1') of the specimen consists of micro-voids surrounded by a large number of dimples (Figure 4.44(c)). Finally, the presence of micro-voids and dimples in the tensile tested specimen confirms that the failure characteristics had similar to that of ductile fracture.

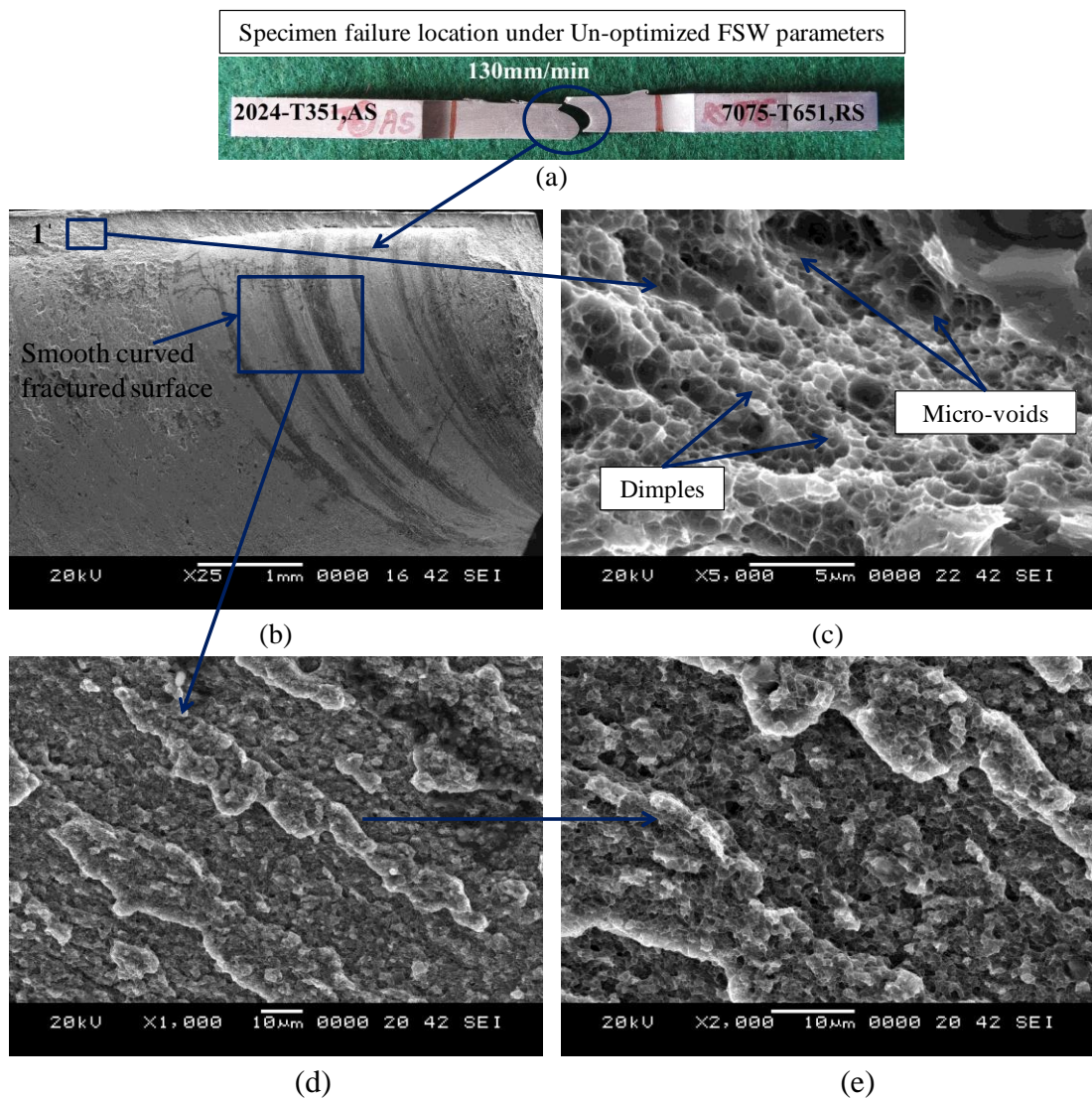


Figure 4.44 (a) Photograph showing fractured FSW joint failure location for un-optimized FSW parameters. (b)- (e) SEM images of FSW joint of (a).

4.6.4.2 FSW dissimilar joint produced from taper triangle tool

Figure 4.45 (a-c) depicts the macrograph of the fracture tensile specimens for the optimized FSW parameters such as TPD, TRS and TTS obtained from the different set of the bottom-up optimization experimental approach and using taper triangle tool.

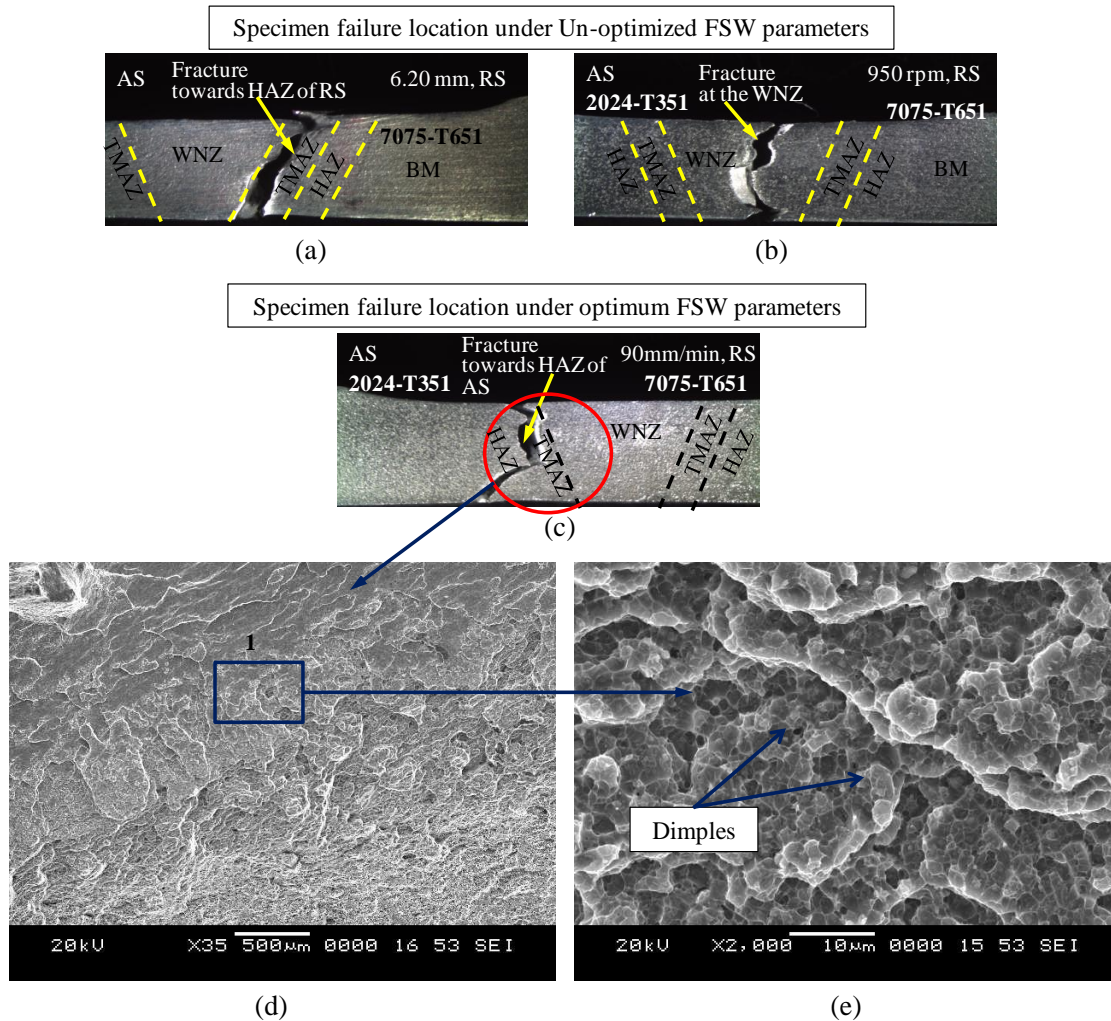


Figure 4.45 Macrographs showing failure location FSW joint at (a) interface boundaries of WNZ/TMAZ towards RS (b) WNZ and (c) TMAZ/HAZ towards AS. (d) and (e) are SEM images of fracture surface of the specimen of (c).

Figure 4.45(a) shows the fracture of the tested tensile specimen of FSW dissimilar aluminium alloys joint fabricated from optimized TPD of 6.20 mm having failure location away from the WNZ of the weld region and at the interface boundaries of WNZ/TMAZ towards RS. In general, higher TPD results in sufficient frictional force and the heat generation beneath the shoulder helps in the consolidation of material

within the WNZ and produce sound weld joints (Kumar and Murugan, 2014). Thus, the tested tensile specimen failed at the lower hardness region (Mishra and Ma, 2005; Dinaharan et al., 2012) and away from the WNZ at the interface between WNZ and TMAZ. These cracks of the failed specimen are inclined at 45° to the tensile axis and occurred at 10 mm away from the weld joint line.

Similarly, Figure 4.45 (b) shows the tensile tested specimen produced with optimum TRS of 950 rpm and having failed in the WNZ. Figure 4.45 (c) depicts the failure location of the specimen fabricated with final optimized FSW parameters such as TPD of 6.20 mm, TRS of 950 rpm, and TTS of 90 mm/min, and having highest tensile strength. The failure location of the sample found to be at the boundary interface of TMAZ/HAZ towards the AS of base material AA2024-T351.

The SEM analysis of the fracture surface of the tested tensile specimen (Figure 4.45 (c)) obtained from the optimum FSW parameters condition are shown in Figure 4.45 (d-e) and fracture surface (marked as '1' in Figure 4.45 (d)) of the sample consists of equiaxed dimples, plenty of tearing edges and cleavages. Thus, it indicates that the tested tensile specimen failure is ductile in nature. All these features indicate that FSW dissimilar joint specimen produced for optimized FSW parameters condition exhibits higher ductility and %EL.

4.6.5 Overall conclusions for optimizing the FSW parameters using the bottom-up experimental approach

The bottom-up experimental approach has been successfully adopted for optimizing the FSW parameters such as TPD range 5.80 to 6.20 mm, TRS range 400 to 1800 rpm and TTS range 20 to 200 mm/min for joining the two dissimilar aluminium alloys joint of AA2024-T351 and AA7075-T651 in butt-joint configuration using both the taper threaded cylindrical and taper triangle tool. The optimization of FSW parameters such as TPD, TRS and TTS involves three stages of the experimental procedure to be carried out viz VPD, VRS and VTS experiments. The results has shown higher mechanical properties and better microstructure characteristics for the FSW dissimilar aluminium alloys joint fabricated by implementing the of the bottom-up approach. Optimized FSW parameters for taper threaded cylindrical tool are TPD,

6.20 mm, TRS, 650 rpm, TTS, 150 mm/min and yields UTS, 435 MPa, YS, 290 MPa, % EL, 13, and η_{WJ} , 92% with defect-free microstructures in the weld region. Similarly, the FSW dissimilar aluminium alloys joint produced from taper triangle tool the optimized FSW parameters are TPD, 6.20 mm, TRS, 950 rpm, TTS, 90 mm/min and yields higher UTS, 440 MPa, YS, 350 MPa, % EL, 17.5 and η_{WJ} , 93% enhanced microstructure characteristics in the weld region. Thus, irrespective of tool geometry or shape, the bottom-up approach has been used successfully for joining the FSW dissimilar aluminium alloys joint that yields higher mechanical properties and better microstructure characteristics.

4.7 SUMMARY

This chapter has revealed the results of an experimental investigation by a bottom-up optimization approach for FSW parameters using a taper threaded cylindrical and taper triangle tool. It was found that the experimental technique associated with the bottom-up approach for obtaining the optimum FSW parameters is found to be one of the potential candidatures to eliminate complexity in the procedure further with few numbers of experimental runs. The range of FSW parameters (TPD or TRS or TTS) that can be investigated using a bottom-up approach in single experimental trial is much larger in numbers when compared to the other DOE techniques (e.g., Taguchi, RSM, ANN, etc.) requires more number of experimental runs and trials. In addition, the specimens tested from the FSW dissimilar aluminium alloys joint fabricated using both tools i.e. taper threaded cylindrical and taper triangle, has shown higher mechanical properties and better microstructure characteristics. This indicates that irrespective of tool geometry, the bottom-up approach could be effectively used as a suitable optimization experimental approach to obtain optimum FSW parameters. Influence of tool probe offset and tool traverse speed on FSW dissimilar aluminium alloy joints keeping optimized TPD and TRS obtained from bottom-up experimental approach has been reported in Chapter 5.

CHAPTER-5

INFLUENCE OF TOOL PROBE OFFSET AND TOOL TRAVERSE SPEED ON FSW DISSIMILAR ALUMINIUM ALLOYS JOINT

5.1 INTRODUCTION

This chapter discusses the experimental investigation to evaluate the effect of tool probe offset in conjunction with the varying the tool traverse speed (TTS) on the mechanical properties and microstructure characteristics of the FSW dissimilar aluminium alloys joint of AA2024-T351 to AA7075-T651 in butt-joint configuration. Taper threaded cylindrical tool is used to fabricate the dissimilar joints. The tool probe offset condition towards AA2024-T351 or AA7075-T651 from the weld joint line has a significant effect on the properties of the FSW joint. In addition, the TTS plays a major role in the generation of sufficient heat input to the weld region of during the FSW process.

5.2 EXPERIMENTAL PROCEDURE FOR TOOL PROBE OFFSET AND VARYING TOOL TRAVERSE SPEED

The tool probe offset and varying TTS approach involves three sets of experimental trials carried out on an individual set of aluminium alloy plates of typically AA2024-T351 and AA7075-T651 in butt-joint configuration. The position of alloy plate of AA2024-T351 is always on the AS, while the higher strength AA7075-T651 is on the RS. The FSW process was performed using a taper threaded cylindrical tool.

Figure 5.1 illustrates the schematic of the three set experiment trials carried out with different tool probe offset condition by varying the TTS. The TTS range 20 -120 mm/min is varied along the weld joint line for a length, 150 mm, while the other two optimum FSW parameters i.e. TRS, 650 rpm and TPD, 6.20 mm obtained by adopting the bottom-up experimental approach technique of the previous Chapter 4, are kept as constant.

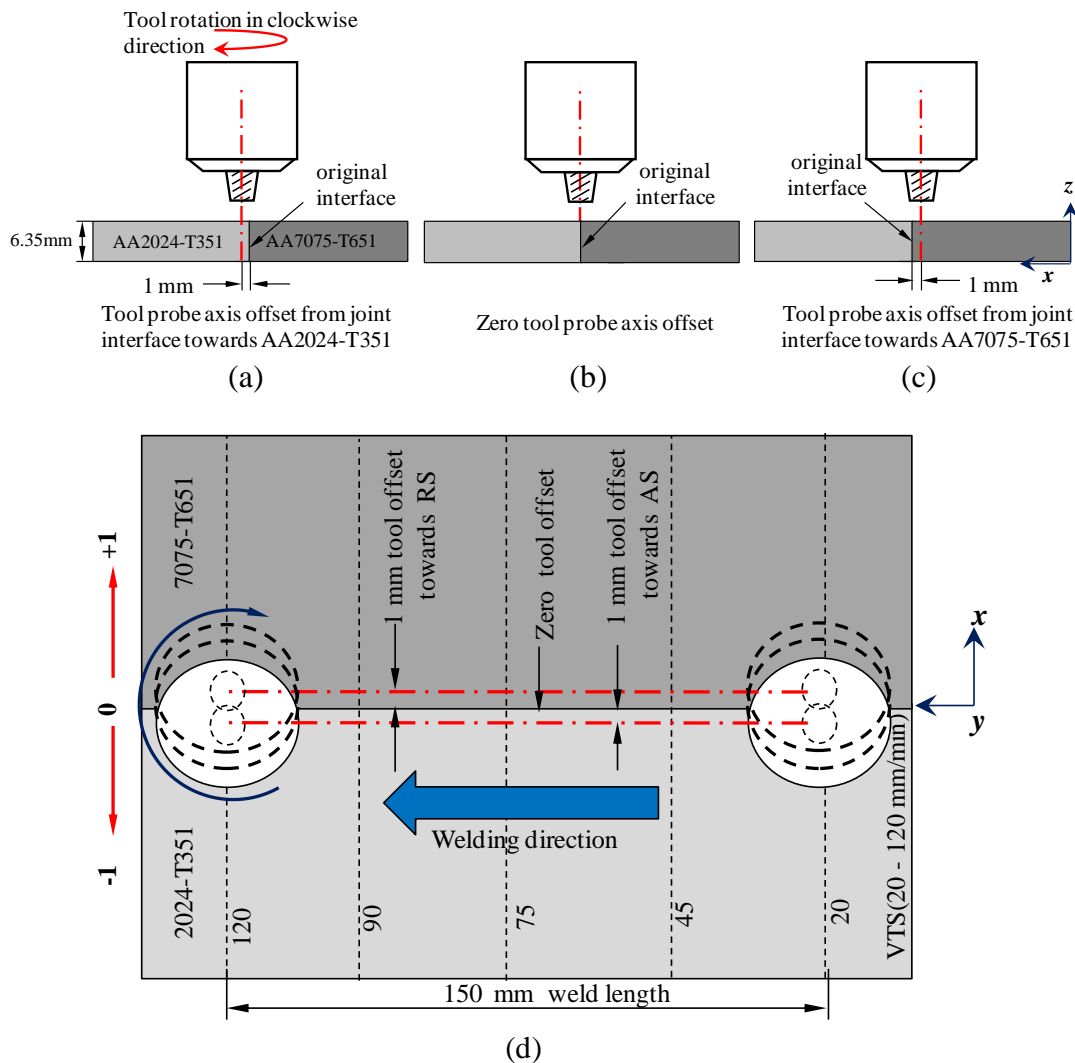


Figure 5.1 Schematic illustrations of tool probe offset and varying the TTS experiment. Tool probe offset of (a) 1 mm towards 2024-T351 (b) 0 mm, zero tool probe offset and (c) 1 mm towards 7075-T651 (d) top view illustrating the experimental procedure.

All the three set of experiment trials are conducted by plunging the TPD to 6.20 mm in the z -direction from the faying surface of the two plates in butt-joint configuration. In the first set, the experiment trial is conducted by considering the tool probe offset distance of 1 mm (indicated as ‘-1’) towards AA2024-T351 from the weld joint line (original joint interface) and by continuously varying the TTS from 20 to 120 mm/min along the weld length of 150 mm as shown in Figure 5.1(a). Similarly, the second and third set of experiment is carried out with zero tool probe offset (indicated as ‘0’) and 1 mm towards AA7075-T651 (indicated as ‘+1’) from the weld joint

interface as shown in the Figure 5.1 (b) and (c), respectively. All the three individual set of experimental procedure are schematically combined and illustrated in Figure 5.1(d). In addition, Figure 5.1(d) depicts the tool rotation direction in CW, tool traverse in the y -direction perpendicular to the rolling x -direction of the two plates fixed in butt joint configuration.

5.2.1 Tensile and microstructure specimen extraction

Figure 5.2 illustrates the schematic of the tensile and microstructure specimens removal layout from the FSW dissimilar aluminium alloys joint of AA2024-T351 and AA7075-T651.

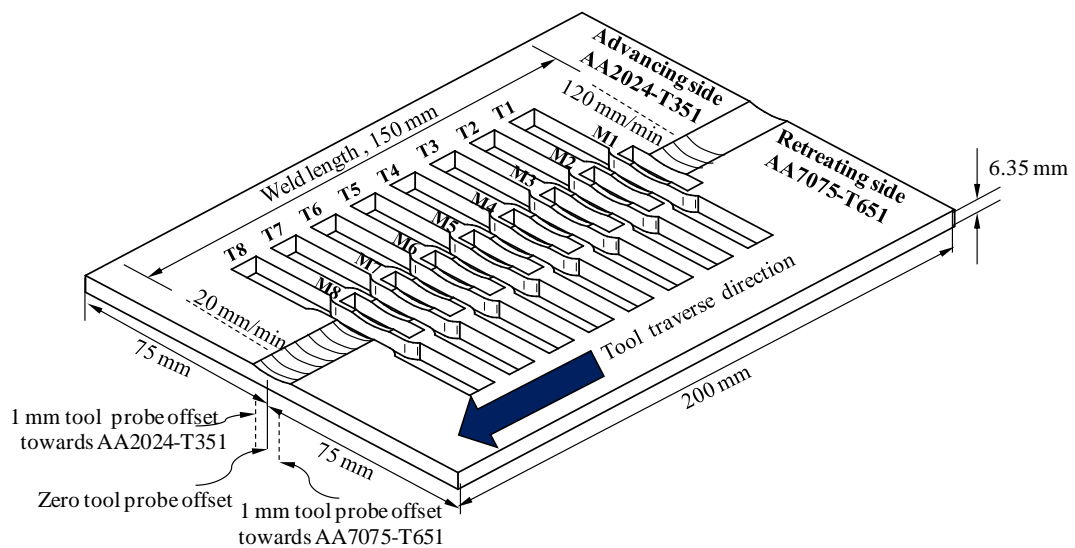


Figure 5.2 Schematic of extraction of tensile specimens (T1-T8) and microstructure specimens (M1-M8) from FSW dissimilar aluminium alloys joint of AA2024-T351 and AA7075-T651 for different tool probe offset conditions.

The tensile specimens are denoted as ‘T’ and microstructure specimens as ‘M’. A wire cut EDM process is used for machining the tensile and microstructure specimens perpendicular to the FSW tool traverse direction, y . The tensile specimens are prepared according to ASTM code of E8M-04 guidelines. Each of the microstructure specimens are removed next to the tensile specimen.

5.3 MECHANICAL TESTING

The tensile properties such as UTS, YS, % EL are measured for the specimens extracted in the AW condition of the FSW dissimilar aluminium alloys joint produced from different tool probe offset conditions and varying the TTS experiments. The details of servo-hydraulic tensile testing machine, experiment condition, test procedure and preparation of tensile specimens standards are given in Chapter 3, Section 3.4.1.

5.4 MACRO AND MICROSTRUCTURE EXAMINATION

The extracted microstructures specimens have been carefully prepared according to the standard metallographic procedure explained in Chapter 3, Section 3.5.1. The details procedure for the investigation of macro and microstructure analysis of the weld joint specimens using OM and SEM machine equipped with EDS are given in the Chapter 3, Section 3.5.2, and Section 3.5.3. The various elemental particle distributions in the WNZ are identified by conducting elemental mapping analysis and compositional characterisation procedure that are explained in Chapter 3, Section 3.5.3 and Section 3.6.1, respectively.

5.5 RESULTS AND DISCUSSION

5.5.1 Macro and microstructure of the joints

The effect of tool probe axis offset positions from the weld joint in conjunction with TTS range 20-120 mm/min on material mixing and flow, grain size at the WNZ, and width of the WNZ of FSW dissimilar aluminium alloys joint of AA2024-T351 to AA7075-T651 are explained in the below section.

5.5.1.1 Effect of tool probe offset towards AA2024-T351 and traverse speed

Figure 5.3 shows macrographs of the cross section of the weld region from the FSW dissimilar aluminium alloys joint produced from the experimental trials for 1 mm tool probe offset condition ('-1') towards AA2024-T351 in conjunction with varying the TTS range 20-120 mm/min.

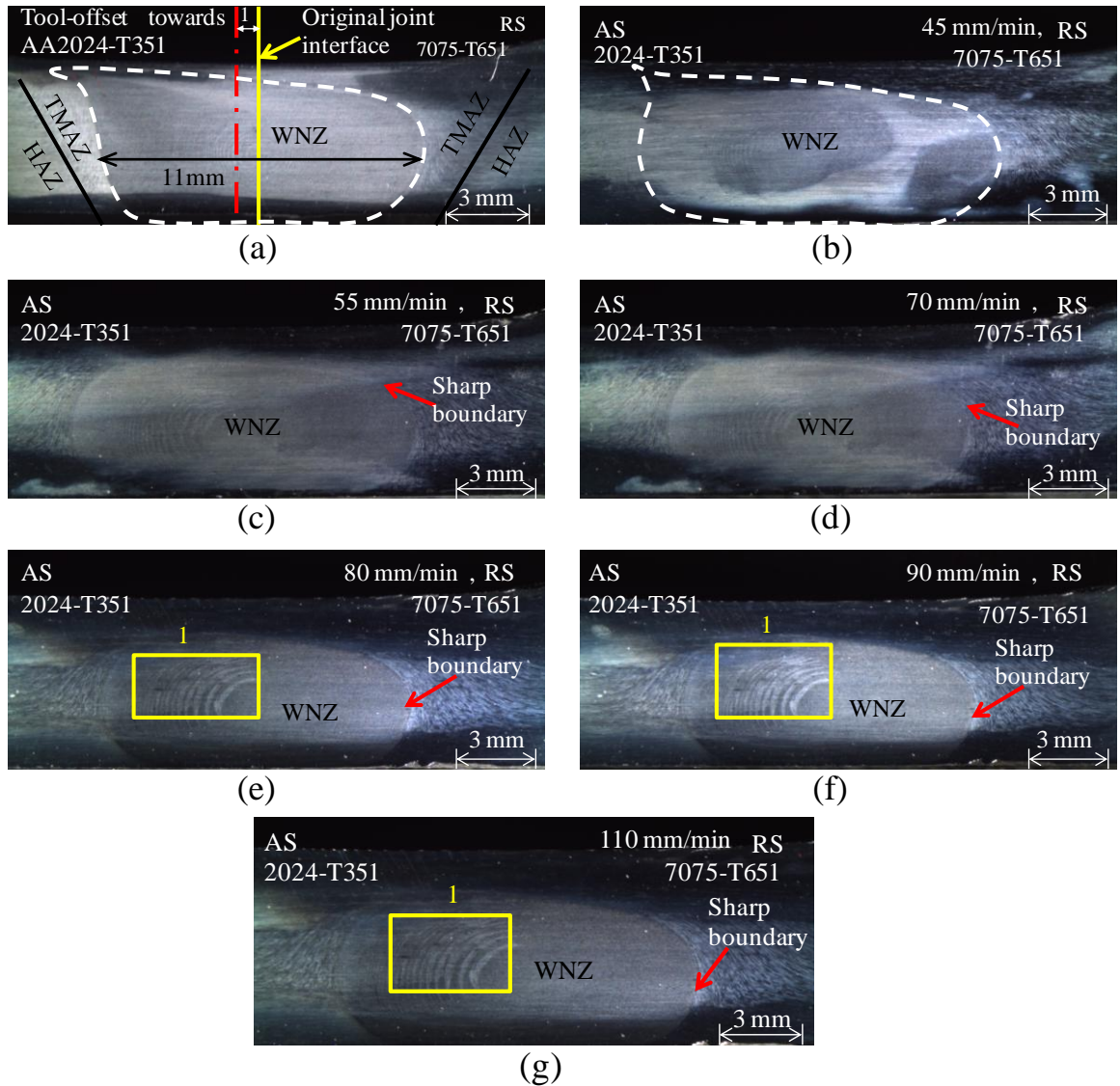


Figure 5.3 Macrographs of FSW dissimilar aluminium alloys joint for tool offset of 1 mm towards AA2024-T351 and VTS range 20-120 mm/min.

As shown in Figure 5.3, the lower TTS range 25- 45 mm/min observes a wider and flat WNZ with intense material mixing as a result of high heat input and plastic flow of both materials (Peel et al., 2003). The increase in the TTS range above 45 mm/min results in the decreased width of WNZ, TMAZ and HAZ due to low heat input and less plastic flow (Peel et al., 2003; Zhang et al., 2015; Li et al., 2014). All the FSW dissimilar aluminium alloys joint weld regions are well consolidated without any internal defects or voids. However, as the TTS increase above 45 mm/min, sharp

boundary defects are observed towards RS between the interface boundaries of WNZ and TMAZ in the weld region. This is due to insufficient diffusion between the two materials. Further, increase in the TTS range above 70 mm/min observes a partial material mixing region at the WNZ shown with a square box marked as '1'. Figure 5.3 (e-g) presents the incomplete material mixing and the majority of the WNZ consists of material kept in the AS i.e. AA2024-T351.

The detailed analysis of the WNZ carried out using SEM are shown in Figure 5.4 (a-j) that depicts an evolution on the mixing state starting from MMR evidenced with intense mixing condition of AA2024-T351 and AA7075-T651 for the lower VTS range 25-40 mm/min. The light etched layers are of AA7075-T651 whereas the dark etched regions are of AA2024-T351. The partially material mixing condition is observed at the AS and bottom of the WNZ for TTS range 45-55 mm/min, followed by UMR condition observed at the RS of the WNZ for the VTS range above 55 mm/min. In the Figure 5.4 (a-b), for TTS of 25 mm/min the WNZ shows intensive mixing, layer-by-layer BS consisting of lamellae pattern of both AA2024-T351 and AA7075-T651 as a result of increase in the tool residence time and stronger stirring of both the alloy (Mastanaiah et al., 2016; Izadi et al., 2013). The classical 'onion ring' structure formation that was observed at the lower TTS range 25 mm/min at the WNZ, could not be seen at the TTS range above 45 mm/min and results in partial material mixing of both the material at the WNZ. The formation of 'onion ring' depends on the heat input. Too low or high heat inputs leads to the vanishing of 'onion ring' structure (Ramachandran et al., 2015) and a more non-uniform WNZ. Thus, the increased TTS in conjunction with tool probe offset towards AS results in non-uniform WNZ with the absence of material mixing.

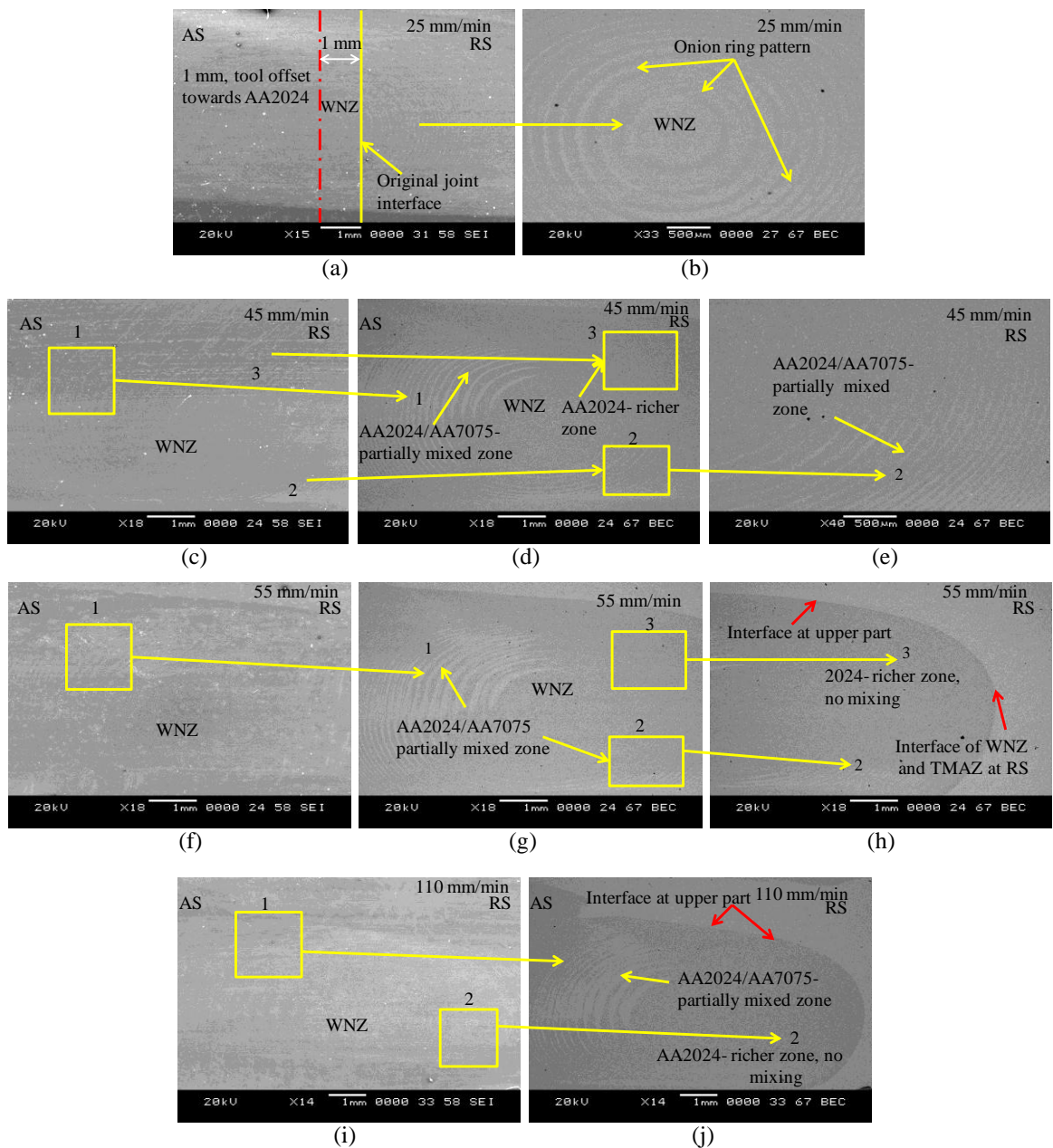


Figure 5.4 SEM images for tool offset of 1 mm towards AA2024-T351 and TTS range 20-120 mm/min.

Figure 5.4 (c-e) produced for TTS of 45 mm/min observes a three distinct region marked as ‘1’, ‘2’, and ‘3’ at the WNZ. The WNZ is mainly composed of material located in the AS (i.e AA2024-T351) and observes a lack of symmetry in material mixing at the WNZ. The AS region marked as ‘1’ in Figure 5.4 (d) and bottom region of WNZ marked as ‘2’ in Figure 5.4 (e) observes a partial mixing of two alloys. The RS marked as ‘3’ in Figure 5.4(d) observes ‘no material mixing’ condition or UMR in

the WNZ consisting of only AA2024-T351. Also, these three distinct regions (marked as 1, 2 and 3) can also be noticed in the BSE images of FSW dissimilar aluminium alloys joint weld region section in Figure 5.4 (h) for TTS of 55 mm/min. Thus, with the increase in TTS the WNZ does not contain any alternate layers of AA2024-T351/AA7075-T651. Further increase in the TTS to 110 mm/min, Figure 5.4 (i-j) observes a UMR marked as '2' in the RS of WNZ. During tool traversing, the softened material in the leading edge moves to the trailing edge with the advance of the tool in y-direction and tool rotation in CW direction (Khodir et al., 2008). These movements of the material from leading edge to the trailing edge depends upon the amount of heat generated thereby amount of material softened (Alvarez et al., 2010).

Observing Figure 5.4 (a-j), the three regions (marked as 1, 2, and 3) observed at the WNZ is attributed to the tool probe offset condition ('-1') and varying the TTS. As the tool probe is offset towards AA2024-T351, the amount of heat acting on the higher strength alloy i.e AA7075-T651 is less. In addition, the proportion of heat generated at the WNZ reduces with the increase in the TTS. As a result, the flow stresses on the high strength material AA7075-T651 increases causing a reduced amount of material flow from leading edge to the trailing edge. Thus, the WNZ observes a partial material mixing ratio with increase in the TTS. In addition, the increase of the TTS above 55 mm/min the RS of the observes a sharp interface boundary between WNZ to TMAZ in the RS and in upper part of the WNZ (Figure 5.4 (h-j)). These sharp boundaries acts as a region of discontinuity and fracture can occur at these points leading to the early failure of the joints.

The various elemental particle distributions in the WNZ are identified by conducting elemental mapping analysis as shown in Figure 5.5 (a-d). Figure 5.5 (e) shows EDS analysis for tool probe offset of 1 mm towards AA2024-351 and TTS of 110 mm/min. In Figure 5.5 (b), the major portion of the WNZ consists of Cu, which is major constituent from 2024-T351 and absence of Zn element a major constituent from the 7075-T651 material. Thus, the WNZ represents a 'no mixing'. In Figure 5.5 (e), the EDS elemental analysis at the WNZ consists of 93.24 Wt.% Al, 2.53 Wt.% Mg and 4.23 Wt.% of Cu.

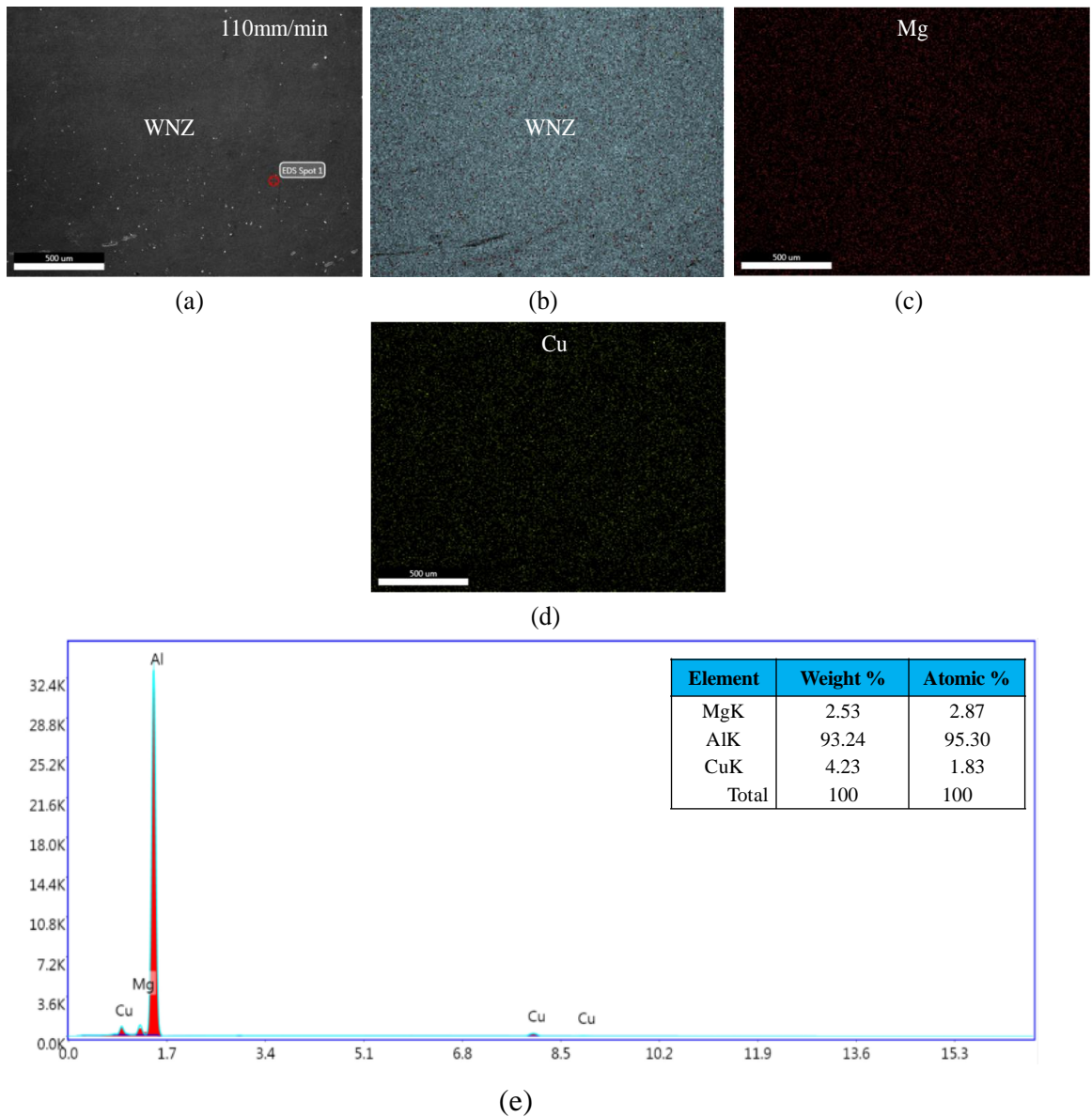


Figure 5.5 (a)-(d) Mapping elemental analysis and (e) EDS elemental analysis in the WNZ of the sample welded for tool probe offset of 1 mm towards 2024-T351 and for TTS of 110 mm/min.

5.5.1.2 Effect of zero tool probe offset and traverse speed

The macrographs for the zero tool probe offset condition (i.e. '0') for TTS range 20-120 mm/min are shown in Figure 5.6. Figure 5.6 (a) and (b) observes a flat and wide WNZ, TMAZ and HAZ for lower TTS range 25-45 mm/min. However, for the TTS range 45-120 mm/min the WNZ observes reduction in the width and a classical

formation of ‘onion rings’. However, these ‘onion rings’ are not identical in shape and depends on the TTS.

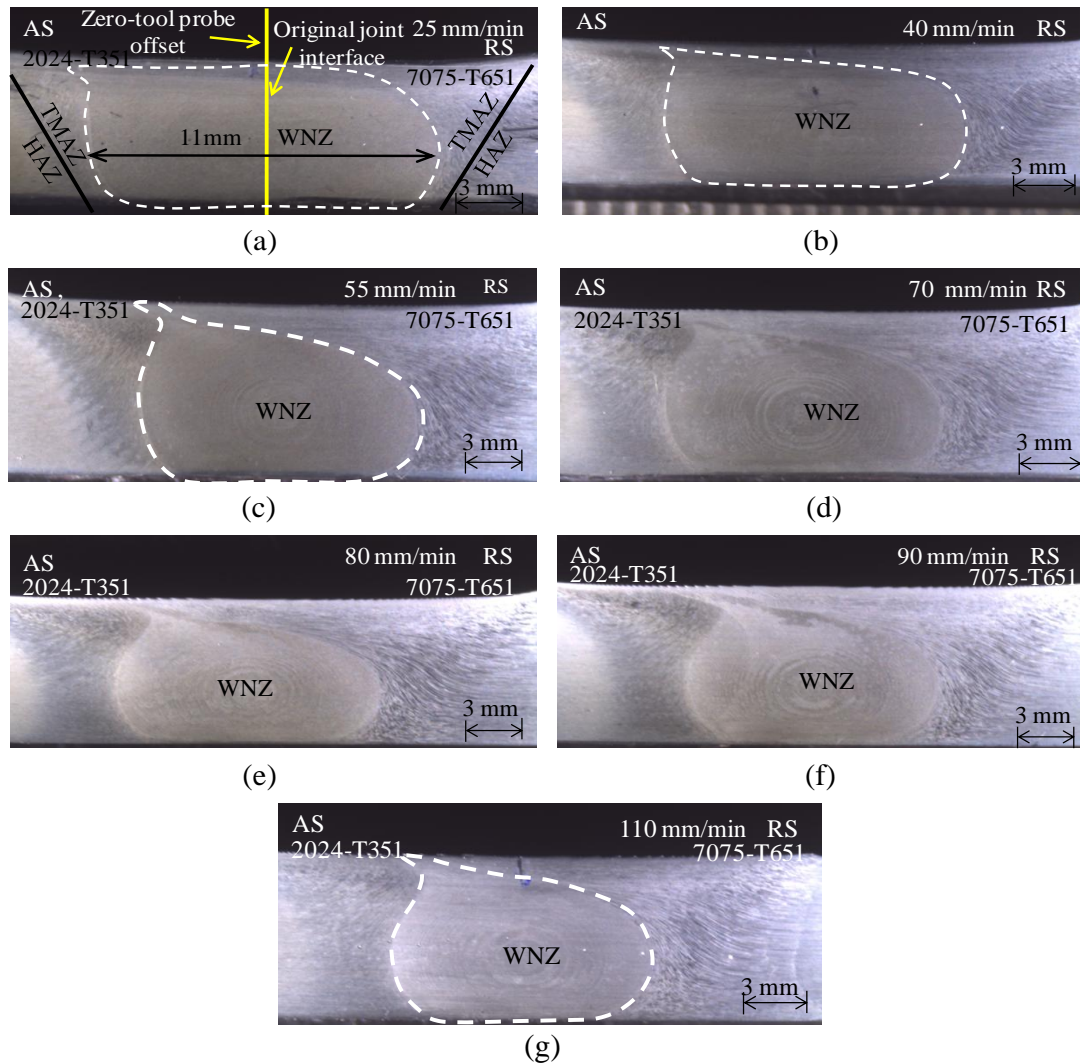


Figure 5.6 Macrographs of FSW dissimilar aluminium alloys joint for zero tool probe offset and TTS range 20-120 mm/min.

Figure 5.7 (a-e) depicts SEM images of microstructures of the WNZ of the FSW dissimilar aluminium alloys joint produced for zero tool probe offset condition and TTS range 20-120 mm/min. It can be observed from Figure 5.7 (a-e) that the WNZ is well developed with intense mixing of both the alloys AA2024-T351 and AA7075-T651 for all the TTS range 20-120 mm/min. The mixing of both the alloys appears as an ‘onion ring’ pattern.

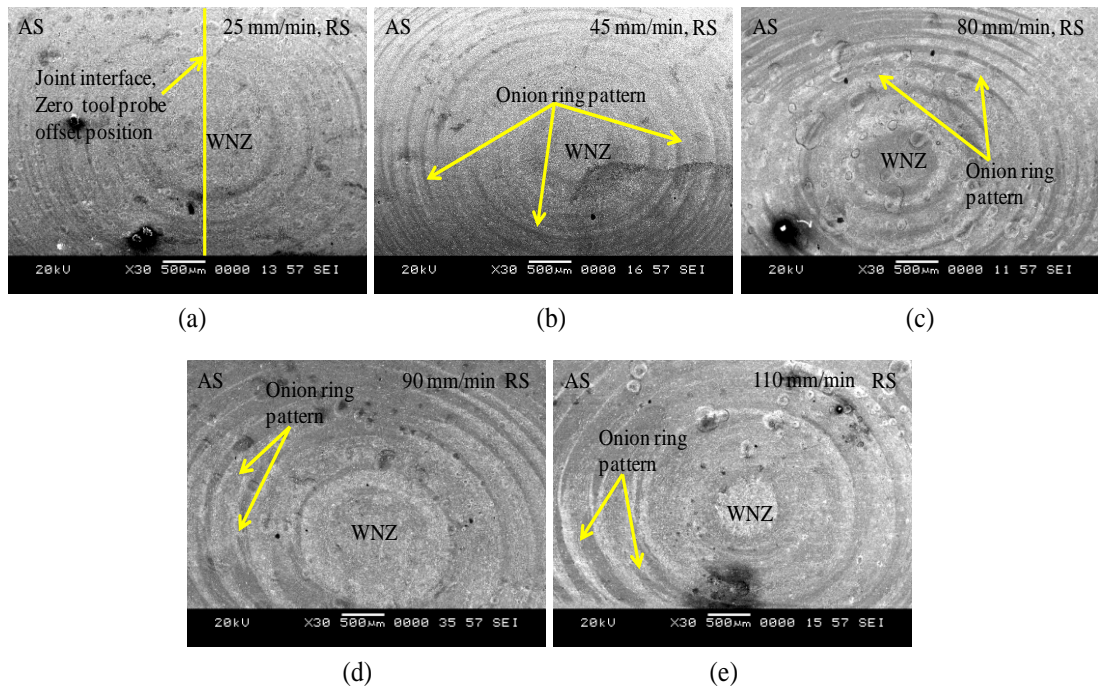


Figure 5.7 (a)-(e) SEM images for zero tool probe offset distance and TTS range 20-120 mm/min.

In the zero tool probe offset condition, as the tool axis exactly coincides with the weld joint interface, the equal amount of faying surface of both the materials of plates AA2024-T351 and AA7075-T651 come in contact beneath the tool shoulder and pin. The heat generated by rotating action of both tool shoulder and plunged tool pin results an equal amount of heat exposure on both the materials kept in AS and RS. Analyzing the cross sections of the welds as shown in Figure 5.7 (a-e), the AA7075-T651 in the RS is extruded and pushed towards the inside of the WNZ. These materials are dragged by the shoulder and mixed around the threaded tool pin and flow from top to the bottom of WNZ forming an axis symmetry consisting of alternate lamellae band pattern of both AA2024-T351 and AA7075-T651 materials. Compared to the tool probe offset of 1 mm towards AA2024-T351, the material mixing of AA2024-T351 and AA7075-T651 shows improvement in the zero tool probe offset. Thus, it indicates that material mixing between the two materials mainly controlled by a tool probe offset condition (Galvão et al., 2012).

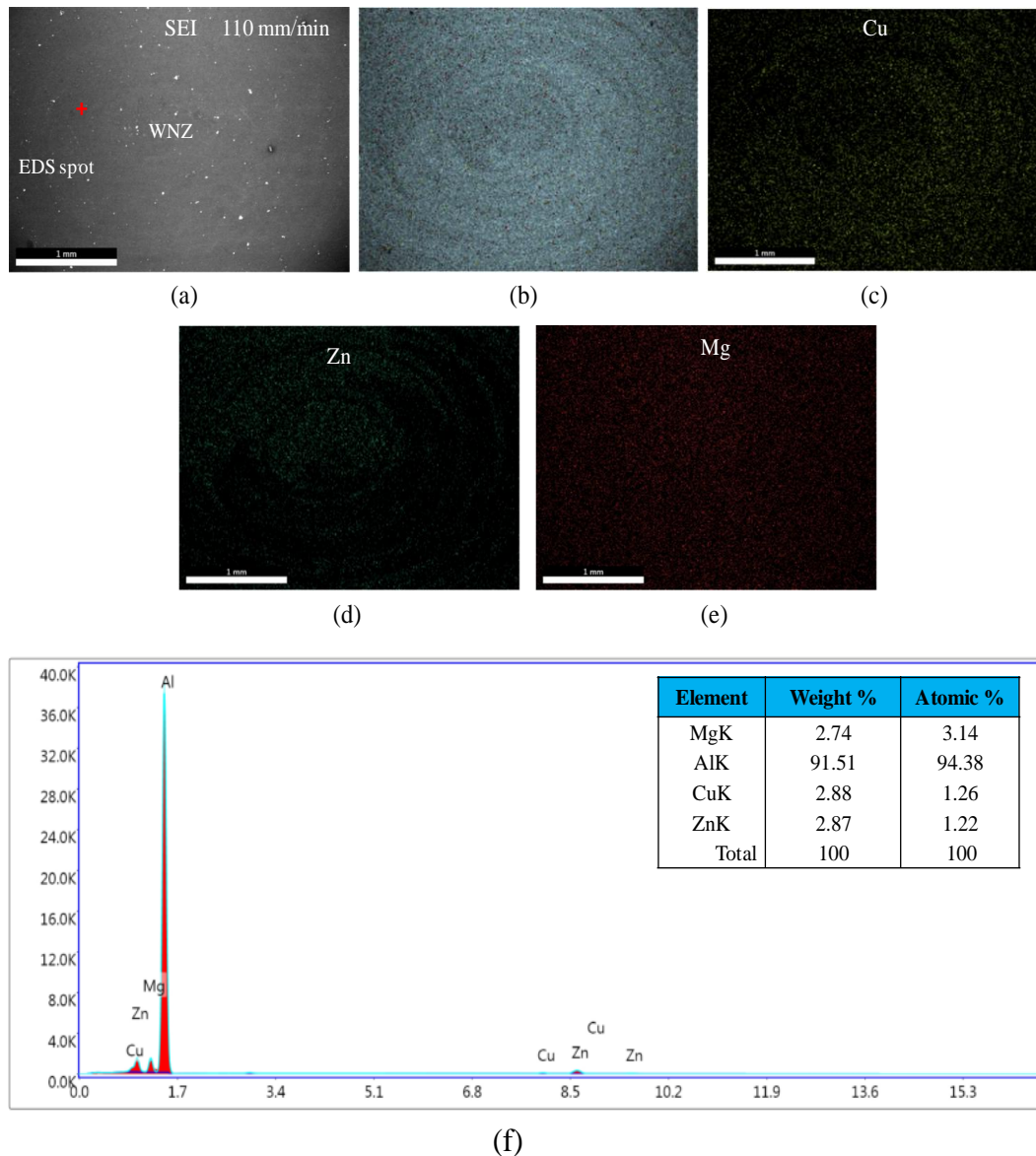


Figure 5.8 (a)-(e) Mapping elemental analysis and (f) EDS elemental analysis in the WNZ of the sample welded for zero tool probe offset and for TTS of 110 mm/min.

Figure 5.8 (a-e) shows the elemental mapping analysis and Figure 5.8 (f) shows EDS elemental analysis for the zero tool probe offset and for TTS of 110 mm/min. Figure 5.8 (b) presents the flow of AA2024-T351 and AA7075-T651 at the WNZ that can be easily observed, and are represented by the grey dark and light areas, respectively. This indicates that the Cu and Zn from AA2024-T351 and AA7075-T651 were uniformly distributed at the WNZ and is attributed to the proper mixing of both the alloy at the zero tool probe offset condition. One can observe from Figure 5.8 (c), the

WNZ consists of element Cu, the major contribution from AA2024-T351 kept at the AS. Similarly, in Figure 5.8 (d) the WNZ consists of element Zn a major alloying element of AA7075-T651 kept at RS. During the FSW process by zero tool probe offset, the tool shoulder and pin exactly coincide at the weld joint interface making both the material faying surface come in equal contact with the tool geometry. Thus, the heat generated by friction between the tool shoulder and the materials helps in plasticizing an equal amount of both the materials and as a result, both the aluminium alloy materials are dragged at an equal amount towards the WNZ. Figure 5.8 (f) shows the EDS elemental analysis of the point marked as '+' (Figure 5.8 (a)) reveals that the gray darker layer contained about 91.51 Wt.% Al, 2.74 Wt.% Mg and equal 2.87 Wt.% of Cu and Zn.

5.5.1.3 Effect of tool probe offset towards AA7075-T651 and traverse speed

The macrographs of the cross section of the weld region of the FSW dissimilar aluminium alloys joint produced for tool probe offset condition of 1 mm ('+1') towards AA7075-T651 for the TTS range 20-120 mm/min is shown in Figure 5.9 (a-g) and corresponding high magnified SEM images are shown in the Figure.5.11 (a-i).

Figure 5.9 (a-g) presents the change in the shape of the WNZ is in accordance with the TTS range 20-120 mm/min that results in variation in the heat input to the weld region. Thus, the width of WNZ measuring 11 mm observed at the lower TTS gradually decrease with increase in the TTS. It can be seen from the SEM images shown in Figure 5.11 (a-c), the lower TTS range 25-45 mm/min results in a well developed WNZ composed of banded alternate lamellae pattern of AA2024-T351 and AA7075-T651 which resembles classical 'onion ring' structure. However, with the increase in the TTS range above 55 mm/min the material mixing and composition at the WNZ changes (Figure 5.11 (d-i)) and the amount of material drawn from the RS increases that result in WNZ losing its symmetry about the weld centreline. For the same TTS parameters, unlike as seen for the tool probe offset 1 mm towards AA2024-T351 (Figure 5.4 (a-j)), the mixing state of the two alloys at the WNZ for tool probe offset 1 mm towards AA7075-T651 appears to be a different and composed the

material mainly located at the RS (AA7075-T651). As shown in Figure 5.11 (d- i), there has been a bulk transference of AA7075-T651 material from RS to the AS.

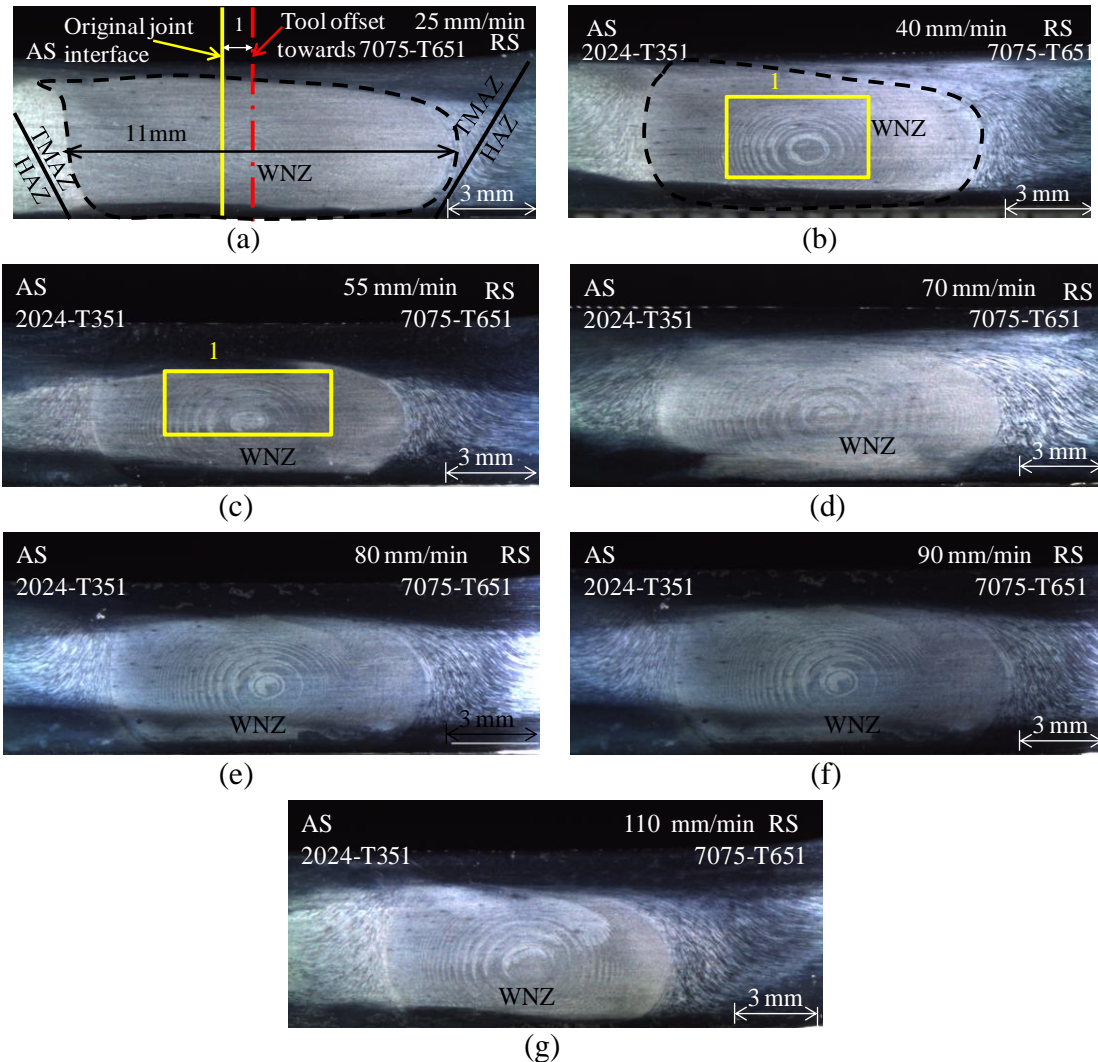


Figure 5.9 (a)-(g) Macrographs of weld section of FSW dissimilar aluminium alloys joint for tool probe offset of 1 mm towards AA7075-T651 and VTS range 20-120 mm/min.

The tool probe offset is considered as one of the important parameters in controlling the mixing of two dissimilar materials ratio at the WNZ and weld quality of the joints (Sahu et al., 2016; Yaduwanshi et al., 2018). The tool probe offset towards RS helps the material AA7075-T651 placed in the RS being dragged to the AS by the shoulder to the trailing side of the tool.

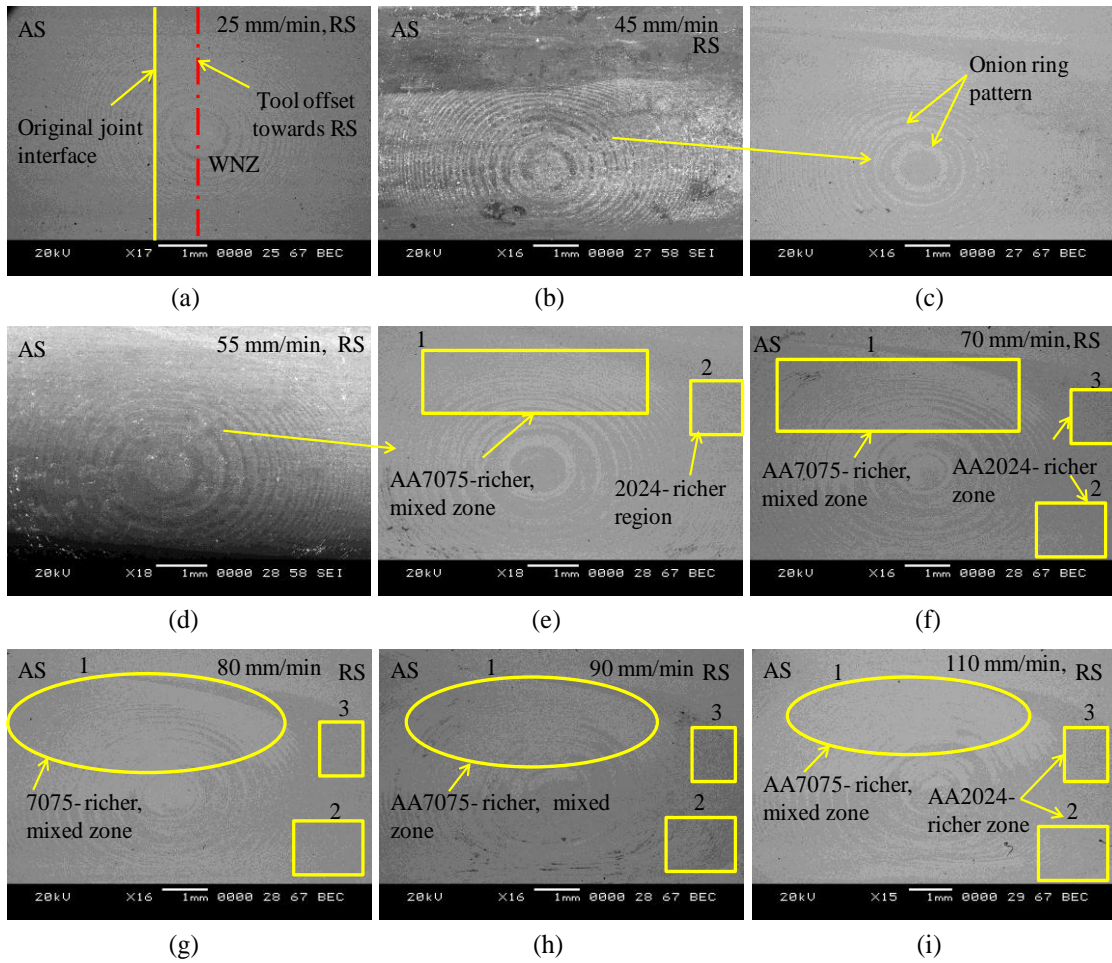


Figure 5.11 SEM images for tool offset of 1 mm towards AA7075-T651 and TTS range 20-120 mm/min.

As it could be seen in the SEM images Figure 5.11(d- i), the material AA7075-T651 transport from the RS towards AS occurs at the top of the WNZ. One can observe from the BSE images of Figure 5.11(c), at lower TTS of 45 mm/min, the gap between the alternate lamellae pattern of the two alloys is clearly visible in the WNZ and above it. However, with further increase in the TTS above 55 mm/min, the lamellae pattern observed at the top of WNZ becomes dense and separation between them diminishes with the increase in the TTS. Since the two aluminium alloys is having different etching responses, the material flow from both the AS and RS can be clearly visible in the WNZ. Judging from the etching response, it can be seen from BSE images in the Figure 5.11 (d- i) the area marked as '1' at the top side of the WNZ consists mainly AA7075-T651. Similarly, the area marked as '2' at the bottom of

WNZ and '3' at the RS of the WNZ mainly consists of mainly AA2024-T351. The harder AA7075-T651 kept in the RS is dragged towards AS and against comparatively softer AA2024-T351. Galvao et al. (2010) reports the similar observation.

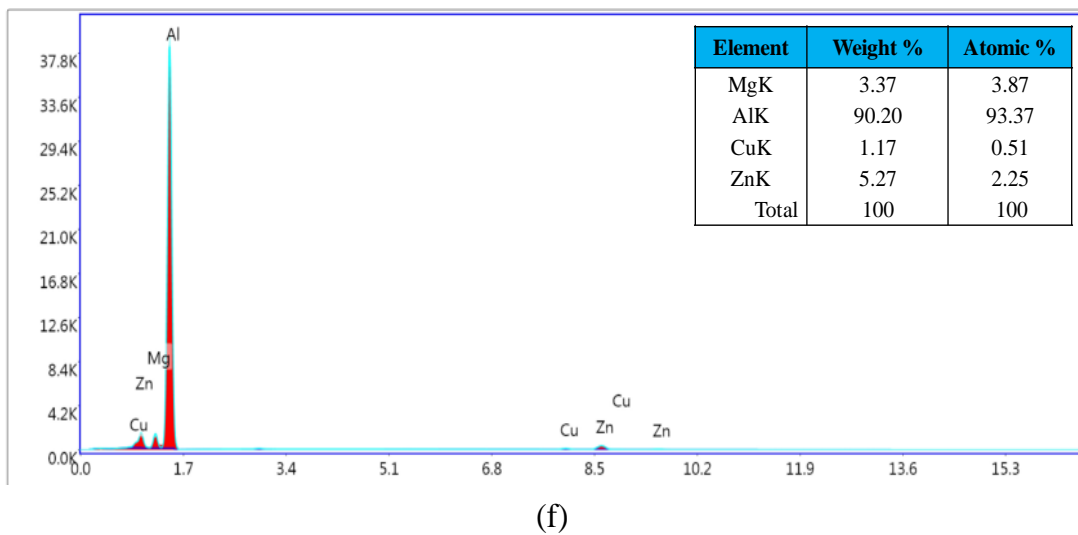
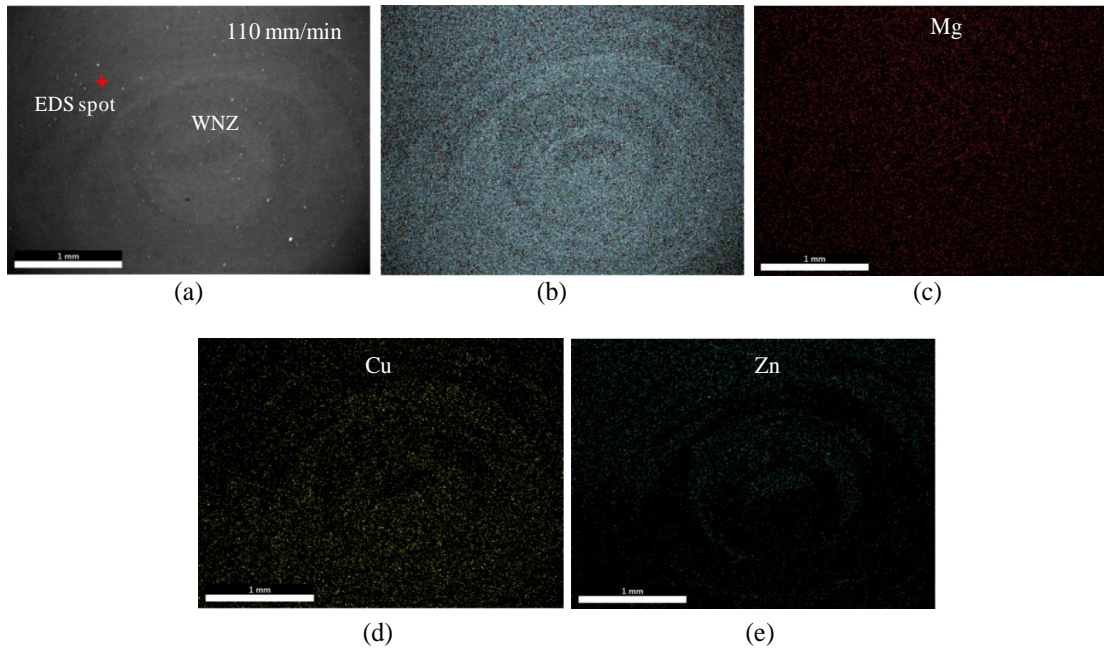


Figure 5.12 (a)-(e) Mapping elemental analysis and (f) EDS elemental analysis in the WNZ of the sample welded for tool probe offset of 1 mm towards AA7075-T651 and for TTS of 110 mm/min.

Figure 5.12 (a-e) shows the elemental mapping analysis and the Figure 5.12 (f) presents EDS elemental analysis for the tool probe offset of 1 mm towards 7075-T651

and for TTS of 110 mm/min. One can observe from Figure 5.12 (a-e) consisting of proper mixing of both the material at the WNZ for the higher TTS of 110 mm/min. The EDS elemental analysis at the WNZ consists of 90.2 Wt.% Al, 3.37 Wt.% Mg, 1.17 Wt.% of Cu and 5.27 Wt.% Zn. The presence of higher Wt.% of Zn indicates that WNZ consists of more amount of AA7075-T651 whose major alloying element is Zn. Therefore, the distribution of Cu and Zn is well documented even for higher TTS of 110 mm/min and the presence of higher Wt.% of Zn indicates that more amount of AA7075-T651 has occupied the WNZ. Thus, the tool probe offset plays a main important parameter that directly influences the flow of material and the final WNZ composition.

5.5.1.4 Effect of tool probe offset and traverse speed on grain size

The Figure 5.13 (a-c) shows the grain size measurement at the WNZ obtained from the microstructure sample specimen produced for TTS of 25 mm/min, 55 mm/min and 110 mm/min, respectively, and for tool probe offset condition of 1 mm towards AA2024-T351.

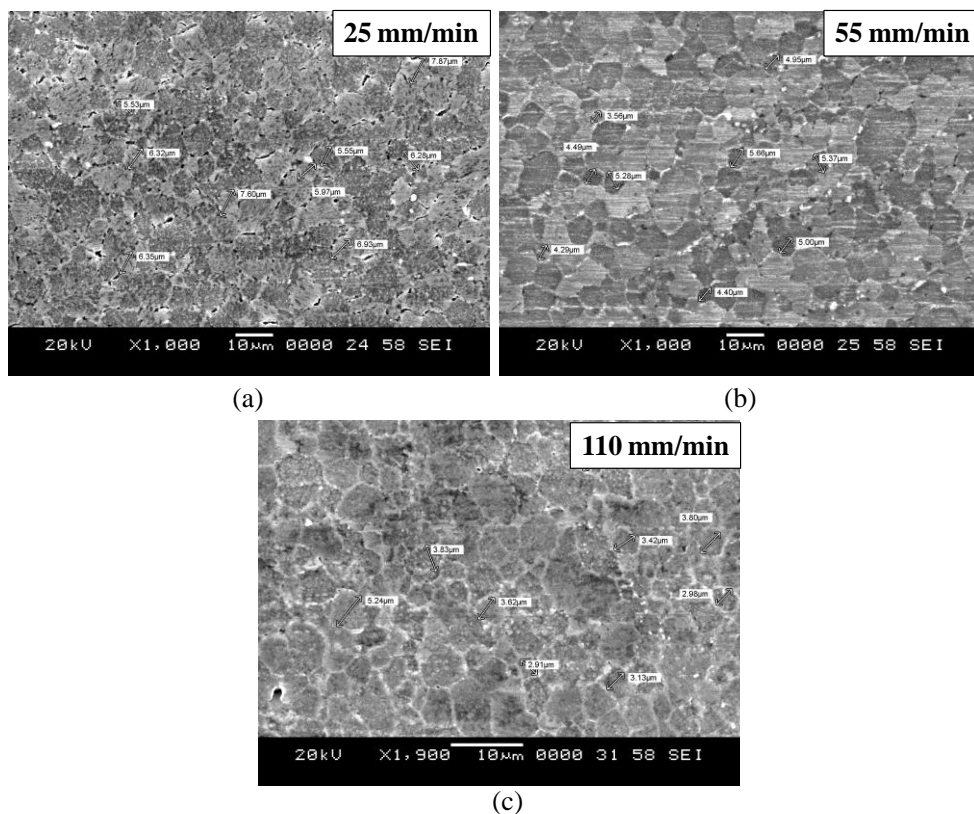


Figure 5.13 (a)-(c) Grain size at the WNZ for tool probe offset of 1 mm towards AA2024-T351.

Figure 5.13 (a) shows higher grain size range 5.5 - 7.5 μm in the WNZ. As expected this is due to the higher heat input generation and severe plastic deformation (SPD) of the material during FSW of dissimilar joints (Peel et al., 2003; Zhang et al., 2015). As the TTS increased from 25 mm/min to 55 mm/min, the WNZ observes a decrease in grain size and range between 3.5 - 5.5 μm . Further increase in the TTS result decrease in average grain size range 3 - 4 μm . This decrease in the grain size with the increase in the TTS is attributed to the lower heat input the WNZ.

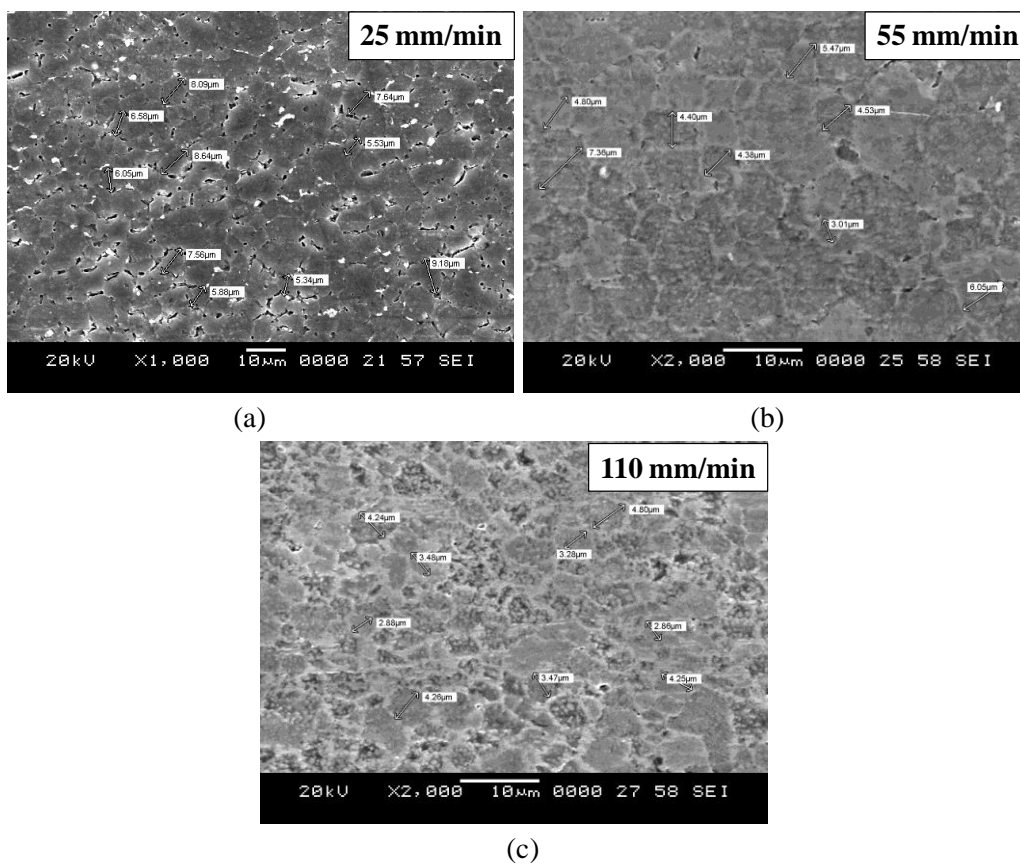


Figure 5.14 (a)-(c) Grain size at the WNZ for zero tool probe offset. A similar observation with regard to the grain size at the WNZ with changing TTS range 20-120 mm/min is presented in the Figure 5.14 (a-c) and Figure 5.15 (a-c) for the zero tool probe offset and with offset distance of 1 mm towards AA7075-T651, respectively. Comparing the Figure 5.13, Figure 5.14 and Figure 5.15, it can be observed that irrespective of tool probe offset conditions, the microstructure at the WNZ of all the FSW dissimilar aluminium alloys joint consists of grains that are almost similar in size for the TTS range 20-120 mm/min.

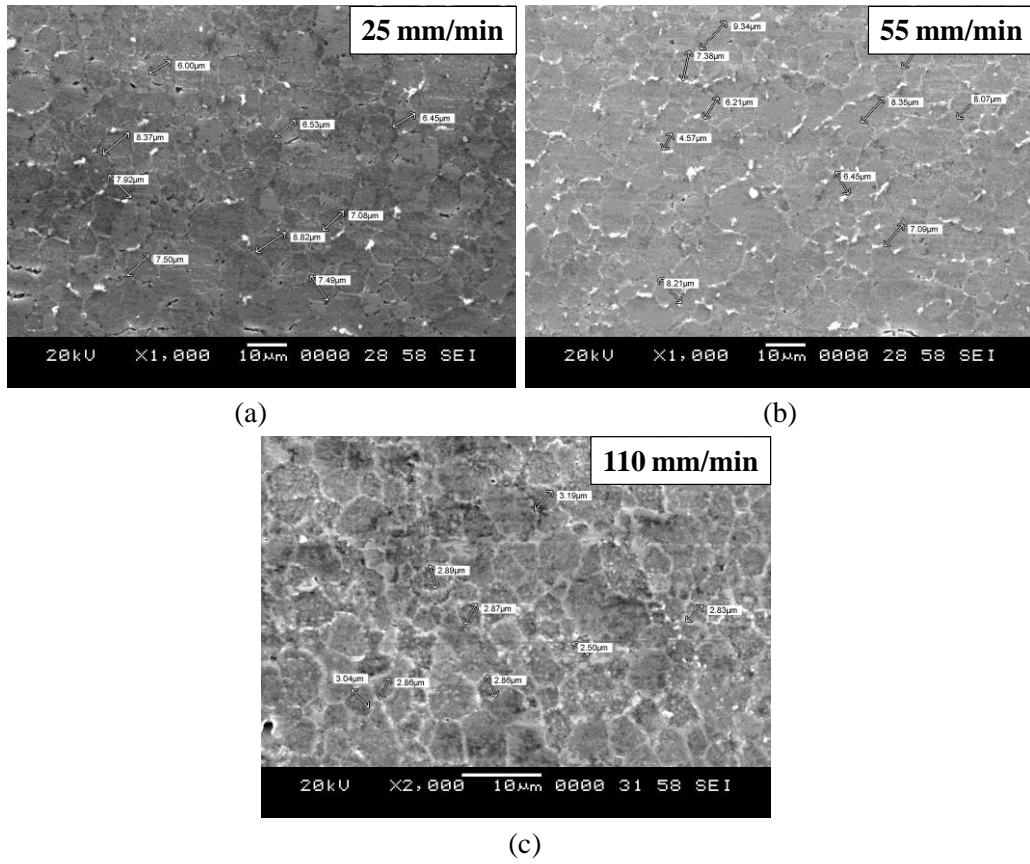


Figure 5.15 (a)-(c) Grain size at the WNZ for tool probe offset of 1 mm towards 7075-T651.

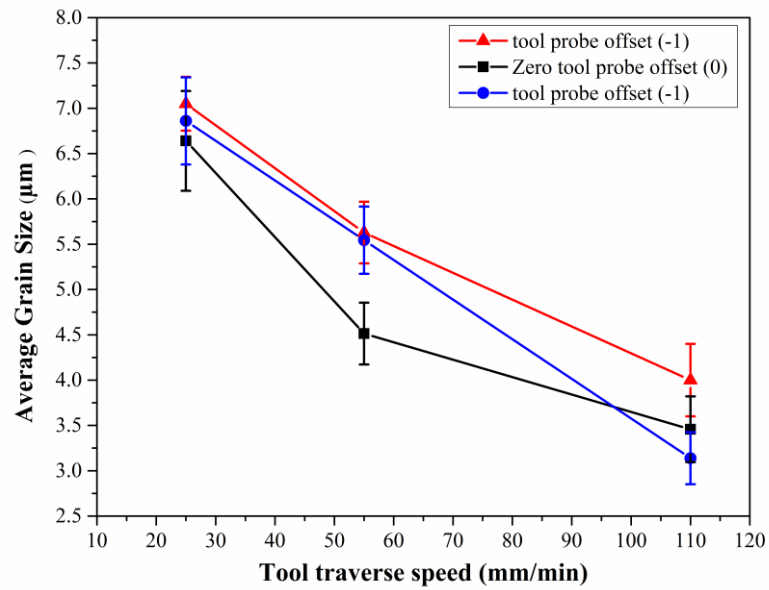


Figure 5.16 Average grain size for the different tool probe offset conditions and for TTS range 20-120 mm/min.

Figure 5.16 shows graph plot for the average grain size calculated using image-J analysis and line interception method for each set of tool probe offset condition (-1, 0, +1) for the TTS of 25, 55 and 110 mm/min. For line interception method, higher magnification SEM images for each case of tool probe offset are used and the number of grains present over the length of the lines drawn on SEM images are calculated for ten trials. One can observe from the Figure 5.16, irrespective of different tool probe offset condition, the average grain size follows the same tendency of decreasing in size of the grain in accordance to the increasing the TTS from 25 to 110 mm/min.

5.5.2 Tensile properties

The specimen extracted from the FSW dissimilar aluminium alloys joint produced from the different tool probe offset conditions (-1, 0, +1) with varying TTS range 20-120 mm/min are tested for tensile properties of UTS, YS and % EL. The tensile specimen preparation, details of the tensile testing machine and testing procedure are explained in Chapter 3, Section 3.4.1.

5.5.2.1 Effect of tool probe offset towards AA2024-T351 on tensile properties

Figure 5.17 shows the variation of tensile properties for the tool probe offset 1 mm towards AA2024-T351 with TTS range 20-120 mm/min. Figure 5.17 for the TTS range 25-45 mm/min, the FSW dissimilar aluminium alloys joint have shown lower tensile properties and are almost constant. The lower UTS of 347- 356 MPa, YS of 210-264 MPa and %EL of 8.6-11.6 was observed for the VTS 20-45 mm/min due to the increasing tool residence time. Even though the WNZ at lower TTS observes a proper mixing (Figure 5.4 (a) and (b)) of both the materials, higher the heat input to the WNZ results in dissolution of the strengthening precipitates and softening of the WNZ, and yields lower tensile properties for the FSW joints (Li et al., 2014; Peel et al., 2003; Zhang et al., 2015). Further, the increase in the TTS range above 50 mm/min has shown a decrease in the tensile properties. The UTS, YS and % EL has shown decreasing trend in the range from 329-253 MPa, YS from 210-165 MPa, % EL from 7.5-5.3 with the increase in the TTS range 65-110 mm/min. Lower UTS of

253 MPa, YS of 165 MPa, % EL of 5.3 are observed for the FSW dissimilar aluminium alloys joint produced for the TTS of 110 mm/min.

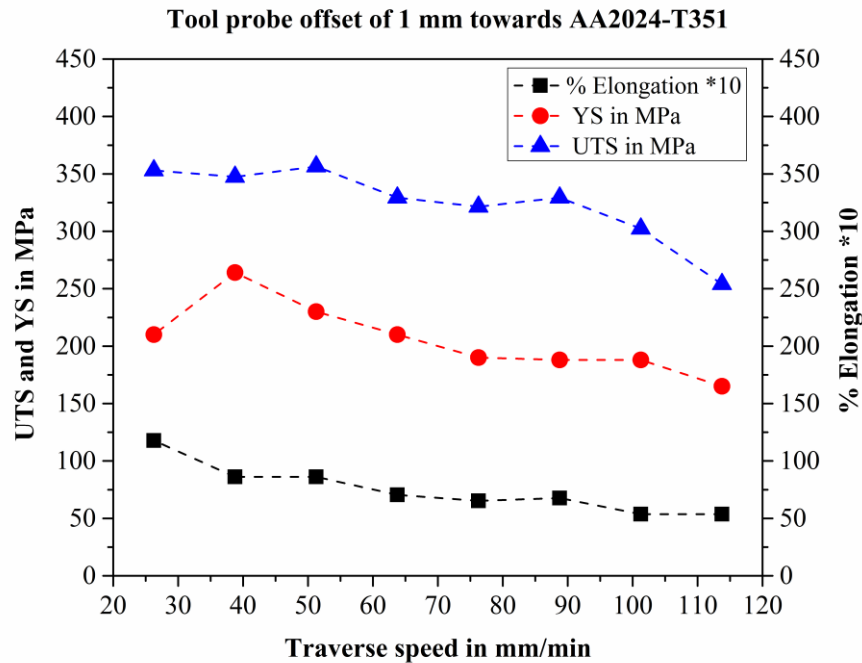


Figure 5.17 Variation of tensile strength for tool probe offset of 1 mm towards AA2024-T351 for the TTS range 20 - 120 mm/min.

In general, at lower TTS, the increase in the tool residence time results in higher heat input, softened WNZ and yields lower tensile properties of the weld joint. Higher TTS results in a reduction in the heat input to the weld region and yields higher tensile properties compared to the FSW joints fabricated with the lower TTS (Li et al., 2014; Peel et al., 2003; Zhang et al., 2015). However, from Figure 5.17, one can observe that with the increase in the TTS, the tensile properties have shown a decreasing trend. This is due to the tool probe offset into the AS results in higher temperature compared to the RS and local temperature determines the weld strength (Cole et al., 2014). Thus, the tool probe offset into the AA2014-T351 results in lower tensile properties. In addition, the increase in the TTS results in a reduction of MMR at the WNZ leading to the decreased tensile properties of the FSW joint. Thus, the FSW dissimilar aluminium alloys joint tensile strength for tool probe offset towards AA2024-T351 condition are influenced by both TTS and mixing of the two materials

AA2024-T351 and AA7075-T651. Tool probe offset towards AA2024-T351 and increase in the TTS results in low heat input to WNZ leading to the lack of metallurgical bonding between two materials (Rajakumar et al., 2011). In addition, since the tool probe is offset towards the AA2024-T351, the material kept in RS (AA7075-T651) experiences a lack of heat input and results in the decreased material flow from the RS to the AS and poor mixed flow of two materials. As a result, the major portion of the material in the WNZ region consists of AA2024-T351 and results in poor metallurgical bonding between the two materials that leads to a sharp boundary (Figure 5.3). Thus, the FSW dissimilar aluminium alloys joint fabricated with tool probe offset towards AA2024-T351 and TTS range 20-120 mm/min have shown lower UTS, YS and %EL with the increase in TTS. Thus, the reduction in the heat input to the WNZ due to the increase in the TTS does not always guarantee the increased tensile properties, rather the presence of the dominant material and mixing of both the material plays an important role.

5.5.2.2 Effect of zero tool probe offset on Tensile properties

Figure 5.18 shows the variation of tensile properties of the tested specimen of FSW dissimilar aluminium alloys joint produced for zero tool probe offset with TTS range 20-120 mm/min. Initially, the zero tool probe offset and lower TTS of 25 mm/min yields in lower UTS of 290 MPa, YS of 170 MPa and % EL of 4.72 MPa. However, with the increase in the TTS above 40 mm/min, the tensile properties found to follow an increasing trend. Higher UTS of 419 MPa, YS of 238 and % EL of 12.3 was observed for the FSW dissimilar aluminium alloys joint produced for zero tool probe offset with TTS of 110 mm/min. The increase in the tensile properties is attributed to the intense mixing of the two alloys as shown in Figure 5.7 (a-e) (Dinharan et al., 2012; Palanivel et al., 2012; Amancio-Filho et al., 2008). In general, the WNZ consists of MMR, UMR and mixed flow region. Mixed flow is required in order to produce sound weld joints without any defects. During the zero tool probe offset condition, an equal amount of contact surface of tool shoulder and pin is established with the faying surface of the dissimilar materials along the weld joint line. As a result, an equal amount of material placed in the AS and RS is expected to flow towards WNZ and there by contributing in proper material mixing of both the

materials consisting of alternate lamellae pattern of AA2024-T351 and AA7075-T651.

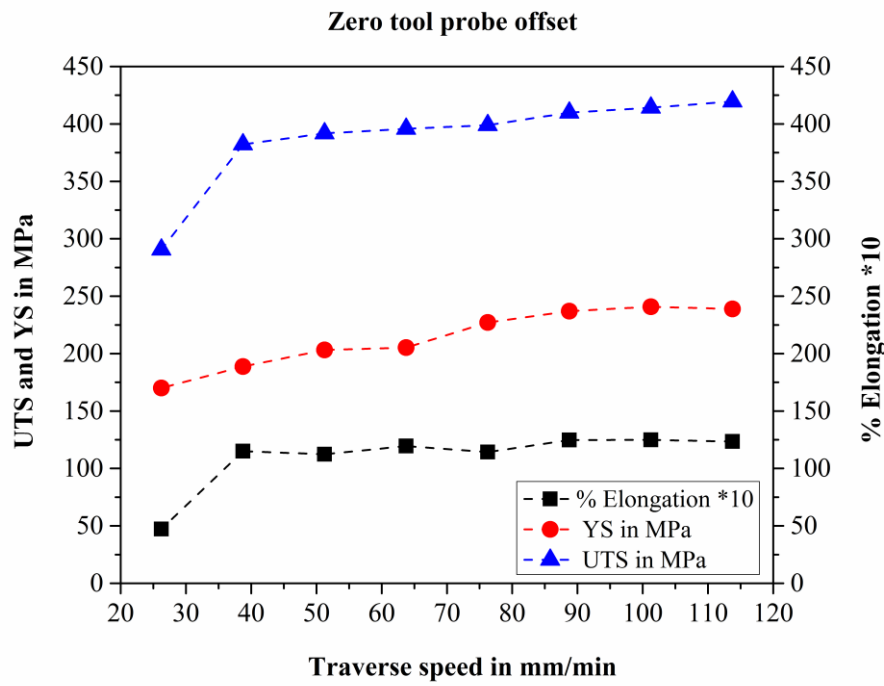


Figure 5.18 Variation of tensile strength for zero tool probe offset and for the TTS range 20 - 120 mm/min.

Figure 5.18 shows the increasing trend in UTS, YS and % EL with the increase in the TTS. The tested tensile specimens from FSW dissimilar aluminium alloys joint produced by zero tool probe offset and TTS range 20-120 mm/min exhibits higher tensile properties compared to the joint produced from tool probe offset of 1 mm towards AA2024-T351. Further, both the zero tool probe offset and increase in the TTS has an influence on the tensile properties of the weld joint. If the zero tool probe offset results in proper MMR, on the other hand, increase in the TTS reduces the heat input to the weld region and yields higher tensile properties.

5.5.2.3 Effect of tool probe offset towards AA7075-T651 on tensile properties

Figure 5.19 shows the tensile properties of tested specimen produced from the FSW dissimilar aluminium alloys joint produced for the tool probe offset of 1 mm towards AA7075-T651 with TTS range 20-120 mm/min. Initially, the specimens produced for the tool probe offset of 1 mm towards AA7075-T651 with lower TTS of 25 mm/min

yields lower UTS of 205 MPa, YS of 140 MPa and % EL of 9.7. However, with the increase in the TTS above 40 mm/min, the tensile properties found to follow an increasing trend and higher UTS of 435 MPa, YS of 375 MPa and % EL of 13.6 were observed for a tested tensile specimen of FSW dissimilar aluminium alloys joint produced for TTS of 110 mm/min.

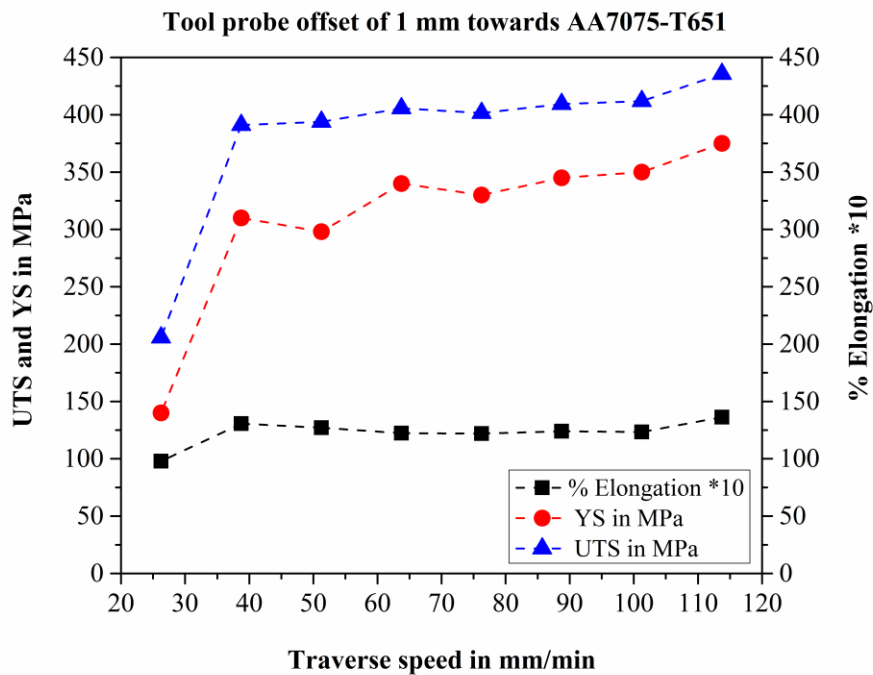


Figure 5.19 Variation of tensile strength for tool probe offset 1 mm towards AA7075-T651 and for the TTS range 20 - 120 mm/min.

Many researchers (Khodir et al., 2008; Guo et al., 2014; Park et al., 2010; Lee et al., 2003) in their investigation reports the effect of material location on the tensile properties of the dissimilar FSW joint. Further, they report that higher tensile properties of the weld joint were obtained when low strength material was kept in the AS and high strength on RS. In the present study, the tool probe offset towards AA7075-T651 results in increased amount of material flow of AA7075-T651 into the WNZ (Figure 5.11, Section 5.5.1.3) and results in enhanced tensile properties of the FSW dissimilar aluminium alloys joint. The tool probe offset towards AA7075-T651 is in favour of the flow characteristics of AA7075-T651 over the AA2024-T351 kept in the AS. In addition, the increase in the TTS range above 40 mm/min results in the decrease heat input to the weld region and helps higher tensile strength of the FSW

dissimilar joint (Cole et al., 2014). The colder welds and tool probe offset into the higher hot strength material helps in retaining the strength of the material in the dissimilar weld (Cole et al., 2014). Thus, from the experimental investigation of the combined effect tool probe offset of 1 mm towards AA7075-T651 and higher TTS results in an increased amount of flow of higher strength material AA7075-T651 and decreased amount of heat input to the WNZ, respectively. Further, it helps in enhancing the material flow characteristics and exhibits higher tensile properties of the dissimilar aluminium alloys joint.

5.5.3 Fractography

Table 5.1 presents the macrograph images of the fracture locations of the tensile specimens of FSW dissimilar aluminium alloys joint produced from the different tool probe offset (-1, 0, +1) for the TTS range 20 - 120 mm/min, constant TRS of 650 rpm and TPD of 6.2 mm. The corresponding SEM images are shown in Figure 5.21.

In Table 5.1, for the tool probe offset of 1 mm towards AA2024-T351, except the specimen produced for TTS for 25 mm/min, invariably all the tested tensile specimens shows the fracture failure location at the joint interface of the WNZ and TMAZ. The presence of sharp boundary and lack of metallurgical bonding between the joint interface of WNZ and TMAZ of the two materials are the reasons for the failure. Figure 5.21 (a-c) shows an example of the SEM images of the fractured surface of the specimen failed at the joint interface and exhibits fracture surface morphology consisting of smooth curved surface features (Figure 5.21 (a)) without any severe deformation with alternate stripes of dark and white bands. Figure 5.21(b) shows the morphology between these two alternate stripes. The higher magnified SEM images (Figure 5.21 (c)) shows the presence of a large number of small size dimples and confirms the failure characteristics resembles that of a ductile fracture.

Referring to the Table 5.1, the tensile specimens of FSW dissimilar aluminium alloys joint produced for zero tool probe offset and TTS 20-120 mm/min shows fracture failure location away from the WNZ and indicates that bonding between the joint interface of the WNZ and TMAZ is stronger. As a result, the specimens produced for TTS range 40-80 mm/min, the deformation was concentrated at the HAZ of AA7075-

T651 and the failure of the specimens is confined in these regions. The specimens produced for TTS above 80 mm/min, both the deformation and failure was observed at the HAZ of AA2024-T351. These kinds of failure indicates that the WNZ is free from sharp boundary defects and the failure was observed at the lower hardness region i.e. HAZ of either AS or RS. Figure 5.21 (d-f) shows the SEM images of the fractured surface of the tensile specimens of FSW dissimilar aluminium alloys joint specimen produced from the zero tool probe offset and TTS of 110 mm/min. These specimen yields higher tensile properties and consists of microvoids surrounded by large number of equiaxed dimples (Figure 5.21(f)).

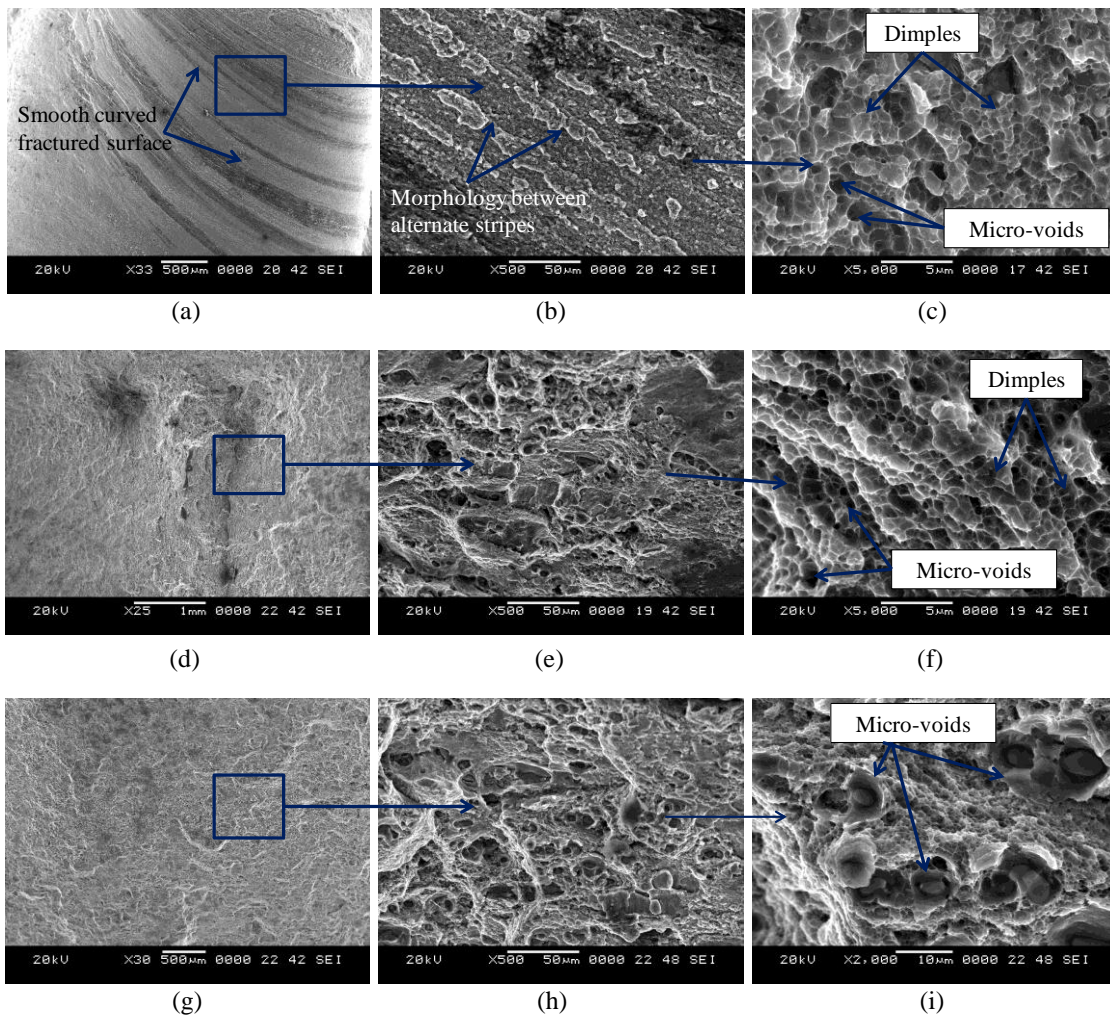
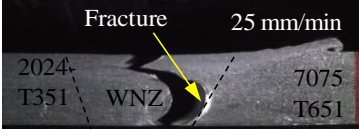
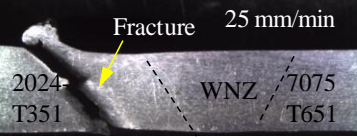
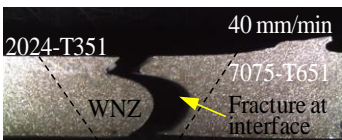
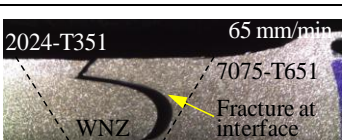
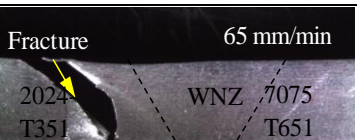
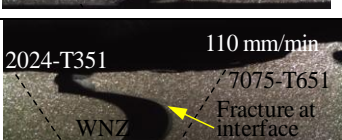


Figure 5.21 SEM images of typical fracture surface of FSW dissimilar aluminium alloys joint for tool probe offset (a)-(c) 1 mm towards AA2024-T351, (d)-(f) Zero offset and (g)-(i) 1 mm towards AA7075-T651 for VTS range 20 - 120 mm/min.

Table 5.1 Failure location of the fracture tensile specimen of FSW dissimilar aluminium alloys joint produced for different tool probe offset and TTS range 20-120 mm/min.

Tool probe offset towards 2024-T351	Zero Tool probe offset	Tool probe offset towards 7075-T651
		
		
		
		
		
		
		
		

Referring to the Table 5.1, the FSW dissimilar aluminium alloys joint produced for tool probe offset of 1 mm towards AA7075-T651 and for TTS range 20-120 mm/min have failed away from the WNZ and at the lower hardness region HAZ of AS. The fracture of the tested tensile specimens usually observed at the HAZ of the heat

treatable alloys is due to severe over ageing (Li et al., 2014; Liu et al., 2003). Figure 5.21(g - i) shows the fractographic analysis of the tensile specimen for the FSW dissimilar aluminium alloys joint that yields higher tensile properties for TTS of 110 mm/min. Similar type of predominant ductile failure mechanism is observed for all other FSW dissimilar aluminium alloys joint produced for tool probe offset of 1 mm towards AA7075-T651. The SEM images consist of microvoids and a large number of dimples surrounding the microvoids.

5.5.4 Overall influence of the tool probe offsets and traverse speed in joining dissimilar aluminium alloys joint by FSW

The combined effect of different tool probe offset condition and TTS range of 20-120 mm/min have been used to produce FSW dissimilar aluminium alloys joint of AA2024-T351 and AA7075-T651 in butt joint configuration by keeping AA2024-T351 in the AS and high strength AA7075-T651 kept in AS. The material flow either from AS and RS towards the WNZ depends upon the tool probe offset distance from the joint interface, whereas the varying TTS plays an in important role in supply the heat to the WNZ during the FSW process.

The tool probe offset distance of 1 mm towards AA2024-T351 in conjunction with increase in the TTS range from 20-120 mm/min has shown a decrease in the UTS, YS and % EL of the FSW dissimilar aluminium alloys joint. As the tool probe is offset towards AA2024-T351, the material kept in RS (AA7075-T651) experiences a lack of heat input and results in the decreased material flow from the RS to the AS. Thus, a poor mixed flow of two material AA224-T351 and AA7075-T651 was observed at the WNZ consisting a major portion of AA2024-T351. For the zero tool probe offset, an equal amount of contact surface of tool shoulder and pin is established with the faying surface of the dissimilar material along the weld joint line. As a result, an equal amount of material placed in the AS and RS flows towards WNZ and thereby contributing in proper material mixing of both the material consisting of alternate lamellae pattern of AA2024-T351 and AA7075-T651 material. In addition, an increase in the from the TTS range 20-120 mm/min has shown increase in the UTS, YS and % EL of the FSW dissimilar aluminium alloys joint. The tool probe offset

distance of 1 mm towards AA7075-T651 is in favour of the flow characteristics of AA7075-T651 over the AA2024-T351 kept in the AS and results in an increased amount of material flow of AA7075-T651 into the WNZ. In addition, an increase in the TTS range 20-120 mm/min has shown higher UTS, YS and %EL.

Based on experimental investigation, the combined effect of moving the tool probe offset by 1 mm towards AA7075-T651 with higher TTS, 110 mm/min result in higher UTS of 435 MPa, YS of 375 MPa and %EL of 13.6 compared to FSW dissimilar aluminium alloys joint produced with tool probe offset condition of 1 mm towards AA2024-T351 and zero tool probe offset.

5.6 SUMMARY

Three FSW experiments trials are carried out on each individual set of plates typically AA2024-T351 and AA7075-T651 in butt-joint configuration. Taper threaded tool considered for fabricating the FSW dissimilar aluminium alloys joint. In the first set of experiment, the FSW process carried out by offsetting the tool probe by 1 mm towards AA2024-T351 and for varying the TTS. Similarly, the second and third set of FSW process carried out by zero tool probe offset and 1 mm towards AA7075-T651. The tensile properties and microstructure characterization are evaluated for the FSW dissimilar aluminium alloys joint to study the influence of tool probe offset and varying TTS. From the evaluated tensile properties and microstructure characterization, the tool probe offset toward AA7075-T651 and increase in the TTS found to be beneficial in enhancing the material flow characteristics and exhibits higher tensile properties of the dissimilar aluminium alloys joint. Effect of silicon carbide nano particles reinforcement and FSW parameters on the properties of FSW dissimilar aluminium alloys joint has been investigated in Chapter 6.

CHAPTER-6

EFFECT OF SILICON CARBIDE NANO PARTICLES REINFORCEMENT AND FSW PARAMETERS ON THE PROPERTIES OF FSW DISSIMILAR ALUMINIUM ALLOYS JOINT

6.1 INTRODUCTION

This chapter discusses the experimental investigations on effect of silicon carbide nano particles (SiC_{NP}) reinforcement and FSW parameters on the properties of FSW dissimilar aluminium alloys joint to fabricate the MMNC at the WNZ by incorporating fixed and varying % volume fractions of SiC_{NP} . There are two stages of experiments. In the first stage, the effects of TRS and FSW first pass are investigated with a fixed concentration of SiC_{NP} . In the second stage, the effects of varying % vol. fractions of SiC_{NP} reinforcement at the WNZ, FSW first and second pass on the microstructure and mechanical properties of dissimilar aluminium alloys joint are investigated.

6.2 PRODUCTION OF FSW DISSIMILAR ALUMINIUM ALLOYS JOINT REINFORCED WITH FIXED VOLUME FRACTION OF SiC_{NP} AND TOOL ROTATION SPEEDS USING FSW FIRST PASS

In the present investigation, the aluminium alloy plates of AA2024-T351 and AA7075-T651 are used in producing the FSW dissimilar aluminium alloys joint reinforced with SiC_{NP} and FSW first pass process is performed by varying the TRS along the weld joint line. The chemical compositions and mechanical properties of AA2024-T351 and AA7075-T651 are given in Tables 3.1 and 3.2 of Chapter 3 and Section 3.2.1.

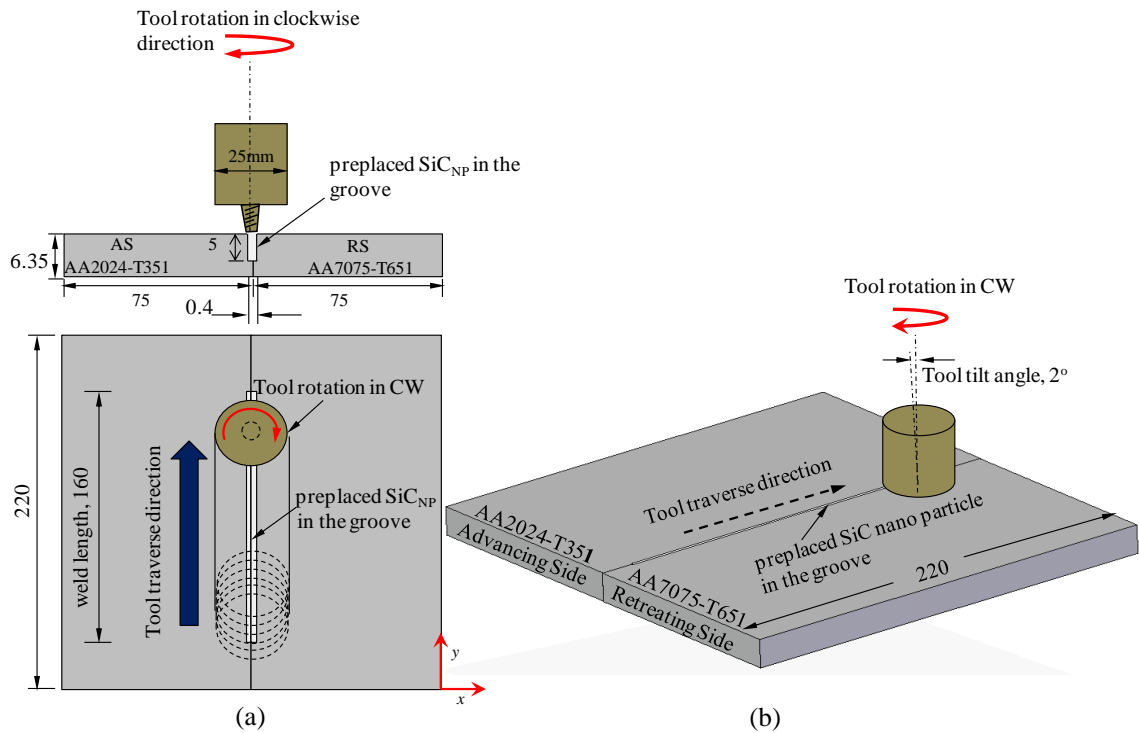


Figure 6.1 Schematic of FSW dissimilar aluminium alloys joint in (a) front and top view (b) isometric view illustrating the FSW experiment process.

Each plate of aluminium alloy typically AA2024-T351 and AA7075-T651 are cut with a rectangular cut profile having the width, 0.2 mm, and depth, 5 mm, for a length of 160 mm was machined on the adjoining side of each strip as shown in Figure 6.1 (a). The plates are fixed in the butt-joint configuration and SiC_{NP} are reinforced into the rectangular groove having a total width of 0.4 mm and pressed tightly before FSW operation. The details of commercially available Beta (β)-Phase SiC_{NP} powder are given in Chapter 3, Section 3.2. A single plane FSW pass is given using a pin-less tool to avoid the reinforced SiC_{NP} coming out of the groove during the actual FSW process. After the FSW plane pass, the actual FSW experiment is carried out using a taper threaded cylindrical tool and by varying the TRS range 400 to 1800 along the weld joint line in the tool traverse direction, y . Figure 6.1(b) depicts the FSW experiment condition with tool tilt angle of 2° , weld length of 160 mm, tool traverse direction along the weld joint line and tool rotation in CW direction. In the first set of experiment, the TRS is varied from 400 to 1100 rpm for a weld length of 160 mm. Similarly, in the second set of experiment, the TRS is varied from 1100 to 1800 rpm

for a weld length of 160 mm. Both the FSW experiments are conducted on a separate individual set of plates.

6.3 PRODUCTION OF FSW DISSIMILAR ALUMINIUM ALLOYS JOINT WITH VARYING PERCENTAGE VOLUME FRACTIONS OF SiC_{NP}, WITHOUT SiC_{NP} USING FSW FIRST AND SECOND PASS

The aluminium alloy plates typically AA2024-T351 and AA7075-T651 are used in producing the dissimilar joint by FSW process with and without the reinforcement of SiC_{NP} at the WNZ. Before the FSW process, each plate is machined on the adjoining side face with typical rectangular section edge-groove as shown in Figure 6.2. In total four pairs of test plates fabricated with the butt joints, one pair of the plates are fabricated without reinforcing the SiC_{NP} at the WNZ. The remaining three pair of plates are fabricated by reinforcing the SiC_{NP} at the WNZ into the rectangular section edge-grooves.

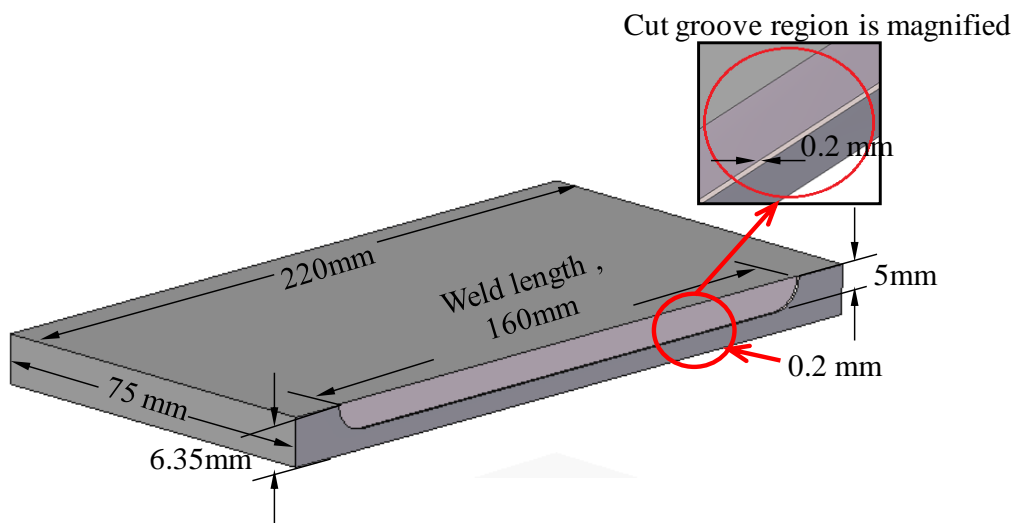


Figure 6.2 Schematic of an example of aluminium alloy plate with rectangular section edge-groove.

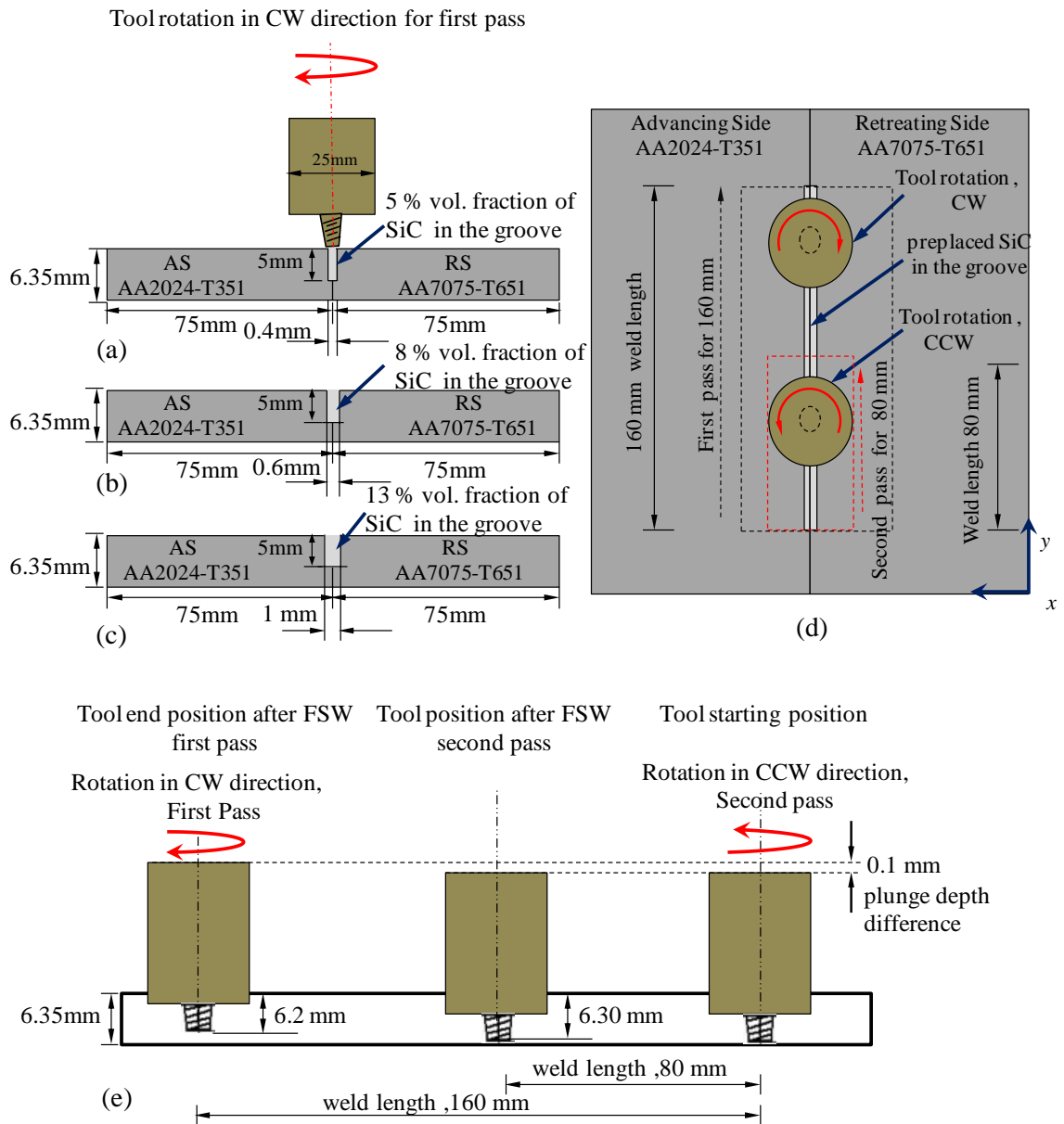


Figure 6.3 Aluminium alloy plates kept in butt configurations having a rectangular section edge-groove of total width (a) 0.4 mm, (b) 0.6 mm (c) 1 mm, and (d) top view showing the tool traverse and rotation direction for FSW first and second pass (e) increment in the plunge depth with difference of 0.1 mm from first to second pass.

Three rectangular section edge-groove dimensions width, 0.2, 0.3 and 0.5 mm, and constant depth, 5 mm and length, 160 mm are considered. Figure 6.3 (a-c) shows the schematic of dissimilar aluminium alloys plates in butt joint configuration having rectangular section edge-grooves of three different dimensions formed with a total width of 0.4, 0.6 and 1 mm. For all the experiments, the FSW dissimilar aluminium

alloys joints were prepared with AA2024-T351 being kept on the AS, whereas AA7075-T651 on the RS. Two aluminium alloy plates are arranged in such way that adjoining end faces containing the rectangular section edge-grooves kept intact and total empty space created in rectangular section edge-grooves was filled with different % vol. fraction of SiC_{NP} to produce MMNC at the WNZ. The SiC_{NP} with varying %vol. fractions (5, 8, 13%) are reinforced into these rectangular section edge-grooves and pressed tightly before FSW operation.

At the beginning of each experimental trial, a single plane FSW pass is given using a pin-less tool along the weld joint interface to ensure that reinforced varying %vol. fractions of SiC_{NP} (5, 8, 13%) should not spill out of the grooves and all the particles embedded completely inside the grooves. During the plane pass, the rotation of the tool shoulder (without pin) helps in removing a layer of base material from the faying surface of two plates kept in butt joint and deposits it on the groove. Thus helps in closing the grooves and avoids loss of reinforcement particles from the grooves. After the FSW plane pass, the FSW dissimilar aluminium alloys joint are fabricated by conducting the actual FSW experiment process using an FSW tool of cylindrical shape with a taper threaded pin. The dissimilar butt joint configuration of two aluminium plates, tool traverse and rotation direction for the FSW first and second pass are shown in Figure 6.3(d). In all the experimental tests, the TRS of 1000 rpm and TTS of 40 mm/min are considered for fabricating the FSW dissimilar aluminium alloys joint. Figure 6.3(e) illustrates the increment of TPD from 6.20 mm during the first pass to 6.30 mm in the second pass. The tool tilt angle was kept at 2° for all the experimental trials. The positions of both the plates are kept in the *x*-direction and tool traverse in the *y*-direction.

6.4 TENSILE AND MICROSTRUCTURE SPECIMENS EXTRACTION

For the first stage of the experiment, Figure 6.4 depicts the tensile specimens (indicated as ‘T’) and microstructure specimens (indicated as ‘M’) removal layout from the FSW dissimilar aluminium alloys joint produced by reinforcing fixed volume fractions of SiC_{NP} into the rectangular groove and using varying TRS experiment trials with FSW single pass. The tensile specimens are prepared according

to the ASTM of code E8M-04 with dimensions as explained in Chapter 3, Section 3.4.1. The microstructure specimens with dimensions of 45 mm × 6.35 mm are cross-sectioned perpendicular to the FSW tool traverse direction, y , using wire cut EDM process. The locations and orientation are as shown in Figure 6.4. All the extracted tensile specimens are tested to find optimum TRS which results in highest UTS, YS and %EL. Similarly, metallographic analyses are carried out on the microstructure specimens to study the microstructure and the distribution of SiC_{NP} at the WNZ.

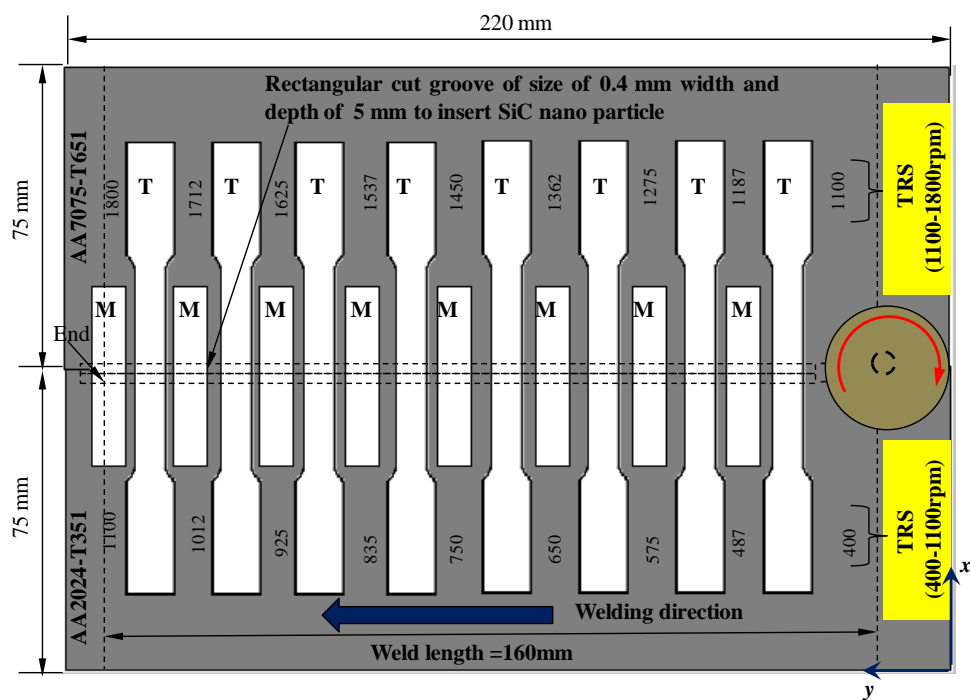


Figure 6.4. Schematic of approximate location of extraction of tensile (T) and microstructure (M) specimens from FSW joint.

Similarly, for the second stage experiment, Figure 6.5 illustrates the tensile and microstructure specimens extraction layout from the FSW dissimilar aluminium alloys joint produced from the individual experimental trials carried out with reinforcing the varying % vol. fractions of SiC_{NP} (5, 8, 13%) and without SiC_{NP} . In addition, Figure 6.5 shows the details of weld length, the direction of tool traverse for FSW first and second pass. To evaluate the tensile properties, three tensile specimens each from the FSW first pass and second pass region denoted by 'T' are extracted perpendicular to the welding direction (y -direction). Similarly, two rectangular specimens each from FSW first pass and second pass region denoted as 'M' are also

extracted for the metallographic analyses as well as evaluation of material hardness using micro-Vicker's hardness tester.

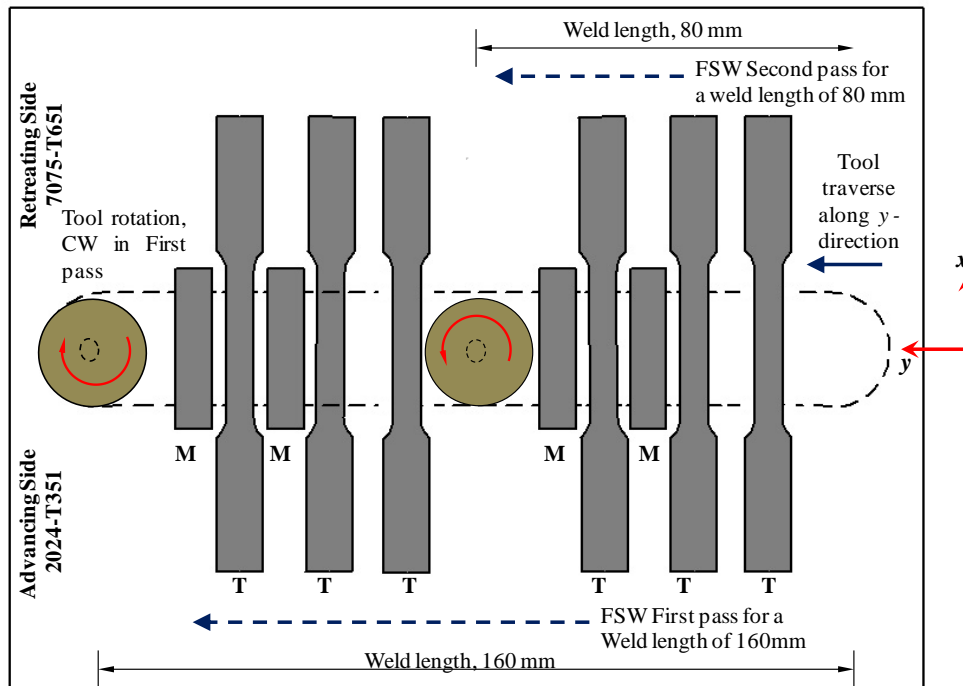


Figure 6.5 Schematic of two plates with butt joint showing the orientations of tensile specimens and micro-structural samples for FSW first pass and second pass.

6.5 MECHANICAL TESTING

The FSW dissimilar aluminium alloys joint produced ensuring the MMNC at the WNZ for the experiments explained in section 6.2 and section 6.3 are evaluated for the mechanical properties such as tensile and hardness.

6.5.1 Tensile testing

The tensile specimens extracted from the FSW dissimilar aluminium alloys joint from the experiments explained in Section 6.2 and Section 6.3 are evaluated for UTS, YS and % EL. The specimens preparation, testing procedure and details of the machine are given in Chapter 3, Section 3.4.1.

6.5.2 Hardness testing

The micro-Vicker's hardness test is performed on the microstructure specimens extracted for the second stage experiment (Figure 6.5) from the FSW dissimilar aluminium alloys joint produced with and without SiC_{NP} for the FSW first pass and second pass experiments. The details of the machine and test procedure are given in the Chapter 3, Section 3.4.2.

6.6 MACRO AND MICROSTRUCTURE EXAMINATION

The micro and macrostructures of the cross section welded region for the experiments explained in Section 6.2 and Section 6.3 are studied by a stereo zoom microscope having a low magnification of 10X and using SEM machine. The distribution of SiC_{NP} reinforcement particles in the WNZ, shape of the WNZ, defects at the interface of WNZ and TMAZ, and HAZ of both AS and RS are investigated. The detail microstructural characterization was performed on the prepared specimens using SEM machine equipped with an EDS.

In addition, the composition of the specimens after the FSW first pass and second pass experiments are investigated using EDS and XRD analyses. The EDS analyses are carried out on the microstructure specimens. The XRD analyses are conducted by using PANalytical X-ray diffractometer to study the intensity of SiC_{NP} peaks after FSW first pass and second pass. The details of the machine and microstructure analyses procedure are given in Chapter 3, Section 3.5.2. and Section 3.5.3. For the compositional characterisation, the details of the machine, specimen preparation and analyses procedure are given in Chapter 3, Section 3.6.1 and Section 3.6.2. Further, to investigate the possible effects of FSW first and second pass on the WNZ and SiC_{NP} distribution at the WNZ, the image analyses are carried out using Image-J software on SEM images of WNZ and macrograph images obtained from stereo zoom microscope. The fractured surface of the tensile tested specimens with varying % vol. fraction (0, 5, 8, 13%) of SiC_{NP} are also examined by SEM.

6.7 RESULTS AND DISCUSSION

6.7.1 Macro and microstructure of the FSW dissimilar aluminium alloys joint produced with SiC_{NP} reinforcement and using varying tool rotation speeds

For the first stage of the experiment, Figure 6.6 shows the photographs of the FSW dissimilar aluminium alloys joint produced with fixed % vol. fractions of SiC_{NP} (5%) reinforcement using varying TRS range 400 rpm to 1800 rpm, constant TTS, 40 mm/min and TPD, 6.2 mm. One can observe from the Figure 6.6 (a) for varying TRS experiment range 400 to 1100 rpm, the surface of the weld crown consists of smooth surface finish for the TRS range from 400 to 750 rpm for the increase in the TRS above 800 rpm results in slightly delaminated surface finish. Figure 6.6 (b) observes the weld crown of the dissimilar materials joint with excessive flash for the FSW experiment carried out for varying TRS range 1100 to 1800 rpm. In addition, a higher TRS above 1500 rpm results in pores and macroscopic defects in the weld crown of the FSW dissimilar joint region. FSW dissimilar aluminium alloys joint for TRS range 400 to 1100 rpm observes defect-free with ‘no excessive’ flash in the weld crown area. On the other hands, in the second FSW experiment for varying TRS range 1500 to 1800 rpm results in clear visible pores and macroscopic defects on the weld crown area. Table 6.1 illustrates the cross sections of the weld regions of the macrostructure of the specimens of the FSW dissimilar aluminium alloys joint produced for varying TRS range from 400 to 1800 rpm.

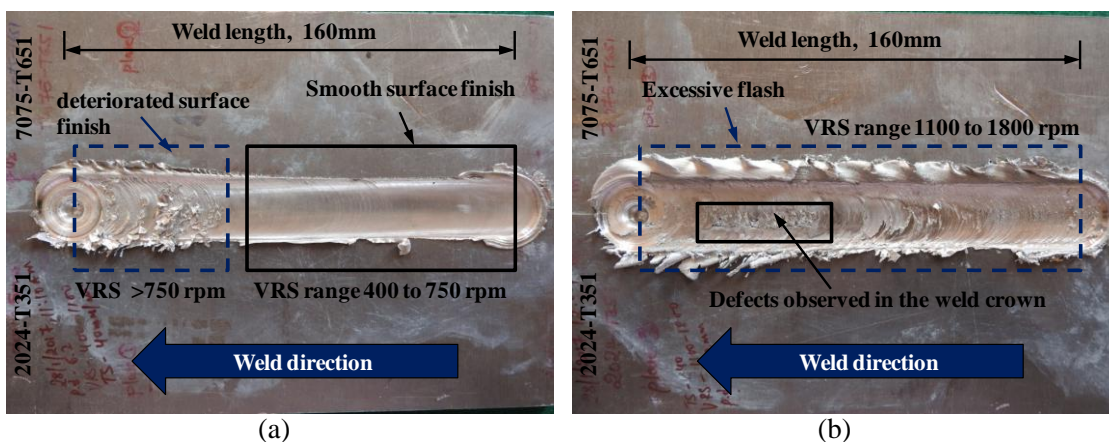


Figure 6.6 FSW dissimilar aluminium alloys joints produced with SiC_{NP} reinforcement for varying TRS experiment for (a) 400 to 1100 rpm (b) 1100 to 1800 rpm.

Table 6.1 Macrostructure for varying FSW tool rotation speeds range 400 rpm to 1800 rpm, constant tool plunge depth, 6.2 mm and traverse speed, 40 mm/min.

TRS in rpm	Macrostructure		TRS in rpm	Macrostructure	
	Advancing side (AS)	Retreating side (RS)		Advancing side (AS)	Retreating side (RS)
450			1182		
575			1275		
650			1360		
750			1450		
925			1535		
1012			1625		
			1710		

For the TRS of 450 rpm, the top region in the WNZ consists a pin-hole defect, which is mainly due to the low heat input resulting in cold processing condition (Sharma et al., 2004). In the macrostructures, the boundary line between the WNZ and TMAZ delimited by dotted line observes changes in the shape of the WNZ with the increase in the TRS and are much clearly visible for the higher TRS above the 1182 rpm. The WNZ are prone to different kind of defects like pin-hole, kissing bond defect, tunnel, wormhole and cavity, etc. These defects are due to both insufficient and excessive heat input at lower TRS and higher TRS, respectively (Vijayavel et al., 2014; Rodriguez et al., 2015). From the macrostructure observed in Table 6.1, the variation in the WNZ size, shape, location and appearance of the defects in the WNZ are affected by the FSW tool parameters and temperature (Vijayavel et al., 2014).

The Figure 6.7 and Figure 6.8 shows the microstructural features of WNZ, distribution of SiC_{NP} and grain size in the WNZ observed under SEM for varying TRS range 400 rpm to 1100 rpm and 1100 rpm to 1800 rpm respectively. Figure 6.7(a) shows the microstructure SEM images of the WNZ for the TRS of 450 rpm. In this case, the entangled SiC_{NP} can be observed at the top portion of the WNZ. The lower TRS results in lower heat input to the WNZ resulting in causing less material flow from the AS to the RS. Similar observation of non-uniform distribution, agglomeration of SiC_{NP} as consequence of improper stirring of the material in the WNZ can be seen in the SEM images shown in Figure 6.7 (b), (c) and (d) for different TRS range 575 rpm to 850 rpm. However, none of the above mentioned problems are observed with the further increase in the TRS to 1000 rpm and the SiC_{NP} distribution becomes homogeneous (Figure 6.7 (g)). Figure 6.7(h) shows BSE images the distributions of SiC_{NP} along the grain boundaries.

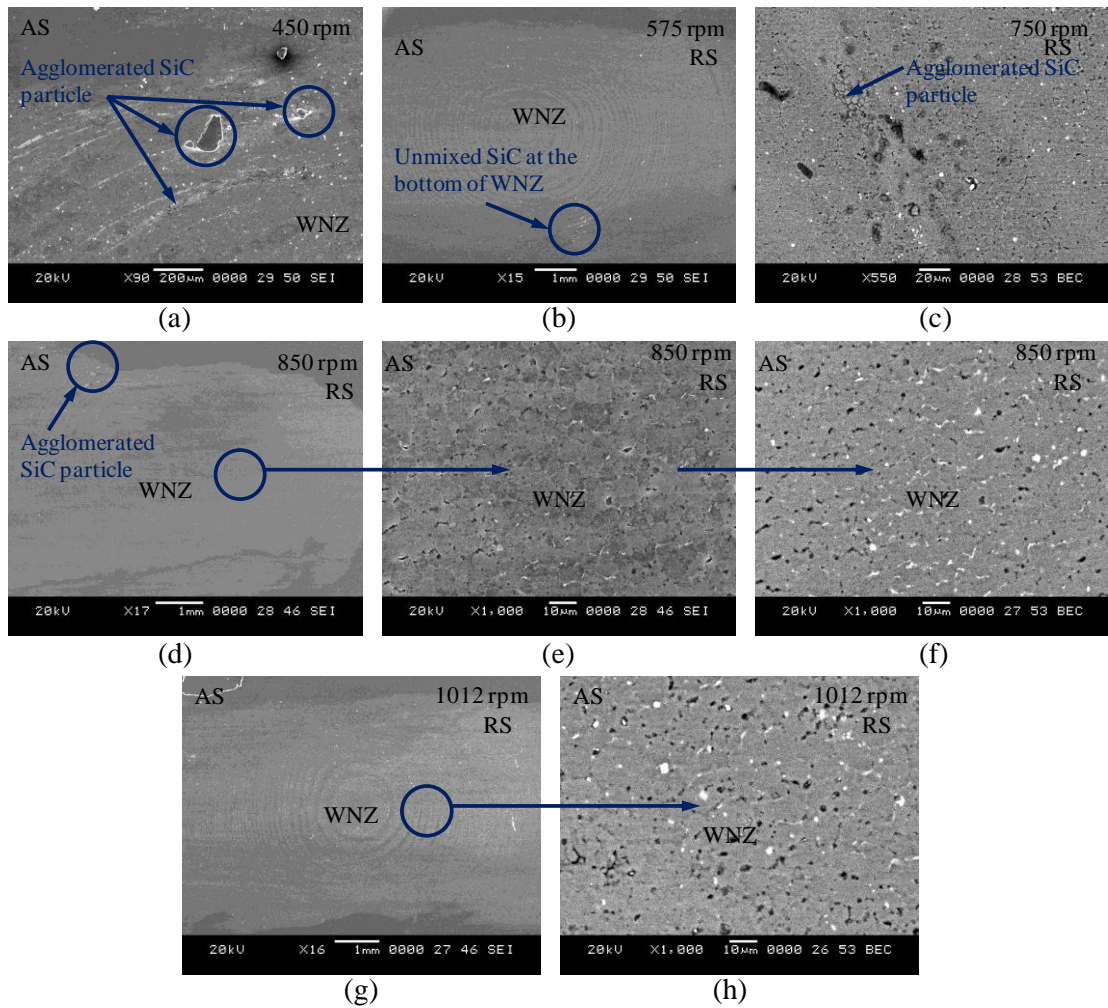


Figure 6.7 (a)-(h) SEM images showing the distribution of SiC_{NP} in the WNZ of FSW dissimilar aluminium alloys joint produced with SiC_{NP} reinforcement for varying TRS range 400 to 1100 rpm.

Figure 6.8 shows the SEM images obtained from the FSW experiment conducted by varying the TRS range 1100 rpm to 1800 rpm. Figure 6.8 (a) shows the SiC_{NP} close to the top surface are stretched towards the RS of the of the weld region. This is due to the increase in the frictional force induced by the tool shoulder (Tutunchilar et al., 2012). The distribution of SiC_{NP} in the WNZ varies in accordance with the varying TRS. Further, increase in the TRS above 1500 rpm results in higher heat generation causing the material near to the top surface stuck to the shoulder and rotates with the shoulder, and results in the formation of defects at the top surface of the WNZ. In addition, Figure 6.8 (g) and (f), shows completely broken WNZ for higher TRS 1625 to 1710 rpm. Thus, from the above varying TRS experiment the optimal FSW

parameters of TRS result homogeneous distribution of SiC_{NP} in the WNZ. In our study, the TRS range of 1012 rpm to 1185 rpm results in defect-free WNZ and homogeneous distribution of SiC_{NP} in the WNZ.

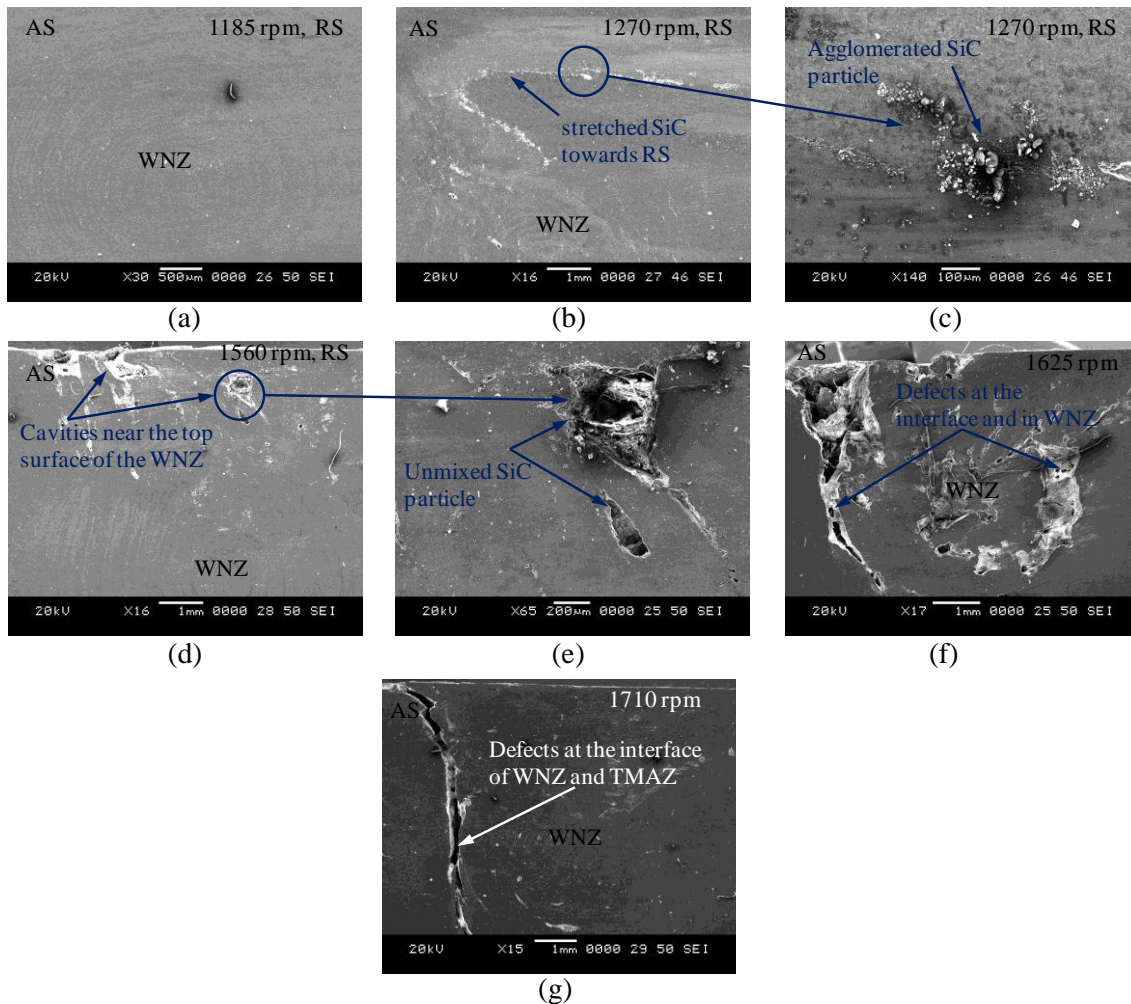


Figure 6.8 (a)-(g) SEM showing the distribution of SiC_{NP} in the WNZ of FSW dissimilar joints specimens produced with SiC_{NP} reinforcement for varying TRS range 1100 to 1800 rpm.

6.7.2 Tensile strength of the FSW dissimilar aluminium alloys joint produced with SiC_{NP} reinforcement and using varying tool rotation speeds

Figure 6.9 shows the tensile behaviour of the FSW dissimilar aluminium alloys joint produced with 5% vol. fraction of SiC_{NP} reinforcement for varying the TRS range 400 rpm to 1100 rpm using FSW single pass. Figure 6.9 shows lower UTS of range 290 to 300 MPa, YS of range 80 to 120 MPa, and %EL of range 5.32 to 6.95 were

recorded for the TRS range 400 rpm to 700 rpm. Lower TRS results in lack of heat input and poor material flow from the AS to the RS. Thus, yields lower tensile strength of the FSW dissimilar joint (Rodriguez et al.2015) owing to the agglomeration of SiC_{NP} reinforcement at the WNZ (Figure 6.7 (a-c)). The UTS, YS and % EL shows the increasing tendency with the increase in the TRS range above 750 rpm. The increase in the TRS results in high heat input and better material flow from AS to RS (Rodriguez et al. 2015). A higher UTS of 380 MPa, YS of 190 MPa and %EL of 13.5 was observed for the TRS of 1050 rpm, constant traverse speed of 40 mm/min and plunge depth of 6.20 mm.

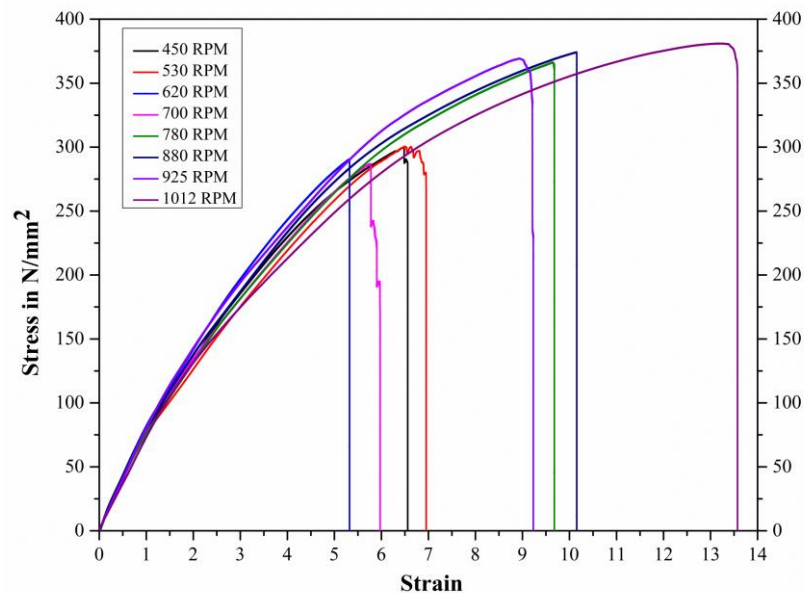


Figure 6.9 Tensile behaviour of the FSW dissimilar aluminium alloys joint produced with SiC_{NP} reinforcement for varying TRS experiment range 400 rpm to 1100 rpm.

The tensile behaviour of the FSW dissimilar aluminium alloys joint produced with SiC_{NP} (5%) reinforcement for varying TRS range 1100 rpm to 1800 rpm is shown in Figure 6.11. One can observe from the stress-strain plot, the UTS, YS and %EL shows a decreasing trend with increase in the TRS above 1275 rpm. The decreasing tensile properties are the result of a non-homogeneous distribution of SiC_{NP}, defects and broken WNZ caused due to the excessive heat input to the weld region. The tensile specimens for the TRS 1625 and 1710 rpm could not be tested as the WNZ

was completely broken and difficulty in machining the specimen from the location FSW dissimilar joint using wire EDM process.

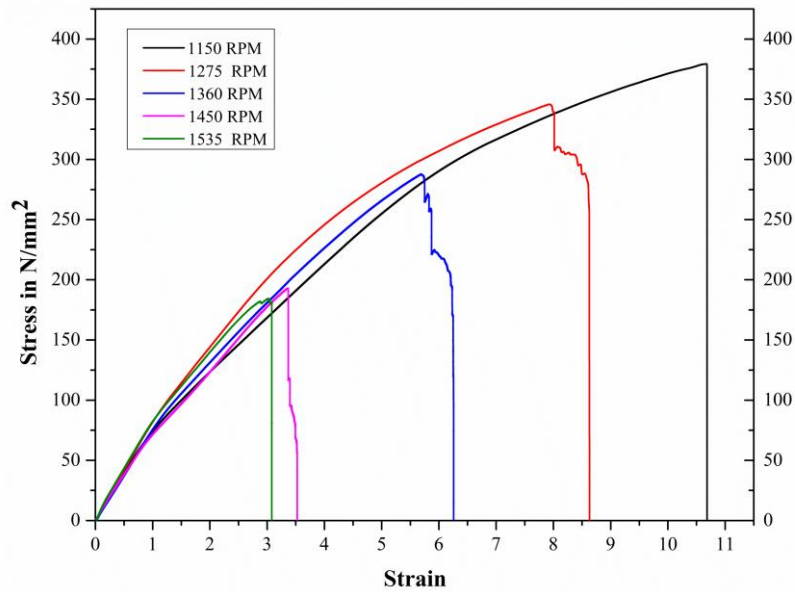


Figure 6.11 Tensile behaviour of the FSW dissimilar joints specimens produced with SiC_{NP} reinforcement for varying TRS 1100 rpm to 1800 rpm.

6.7.3 Macro and microstructure of the FSW dissimilar aluminium alloys joint produced with varying %vol. fractions of SiC_{NP} reinforcement using FSW first and second pass

Figure 6.12 shows the photographs of the FSW dissimilar aluminium alloys joint produced by reinforcing varying % vol. fraction (5, 8, 13 %) SiC_{NP} and without SiC_{NP} for FSW first and second pass conditions. Referring to Figure 6.12 (a-d), the surface morphology of the weld crown for the FSW first pass in all the experimental trials are evidenced with moderate flash, whereas the FSW second pass observes an excessive flash. The reason for excessive flash during the second pass is due to the increase in TPD from 6.20 mm of the FSW first pass to 6.30 mm in the second pass. In addition, the reversal in the rotation direction of the tool leads to an excessive flash on the weld crown.

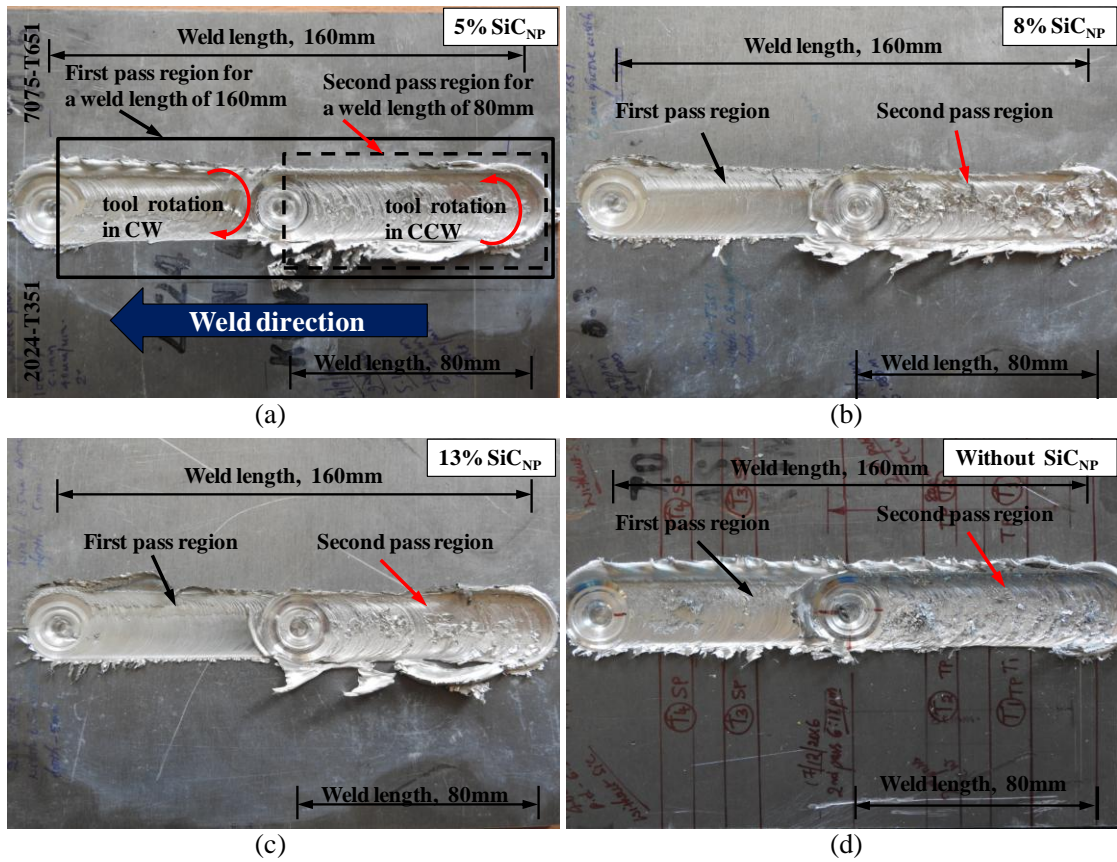


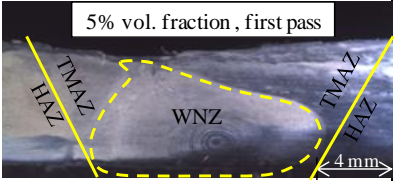
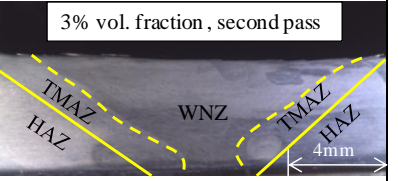
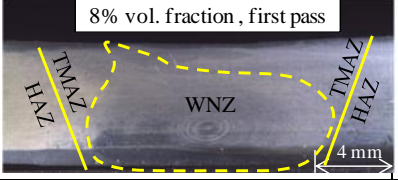
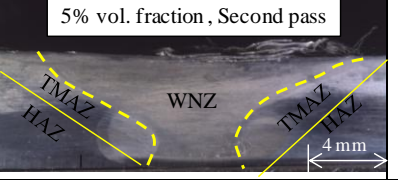
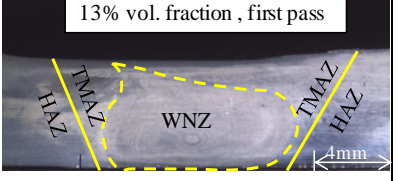
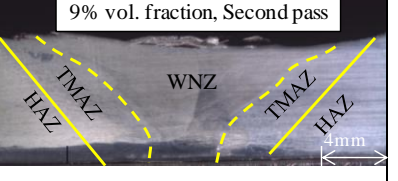
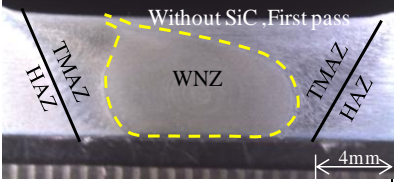
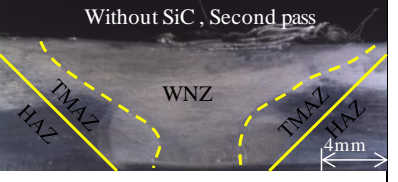
Figure 6.12 (a)-(d) Photographs showing the surface morphology of FSW dissimilar aluminium alloys joint with varying % volume fraction of SiC_{NP} reinforcement.

6.7.3.1 Effect of varying percentage volume fractions of SiC_{NP} and number of FSW pass on the WNZ of the MMNC

Table 6.2 presents the optical macrograph of the cross section of the weld region of the FSW dissimilar aluminium alloys joint produced with the varying % vol. fractions of SiC_{NP} (0, 5, 8, 13%) reinforcement at the WNZ and after performing the FSW first pass and second pass process. It is evident from Table 6.2, that the FSW dissimilar alloys joint produced for FSW first pass and second pass observes the different shape of the WNZ. The FSW first pass observes agglomeration defects of SiC_{NP} at some regions of the WNZ. In the FSW second pass as result of increased stirring effect coupled with the change in the tool rotation direction, the WNZ of the FSW dissimilar joint are defect-free. The shift in the tool rotation direction from the first pass to the second pass, the AS in the first pass becomes the RS in the second pass and this will

help in the uniform distribution of SiC_{NP} across the WNZ (Dolatkhah et al., 2012). However, the detailed analyses of the WNZ is carried out using SEM to investigate for the presence of microscopic level defects such as agglomeration of SiC_{NP} and for the presence of pores around SiC_{NP}.

Table 6.2. Macrograph images of the FSW dissimilar aluminium alloys joint showing the WNZ of MMNC for the varying % vol. fractions of SiC_{NP} reinforcement and without SiC_{NP} for FSW first and second pass.

% Volume fraction (initial)	FSW first pass		FSW second pass		Observation
	Advancing side, 2024-T351	Retreating side, 7075-T651	Retreating side, 2024-T651	Advancing side, 7075-T651	
5%			5% vol. fraction, first pass	3% vol. fraction, second pass	First pass: Defects at the top of WNZ, Second Pass: No defects
8%			8% vol. fraction, first pass	5% vol. fraction, Second pass	First pass: agglomeration of SiC _{NP} Second Pass: No defects
13%			13% vol. fraction, first pass	9% vol. fraction, Second pass	First pass: agglomeration of SiC _{NP} Second Pass: No defects
Without SiC _{NP} (0%)			Without SiC, First pass	Without SiC, Second pass	First pass: No defects Second Pass: No defects

Further, it is observed from the Table 6.2, the WNZ for the FSW first pass appears to be the shape of the “onion ring” structure while the WNZ for the FSW second pass appears like “trapezoid” in shape. The FSW first pass and second pass influenced the area of WNZ and thereby changing the volume fraction of SiC_{NP} in the WNZ (Sathishkumar et al., 2013). In the present study, the macrograph and SEM images of the WNZ for the FSW dissimilar aluminium alloys joint produced with the varying % vol. fractions of SiC_{NP} are used to measure the actual volume fraction of SiC_{NP}

present at the WNZ using image analyzing software (image-J). The area of the WNZ considered for measuring the actual volume fraction of SiC_{NP} for the FSW first pass and the second pass using image-J software are shown in the dotted line in Table 6.2. In addition, the Image-J analyses are carried out on the higher magnification SEM images of the WNZ for finding the actual volume fraction of SiC_{NP} at the WNZ and compared with WNZ area calculation. The theoretical volume fraction (V_{th}), actual volume fraction SiC_{NP} at WNZ after FSW first pass (V_{fp}) and actual volume fraction SiC_{NP} at WNZ after FSW second pass (V_{sp}) are computed as follows (Sathishkumar et al., 2013).

Theoretical volume fraction of SiC_{NP} (V_{th}),

$$V_{th} = (A_g / A_p) \times 100 \quad (6.1)$$

Actual volume fraction of SiC_{NP} at WNZ after FSW first pass (V_{fp}),

$$V_{fp} = (A_g / A_{fp}) \times 100 \quad (6.2)$$

Actual volume fraction of SiC_{NP} at WNZ after FSW second pass (V_{sp}),

$$V_{sp} = (A_g / A_{sp}) \times 100 \quad (6.3)$$

Total area of the groove (A_g)

$$= \text{Total groove width } (G_w) \times \text{Groove depth } (G_d) \quad (6.4)$$

The projected area of the tool pin (A_p) of the taper threaded cylindrical tool used in the experiment is shown in Figure 6.13. The three side lengths i.e. longer side, $a=7.5$ mm, shorter side, $b = 6$ mm, slant side, $c = 5.90$ mm, and height, $h = 5.85$ mm are as shown in Figure 6.13.

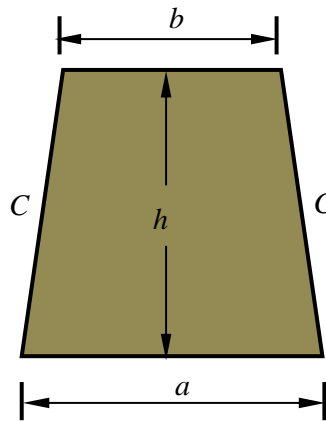


Figure 6.13 Projected area of the tool pin of taper threaded cylindrical used in the experiment.

The calculation of A_p of taper threaded tool is as follows,

$$A_p = \frac{1}{4} \times \sqrt{(a+b)^2 \times (a-b+2c) \times (b-a+2c)} \quad (6.5)$$

The A_p in the calculation is equal to 39.16 mm^2 which remain same irrespective of % vol. fractions of SiC_{NP} reinforcement in each groove.

The calculated V_{th} of SiC_{NP} for each experiment varies because the total area of the groove (A_g) size considered is of the different dimension in each experiment. The Table 6.3 provides the details of the V_{th} calculated using equation (6.1) for each rectangular section edge-grooves of three different dimensions formed with the total width of 0.4, 0.6, 1 mm and depth of 5 mm. The calculated V_{th} for the different dimensions edge-grooves of a total width of 0.4, 0.6, 1 mm is found to be ~5%, ~8% and ~13% respectively.

Table 6.3 Theoretical volume fraction (V_{th}) of SiC_{NP} before the FSW process.

Groove dimension (width × depth), in mm	Area of the groove (A_g), in mm^2	Area of the tool pin (A_p), in mm^2	Theoretical volume fractions of SiC_{NP} (V_{th}) in %
0.4 × 5	2	39.16	~ 5%
0.6 × 5	3		~ 8%
1 × 5	5		~ 13%

The area of the WNZ of the MMNC considered for the FSW first pass, A_{fp} , and FSW second pass, A_{sp} , is shown by the dotted lines in Table 6.2. The A_{fp} measured using image-J analysis by considering the area of the WNZ ensuring the MMNC after the FSW first pass is found to be $\sim 40 \text{ mm}^2$ and it is almost the same for all the % vol. fraction of SiC_{NP} (5, 8, 13%) reinforcement at the WNZ. The change in the % vol. fraction of SiC_{NP} at the WNZ did not have much influence on the area of WNZ of the MMNC. Similarly, the A_{sp} measured using image-J analysis by considering the area of the WNZ after the FSW second pass is found to be $\sim 56 \text{ mm}^2$ and it is almost the same for all the % vol. fractions of SiC_{NP} (5,8,13%) reinforcement at the WNZ.

The V_{fp} is obtained by using equation (6.2) and considering the A_{fp} . Similarly, the V_{sp} is obtained by using equation (6.3) and considering the A_{sp} . These results of V_{fp} , V_{sp} obtained are compared with the actual volume fraction measured from the SEM images of the WNZ from both the first pass and the second pass using image-J analysis software. Figure 6.14 shows some of the examples of SEM images of the WNZ after the FSW first pass process considered for the analysing the % vol. fractions of SiC_{NP} at the WNZ. The calculation of % vol. fractions of SiC_{NP} at the WNZ using Image-J analysis are found to be in good agreement with the measured theoretical value of V_{fp} and V_{sp} using equation (6.2) and equation (6.3), respectively.

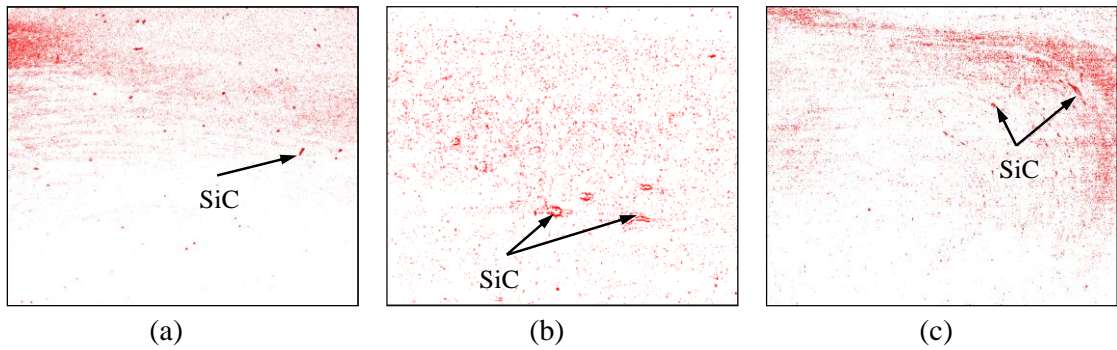


Figure 6.14 SEM images of the FSW first pass WNZ area considered for the Image-J analysis showing (a) ~5% (b) ~8% and (c) ~13% vol. fraction of SiC.

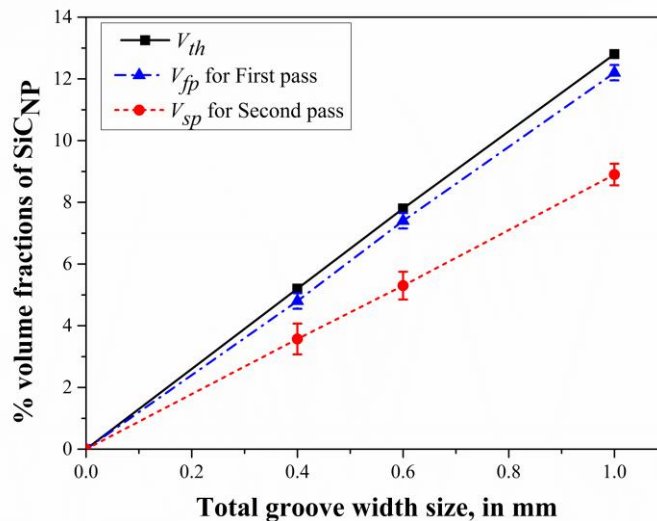


Figure 6.15 Comparison of the volume fractions V_{th} with V_{fp} and V_{sp} , after FSW first pass and second pass processing.

Figure 6.15 shows the comparison of the actual volume fraction of SiC_{NP} for V_{th} , V_{fp} and V_{sp} . As observed in Figure 6.15, the decreasing trend in the % vol. fraction of SiC_{NP} from the FSW first pass to second pass attributes to the corresponding increase in the area of WNZ of the MMNC from the FSW first pass to the second pass (Table 6.2). Considering the area of WNZ of MMNC from the Table 6.2 for each experimental case, the calculated V_{fp} after performing the FSW first pass was found to be ~5, ~8, ~13% vol. fraction and almost equal to V_{th} . Similarly, considering the area of WNZ of MMNC after the second pass, the calculated V_{sp} on the same specimen it was ~3, ~5 and ~9% vol. fraction.

Figure 6.16 shows the SEM images of the WNZ of the FSW dissimilar aluminium alloys joint reinforced with 5% vol. fractions of SiC_{NP} and after performing FSW first and second pass. Figure 6.16 (a-e) shows the SEM images of the WNZ after performing the FSW first pass. Similarly, Figure 6.16 (g-h) are the SEM images of the specimen after performing the FSW second pass on the same FSW dissimilar joint. The Figure 6.16 (a) and (b) reveals the non-homogeneous distribution of SiC_{NP} for FSW first pass with agglomeration of SiC_{NP} and defects are observed at the top of WNZ, and the SiC_{NP} migration along with the material towards RS of the WNZ which exposes the material flow pattern during FSW and FSP. The distribution of SiC_{NP} at the WNZ depends on the number of passes (Pantelis et al., 2016; Byung-Wook et al., 2012). Further, in the Figure 6.16 (c-d), the WNZ is distinguished by the presence of alternate layers of SiC_{NP} rich and free region indicating that the material stirring is incomplete during the FSW first pass (Abbasi et al., 2015; Bahrami et al., 2014). In addition, the higher magnification SEM image (Figure 6.16 (e)) reveals SiC_{NP} rich region surrounded by pores at the WNZ. The difference of physical properties between the SiC and the base materials is the reason for the observation of pores around the particle (Bodaghi M and Dehghani K, 2017; Sun and Fujii, 2011). Thus, the inadequate stirring of the material during the FSW first pass results in porosities in the WNZ and leads to weak interface bonding between the SiC_{NP} and the aluminium matrix.

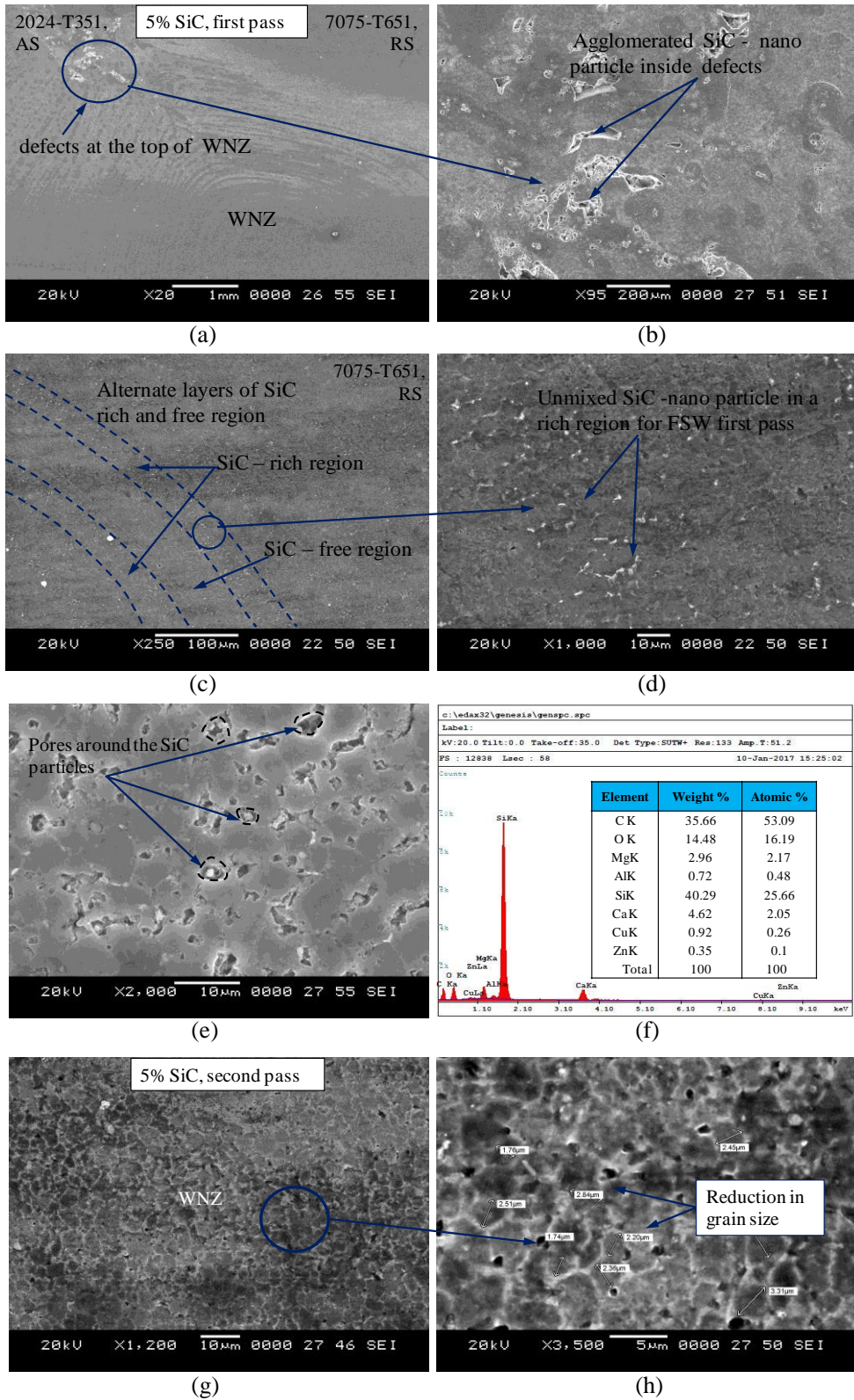


Figure 6.16 The distribution of 5% vol.fraction SiC_{NP} (a) and (b) defects due to agglomeration of SiC_{NP}, (c) and (d) alternate layer of SiC rich and free region, (e) pores around SiC_{NP} (f) EDS peaks of SiC (g) homogeneous distribution of SiC_{NP} and (h) Grain size range 2-3.5 μm.

The EDS analysis shown in Figure 6.16 (f) confirms the presence of agglomerated nano particles in the SiC_{NP} rich region in the RS of the WNZ. In the FSW second pass, the tool rotation applied in the opposite direction results in more heat input, enhanced plasticized flow of material, severe plastic deformation and CDRX in the WNZ (Mishra and Ma, 2005). In the FSW, the grain refinement at the WNZ is achieved by the combined effect of CDRX mechanism and SiC_{NP} reinforcement. The presence of SiC_{NP} pin the grain growth and acts as an additional source for dislocation generation (Kumar et al., 2017). As a result, in the WNZ new fine grains are formed which are strain-free grains (Mishra and Ma, 2005; Kumar et al., 2017). Comparison between Figure 6.16 (a-e) and Figure 6.16 (g-h) at the WNZ, the change in the tool rotation direction and the FSW second pass results in the homogenous distribution of SiC_{NP} at the WNZ. Thus, the pores observed around the SiC_{NP} (Figure 6.16 (e)) during the FSW first pass not seen after the second pass (Byung-Wook et al., 2012; Pantelis et al., 2016; Sun and Fujii, 2011). The Figure 6.16 (h) shows the average grain size in the range 2-3.5 μm for the FSW joint with MMNC at the WNZ and after performing the FSW second pass. After FSW second pass, the SiC_{NP} are homogeneously distributed in the WNZ and occupied the grain boundaries along with the other precipitates. The presence of these nano particles placed along the grain boundaries helps in hindering the grain growth (Azizieh et al., 2011).

Figure 6.17 shows the SEM images of the WNZ of the FSW joint produced after performing the FSW first pass and second pass with 8% vol. fraction of SiC_{NP}. In the Figure 6.17(a) and (b), the SiC_{NP} shows non-homogeneous distribution, severe agglomeration at the RS and part of the material being stretched towards RS due to the frictional shear force induced by the tool shoulder (Tutunchilar et al., 2012). The presence of SiC_{NP} rich and poor regions are also observed in Figure 6.17(c). The surface EDS analyses (Figure 6.17(f)) shows the peaks of Si during the FSW first pass. Compared to the FSW first pass, the second pass results in more homogeneously distributed SiC_{NP} at the WNZ (Figure 6.17(g)) with an average grain size at the WNZ in the range 3-5 μm (Figure 6.17(h)). However, even after applying for the FSW second pass, some area at the lower portion of the WNZ found with the agglomerated SiC_{NP} (Figure 6.17(g)) surrounded by pores.

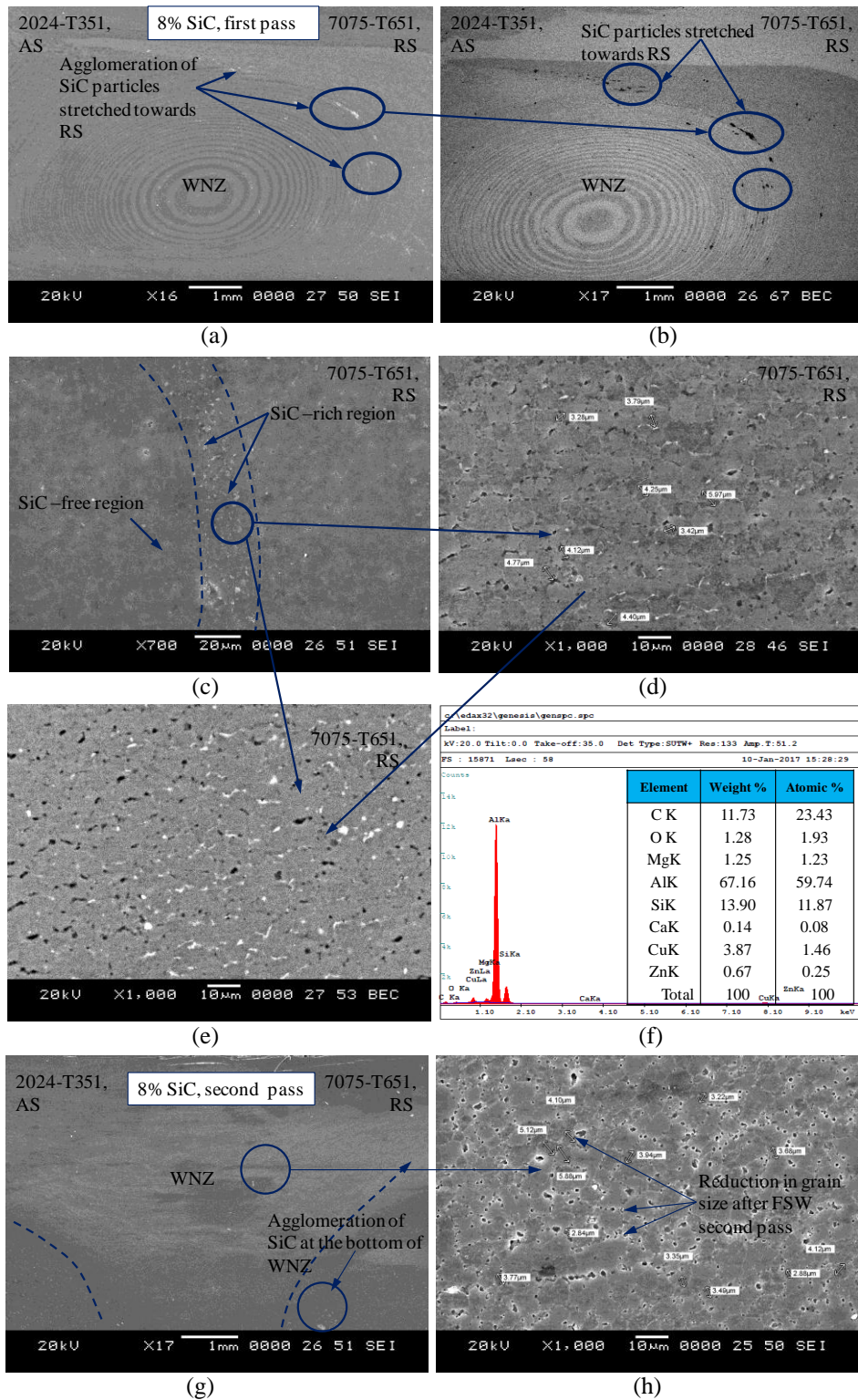


Figure 6.17 SEM images showing the distribution of 8% vol. fraction SiC_{NP} in the WNZ for FSW (a) and (b) first pass. (c) alternate layer of SiC rich and free region (d) magnified image of (c), (e) BSE images of (d), (f) EDS peaks of SiC (g) FSW second pass, (h) Grain size range 3-5 μm in the WNZ.

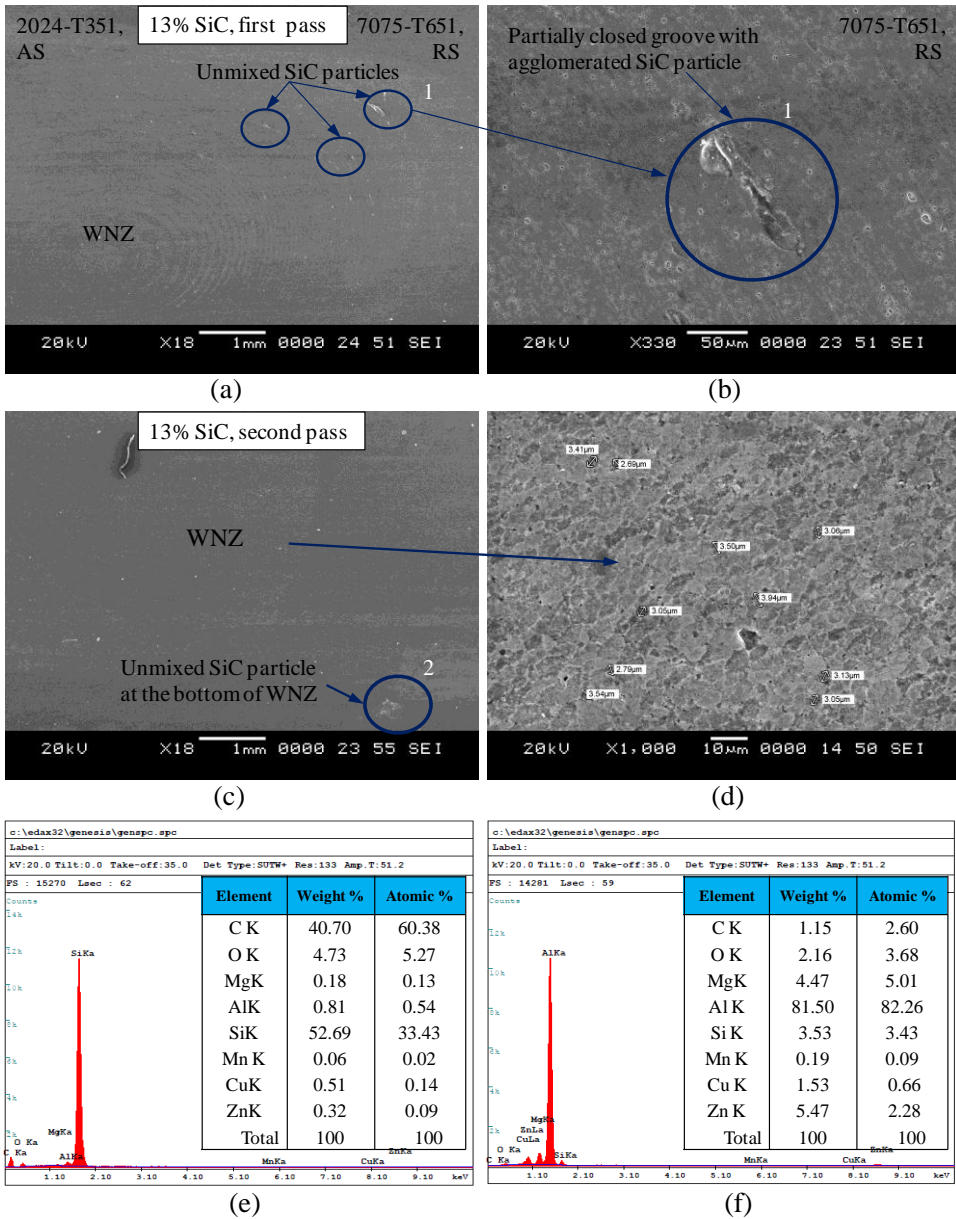


Figure 6.18 SEM images showing the distribution of 13% vol. fraction SiC_{NP} in the WNZ for (a) FSW first pass and (b) partially closed groove (c) FSW second pass (d) Grain size range 3-4 μm in the WNZ (e) Spot EDS analysis for the region 1 of (b). (f) surface EDS for the region 2 of (c).

Figure 6.18 (a-b) and Figure 6.18 (c-d) presents the SEM images of the WNZ of the FSW dissimilar alloys joint fabricated by reinforcing 13% vol. fraction of SiC_{NP} at the WNZ and after performing the FSW first pass and second pass, respectively. Comparing the SEM image of Figure 6.17(a) and Figure 6.18 (a), the amount of agglomeration of SiC_{NP} also increases owing to the increase in the %vol. fractions of

SiC_{NP} and due to the insufficient stirring at the WNZ. As a result, a defect at the WNZ mainly towards the RS (marked as '1') was observed (Figure 6.18 (b)). This indicates that as the amount of reinforcement particles increases, it leads to higher flow stress for the composite materials and offers resistance to the flow of plasticized material from RS to the AS (Sathiskumar et al., 2013). Figure 6.18(e) shows EDS peaks of the SiC_{NP} agglomerated region marked as '1' in Figure 6.18 (b). The FSW second pass helps in breaking of the reinforcement by the tool and results in the homogeneous distribution due to good stirring effects. However, the Figure 6.18(c) illustrates the presence of two distinct regions, middle of the WNZ where no agglomeration of particles was observed and the lower portion of the WNZ (marked as '2') indicator of a non-homogeneous distribution of the SiC_{NP} with lack of stirring of the material. Figure 6.18 (f) shows the EDS peaks of Si and confirms the presence of agglomeration of SiC_{NP} at the lower portion of the WNZ (marked as '2').

Figure 6.19 (a-b) exhibits the SEM images of the WNZ of the FSW dissimilar alloys joint produced without SiC_{NP} (0%) and after performing FSW second pass. Figure 6.19 (b) shows an average grain size range between 6-8 μm in the WNZ. The increase in the grain size is attributed to the higher frictional heat generation during the FSW second pass accompanying with the lower traverse speed (El-Rayes and El-Danaf, 2012; Khodir and Shibayanagi, 2008) of 40 mm/min and a higher rotation speed of 1000 rpm. On the other hand, FSW dissimilar alloys joint produced after the FSW second pass and with the addition of SiC_{NP} , although the heat generation is high, the presence of SiC_{NP} reinforcement acts as an obstacle to the grain growth and grain boundary movement and results in decreased grain size range 2-3.5 μm . This shows that the addition of SiC_{NP} and heat input have opposite effects on grain size (Hamdollahzadeh et al., 2015). In the present study, the pinning effect by SiC_{NP} dominates the heat input by selected FSW parameters. The presence of SiC_{NP} restricts the grain growth because of pinning effect on grain boundaries and by increasing the nucleation sites (Abbasi et al., 2015; Liu et al., 2015; Byung-Wook et al., 2012; Guo et al., 2016; Barmouz et al., 2011). Figure 6.19 (c) demonstrates the comparison in the average grain size for the FSW joints produced for varying % vol. fraction of SiC_{NP} (5, 8, 13%) and without SiC_{NP} in the WNZ for the FSW second pass.

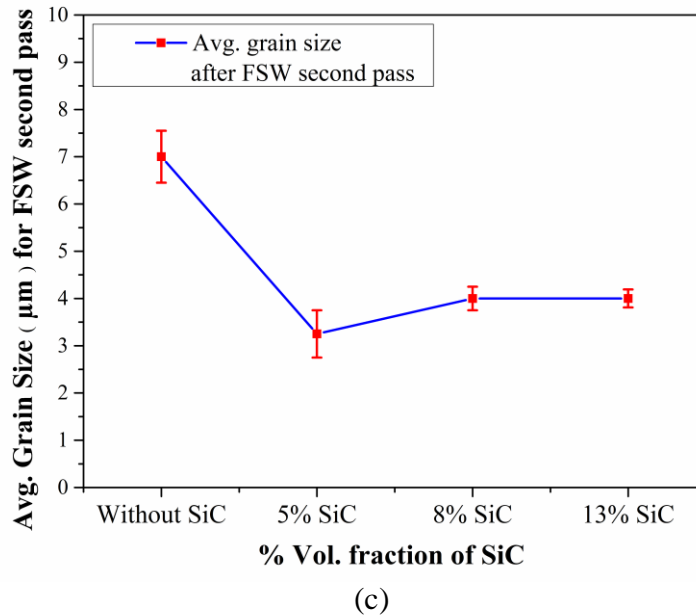
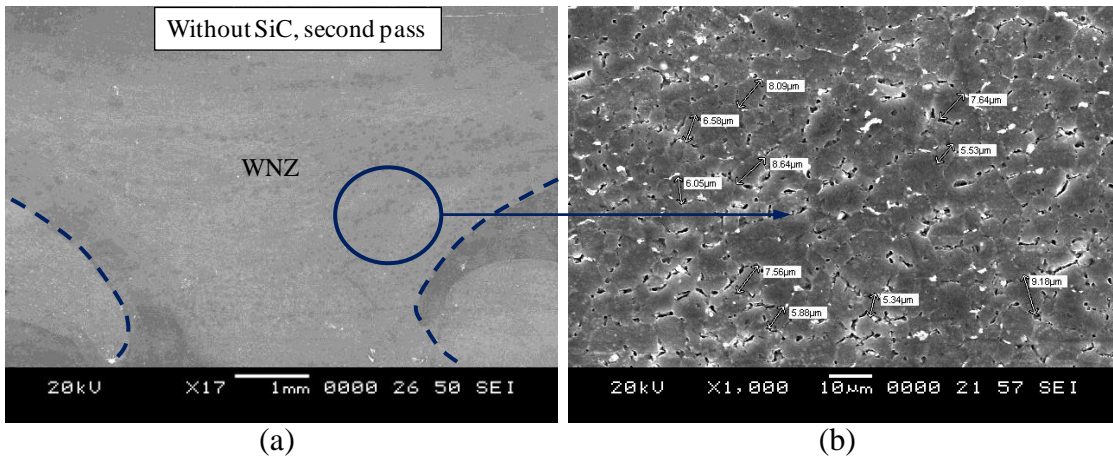


Figure 6.19 (a) SEM images of the WNZ of FSW joint without SiC_{NP} for FSW second pass (b) higher magnified image of showing grain size range 6-8 µm, (c) average grain size after performing FSW second pass on the FSW joint with different % vol. fractions of SiC_{NP} (5, 8, 13%) and without SiC_{NP}.

Thus, the micro-structural analyses and SEM images shows that the FSW dissimilar aluminium alloys joint prepared with the addition of varying % vol. fraction of SiC_{NP} (5, 8, 13) after the FSW second pass shows considerable outcomes in a homogeneous distribution of SiC_{NP} at the WNZ and reduction in grain size compared to the FSW dissimilar aluminium alloys joint produced without SiC_{NP} (0%). The grain size in the

FSW joint reinforced with varying % vol. fractions of SiC_{NP} (5, 8, 13) are in the range 2-5 μm, whereas the FSW joint without SiC_{NP} has shows grain size range 6-8 μm.

The theoretical grain size at the MMNC of the WNZ is calculated by using the Zener-Holoman parameter:

$$dz = \frac{4r}{3v_f} \quad (6.6)$$

where dz - zener limiting grain size, r and v_f are the radius and volume fraction of the reinforcing particles.

Considering the equation (6.6), the grain size decreases with increasing the v_f and decreasing the r . In the present investigation, after performing the FSW second pass and having the presence of the % vol. fraction of SiC_{NP} (3, 5, 9 %) at the WNZ, the calculated theoretical dz is shown in Table 6.4. The calculated dz is 2.2 μm for 3%, 1.3 μm for 5% and 0.7 μm which is much smaller than actual grain size. The actual grain size is in the range 2-3.5 μm for 3%, 3-5 μm for 5% and 9%. This difference between theoretical dz and actual grain size indicates that increasing the % vol. fraction of SiC_{NP} not all the SiC_{NP} contributes for the hindering the grain growth but results in agglomeration at the WNZ.

Table 6.4. Theoretical zener limiting grain size (dz) and actual grain size in the WNZ after performing FSW second pass.

% vol. fraction of SiC_{NP} (%)	zener limiting grain size (dz), in μm	Actual grain size in the WNZ, in μm
3	2	2-3.5
5	3	3-5
9	5	3-5

From above all observations, the homogeneous distribution of SiC_{NP} to produce a defect-free MMNC at the WNZ depends on the three factors as follows,

- (i) Number of FSW pass,
- (ii) The % vol. fraction of SiC_{NP} at the WNZ and
- (iii) Area of WNZ of the MMNC.

In the first case, an increase in the number of FSW pass helps proper stirring of the material and powder distribution becomes homogeneous at the WNZ (Dolatkhah et al., 2012). The second case suggests that there is a limit for the %vol. fractions of SiC_{NP} reinforcement to be incorporated at the WNZ to produce MMNC without any defects and with the best possible uniform distribution of SiC_{NP} (Wang et al., 2011; Slipenyuk et al., 2006). In the third case, increase in the area of WNZ of the MMNC (Table 6.2) from the FSW first pass to the second pass allows the flow of more amount of plasticized material from both the AS and RS, and occupy the WNZ composite area.

6.7.4 X-Ray Diffraction (XRD) analysis

Figure 6.21 shows the XRD patterns of FSW joint produced for a varying % vol. fractions (5, 8 and 13%) of SiC_{NP} reinforcement during FSW first pass. Since the % vol. fractions of SiC_{NP} reinforced is less compared to the aluminium in the MMNC at the WNZ, the SiC peaks of the FSW dissimilar aluminium alloys joint shows less intensity peaks for 8 and 13% vol. fractions. However, no SiC intensity peaks are identified for the FSW joint fabricated with 5% vol. fraction of SiC_{NP}.

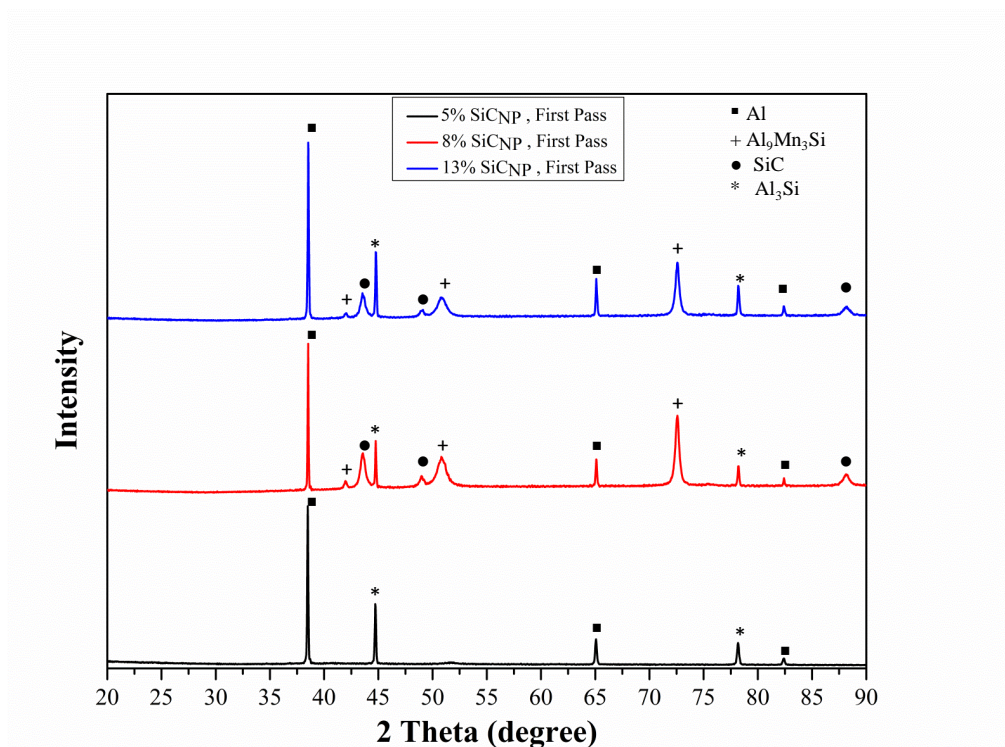


Figure 6.21 XRD analyses showing the intensity peaks in the MMNC at the WNZ for the FSW first pass specimen.

6.7.5 Density measurement at the WNZ

In general, the composites fabricated with varying %vol. fractions of reinforcement, the mechanical properties of the composites depend on the densification mechanism of the composites. In the present investigation, the particle density at the WNZ decides the mechanical behaviour of the composites prepared using FSW technique and by reinforcing the varying %vol. fractions of SiC_{NP} (5, 8, 13%) at the WNZ. The high particle density at the WNZ results in fine grains which exerts a strong pinning effect on the boundaries and hinders the grain growth and helps in strengthening mechanism by dislocations moving along the boundaries of the grains is the main densification mechanism (Markó et al., 2014; Kumar et al., 2017). On the other hand, a low particle density at the WNZ results in the porosity around the SiC_{NP} and this result in interface de-bonding between matrix-SiC_{NP} leading to premature failure of the specimens (Markó et al. 2014).

In the present investigation, the MMNC are produced by using FSW technique and reinforcing the varying % vol. fractions of SiC_{NP} at the WNZ, and the mechanical properties of the MMNC depend on the densification mechanism, especially around the SiC_{NP}. Thus, an attempt is made to find the density of the MMNC at the WNZ using the Rule of Mixture (ROM) and compared with experimental data of the FSW dissimilar aluminium alloys joint produced after FSW second pass. The ROM considers the property (density) of the composite as the volume weighted averages of the properties of the components assuming the components are non-interacting during deformation (Scudino et al., 2009; Wang et al., 2015). The ROM describes the effect of varying % vol. fraction of reinforcement on the properties of MMNC at the WNZ and is calculated as follows,

$$P_c = V_m \cdot P_m + V_f \cdot P_f \quad (6.7)$$

where, P , is the property (density), P_c is the density of the composite, P_m is the density of the aluminium alloy used as matrix, 2.7 gm/cc, P_f is the density of the reinforcement (SiC_{NP}), 3.1 gm/cc, V is volume fraction, V_m is the volume fraction of

the matrix, V_f is volume fraction of the reinforcement. The subscripts c, m, f represents composite, matrix and reinforcement at the WNZ.

For measuring the actual density of the FSW joint produced with reinforcing the varying %vol. fractions of SiC_{NP} (5, 8, 13%) and after the FSW second pass, the specimens are extracted carefully by wire EDM process from the WNZ region. The specimen in a ‘cube’ shape with equal dimensions of length, width and height equal to 2.15 mm are extracted from three different regions of WNZ including the porous region present around the SiC_{NP} . Figure 6.22 shows an example of specimen extraction locations from the WNZ for measuring the ‘mass’ of each specimen. The ‘mass’ of each specimen extracted having the distribution of SiC_{NP} (5, 8, 13%) at the WNZ is measured using density weighing machine VibraHT (make: ESSAE) having precision up to 0.0001 gm. The details of the machine and density measurement procedures are given in the Chapter 3, Section 3.7.

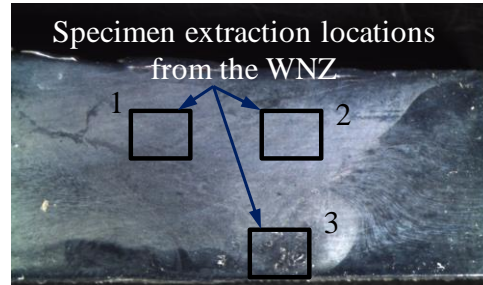


Figure 6.22 An example of the specimen extraction locations marked ‘1’, ‘2’, and ‘3’ from the MMNC at the WNZ after the FSW second process.

The average actual density is calculated for each of the specimen extracted from the WNZ. The predicted density P_c from the equation (6.7) and measured the actual density of the FSW joint are shown in Table 6.5.

Figure 6.23 shows the comparison between the theoretically calculated densities using ROM of equation (6.7) with the actual measured density of the specimen extracted from the WNZ. Figure 6.23 is plotted for density for the FSW second pass, which ensures homogeneous dispersion of SiC_{NP} compared to FSW first pass.

Table 6.5. Theoretical density from ROM and the actual density of the composite with varying % vol. fractions of SiC_{NP} as a reinforcement at the WNZ.

% vol. fraction of SiC _{NP} (%)	Parameters	Predicted density from ROM, in gm/cc	Actual density measured experimentally, in gm/cc
0	$V_m=1, P_m=2.7$ $V_f=0, P_f=0$	2.7	2.7
5	$V_m=0.95, P_m=2.7$ $V_f=0.05, P_f=3.1$	2.72	2.71±0.02
8	$V_m=0.92, P_m=2.7$ $V_f=0.08, P_f=3.1$	2.732	2.7±0.02
13	$V_m=0.87, P_m=2.7$ $V_f=0.13, P_f=3.1$	2.8	2.73±0.02

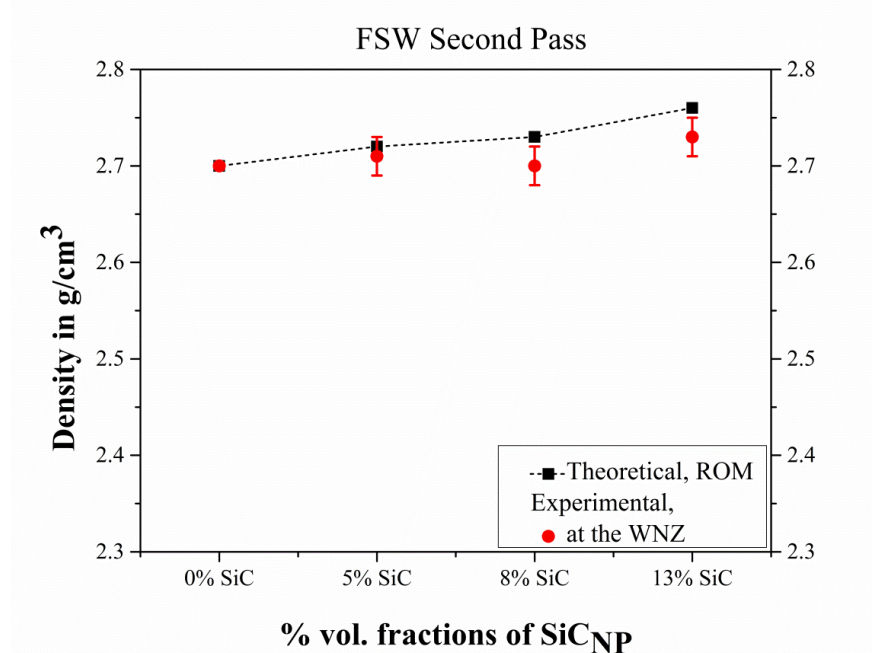


Figure 6.23 Comparison of the density of the FSW joint as a function of varying % vol. fraction of SiC_{NP} at the WNZ for the FSW second pass.

In Figure 6.23, the experimental density of the specimen with 5% SiC_{NP} at the WNZ shows a relative density of 99% confirming homogeneous distribution of reinforcement at the WNZ during FSW second pass. However, with the increase in the % vol. fractions of SiC_{NP} at the WNZ to 8 and 13% shows a decrease in the relative density to 98 and 97.5% respectively. Increase in the % vol. fractions of

SiC_{NP} leads to the inhomogeneous distribution of reinforcement and porosities are formed at the WNZ. These differences in the densities are validated by density measurement shown in Figure 6.23. From the Figure 6.23, the observed low particle density for the FSW joint specimen with high % vol of SiC_{NP} (8, 13%) at the MMNC are the result due to increase in the porosity around the SiC_{NP} and this result in interface de-bonding between matrix-SiC_{NP} leading to premature failure of the specimens (Markó et al., 2014).

6.7.6 Mechanical properties

The FSW dissimilar aluminium alloys joint produced with varying % vol. fractions of SiC_{NP} (5, 8, 13%) reinforcement and without SiC_{NP} at the WNZ are evaluated for the mechanical properties such as tensile and hardness. The below section provides the results of the evaluation of the mechanical properties.

6.7.6.1 Effect of varying percentage volume fractions of SiC_{NP} on tensile properties

The effect of varying % vol. fractions of SiC_{NP} (0, 5, 8, 13%) on the tensile properties of the FSW dissimilar aluminium alloys joint fabricated for FSW first pass and second pass experiment is shown in the Figure 6.24 and Figure 6.25, respectively. The results are also tabulated in Table 6.6 for UTS, YS and % EL of tested specimens.

Referring to the Figure 6.24 and Table 6.6, during the FSW first pass, the tensile specimen of FSW joint produced without SiC_{NP}(0%) for the first pass have shown maximum UTS of 333±8 MPa, YS of 177±3 MPa and %EL of 6.5±0.4. Further, tested tensile specimens of FSW joint produced with 5% vol. fraction of SiC_{NP} at the WNZ observes lower tensile properties, UTS of 273±8 MPa, YS of 166±4 MPa and % EL of 5.58±0.5. Likewise, a lower UTS of 299±7 MPa and 256±6 MPa, YS of 170±3 MPa and 158±4 MPa, and % EL of 6.48±0.5 and 4.03±1.5 are observed for the FSW joint produced with 8 and 13 % vol. fractions SiC_{NP}, respectively. The lower tensile properties observed in the FSW joint reinforced with SiC_{NP} is attributed to the presence of non-homogeneous distribution and agglomeration of reinforcement SiC_{NP} at the WNZ during the FSW first pass as discussed in the preceding sections.

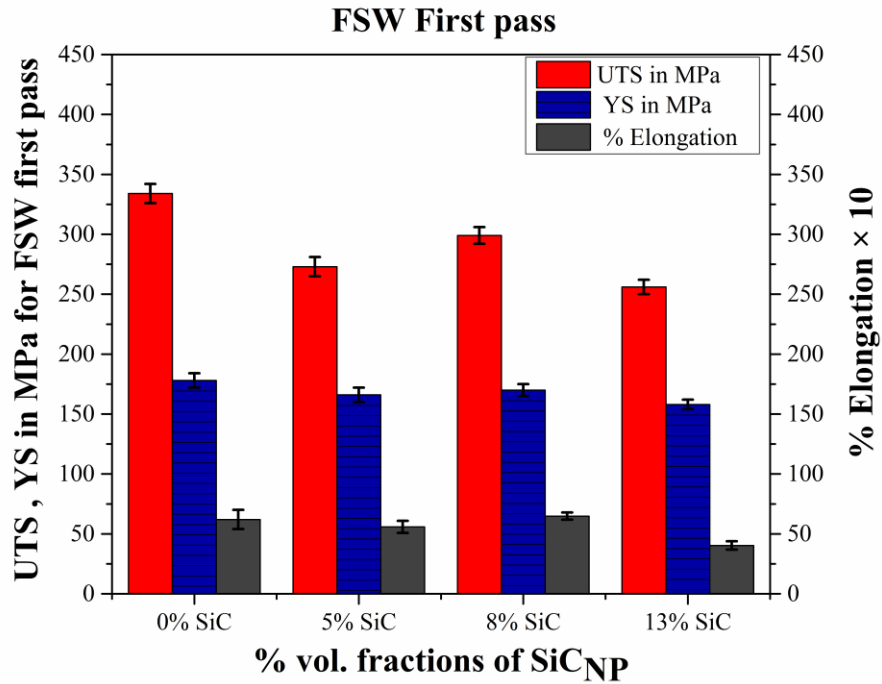


Figure 6.24 Comparison of UTS, YS and %EL for varying % vol. fractions of SiC_{NP} (5, 8, 13%) and without SiC_{NP} (0%) at the WNZ and after the FSW first pass.

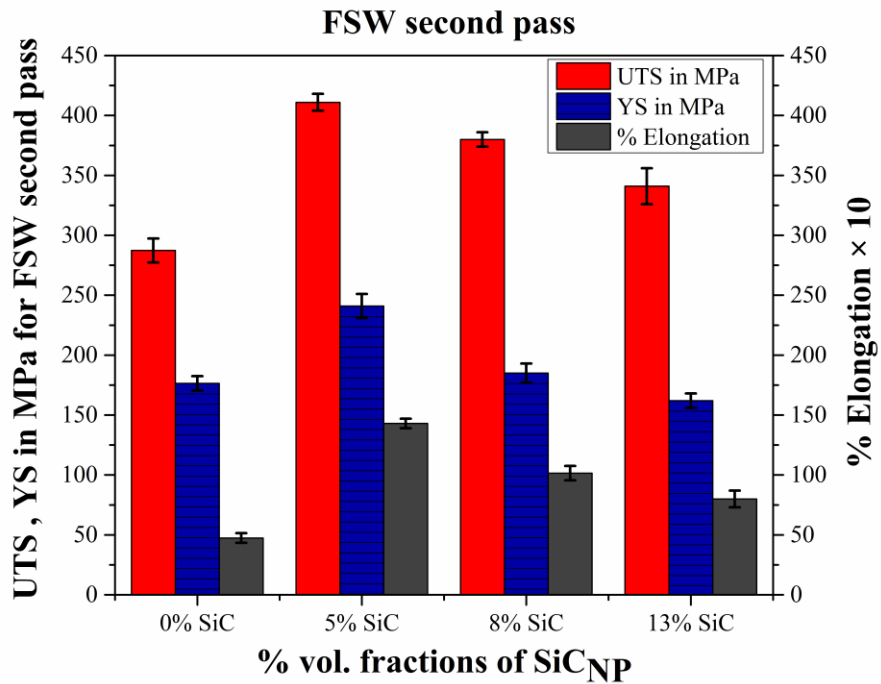


Figure 6.25 Comparison of UTS, YS and %EL for varying % vol. fractions of SiC_{NP} (5, 8, 13%) and without SiC_{NP} (0%) at the WNZ and after the FSW second pass.

Table 6.6 Tensile properties of FSW dissimilar aluminium alloys joint fabricated with varying % vol. fractions of SiC_{NP} (5, 8,13%) and without SiC_{NP} (0%) at the WNZ for FSW first pass and second pass.

FSW First Pass			
% Vol. fractions of SiC_{NP}	UTS (MPa)	YS (MPa)	% Elongation
0%	333±8	177±3	6.5±0.4
5%	273±8	166±4	5.58±0.5
8%	299±7	170±3	6.48±0.5
13%	256±6	158±4	4.03±1.5
FSW Second Pass			
% Vol. fraction of SiC_{NP}	UTS (MPa)	YS (MPa)	% Elongation
0%	287±4	176±6	4.7±0.2
5%	411±7	241±6	14.3±0.2
8%	380±6	185±6	10.1±0.3
13%	341±10	162±4	8±0.3

The tensile properties depend on the factors like amount of SiC_{NP} agglomeration in the WNZ, grain size, amount of dislocation and porosities, the bonding between the reinforcement particle and the alloys (Barmouz et al., 2011). Also, the measured area of WNZ of 40 mm² having accommodated the different V_{fp} for varying % vol. fractions of SiC_{NP} dictates the final tensile properties of the MMNC at the WNZ. For the FSW first pass, an increase in the % vol. fractions of SiC_{NP} in the WNZ from 5 to 8% results increase in the tensile properties of the joints while further increasing the % vol. fractions from 8 to 13% the tensile properties are decreased. These differences in tensile properties are may be due to the influence of “heat input” and “pinning effect” in controlling the grain size as reported by Hamdollahzadeh et al. (2015). In the present investigation, the selected two FSW parameters, TRS of 1000 rpm and TTS of 40 mm/min resulted in the higher heat generation at the WNZ. In the FSW dissimilar aluminium alloys joint fabricated with the 8% vol. fraction of SiC_{NP}, the “pinning effect” dominates the “heat input”, whereas the same is not true in the case of FSW specimen with 5 and 13 %vol. fraction, in the former the “heat input” being dominating and the later results in the severe agglomeration of SiC_{NP} at the WNZ.

From the Figure 6.25 and Table 6.6 for the FSW second pass, the FSW dissimilar aluminium alloys joint fabricated without SiC_{NP} observes a decreasing trend with UTS of 287±4 MPa, YS of 176±6 MPa and %EL of 4.7±0.2 compared to the FSW joint produced without SiC_{NP} for FSW first pass (Figure 6.24). This is due to the softening effect of the WNZ because of an increase in the number of the pass (Barmouz et al., 2011). On the other hand, compared to the FSW first pass, the FSW joint fabricated after performing FSW second pass having 5% vol. fraction of SiC_{NP} at the WNZ observes an increasing trend and results in maximum UTS of 411±7 MPa, YS of 241±6 MPa and % EL of 14.3±0.2. Likewise, compared to the FSW first pass, the FSW joint fabricated after performing the FSW second pass having 8 and 13% SiC_{NP} in the WNZ observes an increasing trend in the tensile properties. Among these FSW dissimilar aluminium alloys joint, the FSW joint with 5% SiC_{NP} yields higher tensile properties compared to the FSW joint produced with 8 and 13% SiC_{NP}. The increase in the tensile properties of the FSW joint tested for a varying % vol. fraction of SiC_{NP} at the WNZ and for the FSW second pass is the result of the homogeneous distribution of SiC_{NP} (Byung-Wook et al., 2012; Hamdollahzadeh et al., 2015). Thus, these experimental investigations results shows that irrespective of the varying % vol. fractions of SiC_{NP} (5, 8, 13%) reinforcement in the WNZ, and compared to the first pass, the tensile properties of the FSW dissimilar aluminium alloys joint produced after the FSW second pass shows an increasing trend in the tensile properties. In addition, the increase in the area of WNZ measuring 40 mm² from FSW first pass to the area of 56 mm² after performing FSW second pass contributes for having accommodated the homogeneous distribution of different %vol. fraction of SiC_{NP} and yields higher tensile properties of the FSW joint.

6.7.6.2 Effect of varying percentage volume fractions of SiC_{NP} and number of FSW pass on hardness properties

Figure 6.26 and Figure 6.27 depicts the microhardness profile for the FSW dissimilar aluminium alloys joint fabricated with varying % vol. fractions of SiC_{NP} and without SiC_{NP} at the WNZ after the FSW first pass and second pass experiments, respectively. As shown in Figure 6.26 after the FSW first pass, the FSW joint exhibit a non-

homogeneous microhardness profile from the AS to RS covering the WNZ and TMAZ.

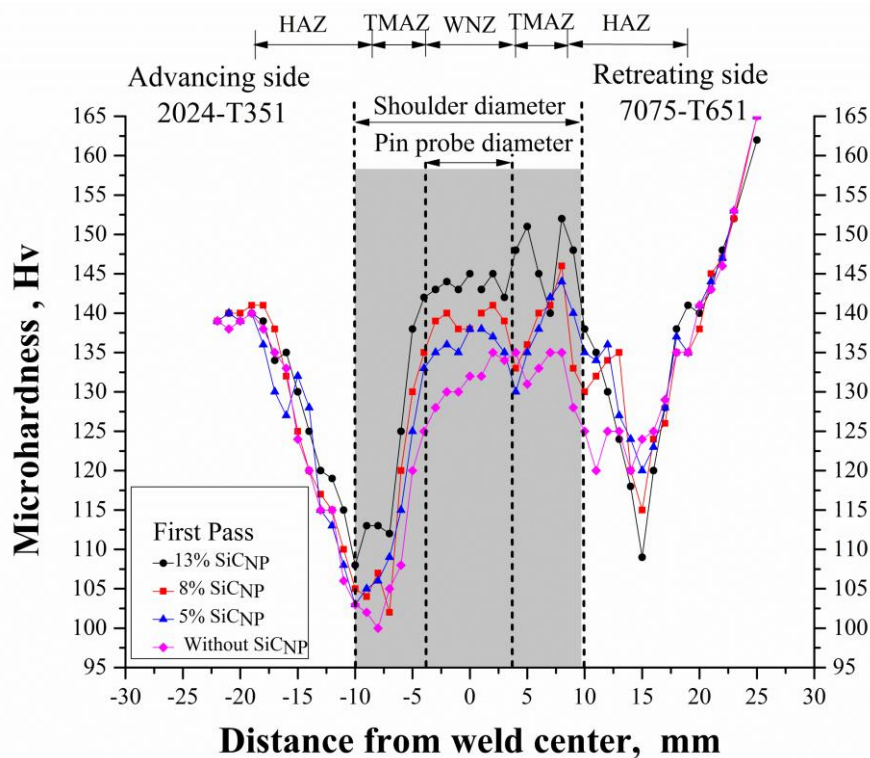


Figure 6.26 Microhardness profile for varying % vol. fractions of SiCNP (0, 5, 8 and 13%) after FSW first pass.

Also, in Figure 6.26, the TMAZ of RS observes higher hardness for all the FSW joint produced with varying % vol. fraction of SiCNP (5, 8, 13%) at the WNZ. The FSW joint with 13% SiCNP and after the FSW first pass have shown the maximum hardness of 152 ± 2 at the TMAZ of RS. However, for all the FSW joint with first pass, the TMAZ and HAZ of AS observe a significant reduction in hardness. These non-homogeneous distributions of hardness are due to lack of stirring and migration of SiCNP towards RS of the TMAZ during the FSW first pass (Dolatkhah et al., 2012; Hamdollahzadeh et al., 2015).

Similarly, in the Figure 6.27, the FSW second pass coupled with the change in the tool rotation direction helps in uniform distributions of SiCNP and observes homogeneity in the microhardness profile of the FSW joint in the WNZ, TMAZ of both AS and RS. However, because of the high heat generation in the second pass, the HAZ of all the FSW joint observes a significant reduction in the hardness. In the

present study, higher hardness of 150 ± 2 Hv was observed at the WNZ for the FSW joint produced with 13% vol. fractions of SiC_{NP} and after the second pass. The hardness of these specimen records an increase of 12 Hv compared to the base metal AA2024-T351 hardness of 138 Hv and remains at a lower hardness by 25 Hv compared to the base metal AA707-T351 hardness of 175 Hv. The FSW dissimilar aluminium alloys joint fabricated without SiC_{NP} shows the much lower hardness of 125 Hv and 115 Hv for FSW first pass and second pass experiment, respectively, compared to the base metal AA2024-T351 and AA7075-T651.

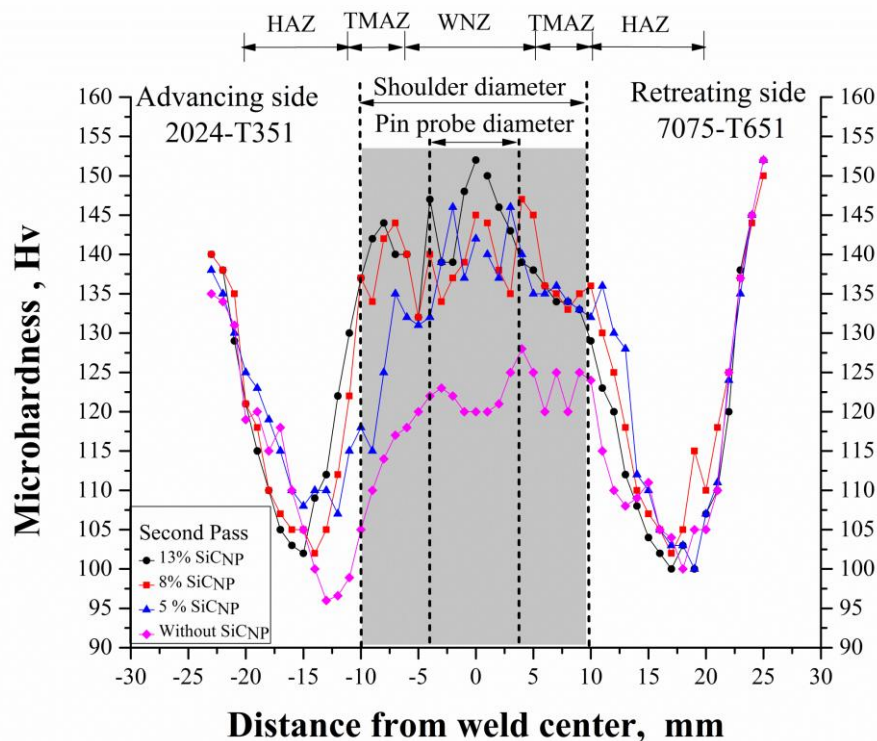


Figure 6.27 Microhardness profile for varying % vol. fractions of SiC_{NP} (0, 5, 8 and 13%) after FSW second pass.

6.7.7 Strengthening mechanism

There are various potential strengthening mechanisms, which are effective in determining the strength of MMC reinforced with nano or micro-particles. The major strengthening mechanisms are as follows,

- (i) Strengthening from coefficient of thermal expansion (CTE), ρ_{CTE}
- (ii) ROM strengthening mechanism, σ_y

- (iii) Load bearing mechanism, $\Delta\sigma_{load}$
- (iv) Hall-Petch strengthening (grain refinement strengthening), σ_o
- (v) Orowan-strengthening, σ_{orowan} , from dislocation bowing by reinforcing particles

The individual strengthening mechanism and its suitability for evaluating the strength of the MMC reinforced with nano or micro particles are discussed in the proceeding section.

6.7.7.1 Coefficient of thermal expansion (CTE)

The strength from CTE mismatch mechanism, $\Delta\sigma_{the}$, (Scudino et al., 2009, Hansen, 1977) is given by,

$$\Delta\sigma_{the} = \eta\mu^m b^m \sqrt{\rho} \quad (6.8)$$

where η is constant of order 1, μ^m is the shear modulus of the matrix, b^m is the burger vector of the matrix and ρ is the dislocation density.

The dislocation density, ρ , is given by,

$$\rho = \frac{12 \Delta T \Delta\alpha f}{b^m D (1 - f)} \quad (6.9)$$

where $\Delta\alpha$ is the difference in thermal expansion between matrix and reinforcement material, ΔT is temperature change from processing temperature to room temperature, f is the volume fraction and D is the average particle diameter of the reinforcement.

From the equation (6.8) and equation (6.9) it is clear that the strength from CTE mismatch mechanism, $\Delta\sigma_{the}$, depends on the density of dislocations, ρ , occurring due to CTE mismatch between matrix and reinforcement, $\Delta\alpha$ (Scudino et al., 2009; Hansen et al., 1977; Kim et al., 2000).

When the particles are in micron size the contribution of $\Delta\sigma_{the}$ to the YS is much larger compared to Orowan strengthening (σ_{orowan}) (Scudino et al., 2009). Further, they report that in the MMNC, the strengthening contribution from CTE mismatch is

minor compared to Orowan-strengthening (σ_{orowan}) and Hall-Petch (Kim et al., 2013; Redsten et al., 1995). However, as reported in the investigation by Kim et al. (2000), Redsten et al. (1995) and Vogt et al. (2009), the strengthening due CTE mismatch is negligible and can be ignored in the composites having particles size below the range 70-80 nm. In the present investigation, as the SiC_{NP} reinforcement average particle diameter, D , is ~50 nm, and the strengthening from CTE mismatch, $\Delta\sigma_{the}$, is ignored. Thus, strength from CTE mismatch mechanism is not suitable for the present investigation.

6.7.7.2 Rule of mixture (ROM)

The yield strength through the ROM, (σ_y), is given by, (Scudino et al., 2009; Humphreys et al., 1988)

$$\sigma_y = \sigma_y^o + \sqrt{(\Delta\sigma_{orowan})^2 + (\Delta\sigma_{the})^2 + (\Delta\sigma_{geo})^2} \quad (6.10)$$

The yield strength through the ROM, σ_y , depends on the yield strength of matrix, σ_{orowan} , strength from CTE mismatch mechanism, $\Delta\sigma_{the}$, and stress contribution due to strain gradient effect (σ_{geo}).

The strength, σ_y , cannot be accurately measured and explained for the composites having a higher volume fraction of reinforcement with relatively large size particles due to particle contiguity (Scudino et al., 2009). In the present study, an increase in the % vol. fractions of SiC_{NP} results in the particle agglomeration. In addition, the σ_y through ROM considers the σ_{the} from CTE mismatch. In the present study, the particle size is ~50 nm the strength from CTE mismatch is ignored. This indicates that strength increase through ROM cannot be explained by considering only dislocation strengthening by σ_{orowan} and σ_{geo} . Thus, the strengthening from ROM is not suitable in the present study.

6.7.7.3 Load bearing mechanism

The load bearing strengthening mechanism, $\Delta\sigma_{load}$, explains the direct strengthening contribution from the presence of reinforcement particles (Kim et al., 2013; Redsten et al., 1995). The $\Delta\sigma_{load}$ is given by,

$$\Delta\sigma_{load} = v_p \sigma_p \quad (6.11)$$

where v_p is volume fraction of reinforcement, σ_p is the yield strength of the particles, σ_m is YS of the matrix, given by,

$$\sigma_m = \frac{1}{2} \sigma_p \quad (6.12)$$

However, the contribution of small % vol. fractions of nano size particles towards strength improvement by the load, $\Delta\sigma_{load}$, in load bearing mechanism can be ignored (Kim et al., 2013; Redsten et al., 1995). Because, the strength improvement in the $\Delta\sigma_{load}$ by nano particles are estimated in the range of 0.5 to 2.5% of the original YS of the matrix (Kim et al., 2013; Redsten et al., 1995). Thus, the strengthening from $\Delta\sigma_{load}$ is not suitable in the present investigation.

6.7.7.4 Hall-Petch strengthening

The Hall-Petch strengthening mainly due to the grain refinement at the WNZ also contributes to the strengthening of the MMNC. The Hall-Petch grain refinement strengthening (Dieter and Bacon, 1988) model is expressed as,

$$\sigma_o = \sigma_i + \kappa D^{-\frac{1}{2}} \quad (6.13)$$

where σ_o is the yield stress which depends on the grain size diameter (D), friction stress (σ_i) resulting from resistance to the crystal lattice dislocation movement and hardening contribution parameter (κ).

However, the equation (6.13) assumes that other Hall-Petch parameters, κ and σ_i cannot be predicted experimentally and must be considered as constant during changes in the processing (Kim et al., 2013). Thus, only grain size, D , must be

considered for calculation of σ_o . Thus, in the present study Hall-Petch strengthening is not considered.

6.7.7.5 Orowan-strengthening

In the present study, the net change in the YS for varying % vol. fraction of SiC_{NP} (5, 8, 13%) and after the FSW second pass is calculated as follows from Orowan-Ashby given by,

$$\sigma_{orowan} = \frac{0.13 G_m b}{\lambda} \ln \frac{r}{b} \quad (6.14)$$

where G_m is the shear modulus of the matrix, b is the burgers vector, r is the radius of reinforcement particles and λ is the mean inter-particle spacing. For the aluminium matrix, G_m is 27 GPa, and b is 0.286 nm.

The inter particle spacing, λ , for the varying % vol. fraction of SiC_{NP} (5, 8, 13%) is given by,

$$\lambda = d_p \left[\left(\frac{1}{2v_p} \right)^{1/3} - 1 \right] \quad (6.15)$$

where d_p is the diameter of SiC_{NP}, v_p is the volume fraction of the reinforcement (Ashby, 1968; Dieter and Bacon, 1988). In the present investigation, the d_p is ~50 nm, and for varying % vol. fraction of SiC_{NP} of 5, 8, 13, the v_p is 0.05, 0.08 and 0.13, respectively.

Table 6.7 shows the predicted results of λ and σ_{orowan} in correspondence with varying %vol. fractions of SiC_{NP} (5, 8, 13) reinforcement in the WNZ ensuring MMNC. Thus, from the Table 6.7, the calculated λ is 57.5 nm, 42.1 nm, 28.3 nm for v_p of 5, 8 and 13% vol. fraction of SiC_{NP}, respectively. Accordingly, the σ_{orowan} predicts a YS of 78 MPa, 106 MPa, 158 MPa for λ of 57.5 nm, 42.1 nm, 28.3 nm, respectively.

Table 6.7 Predicted inter particle spacing, λ , and Orowan strengthening, σ_{orowan} , for the composite with varying %vol. fractions of SiC_{NP} (5, 8, 13) as a reinforcement at the WNZ.

% vol. fraction of SiC _{NP} (%)	Constant Parameters	Interparticle spacing, λ , in nm	Orowan strengthening, σ_{orowan} , in MPa
5	$G_m = 27 \text{ GPa}$ $= 27 \times 10^3 \text{ MPa}$ $b = 0.286 \text{ nm}$ $r = 25 \text{ nm}$	57.5	78
8		42.1	106
13		28.33	158.4

For the varying %vol. fractions of SiC_{NP} (5, 8, 13) and after the FSW second pass, the YS is tabulated and shown in Table 6.8. The experimental YS from the Table 6.8 are 176±6 MPa for the specimen without SiC_{NP}, 241±6 MPa for 5% SiC_{NP}, 185±6 MPa for 8% SiC_{NP} and 162±4 MPa for 13% SiC_{NP}.

Table 6.8. Experimental yield strength obtained for the composites with varying %vol. fractions of SiC_{NP} (0, 5, 8, 13) as a reinforcement at the WNZ.

% vol. fraction of SiC _{NP} (%)	Yield strength, in MPa
0	176±6
5	241±6
8	185±6
13	162±4

It must be noted that σ_{orowan} prediction in YS is based on the facts that there are no agglomeration defects of SiC_{NP} in the WNZ (Kim et al., 2013). Thus, in the present investigation such a situation of defect-free WNZ was observed for the FSW joint having 5% vol. fraction of SiC_{NP}. Hence, the tested tensile specimen of FSW joint without SiC_{NP} yields YS of 176±6 MPa and FSW joint with 5% vol. fraction of SiC_{NP} results in YS of 241±6 MPa. Thus, the difference of YS between these two tested specimens is 65±6 MPa which is in good agreement with the predicted Orowan strengthening of 78 MPa from Table 6.7 which is a contribution from σ_{orowan} .

However, predicted YS from σ_{orowan} for the FSW dissimilar aluminium alloys joint with 8 and 13% vol. fraction of SiC_{NP} is not in good agreement with the experimental YS. The lower YS observed in the experimental data tested FSW joint with 8 and 13% of SiC_{NP} are mainly due to the increase in the % vol. fractions of SiC_{NP} which results in agglomeration of SiC_{NP} in some regions of the WNZ. Thus, in the present study strength contribution from the σ_{orowan} is more suitable and the same is considered.

6.7.8 Fractography

Figure 6.28 (a-c) shows the photograph of the failure locations of the FSW dissimilar aluminium alloys joint tested for the tensile load. Figure 6.28 (a), the FSW joint produced with 5% vol. fraction of SiC_{NP} using FSW first pass and second pass has shown different failure locations. The FSW joint processed with FSW first pass has failed at the WNZ. This kind of premature failure location at the WNZ is due to non-homogeneous distributions and agglomeration of the SiC_{NP}. However, in the Figure 6.28 (a), the same FSW joint after performing the FSW second pass, the fracture took place is away from the WNZ and occurs in the HAZ of either AS or RS. This is due to the homogeneous distributions of SiC_{NP} and its good interfacial bonding with aluminium alloy matrix at the WNZ. Figure 6.28 (b-c) shows the failure location at the WNZ for both the tensile tested specimen of FSW dissimilar alloys joint produced with 8 and 13% vol. fraction of SiC_{NP}, and after FSW first pass and the second pass. This is due to the increase in the % vol. fractions of SiC_{NP} reinforcement that results in more clusters of the SiC_{NP} and segregation of the nano particles from the matrix.

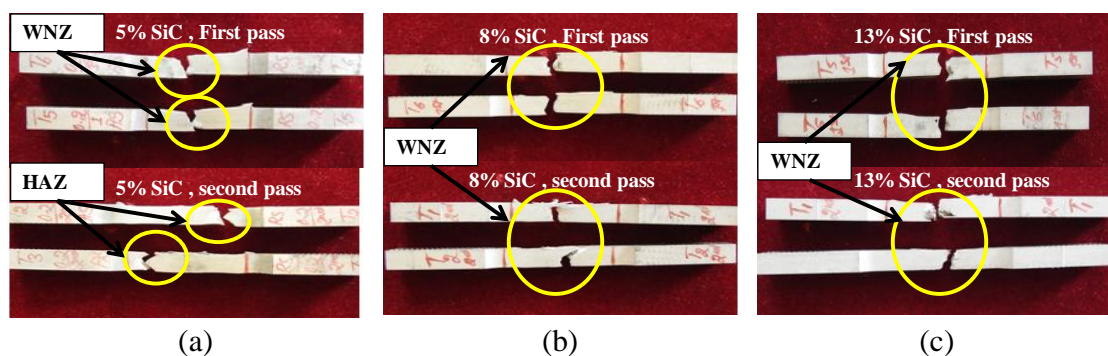


Figure 6.28 Tested tensile specimens and fracture locations corresponding to each % vol. fractions of SiC_{NP} (a) 5% , (b) 8% , (c) 13% , and FSW pass.

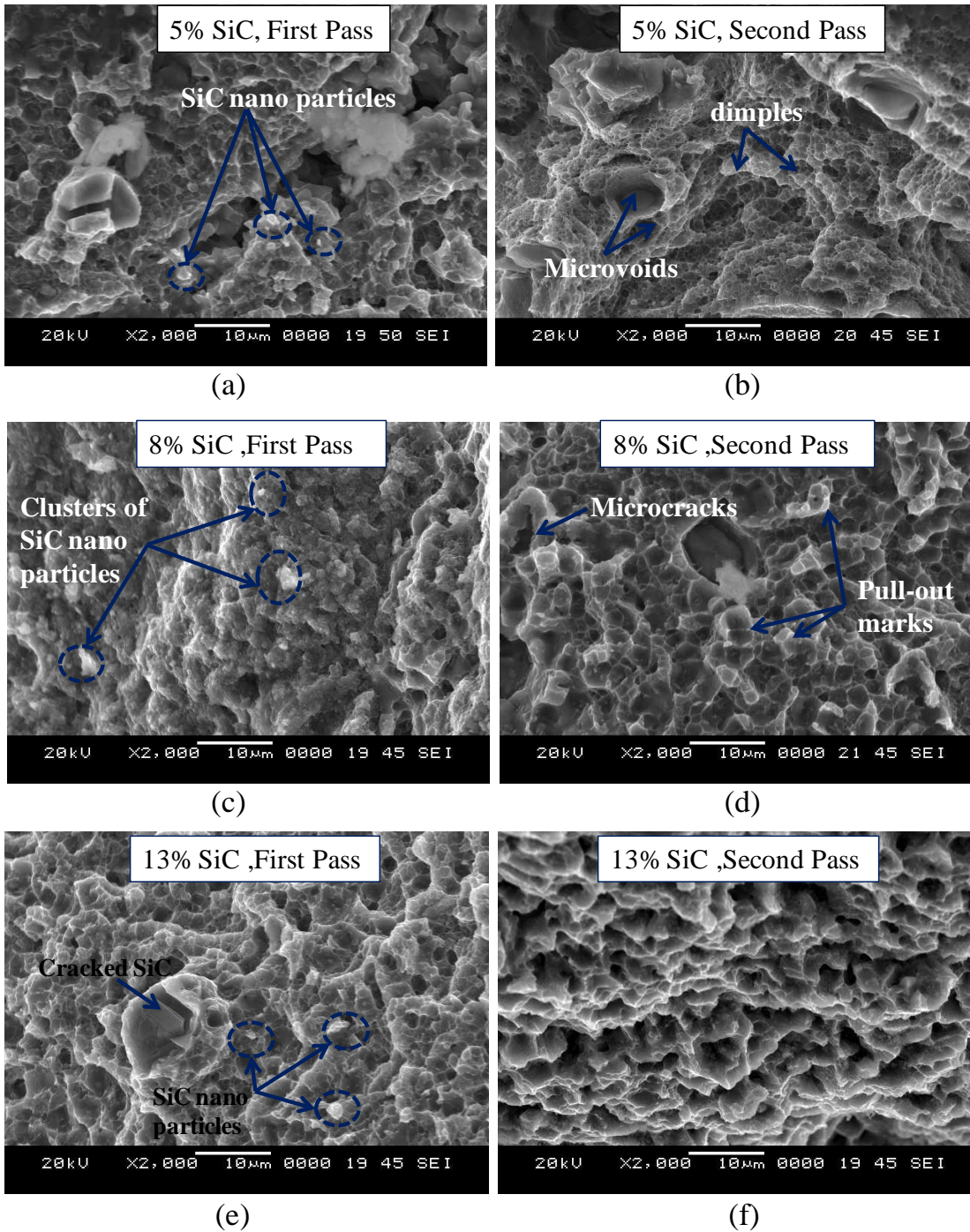


Figure 6.29 SEM images showing fracture features of FSW joint for varying % vol. fractions of SiC_{NP} 5% with FSW (a) first pass and (b) second pass; 8% with FSW (c) first pass and (d) second pass ; and 13 % with FSW (e) first pass and (f) second pass.

Figure 6.29 (a) shows the SEM image of the tensile specimen fracture locations of FSW dissimilar alloys joint reinforced with 5% vol. fractions of SiC_{NP} and processed with FSW first pass. The SEM images shows clusters and agglomerated SiC_{NP} that

leads to lower UTS, YS and % elongation, and the failure occurs at WNZ (Figure 6.28 (a)). However, the SEM images of the tensile specimen fracture locations for the same FSW joint after the FSW second pass is shown in the Figure 6.29 (b) consisting of a large number of small-sized fine dimples and these features results in higher tensile properties, and specimen failure exhibits ductility nature. The SEM images in the Figure 6.29 (c) and Figure 6.29 (e) shows the presence of more clusters of the SiC_{NP} and segregation of the nano particles from the matrix because of the increase in the %vol. fraction of SiC_{NP} reinforcement to 8 and 13%, respectively. On the other hand, fracture surface SEM images shown in Figure 6.29 (d) for the FSW dissimilar alloys joint consisting of 8% vol. fractions of SiC_{NP} after the FSW second pass exhibits a much refined and good interfacial bonding between matrix and SiC_{NP} evidenced with pull-out marks.

6.7.9 Overall conclusion from the effects of SiC_{NP} reinforcement on FSW dissimilar aluminium alloys joint

The FSW dissimilar aluminium alloys joints are fabricated by reinforcing the SiC_{NP} at the WNZ and performing FSW process to obtain MMNC at the WNZ. In the first stage of the experimental investigation, fixed % vol. fractions of SiC_{NP} (5%) are reinforced in the rectangular groove and FSW joint are fabricated by considering varying TRS range 400 rpm to 1800 rpm, constant TTS, 40 mm/min, TPD, 6.20 mm and FSW first pass. In the second stage of experimental investigations, FSW dissimilar aluminium alloys joint have been fabricated by reinforcing the varying % vol. fraction (5, 8, 13%) of SiC_{NP} and without SiC_{NP} (0%). The FSW parameters of TRS 1000 rpm, TTS of 40 mm/min are kept constant and FSW first pass and the second pass was performed to obtain MMNC at the WNZ.

In the first stage of experiments, it was found that the TRS influenced the distribution of SiC_{NP} in the WNZ, macro and microstructure, tensile properties of the FSW dissimilar aluminium alloys joint. Higher tensile properties such as UTS, 380 MPa, YS, 190 MPa and % EL, 13.5 was obtained for the optimum TRS, 1012 rpm, constant TTS, 40 mm/min, TPD, 6.2 mm and with the combination of FSW first pass. Lower UTS, YS and % EL are observed for decreasing the TRS below 800 rpm and as well

as increasing the TRS above 1275 rpm. The decreasing in the TRS reduces the heat input to the WNZ resulting in poor material flow from the AS to the RS and distribution of SiC_{NP} within the WNZ. On the other hand, increasing the TRS above 1275 rpm results in excessive heat input causing defects at the top portion of the WNZ and broken WNZ. Thus, the distribution of SiC_{NP} at the WNZ of FSW dissimilar aluminium alloys joint depend on the optimum TRS. The optimized TRS results in joints with defect-free WNZ and higher tensile strength. These experimental investigations help in understanding the effect of TRS on the FSW dissimilar aluminium alloys joint and helps in carrying out further experiments using the optimized TRS.

In the second stage of the experiments, the FSW dissimilar aluminium alloys joint of AA2024-T351 and AA7075-T651 fabricated with varying % vol. fraction of SiC_{NP} (5, 8, 13%), compared to the FSW first pass, the FSW second pass experiment results in a much homogeneous dispersion of SiC_{NP} in the WNZ and yields higher mechanical properties with better microstructure characteristics compared to the FSW dissimilar aluminium alloys joint without SiC_{NP}. In addition, compared to the area of the WNZ after the FSW first pass (A_{fp}), the increase in the area of the WNZ after the FSW second pass (A_{sp}) helps in accommodating the reinforced SiC_{NP} more homogeneously at the WNZ and results in higher mechanical properties and better microstructure characteristics of the joints. Higher UTS of 411 ± 7 MPa, YS of 241 ± 6 MPa and % EL of 14.3 ± 0.2 was gained for the FSW dissimilar aluminium alloys joint produced with 5% vol. fraction SiC_{NP} reinforcement and after performing FSW second pass. The dissimilar aluminium alloys joint without SiC_{NP} after the FSW second pass has shown results in lower UTS of 287 ± 4 MPa, YS of 176 ± 6 MPa and %EL of 4.7 ± 0.2 compared to all other FSW dissimilar aluminium alloys joint produced with reinforcement of SiC_{NP} after FSW second pass process. The presence of varying % vol. fractions (5, 8, 13%) of SiC_{NP} in the WNZ after FSW second pass observes a decrease in the grain size range 2-4 μm compared to the joint without SiC_{NP} having grain size range 6-8 μm . The higher hardness of 150 Hv was observed for the FSW dissimilar aluminium alloys joint fabricated with 13% vol. fraction SiC_{NP} for the FSW second pass. On the other hand, a lower hardness of 115 Hv was recorded for the

dissimilar aluminium alloys joint fabricated without SiC_{NP} and for the FSW second pass. Based on the experimental investigations, a defect-free MMNC at the WNZ with higher mechanical properties and enhanced microstructures depends on the fixed amount of reinforcement of nano-particle into the WNZ, the number of FSW pass, and the area of the WNZ ensuring MMNC.

6.8 SUMMARY

This chapter has revealed based on the experimental investigations the significant effect of TRS on the distributions of the SiC_{NP} at the WNZ using FSW first pass, and effect of varying % vol. fractions of SiC_{NP} and the role of FSW first and second pass on mechanical properties and microstructure characteristics of the FSW dissimilar aluminium alloys joint. FSW dissimilar aluminium alloys joint produced with 5% vol. fraction SiC_{NP} reinforcement and after performing FSW second pass yields higher UTS of 411±7 MPa, YS of 241±6 MPa and % EL of 14.3±0.2. Also, the presence of varying % vol. fractions (5, 8, 13%) of SiC_{NP} in the WNZ helps in pinning the grain boundaries and observes a decrease in the grain size range 2-4 µm compared to the FSW dissimilar aluminium alloys joint without SiC_{NP} having grain size range 6-8 µm.

CHAPTER-7

CONCLUSIONS

7.1 SUMMARY

Welding and joining of the materials are considered the key step in the manufacturing process. In most of the industries, the metallic structure is joined either by mechanical fastening or metallurgical bonding. The FSW is considered as recent technology of joining the material by solid-state joining technique without melting the material into the molten state. The quality and the properties of the similar or dissimilar materials FSW joint depend upon choosing the FSW major parameters such as rotation speed, traverse speed, plunge depth etc.,. Although, considerable research work has been reported in the field of FSW to arrive optimum FSW parameters by a different method. However, there is a scope to adopt a new optimization method that reduces the complexity in the optimization process and, further with few experimental runs. Present research work has been planned to achieve this goal by optimizing the FSW parameters by a bottom-up experimental approach applied for joining dissimilar aluminium alloys joint by FSW techniques. The bottom-up approach is one of the potential candidatures to eliminate complexity in optimization procedure and number of experimental trials observed in most of the optimization techniques such as DOE statistical tools (Taguchi, RSM), computational and simulation techniques (ANN, CA, ANOVA, ANFIS, etc.). The bottom-up approach involves optimizing the FSW parameters by conducting three stages of experiments, they are (i) optimization of plunge depth by conducting the varying plunge depth (VPD) experiment (ii) optimization of rotation speed by conducting the varying rotation speed (VRS) experiment (iii) optimization of traverse speed by conducting the varying traverse speed (VTS) experiment.

As the research work involves the production of FSW joints using dissimilar materials, the properties of the joints depends on the composition at the weld nugget zone (WNZ). The different tool probe offset with a combination of VTS from the

weld joint line is implemented in order to investigate its effect on the material flow, mechanical properties and microstructure characteristics of the FSW dissimilar aluminium alloys joint. The tool probe offset towards AA7075-T651 was found to be beneficial in enhancing the material flow characteristics and exhibits higher mechanical properties of the FSW dissimilar aluminium alloys joint.

Present research work also concerned with the production of composites at the WNZ of the FSW dissimilar aluminium alloys joint by reinforcing the SiC_{NP} into the rectangular grooves cut on the adjoining surfaces of the individual set of aluminium alloy plates. Investigation involves reinforcing fixed and varying %vol. fractions of SiC_{NP}, and studying the effect of FSW first and second pass on mechanical properties and microstructure characteristics of the composites at the WNZ. The results have shown higher mechanical properties and enhanced microstructure characteristics for the FSW dissimilar aluminium alloys joint reinforced with SiC_{NP} compared to that of without SiC_{NP}.

7.2 KEY CONTRIBUTIONS

The main contributions of this research work are as follows,

1. In this present research work, an attempt has been made to optimize FSW parameters by using a bottom-up experimental approach technique applied to fabricate FSW dissimilar aluminium alloys joint.
2. Combination of different tool probe offset from weld joint line and traverse speed in joining dissimilar aluminium alloys joint by FSW technique has been studied.
3. The effect of tool rotation speed and FSW first pass on properties of FSW dissimilar aluminium alloys joint reinforced with a fixed concentration of SiC_{NP} at the WNZ has been evaluated.
4. The effect of varying percentage of volume fractions of SiC_{NP} reinforcement on the mechanical properties and microstructure characteristics of FSW dissimilar aluminium alloys joint are evaluated and are compared that of joint without SiC_{NP}.

7.3 CONCLUSIONS

Experimental investigations have been carried out to meet the objectives of the research work. A bottom-up experimental approach has been utilized to optimize the FSW parameters for joining the FSW dissimilar aluminium alloys of plate typically AA2024-T351 and AA7075-T651. The influence of tool probe offset and traverse speed have also been investigated. Effect of tool rotation speed and FSW first and second pass on distributions of fixed and varying % vol. fractions of reinforced SiC_{NP} at the WNZ and tensile properties of dissimilar aluminium alloys joint have been investigated. Based on the results and discussion presented in the Chapters 4 to 6, the following conclusions are drawn.

- The optimization of FSW parameters by using DOE statistical tools (Taguchi, RSM), analytical methods, computational and simulation techniques (ANN, CA, ANOVA, ANFIS, etc.) requires more number of experimental runs and trials. An experimental technique associated with the bottom-up approach for obtaining the optimum FSW parameters is one of the potential candidatures to eliminate complexity in the procedure further with few numbers of runs. The range of parameters that can be investigated using a bottom-up approach in a single experimental trial is much larger in numbers when compared to the other optimization techniques.
- The FSW dissimilar aluminium alloys joint of AA2024-T451 and AA7075-T651 are fabricated using two different types of tool geometry. The current study of using the bottom-up experimental approach for optimizing the FSW parameters reveals that the approach has provided better results for FSW dissimilar aluminium alloys joint properties irrespective of tool geometry. Optimized FSW parameters for taper threaded cylindrical tool are TPD, 6.20 mm, TRS, 650 rpm and TTS, 150 mm/min yields higher tensile properties such as ultimate tensile strength (UTS) of 435 MPa, yield strength (YS) of 290 MPa, percentage elongation (% EL) of 13, and maximum weld joint efficiency (η_{WJ}) of 92% with defect-free microstructures of weld region. Similarly, for taper triangle tool the TPD, 6.20 mm, TRS, 950 rpm and TTS,

90 mm/min yields a higher UTS, 440 MPa, YS, 350 MPa, % EL, 17.5 and η_{WJ} of 93% with enhanced microstructure characteristics at the weld region. This approach can be recommended for producing FSW similar or dissimilar materials joint using different types of tool geometries to obtain better mechanical properties of the FSW joints.

- The experimental investigation involving the production of FSW dissimilar aluminium alloys joint of AA2024-T451 and AA7075-T651 using tool probe offset method in conjunction with traverse speed have shown enhanced mechanical properties and better metallurgical characteristics when the tool probe is made offset towards high strength AA7075-T651 for higher traverse speed. FSW dissimilar aluminium alloys joint produced with tool offset distance of 1 mm towards AA7075-T651 with TTS of 110 mm/min, constant TPD of 6.20, and TRS of 650 rpm yields UTS of 435 MPa, YS of 375 MPa, % EL of 13.6 and η_{WJ} of 92% .
- The homogeneous distribution of the SiC_{NP} in the WNZ of the FSW dissimilar aluminium alloys joint depends upon the selected FSW parameters and among those the important is rotation speed. The investigation on the effect of tool rotation speed and FSW single pass on FSW dissimilar aluminium alloys joint reinforced with a fixed concentration of SiC_{NP} (5%) have shown a uniform distribution of SiC_{NP} at the WNZ with higher rotation speed range 1000 to 1100 rpm.
- The experimental investigations to study the effect of varying volume fractions of SiC_{NP} (5, 8, 13%) reinforcement to fabricate composites at the WNZ of the FSW dissimilar aluminium alloys joint have shown higher mechanical and better metallurgical characteristics after FSW second pass, compared to the FSW joint without SiC_{NP} . The FSW joint reinforced with 5% vol. fraction and after performing the FSW second pass results in UTS of 418 MPa, YS of 247 MPa and % EL of 14.5 . The decrease in the grain size range 2-4 μm observed at the WNZ of the MMNC of the FSW dissimilar

aluminium alloys joint reinforced with varying % vol. fractions of SiC_{NP} (5, 8, 13%) compared to the WNZ without SiC_{NP} having grain size range 6-8 μm.

- The experimental investigations involving production of FSW dissimilar aluminium alloys joint reinforced with varying % vol. fractions of SiC_{NP} (5, 8, 13%) reveals that the strength of FSW joint reinforced with SiC_{NP} depends upon the percentage volume fractions reinforcement at the WNZ, number of FSW pass and the area of the WNZ.

7.4 SCOPE FOR FURTHER RESEARCH

The scope for further research enables to:

- investigate the influence of tool tilt angle and tool geometries that includes types of shoulder features (concave, convex, scrolled), pin profile (square, triflute, straight cylinder etc.) on the FSW dissimilar aluminium alloys joint using a bottom-up experimental approach.
- investigate the influence of different types of tool probe profile and their offset from weld joint interface in conjunction with tool rotation and traverse speed.
- investigate the effect of SiC_{NP} reinforcement on grain growth stability of the heat treated FSW joints and FSP surface composites.

REFERENCES

- Abbasi, M., Abdollahzadeh, A., Bagheri, B., and Omidvar, H. (2015). "The effect of SiC particle addition during FSW on microstructure and mechanical properties of AZ31 magnesium alloy". *Journal of Materials engineering and performance*, 24(12), 5037-5045.
- Akramifard, H.R., Shamanian, M., Sabbaghian, M., and Esmailzadeh, M. (2014). "Microstructure and mechanical properties of Cu/ SiC metal matrix composite fabricated via friction stir processing". *Material & Design*, 54, 838-844.
- Alvarez, P., Janeiro, G., Da Silva A.A.M., Aldanondo, E., and Echeverría, A. (2010). "Material flow and mixing patterns during dissimilar FSW". *Science and Technology of Welding and Joining*, 15 (8), 648-653.
- Al-Roubaiy, A. O., Nabat, S. M., and Batako, A. D. (2014). "Experimental and theoretical analysis of friction stir welding of Al–Cu joints". *The International Journal of Advanced Manufacturing Technology*, 71(9-12), 1631-1642.
- Amancio-Filho, S.T., Sheikhi, S., Dos Santos, J.F., and Bolfarini, C. (2008). "Preliminary study on the microstructure and mechanical properties of dissimilar friction stir welds in aircraft aluminium alloys 2024-T351 and 6056-T4". *Journal of Materials Processing Technology*, 206(1), 132-142.
- Aonuma, M., and Nakata, K. (2012). "Dissimilar metal joining of ZK60 magnesium alloy and titanium by friction stir welding". *Materials Science and Engineering: B*, 177(7), 543-548.
- Ashby, M. F. (1968). "The theory of the critical shear stress and work hardening of dispersion-hardened crystals". In: *Proceeding of second Bolton landing conference on oxide dispersion strengthening*. Gordon and Breach, Science Publishers, Inc., New York, 143.

Astarita, A., Squillace, A., and Carrino, L. (2014). "Experimental study of the forces acting on the tool in the friction-stir welding of AA2024-T3 sheets". *Journal of materials engineering and performance*, 23(10), 3754-3761.

Aval, H. J. (2015). "Influences of pin profile on the mechanical and microstructural behaviors in dissimilar friction stir welded AA6082-AA7075 butt Joint". *Materials and Design*, 67, 413-421.

Aval, H. J., Serajzadeh, S., and Kokabi, A. H. (2011). "Thermo-mechanical and microstructural issues in dissimilar friction stir welding of AA5086-AA6061". *Journal of materials science*, 46(10), 3258-3268.

Azizieh, M, Kokabi, A.H., and Abachi, P. (2011). "Effect of rotational speed and probe profile on microstructure and hardness of AZ31/Al₂O₃ nanocomposites fabricated by friction stir processing". *Material & Design*, 32(4), 2034-2041.

Bahrami, M., Dehghani, K., and Givi, M.K., (2014). "A novel approach to develop aluminum matrix nano-composite employing friction stir welding technique". *Material & Design*, 53: 217-225.

Bahrami, M., Givi, M.K., Dehghani, K., and Parvin, N.(2014). "On the role of pin geometry in microstructure and mechanical properties of AA7075/SiC nano-composite fabricated by friction stir welding technique". *Material & Design*, 53, 519-527.

Bahrami, M., Nikoo,M.F., and Givi, M.K.B.(2015). "Microstructural and mechanical behaviors of nano-SiC-reinforced AA7075-O FSW joints prepared through two passes". *Materials Science and Engineering: A*, 626, 220-228.

Balasubramanian., V.(2008). "Relationship between base metal properties and friction stir welding process parameters". *Materials Science and Engineering: A*, 480(1), 397-403.

Barmouz, M., Asadi, P., Givi, M.B., and Taherishargh, M. (2011). "Investigation of mechanical properties of Cu/SiC composite fabricated by FSP: effect of SiC particles

size and volume fraction”. *Materials Science and Engineering: A*, 528(3), 1740-1749.

Bodaghi M., and Dehghani, K. (2017). “Friction stir welding of AA5052: the effects of SiC nano-particles addition”. *International Journal of Advanced Manufacturing Technology*, 88 (9-12), 2651-2660.

Buffa, G., Hua, J., Shivpuri, R., and Fratini, L. (2006). “Design of the friction stir welding tool using the continuum based FEM model”. *Materials Science and Engineering: A*, 419 (1), 381-388.

Buffa, G., Fratini, L., & Shivpuri, R. (2007). “CDRX modelling in friction stir welding of AA7075-T6 aluminum alloy: Analytical approaches”. *Journal of Materials Processing Technology*, 191(1-3), 356-359.

Byung-Wook, A.H., Don-Hyun, C.H., Yong-Hwan, K.I., and Seung-Boo, J.U.(2012). “Fabrication of SiCp/AA5083 composite via friction stir welding”. *Transactions of Nonferrous Metals Society of China*, 22, 634-638.

Cavaliere, P., and Panella, F.W., (2008). “Effect of tool position on the fatigue properties of dissimilar 2024-7075 sheets joined by friction stir welding”. *Journal of materials processing technology*, 206(1), 249-255

Chen, C. M., and Kovacevic, R. (2004). “Joining of Al 6061 alloy to AISI 1018 steel by combined effects of fusion and solid state welding”. *International Journal of Machine Tools and Manufacture*, 44(11), 1205-1214.

Cole, E. G., Fehrenbacher, A., Duffie, N. A., Zinn, M. R., Pfefferkorn, F. E., and Ferrier, N. J. (2014). “Weld temperature effects during friction stir welding of dissimilar aluminum alloys 6061-T6 and 7075-T6”. *The International Journal of Advanced Manufacturing Technology*, 71(1-4), 643-652.

Colegrove, P. A., and Shercliff, H. R. (2005). “3-Dimensional CFD modelling of flow round a threaded friction stir welding tool profile”. *Journal of materials processing technology*, 169(2), 320-327.

D'Urso, G., Giardini, C., Lorenzi, S. and Pastore, T. (2014). "Fatigue crack growth in the welding nugget of FSW joints of a 6060 aluminum alloy". *Journal of Materials processing and Technology*, 214(10), 2075-2084.

Da Silva, A.A.M., Arruti, E., Janeiro, G., Aldanondo, E., Alvarez, P., and Echeverria, A. (2011) "Material flow and mechanical behaviour of dissimilar AA2024-T3 and AA7075-T6 aluminium alloys friction stir welds". *Materials and Design*, 32(4), 2021-2027.

DebRoy, T., and Bhadeshia, H. K. D. H. (2010). "Friction stir welding of dissimilar alloys—a perspective". *Science and Technology of Welding and Joining*, 15(4), 266-270.

Derazkola, H. A., Aval, H. J., and Elyasi, M. (2015). "Analysis of process parameters effects on dissimilar friction stir welding of AA1100 and A441 AISI steel". *Science and Technology of Welding and Joining*, 20(7), 553-562.

Dieter, G.E., and Bacon, D. (1988). *Mechanical Metallurgy*, McGraw-Hill.

Dinakaran I., Kalaiselvan, K., Vijay, S.J., and Raja, P. (2012). "Effect of material location and tool rotational speed on microstructure and tensile strength of dissimilar friction stir welded aluminum alloys". *archives of civil and mechanical engineering*, 12(4),446-454.

Dolatkhah, A., Golbabaie, P., Givi, M.B., and Molaiekiya, F. (2012). "Investigating effects of process parameters on microstructural and mechanical properties of Al5052/SiC metal matrix composite fabricated via friction stir processing". *Material & Design*, 37, 458-464.

Don-Hyun, C., Yong-II, K., Dae-Up, K., and Seung-Boo, J.U., (2012). "Effect of SiC particles on microstructure and mechanical property of friction stir processed AA6061-T4". *Transactions of Nonferrous Metals Society of China*, 22, 614-618.

Elangovan, K., and Balasubramanian, V. (2008). "Influences of tool pin profile and welding speed on the formation of friction stir processing zone in AA2219 aluminium alloy". *Journal of materials processing technology*, 200(1-3), 163-175.

El-Rayes, M.M., and El-Danaf, E.A., (2012). "The influence of multi-pass friction stir processing on the microstructural and mechanical properties of Aluminum Alloy 6082". *Journal of Materials processing and Technology*, 212(5), 1157-1168.

Fratini, L. I. V. A. N., Pasta, S. A. L. V. A. T. O. R. E., and Reynolds, A. P. (2009). "Fatigue crack growth in 2024-T351 friction stir welded joints: Longitudinal residual stress and microstructural effects". *International Journal of Fatigue*, 31(3), 495-500.

Fratini, L., Buffa, G., and Palmeri, D. (2009). Using a neural network for predicting the average grain size in friction stir welding processes. *Computers & Structures*, 87(17-18), 1166-1174.

Firouzdor, V., and Kou, S. (2012). "Al-to-Cu friction stir lap welding". *Metallurgical and Materials Transactions A*, 43(1), 303-315.

Fu, B., Qin, G., Li, F., Meng, X., Zhang, J., and Wu, C. (2015). "Friction stir welding process of dissimilar metals of 6061-T6 aluminum alloy to AZ31B magnesium alloy". *Journal of Materials Processing Technology*, 218, 38-47.

Galvao, I., Leal, R. M., Loureiro, A., and Rodrigues, D. M. (2010). "Material flow in heterogeneous friction stir welding of aluminium and copper thin sheets". *Science and technology of welding and joining*, 15(8), 654-660.

Galvao, I., Loureiro, A., Verdera, D., Gesto, D., and Rodrigues, D. M. (2012). "Influence of tool offsetting on the structure and morphology of dissimilar aluminum to copper friction-stir welds". *Metallurgical and Materials Transactions A*, 43(13), 5096-5105.

Guo, J., Lee, B.Y., Du, Z., Bi, G., Tan, M.J., and Wei, J. (2016). "Effect of nano-particle addition on grain structure evolution of friction stir-processed Al6061 during postweld annealing". *JOM*, 68(8), 2268-2273.

Guo, J.F., Chen, H.C., Sun, C.N., Bi, G., Sun, Z. and Wei, J. (2014). “Friction stir welding of dissimilar materials between AA6061 and AA7075 Al alloys effects of process parameters”. *Materials and Design*, 56, 185-192.

Hall, E.O. (1951) “The deformation and ageing of mild steel: III discussion of results. *Proceedings of the Physical Society. Section B*, 64(9), 747

Hamdollahzadeh, A., Bahrami, M., Nikoo, M.F., Yusefi, A., Givi, M.B., and Parvin, N.(2015). “Microstructure evolutions and mechanical properties of nano-SiC-fortified AA7075 friction stir weldment: The role of second pass processing”. *Journal of Manufacturing processes*, 20, 367-373.

Hansen, N. (1977). “The effect of grain size and strain on the tensile flow stress of aluminium at room temperature”. *Acta Metallurgica*, 25(8), 863-869.

Heidarzadeh, A., Khodaverdizadeh, H., Mahmoudi, A., and Nazari, E. (2012). “Tensile behavior of friction stir welded AA 6061-T4 aluminum alloy joints”. *Materials and Design*, 37, 166-173.

Humphreys, F. J. (1997). “A unified theory of recovery, recrystallization and grain growth, based on the stability and growth of cellular microstructures—II. The effect of second-phase particles”. *Acta materialia*, 45(12), 5031-5039.

Ilangovan, M., Boopathy, S. R., and Balasubramanian, V. (2015). “Effect of tool pin profile on microstructure and tensile properties of friction stir welded dissimilar AA 6061–AA 5086 aluminium alloy joints”. *Defence Technology*, 11(2), 174-184.

Izadi, H., Fallu, J., Abdel-Gwad, A., Liyanage, T., and Gerlich, A.P. (2013). “Analysis of tool geometry in dissimilar Al alloy friction stir welds using optical microscopy and serial sectioning”. *Science and Technology of Welding and Joining*, 18(4), 307-313.

Javadi, Y., Sadeghi, S. and Najafabadi., M.A.(2014). “Taguchi optimization and ultrasonic measurement of residual stresses in the friction stir welding”. *Materials and Design*, 55, 27-34.

- Khadem, S.A., Nategh, S., and Yoozbashizadeh, H. (2011). "Structural and morphological evaluation of Al-5vol.% SiC nanocomposite powder produced by mechanical milling". *Journal of Alloys and Compounds*, 509 (5), 2221-2226.
- Khodir, S.A. and Shibayanagi, T. (2008). "Friction stir welding of dissimilar AA2024 and AA7075 aluminum alloys". *Materials Science and Engineering: B*, 148(1), 82-87.
- Kim, C.S., Sohn, I., Nezafati, M., Ferguson, J.B., Schultz, B.F., Bajestani-Gohari, Z., Rohatgi, P.K., and Cho, K. (2013). "Prediction models for the yield strength of particle-reinforced unimodal pure magnesium (Mg) metal matrix nanocomposites (MMNCs)". *Journal of Materials Science*, 48(12), 4191-4204.
- Kim, H.S. (2000). "On the rule of mixtures for the hardness of particle reinforced composites". *Materials Science and Engineering: A*, 289, 30-33.
- Kim, Y.G., Fujii, H., Tsumura, T., Komazaki, T., and Nakata, K. (2006). "Three defect types in friction stir welding of aluminum die casting alloy". *Materials Science and Engineering: A*, 415(1), 250-254.
- Koilraj, M., Sundareswaran, V., Vijayan, S., & Rao, S. K. (2012). Friction stir welding of dissimilar aluminum alloys AA2219 to AA5083—Optimization of process parameters using Taguchi technique. *Materials & Design*, 42, 1-7.
- Kouzeli, M., and Mortensen, A (2002). "Size dependent strengthening in particle reinforced aluminium". *Acta Materialia*, 50(1), 39-51.
- Kumar, A., Yadav, D., Perugu, C.S., and Kailas, S.V. (2017). "Influence of particulate reinforcement on microstructure evolution and tensile properties of in-situ polymer derived MMC by friction stir processing". *Material & Design*, 113, 99-108.
- Kumar, B.A., and Murugan, N. (2014). "Optimization of friction stir welding process parameters to maximize tensile strength of stir cast AA6061-T6/AlNp composite". *Material & Design*, 57, 383-393.
- Kumar, K., and Kailas, S.V. (2008). "The role of friction stir welding tool on material flow and weld formation". *Materials Science and Engineering: A*, 485(1), 367-374.

Kumar, K., and Satish V. Kailas. (2008). "On the role of axial load and the effect of interface position on the tensile strength of a friction stir welded aluminium alloy". *Materials & Design*, 29 (4), 791-797.

Kwon, Y. J., Saito, N., and Shigematsu, I. (2002). "Friction stir process as a new manufacturing technique of ultrafine grained aluminium alloy". *Journal of materials science letters*, 21(19), 1473-1476.

Lan, S., Liu, X., and Ni, J. (2016). "Microstructural evolution during friction stir welding of dissimilar aluminum alloy to advanced high-strength steel". *The International Journal of Advanced Manufacturing Technology*, 82(9-12), 2183-2193.

Lee, C. J., Huang, J. C., and Hsieh, P. J. (2006). "Mg based nano-composites fabricated by friction stir processing". *Scripta Materialia*, 54(7), 1415-1420.

Lee, W. B., Yeon, Y. M., and Jung, S. B. (2003). "The mechanical properties related to the dominant microstructure in the weld zone of dissimilar formed Al alloy joints by friction stir welding". *Journal of materials science*, 38(20), 4183-4191.

Li, Y., Murr, L. E., and McClure, J. C. (1999). "Flow visualization and residual microstructures associated with the friction-stir welding of 2024 aluminum to 6061 aluminum". *Materials Science and Engineering: A*, 271(1-2), 213-223.

Lim, D. K., Shibayanagi, T., and Gerlich, A. P. (2009). "Synthesis of multi-walled CNT reinforced aluminium alloy composite via friction stir processing". *Materials Science and Engineering: A*, 507(1), 194-199.

Li, D., Yang, X., Cui, L., He, F., and Shen, H. (2014). "Effect of welding parameters on microstructure and mechanical properties of AA6061-T6 butt welded joints by stationary shoulder friction stir welding". *Materials and Design*, 64, 251-260.

Liang, Z., Chen, K., Wang, X., Yao, J., Yang, Q., Zhang, L., and Shan, A. (2013). "Effect of tool offset and tool rotational speed on enhancing mechanical property of Al/Mg dissimilar FSW joints". *Metallurgical and Materials Transactions A*, 44(8), 3721-3731.

- Liu, G., Murr, L. E., Niou, C. S., McClure, J. C., and Vega, F. R. (1997). "Microstructural aspects of the friction-stir welding of 6061-T6 aluminum". *Scripta materialia*, 37(3), 355-361.
- Liu, H., Fujii, H., Maeda, M., and Nogi, K. (2003). "Tensile properties and fracture locations of friction-stir welded joints of 6061-T6 aluminum alloy". *Journal of materials science letters*, 22(15), 1061-1063.
- Liu, H., Hu, Y., Zhao, Y., and Fujii, H. (2015). "Microstructure and mechanical properties of friction stir welded AC4A+ 30vol.% SiCp composite". *Materials & Design*, 65, 395-400.
- Liu, P., Shi, Q., Wang, W., Wang, X., and Zhang, Z. (2008). "Microstructure and XRD analysis of FSW joints for copper T2/aluminium 5A06 dissimilar materials". *Materials letters*, 62(25), 4106-4108.
- Lomolino, S., Tovo, R., and Dos Santos., J.(2005). "On the fatigue behaviour and design curves of friction stir butt-welded Al alloys". *International Journal of Fatigue*, 27(3), 305-316.
- Ma, Z.Y., Li, Y.L., Liang, Y., Zheng, F., Bi, J., and Tjong, S.C. (1996). "Nanometric Si₃N₄ particulate-reinforced aluminum composite". *Materials Science and Engineering: A*, 219(1-2), 229-231.
- Ma, Y. E., Xia, Z. C., Jiang, R. R., and Li, W. (2013). "Effect of welding parameters on mechanical and fatigue properties of friction stir welded 2198-T8 aluminum–lithium alloy joints". *Engineering fracture mechanics*, 114, 1-11.
- Mahoney, M. W., Rhodes, C. G., Flintoff, J. G., Bingel, W. H., and Spurling, R. A. (1998). "Properties of friction-stir-welded 7075 T651 aluminum". *Metallurgical and materials transactions A*, 29(7), 1955-1964.
- Markó, D., Prashanth, K.G, Scudino, S., Wang, Z., Ellendt, N., Uhlenwinkel, V., and Eckert, J. (2014). "Al-based metal matrix composites reinforced with

Fe_{49.9}Co_{35.1}Nb_{7.7}B_{4.5}Si_{2.8} glassy powder: Mechanical behavior under tensile loading”. *Journal of Alloys and compounds*, 615, 382-385.

Mastanaiah, P., Abhay Sharma, and Madhusudhan Reddy, G. (2016). “Dissimilar friction stir welds in AA2219-AA5083 aluminium alloys: Effect of process parameters on material inter-mixing, defect formation, and mechanical properties”. *Transactions of the Indian Institute of Metals*, 69 (7), 1397-1415.

Min, S.O. (2009). “Effects of volume fraction of SiC particles on mechanical properties of SiC/Al composites”. *Transactions of Nonferrous Metals Society of China*, 19(6), 1400-1404.

Mishra, R.S., and Ma, Z.Y. (2005). “Friction stir welding and processing”. *Materials Science Engineering proceedings conference reports*, 50, 1-78.

Mishra, R.S., Ma, Z.Y., and Charit, I. (2003). “Friction stir processing: a novel technique for fabrication of surface composite”. *Materials Science and Engineering: A*, 341(1), 307-310.

Mohammadi, J., Behnamian, Y., Mostafaei, A., Izadi, H., Saeid, T., Kokabi, A. H., and Gerlich, A. P. (2015). Friction stir welding joint of dissimilar materials between AZ31B magnesium and 6061 aluminum alloys: Microstructure studies and mechanical characterizations. *Materials Characterization*, 101, 189-207.

Montgomery, D. C. (2017). *Design and analysis of experiments*. John wiley & sons.

Morisada, Y., Fujii, H., Nagaoka, T., and Fukusumi, M. (2006). “Effect of friction stir processing with SiC particles on microstructure and hardness of AZ31”. *Materials Science and Engineering: A*, 433(1-2), 50-54.

Moshwan, R., Yusof, F., Hassan, M. A., and Rahmat, S. M. (2015). “Effect of tool rotational speed on force generation, microstructure and mechanical properties of friction stir welded Al–Mg–Cr–Mn (AA 5052-O) alloy”. *Materials and Design*, 66, 118-128.

Mouritz, A. P. (2012). *Introduction to aerospace materials*. Elsevier.

Murr, L. E., Li, Y., Flores, R. D., Trillo, E. A., and McClure, J. C. (1998). "Intercalation vortices and related microstructural features in the friction-stir welding of dissimilar metals". *Materials Research Innovations*, 2(3), 150-163.

Nadammal, N., Kailas, S.V., and Suwas, S. (2015). "A bottom-up approach for optimization of friction stir processing parameters; a study on aluminium 2024-T3 alloy". *Materials and Design*, 65, 127-138.

Ni, D. R., Chen, D. L., Xiao, B. L., Wang, D., and Ma, Z. Y. (2013). "Residual stresses and high cycle fatigue properties of friction stir welded SiCp/AA2009 composites". *International Journal of Fatigue*, 55, 64-73.

Okuyucu, H., Kurt, A., and Arcaklioglu, E. (2007). "Artificial neural network application to the friction stir welding of aluminum plates". *Materials and Design*, 28(1), 78-84.

Ouyang, J.H., and Kovacevic, R. (2002). "Material flow and microstructure in the friction stir butt welds of the same and dissimilar aluminum alloys". *Journal of materials Engineering and performance*, 11(1), 51-63.

Palanivel, R., Mathews, P.K., Murugan, N., and Dinaharan, I. (2012). "Effect of tool rotational speed and pin profile on microstructure and tensile strength of dissimilar friction stir welded AA5083-H111 and AA6351-T6 aluminum alloys". *Materials & Design*, 40, 7-16.

Palanivel, R., Mathews, P. K., Dinaharan, I., and Murugan, N. (2014). "Mechanical and metallurgical properties of dissimilar friction stir welded AA5083-H111 and AA6351-T6 aluminum alloys". *Transactions of Nonferrous Metals Society of China*, 24(1), 58-65.

Pantelis, D.I., Karakizis, P.N., Daniolos, N.M., Charitidis, C.A., Koumoulos, E.P., and Dragatogiannis, D.A. (2016). "Microstructural study and mechanical properties of dissimilar friction stir welded AA5083-H111 and AA6082-T6 reinforced with SiC nanoparticles". *Materials and Manufacturing Processes*, 31(3), 264-274.

Park, S.K., Hong, S.T, Park, J.H., Park, K.Y., Kwon, Y.J. and Son, H.J. (2010). “Effect of material locations on properties of friction stir welding joints of dissimilar aluminium alloys”. *Science Technology Welding Joining*, 15(4), 331-336.

Peel, M., Steuwer, A., Preuss, M., and Withers, P.J.(2003).“Microstructure, mechanical properties and residual stresses as a function of welding speed in aluminium AA5083 friction stir welds”. *Acta Materialia*, 51(16), 4791-4801.

Periyasamy, P., Mohan, B., Balasubramanian, V., Rajakumar, S., and Venugopal, S. (2013). “Multi-objective optimization of friction stir welding parameters using desirability approach to join Al/SiC p metal matrix composites”. *Transactions of Nonferrous Metals Society of China*, 23(4), 942-955.

Pirondi, A., and Collini, L. (2009). “Analysis of crack propagation resistance of Al–Al₂O₃ particulate-reinforced composite friction stir welded butt joints” *International Journal of Fatigue*, 31(1), 111-121.

Qian, J., Li, J., Sun, F., Xiong, J., Zhang, F., and Lin, X. (2013). An analytical model to optimize rotation speed and travel speed of friction stir welding for defect-free joints. *Scripta Materialia*, 68 (3-4), 175-178.

Radisavljevic, I., Zivkovic, A., Radovic, N., and Grabulov, V. (2013). “Influence of FSW parameters on formation quality and mechanical properties of Al 2024-T351 butt welded joints”.*Transactions of Nonferrous Metals Society of China*, 23(12), 3525-3539.

Rai, R., De, A., Bhadeshia, H. K. D. H., and DebRoy, T. (2011). “friction stir welding tools”. *Science and Technology of welding and Joining*, 16(4), 325-342.

Rajakumar, S., and Balasubramanian, V. (2012). “Establishing relationships between mechanical properties of aluminium alloys and optimised friction stir welding process parameters”. *Materials and Design*, 40, 17-35.

Rajakumar, S., Muralidharan, C., and Balasubramanian, V. (2011). "Predicting tensile strength, hardness and corrosion rate of friction stir welded AA6061-T 6 aluminium alloy joints". *Materials and Design*, 32(5), 2878-2890.

Rahimian, M., Ehsani, N., Parvin, N., and Baharvandi, H.R. (2009). "The effect of sintering temperature and the amount of reinforcement on the properties of Al–Al₂O₃ composite". *Materials & Design*, 30(8), 3333-3337

Rahimian, M., Parvin, N., and Ehsani, N. (2002). "Size dependent strengthening in particle reinforced aluminium". *Acta Materialia*, 50(1), 39-51.

Rahimian, M., Parvin, N., and Ehsani, N. (2010). "Investigation of particle size and amount of alumina on microstructure and mechanical properties of Al matrix composite made by powder metallurgy ". *Materials Science and Engineering: A*, 527(4), 1031-1038.

Rajakumar, S., and Balasubramanian., V. (2012) "Multi-response optimization of friction-stir-welded AA1100 aluminum alloy joints". *Journal of Materials Engineering and Performance.*, 21(6), 809-822.

Rajakumar, S., Muralidharan, C., and Balasubramanian, V. (2010). Establishing empirical relationships to predict grain size and tensile strength of friction stir welded AA 6061-T6 aluminium alloy joints. *Transactions of Nonferrous Metals Society of China*, 20(10), 1863-1872.

Rajakumar, S., Muralidharan, C., and Balasubramanian,V.(2011). "Influence of friction stir welding process and tool parameters on strength properties of AA7075-T 6 aluminium alloy joints". *Materials and Design*, 32(2), 535-549.

Ramachandran, K. K., Murugan, N., and Shashi Kumar, S. (2015). "Effect of tool axis offset and geometry of tool pin profile on the characteristics of friction stir welded dissimilar joints of aluminum alloy AA5052 and HSLA steel". *Materials Science and Engineering: A*, 639, 219-233.

Redsten, A.M., Klier, E.M., Brown, A.M., and Dunand, D.C. (1995). “Mechanical properties and microstructure of cast oxide-dispersion-strengthened aluminum”. *Materials Science and Engineering: A*, 201(1-2), 88-102

Rhodes, C. G., Mahoney, M. W., Bingel, W. H., Spurling, R. A., and Bampton, C. C. (1997). “Effects of friction stir welding on microstructure of 7075 aluminum”. *Scripta materialia*, 36(1).

Rodriguez, R.I., Jordon, J.B., Allison, P.G., Rushing, T., and Garcia., L.(2015). “Microstructure and mechanical properties of dissimilar friction stir welding of 6061 to 7050 aluminum alloys”. *Materials and Design*, 83, 60-65.

Roshan, S. B., Jooibari, M. B., Teimouri, R., Asgharzadeh-Ahmadi, G., Falahati-Naghibi, M., and Sohrabpoor, H. (2013). “Optimization of friction stir welding process of AA7075 aluminum alloy to achieve desirable mechanical properties using ANFIS models and simulated annealing algorithm”. *The International Journal of Advanced Manufacturing Technology*, 69(5-8), 1803-1818.

Sahu, P. K., Pal, S., Pal, S. K., and Jain, R. (2016). “Influence of plate position, tool offset and tool rotational speed on mechanical properties and microstructures of dissimilar Al/Cu friction stir welding joints”. *Journal of Materials Processing Technology*, 235, 55-67.

Sahu, P. K., and Pal, S. (2015). “Multi-response optimization of process parameters in friction stir welded AM20 magnesium alloy by Taguchi grey relational analysis”. *Journal of Magnesium and Alloys*, 3(1), 36-46.

Sakthivel, T., Sengar, G. S., and Mukhopadhyay, J. (2009). “Effect of welding speed on microstructure and mechanical properties of friction-stir-welded aluminium”. *The International Journal of Advanced Manufacturing Technology*, 43(5-6), 468-473.

Salehi, M., Farnoush, H., and Mohandesi, J.A. (2014). “Fabrication and characterization of functionally graded Al–SiC nanocomposite by using a novel multistep friction stir processing”. *Materials and Design*, 63, 419-426.

- Salehi, M., Saadatmand, M., and Mohandesi, J.A. (2012). "Optimization of process parameters for producing AA6061/SiC nanocomposites by friction stir processing". *Transactions of Nonferrous Metals Society of China*, 22(5), 1055-1063.
- Sathiskumar, R., Murugan, N., Dinaharan, I., and Vijay, S.J. (2013). "Characterization of boron carbide particulate reinforced in situ copper surface composites synthesized using friction stir processing". *Materials Characterization*, 84, 16-27.
- Sato, Y.S., Kokawa, H., Enomoto, M. and Jogan, S. (1999). "Microstructural evolution of 6063 aluminum during friction-stir welding". *Metallurgical and Materials Transactions A*, 30(9), 2429-2437.
- Sato, Y. S., Kurihara, Y., and Kokawa, H. (2006). "Microstructural characteristics of dissimilar butt friction stir welds of AA7075 and AA2024". *Proc., 6th Int. FSW Symp., Saint-Sauveur, Que., Canada*.
- Scudino, S., Liu, G., Prashanth, K.G., Bartusch, B., Surreddi, K.B., Murty, B.S., and Eckert, J. (2009). "Mechanical properties of Al-based metal matrix composites reinforced with Zr-based glassy particles produced by powder metallurgy". *Acta Materialia*, 57(6), 2029-2039.
- Shafiei-Zarghani, A., Kashani-Bozorg, S.F. and Zarei-Hanzaki, A. (2009). "Microstructures and mechanical properties of Al/Al₂O₃ surface nano-composite layer produced by friction stir processing". *Materials Science and Engineering: A*, 500(1), 84-91.
- Sharma, C., Dwivedi, D. K., and Kumar, P. (2012). "Effect of welding parameters on microstructure and mechanical properties of friction stir welded joints of AA7039 aluminum alloy". *Materials & Design (1980-2015)*, 36, 379-390.
- Sharma, S. R., Ma, Z. Y., and Mishra, R. S. (2004). "Effect of friction stir processing on fatigue behavior of A356 alloy". *Scripta Materialia*, 51(3), 237-241.

Shojaeefard, M. H., Akbari, M., Khalkhali, A., Asadi, P. and Parivar, A.H. (2014). “Optimization of microstructural and mechanical properties of friction stir welding using the cellular automaton and Taguchi method”. *Materials and Design*, 64, 660-666.

Shojaeefard, M.H., Behnagh, R.A., Akbari, M., Givi, M.K.B and Farhani, F.(2013) “Modelling and Pareto optimization of mechanical properties of friction stir welded AA7075/AA5083 butt joints using neural network and particle swarm algorithm”. *Materials and Design*, 44,190-198.

Slipenyuk, A., Kuprin, V., Milman, Y., Goncharuk, V., and Eckert, J. (2006). “Properties of P/M processed particle reinforced metal matrix composites specified by reinforcement concentration and matrix-to-reinforcement particle size ratio”. *Acta Materialia*. 54(1), 157-166.

Song, Z., Nakata, K., Wu, A., Liao, J., and Zhou, L. (2014). Influence of probe offset distance on interfacial microstructure and mechanical properties of friction stir butt welded joint of Ti6Al4V and A6061 dissimilar alloys. *Materials & Design*, 57, 269-278.

Steuwer, A., Peel, M.J., and Withers, P.J. (2006). “Dissimilar friction stir welds in AA5083–AA6082: the effect of process parameters on residual stress”. *Materials Science and Engineering: A*, 441(1), 187-196.

Su, J.Q., Nelson, T.W., Mishra, R. and Mahoney, M. (2003). “Microstructural investigation of friction stir welded 7050-T651 aluminium”. *Acta Materialia*, 51(3), 713-729.

Sun, Y.F., and Fujii, H. (2011). “The effect of SiC particles on the microstructure and mechanical properties of friction stir welded pure copper joints”. *Materials Science and Engineering: A*, 528(16), 5470-5475.

Sundaram, N.S., and Murugan, N. (2010). “Tensile behavior of dissimilar friction stir welded joints of aluminium alloys”. *Materials and Design*, 31(9), 4184-4193.

- Tabasi, M., Farahani, M., Givi, M.B., Farzami, M., and Moharami, A. (2016). "Dissimilar friction stir welding of 7075 aluminum alloy to AZ31 magnesium alloy using SiC nanoparticles". *International Journal of Advanced Manufacturing Technology*. 86(1), 705-715.
- Tang, W., Guo, X., McClure, J. C., Murr, L. E., and Nunes, A. (1998). "Heat input and temperature distribution in friction stir welding". *Journal of Materials Processing and Manufacturing Science*, 7, 163-172.
- Thomas, W.M., Nicholas, E.D., Needham, J.C., Murch, M.G., Templesmith, P., and Dawes, C.J.(1991). "Friction stir welding". GB Patent Application No. 9125978 and US Patent No. 5460317, October 1995
- Tjong, S. C. (2007). Novel Nanoparticle-Reinforced Metal Matrix Composites with Enhanced Mechanical Properties. *Advanced engineering materials*, 9(8), 639-652.
- Trimble, D., Monaghan, J., and O'donnell, G. E. (2012). "Force generation during friction stir welding of AA2024-T3". *CIRP annals*, 61(1), 9-12.
- Trimble, D., O' donnell, G.E., and Monaghan, J. (2015). "Characterization of tool shape and rotational speed for increased speed during friction stir welding of AA2024-T3". *Journal of Manufacturing processes*, 17, 141-150.
- Tutunchilar, S., Haghpanahi, M., Givi, M.B., Asadi, P., and Bahemmat. P. (2012). "Simulation of material flow in friction stir processing of a cast Al-Si alloy". *Materials & Design*, 40, 415-426.
- Vijayavel, P., Balasubramanian, V., and Sundaram, S. (2014). "Effect of shoulder diameter to pin diameter (D/d) ratio on tensile strength and ductility of friction stir processed LM25AA-5% SiCp metal matrix composites". *Materials and Design*, 57, 1-9.
- Vijayan, S., Raju, R., & Rao, S. K. (2010). "Multiobjective optimization of friction stir welding process parameters on aluminum alloy AA 5083 using Taguchi-based grey relation analysis". *Materials and Manufacturing Processes*, 25(11), 1206-1212.

Vogt, R., Zhang Z., Li Y., Bonds M., Browning N.D., Lavernia, E.J., and Schoenung, J.M. (2009). “The absence of thermal expansion mismatch strengthening in nanostructured metal–matrix composites”. *Scripta Materialia*, 61(11), 1052-1055.

Wan, Z., Qu, R.T., Scudino, S., Sun, B.A., Prashanth, K.G., Louzguine-Luzgin, D.V., Chen, M.W., Zhang, Z.F., and Eckert, J. (2015). “Hybrid nanostructured aluminum alloy with super-high strength. *NPG Asia Materials*, 7(12), e229

Wang, W., Shi, Q.Y., Liu, P., Li, H.K., and Li, T. (2009). “A novel way to produce bulk SiCp reinforced aluminum metal matrix composites by friction stir processing”. *Journal of Materials Processing Technology*. 209(4), 2099-2103.

Wang, Z., Song, M., Sun, C., and He, Y. (2011). “Effects of particle size and distribution on the mechanical properties of SiC reinforced Al–Cu alloy composites”. *Materials Science and Engineering: A*, 528(3), 1131-1137.

Wang, Z., Qu, R. T., Scudino, S., Sun, B. A., Prashanth, K. G., Louzguine-Luzgin, D. V., Louzguine-Luzgin, Chen, M.W., Zhang, Z.F., and Eckert, J. (2015). “Hybrid nanostructured aluminum alloy with super-high strength”. *NPG Asia Materials*, 7(12), e229.

Wu, A., Song, Z., Nakata, K., Liao, J., & Zhou, L. (2015). “Interface and properties of the friction stir welded joints of titanium alloy Ti6Al4V with aluminum alloy 6061”. *Materials & Design*, 71, 85-92.

Xue, P., Xiao, B. L., Ni, D. R., and Ma, Z. Y. (2010). “Enhanced mechanical properties of friction stir welded dissimilar Al–Cu joint by intermetallic compounds”. *Materials science and engineering: A*, 527(21-22), 5723-5727.

Yaduwanshi, D. K., Bag, S., and Pal, S. (2018). “On the effect of tool offset in hybrid-FSW of copper-aluminium alloy.” *Materials and Manufacturing Processes*, 33(3), 277-287.

Yang, Y., Lan, J., and Li, X. (2004). “Study on bulk aluminum matrix nano-composite fabricated by ultrasonic dispersion of nano-sized SiC particles in molten aluminum alloy”. *Materials Science and Engineering: A* , 380(1), 378-383.

Yazdipour, A., and Heidarzadeh, A. (2016). “Effect of friction stir welding on microstructure and mechanical properties of dissimilar Al 5083-H321 and 316L stainless steel alloy joints”. *Journal of Alloys and Compounds*, 680, 595-603.

Zhang, F., Su, X., Chen, Z., and Nie, Z. (2015). “Effect of welding parameters on microstructure and mechanical properties of friction stir welded joints of a super high strength Al–Zn–Mg–Cu aluminum alloy”. *Materials & Design*, 67,483-491.

Zhang, Z., Xiao, B.L. and Ma, Z.Y. (2014). “Hardness recovery mechanism in the heat-affected zone during long-term natural aging and its influence on the mechanical properties and fracture behavior of friction stir welded 2024Al–T351 joints”. *Acta Materialia*, 73,227-239.

Zhang, Z., and Zhang, H. W. (2009). Numerical studies on the effect of transverse speed in friction stir welding. *Materials & Design*, 30(3), 900-907.

List of Publications based on PhD Research Work

Sl. No.	Title of the Paper	Authors (In the same order as in the paper, underline the Research Scholar's name)	Name of the Journal / Conference / Symposium, Vol., No., Pages	Month & Year of Publication	Category *
1	A Bottom-Up Optimization Approach for Friction Stir Welding Parameters of Dissimilar AA2024-T351 and AA7075-T651 Alloys	<u>Anil Kumar, K.S.</u> , Murigendrappa, S.M., and Hemantha Kumar	Journal of Materials Engineering and Performance, Volume 27, Issue 7, pages 3347-3367. DOI : 10.1007/s11665-017-2746-z (<i>Scopus Indexed, Springer Publication, IF- 1.476</i>)	July, 2017	1
2	Experimental investigation on effects of varying volume fraction of SiC nano particle reinforcement on microstructure and mechanical properties in friction stir welded dissimilar joints of AA2024-T351 and AA7075-T651	<u>Anil Kumar, K.S.</u> , Murigendrappa, S.M., and Hemantha Kumar	Journal Of Materials Research, Volume 34, Issue 7, pages 1229-1247 DOI: 10.1557/jmr.2018.445. (<i>SCI Indexed, Scopus Indexed, Cambridge University Publication, IF-1.495</i>)	April, 2019	1
3	Effect of tool rotation speed on microstructure and tensile properties of FSW joints of 2024-T351 and 7075-T651 reinforced with SiC nano particle: The role of FSW single pass	<u>Anil Kumar, K.S.</u> , Murigendrappa, S.M., Hemantha Kumar and Himanshu Shekhar	International conference on Design, Materials and Manufacture (IcDEM 2018) AIP Conference Proceedings, Volume 1943, Issue No.1, p.020056 (2018), AIP Publishing, DOI : 10.1063/1.5029632 (<i>web of science, Scopus Indexed</i>)	April, 2018	3

4	Influence of tool probe offset and varying traverse speed on microstructure and mechanical properties of FSW dissimilar joints of AA2024-T351 and AA7075-T651	<u>Anil Kumar, K.S.</u> , Murigendrappa, S.M., and Hemantha Kumar	7th International and 28th All India Manufacturing Technology, Design and Research conference (AIMTDR 2018), College of Engineering (CEG), Anna University, Chennai, India (Accepted by <i>springer publication in conference proceedings</i>)	December, 2018	3
---	---	---	--	----------------	---

* Category: 1 : Journal paper, full paper reviewed
2 : Journal paper, Abstract reviewed
3 : Conference/Symposium paper, full paper reviewed
4 : Conference/Symposium paper, abstract reviewed
5 : others (including papers in Workshops, NITK Research Bulletins, Short notes etc.)
(If the paper has been accepted for publication but yet to be published, the supporting documents must be attached.)

Research Scholar

Anil Kumar K.S.

Research Guide

Prof. S.M. Murigendrappa

Research Guide

Dr. Hemantha Kumar

BIO-DATA

1. **Name** : Anil Kumar K.S.
2. **Father's Name** : Shivamurthy K.P.
3. **Date of Birth** : 1/12/1979
4. **Nationality** : Indian
5. **Marital Status** : Married
6. **Address** :

Permanent Address

S/o. Shivamurthy K.P.
D.No. 10/67, Ward No. 10,
"Arunodaya Nilaya",
Karinanjanapura Extension,
Chamarajanagara Talluk & District,
Pin-571313,
Karnataka, India

Work Place

Assistant Professor,
Department of Mechanical Engineering,
JSS Academy of Technical Education,
Dr. Vishnuvardhana Road,
Srinivasapura post,
Bengaluru,
Pin-560060, Karnataka, India.

7. **Mobile Number** : +91-9741207020
8. **E-mail id.** : anilkumar_aks@rediffmail.com
9. **Educational Qualification :**

Qualification	College/school	University/Board	Year of Passing	Performance
Ph.D. in Mechanical Engineering	National Institute of Technology Karnataka	National Institute of Technology Karnataka (NITK), Surathkal, Karnataka	Pursuing	-----
M.Tech in Maintenance Engineering	SJCE College of Engineering, Mysuru, Karnataka.	Visvesvaraya Technological University (VTU), Belagavi, Karnataka.	2005	74.95%
B.E in Mechanical Engineering	SSIT, Tumkur, Karnataka.	Bangalore University (BU), Bangalore, Karnataka.	2001	64.2%

I declare that above information is true and correct to best of my knowledge and belief.

(Anil Kumar K.S.)